

N73-11898

NASA CONTRACTOR
REPORT



NASA CR-2102

NASA CR-2102

CASE FILE
COPY

THERMAL-STRUCTURAL
COMBINED LOADS
DESIGN CRITERIA STUDY

*by V. Deriugin, E. W. Brogren, C. L. Jaeck,
A. L. Brown, and B. E. Clingan*

Prepared by
THE BOEING COMPANY
Seattle, Wash.
for Langley Research Center

NATIONAL AERONAUTICS AND SPACE ADMINISTRATION • WASHINGTON, D. C. • OCTOBER 1972

1. Report No. NASA CR-2102		2. Government Accession No.		3. Recipient's Catalog No.	
4. Title and Subtitle Thermal-Structural Combined Loads Design Criteria Study				5. Report Date October 1972	
				6. Performing Organization Code	
7. Author(s) V. Deriugin, E. W. Brogren, C. L. Jaeck, A. L. Brown, and B. E. Clingan				8. Performing Organization Report No. D180-14647-1	
				10. Work Unit No.	
9. Performing Organization Name and Address The Boeing Company Seattle, Washington				11. Contract or Grant No. NAS1-6024	
				13. Type of Report and Period Covered Contractor Report 1971-72	
12. Sponsoring Agency Name and Address National Aeronautics and Space Administration Washington, D.C. 20546				14. Sponsoring Agency Code	
15. Supplementary Notes					
16. Abstract The objective of this study was to determine methodology for combining thermal structural loads and assessing the effects of the combined loads on the design of a thermal protection system and a hot structure of a high cross range delta wing space shuttle orbiter vehicle. The study presents guidelines for establishing a basis for predicting thermal and pressure environments and for determining limit and ultimate design loads on the vehicle during reentry. Limit trajectories were determined by using dispersions on a representative nominal mission and system parameters expected during the life of the vehicle. Nine chosen locations on the vehicle surface having TPS or hot structures were examined, and weight sensitivity analyses were performed for each location.					
17. Key Words (Suggested by Author(s)) Thermal structural combined loads Space shuttle orbiter Design criteria and recommended practices Structural design weight sensitivities			18. Distribution Statement Unclassified and unlimited		
19. Security Classif. (of this report) Unclassified		20. Security Classif. (of this page) Unclassified		21. No. of Pages 280	22. Price* \$3.00

PREFACE

This is a final report describing a 12-month study conducted between March 1, 1971 and February 29, 1972, by the Research and Engineering Division, Aerospace Group of The Boeing Company, Seattle, Washington 98124. The work was conducted under Contract No. LS-2598-A3 with McDonnell Douglas Astronautics Company (MDAC), with Messrs. C.P. Berry and H.P. Adam as MDAC Task Managers. This contract was funded under Contract NAS1-6024 from NASA Langley Research Center.

The Boeing Company Study Manager was Mr. Vladimir Deriugin, with Mr. E.W. Brogren as Principal Investigator, supported by Mr. C.L. Jaeck in aerothermodynamics, Mr. A.L. Brown in stress, Mr. B.F. Clingan in loads analysis, and Mr. L.H. Hillberg who assisted with the heat-transfer prediction program and the Boeing CHAP program used for the thermal analysis.

The authors wish to acknowledge helpful discussions with Mr. S.I. Gravitz and the contributions of Mr. D.W. Hahn in trajectory analysis, Messrs. H.A. Johnson and F.H. Simpson in material-property determination, Mr. D.W. French in computation support, and Messrs. K.W. Osborne and G. Jensen in art support.

Particular credit is due the Grumman Space Shuttle program team and Mr. Fred Wood, who cooperated very willingly in supplying information required for the characterization of the Grumman G3A orbiter vehicle, and to Boeing Space Shuttle personnel for their helpful discussions and recommendations.

Page Intentionally Left Blank

CONTENTS

	Page
SUMMARY	1
INTRODUCTION	2
SYMBOLS	4
NOMINAL SYSTEM DEFINITION AND CONCEPT SELECTION	10
Configuration Geometry	10
Trajectories	10
Locations and Concepts	11
LIMIT TRAJECTORIES	13
System Constraints	13
Trajectory Dispersions	15
Trajectory Selection Criteria and Tolerance Application	16
Late Reentry and Transition Trajectory Definition	22
THERMAL-STRUCTURAL COMBINED LOADS ANALYSIS	24
Loads Analysis	24
Thermal Analysis	25
Strength Analysis	29
THERMAL PROTECTION SYSTEM AND HOT STRUCTURE DESIGN	32
Baseline Designs	32
Design Parameter Perturbations	34
Final Designs	37
Weight Sensitivity Determination	37
Combined Thermal-Structural Loads Sensitivities	41
TPS Design Margins	47
Reliability Assessment	48
CONCLUSIONS AND RECOMMENDATIONS	51
Aerothermodynamic Environment	51
Loads and Stresses	52
Temperatures and Heat Loads	53
Combination of Weight Sensitivities	55
Maneuver Excursions	56
Recommended Practices and Criteria	56

CONTENTS (Cont.)

	Page
APPENDIX A Geometry Definition	58
APPENDIX B Loads Analysis	60
APPENDIX C Aerothermodynamic Analysis	67
APPENDIX D Thermal Analysis	91
APPENDIX E Strength Analysis and Design Definition	104
APPENDIX F Sample Computation	114
APPENDIX G Recommended Practices and Criteria	120
APPENDIX H Conversion of U.S. Customary Units to S-I Units	129
REFERENCES	273

THERMAL-STRUCTURAL COMBINED LOADS
DESIGN CRITERIA STUDY

By V. Deriugin, E. W. Brogren, C. L. Jaeck, A. L. Brown, and B. E. Clingan
The Boeing Company
Seattle, Washington

SUMMARY

A study was made of the sensitivity of structural design weights at nine selected locations on a high cross-range delta wing Space Shuttle orbiter vehicle. Two groups of parameters were investigated. The first group dealt with vehicle systems and trajectory parameters which included angles of attack and yaw, altitude and atmospheric conditions. The second group included methods and criteria for establishing the thermal and loads environments. The effects of variations of these parameters were expressed in terms of changes in weights of structural or thermal protection system concepts characteristic of a Space Shuttle orbiter design.

The design concepts included radiation-cooled metallic and non-metallic surfaces such as reusable external insulation and carbon/carbon composites, ablators, and hot structure, resulting in fourteen study points. The parameter perturbations were applied only for vehicle reentry, although in assessing design criticality and defining baseline designs the entire vehicle mission was considered. The weight sensitivity comparisons showed that the influence of trajectory and systems parameters were generally comparable to that of method and criteria parameters. The sensitivities to the individual parameters were combined using a root-sum-square technique. Here, no consistent trends could be established, possibly due to the lack of a complete data base. It was shown, however, that over-conservatism could be reduced by using a root-sum-square combination of effects rather than a worst-to-worst case approach. It is suggested that, given adequate dispersion data, a more rigorous probabilistic technique such as the Monte Carlo method should be used for determining combined effects and thus for defining a properly based set of design conditions.

The effects of certain reentry maneuver excursions upon metallic and REI TPS were assessed. The results of this exercise permitted a limited evaluation of the ability of the metallic TPS, designed for limit reentry conditions only, to survive excursions to ultimate loads and corresponding temperatures.

An attempt was made to assess qualitatively the design reliability of the fourteen study point designs by rating the respective design concepts in terms of a set of estimated reliability-related characteristics.

Although all conclusions of this study were very much influenced by the initial assumptions and were dependent on the configuration, trajectory, methods and criteria employed, some general conclusions were reached. Therefore, as a result of this study several recommendations for design practices and criteria were made pertaining to thermal-structural combined loads design procedures.

INTRODUCTION

Early in 1970, NASA initiated a program to prepare structural design criteria applicable to manned Space Shuttle vehicles. The efforts of a NASA/industry committee formed for this purpose resulted in general and mission-oriented criteria which were presented in NASA SP-8057, "Structural Design Criteria Applicable to a Space Shuttle," in November 1970. This document is now accepted and used by industry as a starting point and guideline for structural design criteria. Since the initiation of work on NASA SP-8057, a new awareness of criteria and requirements has evolved among the Space Shuttle Phase B contractors, resulting in additional design criteria documentation applicable to particular contractor vehicle concepts and/or configurations. The criteria thus formulated are largely based on the related experience of the particular contractors in the field of aircraft and space and reentry vehicles. These criteria either confirm and expand the information available in SP-8057 or supplement that document with information developed on the basis of new and, in some cases, tentative concepts or data.

It should be recognized that due to the paucity of data and the as-yet incomplete picture of possible problem areas, this process will continue until enough of a data base can be generated in order to arrive at criteria of a quality and completeness similar to that of the structural design criteria applied presently to modern air transportation systems.

Another task of the NASA/industry committee was the identification of important design criteria problem areas requiring further investigation. One such problem area is the subject of the study described in the present report dealing with thermal-structural combined design criteria. Conceived as an analytical investigation pointing out the leverage of various criteria and a spectrum of both man-independent (trajectory and systems) and man-dependent (methods and criteria) parameters, this study attempted to develop a realization of the relative importance of various criteria design parameters and alternative analysis methods.

The objective of the present program was to assess the effects of combined thermal-structural loading on the design of the thermal protection system and the hot structure of a high cross-range delta wing Space Shuttle orbiter vehicle. The results of the study are intended to assist in establishing a rational basis for predicting thermal and pressure environments and for determining limit and ultimate design loads and temperatures, as expressed by design criteria and recommended practices.

The approach taken in conducting the present study is shown in the form of a flow chart in figure 1. In order to keep the study within limits consistent with the intended scope, a selective approach to the amount of detail was adopted without compromising the overall results and the ensuing conclusions. Selection of detail was based on generally accepted preliminary design practices, previous experience, already available data, inspection procedures using considerations of similarity, and data comparison and extrapolation.

The study began with definition of a nominal system consisting of the vehicle configuration and a representative nominal mission trajectory. The vehicle was a high cross-range delta wing orbiter, the description of which included mass property distribution and the aerodynamic characteristics.

Limit trajectories, leading to the most severe combined thermal and loads design conditions for nine chosen locations having TPS or hot structure on the orbiter were defined. (See Appendix A.) The limit trajectories were determined using dispersions in trajectory and systems parameters reasonably expected during the life of the vehicle.

Thermal and structural analyses were conducted at these nine locations, some of which had alternate design concepts, resulting in a total of fourteen study points. These analyses supported the definition of details and ultimately the weights of the baseline designs at the respective study points. The analysis and sizing operations were repeated for varying requirements arising from different heating and pressure prediction techniques, and varying criteria for determination of limit and ultimate loads and temperatures. These design parameter perturbations led to the final designs. Having obtained the baseline and the final designs, as well as the effects of the perturbations, relations and comparisons were developed expressing the sensitivity of the weight of the thermal protection system and hot primary structure designs at the selected locations to the choice of prediction methods and the variation of criteria. Distinction was made between weight sensitivity to dispersions that are statistically or otherwise rationally predictable and sensitivity to uncertainty factors, estimating techniques and other inexact criteria. In addition to the weight sensitivity comparisons, differences in design reliability associated with the different design techniques were assessed.

The detailed description of the various steps of the study is contained in the following chapters with the computation of a sample point and other background information located in the appropriate appendices.

Some appendices were authored by the specialists responsible for the particular technical disciplines of major importance to this study. Thus, Appendix B on loads was authored by Mr. B. E. Clingan and Mr. A. L. Brown, Appendix C on aerothermodynamics by Mr. C. L. Jaeck, Appendix D on thermal analysis by Mr. E. W. Brogren, and Appendix E on strength analysis by Mr. A. L. Brown.

Appendix F presents an example of the computation procedures used to obtain the TPS weights at the nine selected study points. Specific recommended practices and criteria to supplement NASA SP-8057 are listed in Appendix G. A table for the conversion of U.S. customary engineering units to S-I units is presented in Appendix H.

SYMBOLS

b_{eq}	equivalent distance parameter
BL	boundary layer
BMN	Boeing Modified Newtonian
C	chord of wing or fin
C/C	carbon/carbon composite
C_L	lift coefficient
C_f	friction coefficient
C_n	normal force coefficient
C_p	pressure coefficient
c_p	specific heat
C129Y	columbium alloy
D	diameter of leading edge ($2r_{LE}$)
d	stiffener height
E	elastic modulus
\bar{E}	crossflow momentum thickness ratio
EA	elastic axis
F	heat transfer uncertainty factor
F_c	Spalding-Chi compressibility parameter
F_{rx}	Spalding-Chi compressibility parameter
f(M)	Mach number function
f	streamline divergence parameter for crossflow pressure effects
F_{cy}	allowable yield compressive stress
F_{su}	allowable ultimate shear stress
F_{sy}	allowable yield shear stress

F_{tu}	allowable ultimate tensile stress
F_{ty}	allowable yield tensile stress
GAC	Grumman Aerospace Corporation
GD	General Dynamics Corporation
G&C	guidance and control
CPS	cycles per second
GW	gross weight
g	acceleration of gravity
HCF	hardened compacted fibers
HCR	high cross range
H	heat transfer coefficient
ht	heat transfer
IR&D	Independent Research and Development
I718	Inconel 718 alloy
i	enthalpy
i_o	stagnation (total) enthalpy
i^*	Eckert reference enthalpy
K	flat-faced cylinder velocity gradient normalized by corresponding hemisphere value
k	thermal conductivity
L	length
LCR	low cross range
LE	leading edge
LRA	load reference axis
LSCL	lower surface center line
M	Mach number

MDAC	McDonnell Douglas Astronautics Company
NAR	North American Rockwell Corporation
NASA	National Aeronautics and Space Administration
n	normal load factor
n.mi.	nautical mile
PN	phenolic nylon
PNM	phenolic nylon with microballoons
p	pressure
q	dynamic pressure
\dot{q}	heating rate
R	roughness factor: radius
REI	reusable external insulation
R_e	Reynolds number at boundary layer edge
R_e/ft	boundary layer edge unit Reynolds number
$R_{e\delta^*}$	displacement thickness Reynolds number based on edge conditions
$R_{e\theta}$	momentum thickness Reynolds number based on edge conditions
Rho-mu	Boeing reference density-reference viscosity momentum integral heat transfer prediction method
RTV	room temperature vulcanizing elastomer
RZ	reaction zone
r	streamline divergence parameter for body geometry effects; radius
SL	stagnation line
T	temperature
TBD	to be determined
TPS	thermal protection system

t thickness; time, measured from initiation of reentry (for nominal trajectory time is measured from 400 000 ft)

\bar{t} effective thickness (thickness of a skin alone whose mass per unit area equals average mass per unit area of the component represented by t)

UFS ultimate factor of safety

u velocity in x direction

V vehicle relative velocity; virgin ablation material

v velocity in y direction

x surface distance in streamwise direction; longitudinal body coordinate

y surface distance in direction normal to vehicle axis; lateral body coordinate

Z altitude

z vertical body coordinate

α angle of attack

β sideslip or yaw angle

γ ratio of specific heats

Δ increment or difference

δ local flow deflection angle

δ^* boundary layer displacement thickness

ϵ shock stand-off angle; emittance

θ boundary layer momentum thickness

θ_r rudder deflection angle

λ sweep angle

μ viscosity

μ_0 viscosity based on stagnation enthalpy and local pressure (used in Rho- μ methods)

ρ mass density
 σ partial Prandtl number; standard deviation

Subscripts:

aw adiabatic wall
B Body
beg beginning of transition
bl bond line
C chine
CL centerline
cyl cylinder
e boundary layer edge
eff effective
end end of transition
eq equivalent
ext external
i initial
int internal
L, lam laminar
LE leading edge
max maximum
min minimum
n normal
r reference
s stiffener
T Turbulent
tr transition

w wall
x measured along or based on distance measured along the axis
z measured along the z axis
 ∞ freestream

NOMINAL SYSTEM DEFINITION AND CONCEPT SELECTION

The following paragraphs describe the selection of a study model intended to represent all the features characteristic of a high cross-range delta wing orbiter, including typical mass property distributions, aerodynamic characteristics and an ensuing typical reentry trajectory. The model should also reflect enough design realism and generality such that by analyzing only the judiciously selected points and design concepts, meaningful comparisons and generalized conclusions can be made concerning the sensitivity of various designs to design parameter perturbations and criteria.

Configuration Geometry

The Grumman G3A (internal tankage) orbiter shown in figure 2 was selected for the study with some conceptual variations in structural arrangements adopted from the orbiter vehicles of the Phase B Space Shuttle program contractors. The G3A orbiter carried all fuel and oxidizer in internal body tanks, had a 40 000-lb payload capability and, although an early study version, was a mature, fully reusable vehicle concept directly comparable to the other Phase B designs of the early 1971 time period.

The G3A vehicle is a delta wing vehicle with an approximate overall length of 180 ft, a span of 100 ft, an overall height (gear up) of 63 ft, and a reentry weight of 247 550 lbs. The modified delta wing has a 60° leading edge sweep with a trailing edge swept forward 8°, a faired wing tip and blended leading edge fillet to reduce wing-body interaction during reentry. The 2800-sq-ft exposed area wing has a 9-1/2% thickness ratio with maximum thickness at 35% chord at the root and 30% chord at the tip (see fig. 2). A single 800-sq-ft vertical fin and split rudder provide both high and low speed directional stability and yaw control. A predominantly flat and single curvature surface body is built up around a 16-ft-diameter, 65-ft-long cylindrical cargo compartment, twin floating cylindrical main fuel tanks, and a single floating cylindrical main oxidizer tank. The design was considered to have achieved a good compromise between volumetric efficiency, tank and structural weight, and manufacturing, assembly, installation and maintenance costs. Floating tanks decouple the development risks associated with large tanks and permit parallel design, fabrication, and testing of critical items.

Trajectories

Figure 3 shows the nominal reentry trajectory selected for the program and includes a comparison with the trajectories of the two Phase B contractors. The selected trajectory was based on the 1962 standard atmosphere with no wind and was used for establishing the baseline limit trajectory for the development of design loads and heating environments. It was computed for the Grumman G3A orbiter configuration shown in figure 2. The vehicle reentry weight was taken as 247 550 lbs with a reference area of 5400 ft².

The selected trajectory was chosen from a study of a group of seven 1100 nautical mile cross-range trajectories furnished by Grumman Aerospace Corporation. Among this group the selected trajectory is an intermediate in terms of peak heat rates, total heat load, longitudinal range, and complexity of angle of attack programs. The altitude, velocity, angle of attack, and time data shown in figure 3 were employed in detailed form for the analyses. Also available in detailed digital form furnished by Grumman were bank angle, heading, flight path angle, acceleration, range values versus time, as well as vehicle weight, area, and aerodynamic properties.

A constant heat rate/constant drag guidance system was postulated in the formulation of the G3A trajectory. The guidance to target was based on a constant terminal drag control system. A constant heat rate phase has been incorporated to minimize peak heating rates. The entry interface was at 400 000 feet altitude and initial velocity was toward the East. The entry velocity and angle result from deorbiting from a 270-n.mi. circular orbit. The entry angle was chosen by iteration to yield minimum heat rate for the given target. The angle of attack was held at 50° until pull-up when it was changed to 20°. Bank angle was modulated through the high-heating portion of the trajectory with the intent to produce an extended period of constant heating rates, avoiding excessively sharp heating peaks and high total heat loads. The G3A trajectory is seen in figure 3 to lie slightly below those of the Phase B contractors for part of its duration and therefore may be expected to yield somewhat higher TPS temperatures.

Figure 4 shows the ascent trajectory selected for this study. Like the nominal reentry trajectory, the ascent trajectory was furnished by Grumman and applies specifically to the G3A configuration. The figure also shows the ascent trajectories used by the two Phase B contractors.

Although the selected reentry trajectory is more severe than the Phase B contractor counterparts, the G3A reentry and ascent trajectories were chosen as typical flight profiles for the purpose of this study.

Locations and Concepts

Figure 5 and table 1 summarize the locations and concepts chosen for the 9 selected study point locations. The concepts are characteristic of the most commonly applied designs, including hot structure, composites, metallic and nonmetallic, as well as ablator TPS. These are a typical cross section of design techniques being considered for use on Space Shuttle Orbiter vehicles. Some concepts would also apply to booster vehicles. Figure 6 shows the details of the TPS and structural design concepts selected for the study. Where primary and alternate TPS and structural concepts are indicated, the primary concept was employed for detailed analysis and the alternate concepts were analyzed in less detail.

Although the orbiter configuration, for the purposes of external geometry and general structural and system arrangement, is that of the Grumman G3A vehicle, the detailed TPS and structural concepts are not necessarily those of the G3A orbiter. They rather reflect a hybrid design incorporating some characteristic design approaches used by other Phase B contractors. Thus, e.g., point 2 shows

a shear wall approach used for the MDAC orbiter (ref. 1), point 3A shows REI, point 7 uses ablators, etc. Thus, including the alternate concepts at several point locations, a total number of 14 study points was established. The next step was the sizing of the selected design concepts using a realistic limit trajectory in order to arrive at a baseline to be used for comparisons with other designs (or differently sized similar designs) obtained as a result of the various design parameter perturbations.

Table 1: - LIST OF VEHICLE STUDY POINTS

POINT NUMBER	LOCATION	TPS OR STRUCTURAL CONCEPT
1	LOWER MID-BODY	METAL HEAT SHIELD
2	UPPER MID-BODY SIDE	HOT STRUCTURE
3	LOWER WING, MID-SEMI-SPAN, MID-CHORD	METAL HEAT SHIELD
3A	SAME AS 3	REUSABLE EXTERNAL INSULATION
4	UPPER WING, MID-SEMI-SPAN, MID-CHORD	HOT STRUCTURE
5	LOWER WING, MID-SEMI-SPAN, L. E. BEAM LOCATION	METAL HEAT SHIELD
6	WING LEADING EDGE STAGNATION LINE	CARBON/CARBON COMPOSITE
6A	SAME AS 6	METAL HEAT SHIELD
7	NOSE STAGNATION POINT	CARBON/CARBON COMPOSITE
7A	SAME AS 7	NASA SILICONE ABLATOR
7B	SAME AS 7	PHENOLIC NYLON ABLATOR WITH MICROBALLOONS
7B1	SAME AS 7	PHENOLIC NYLON ABLATOR
7C	SAME AS 7	APOLLO MATERIAL ABLATOR
8	FIN SIDE, MID-SPAN, MID-CHORD	HOT STRUCTURE
9	LOWER AFT-BODY	METAL HEAT SHIELD

LIMIT TRAJECTORIES

The limit reentry trajectory shown in figures 7 and 8 from which all baseline reentry airload and thermal environment data were developed was based on the nominal reentry trajectory (fig. 3) and is defined as follows:

Atmospheric Properties:	1962 Standard Atmosphere (ref. 2)
Altitude:	(Nominal Value) - 3000 ft.
Velocity:	Nominal Value
Angle of Attack:	(Nominal Value) $+5^\circ$
Angle of Yaw:	$+5^\circ$ (Nominal Value is 0)
Bank Angle:	Nominal Value

The tolerances in altitude, angle of attack, and angle of yaw were based on design trajectory dispersions used by the Space Shuttle Phase B contractors, recommendations from Grumman personnel, and a detailed review of Boeing X-20 simulator study results. A review of these background data is given in table 2.

It was expected that some orbiter study points, especially those involving hot primary structure may be designed by conditions other than reentry. Therefore, the selected limit trajectory would be inadequate for designing the entire vehicle. It was also found early in the study, that none of the study points would experience critical heating conditions during ascent. Therefore, the approach taken in determining loads was to use the nominal ascent trajectory and/or other discrete vehicle design conditions in order to determine limit loads on an individual basis rather than establishing a complete limit ascent trajectory. This approach is described in more detail in the loads analysis section. Additionally, in order to assess reentry maneuver capability and vehicle tolerances, several maneuver trajectories were postulated as shown in figure 9.

The rationale for selection of the particular limit trajectory features and the means of their application to the orbiter study points are discussed in the following paragraphs.

System Constraints

In addition to the usual system constraints characteristic of conventional aircraft, the Space Shuttle is exposed to severe environmental effects resulting in serious physical limitations requiring considerably more sophisticated techniques for safe operation of such vehicles. The most important limitations are due to a combination of elevated temperatures and structural loads which can easily extend beyond the endurance capability of many of the advanced structural and thermal protection materials. With this in mind, the limit trajectory was selected in such a manner that it would represent a realistic typical vehicle flight condition, would not overload current material capability, and would not be too severe to permit a reasonable comparison of effects of deviations and tolerances.

Table 2. -- TOLERANCES FOR LIMIT REENTRY TRAJECTORY DEFINITION

VEHICLE	TOLERANCES			REFERENCE	BASIS
	ALTITUDE ΔZ , FT	ANGLE OF ATTACK $\Delta \alpha$, DEG	YAW ANGLE β , DEG		
BACKGROUND DATA					
MDAC ORBITER	-2500			1	ESTIMATED "TO ACCOUNT FOR DISPERSIONS AND TRANSIENTS"
NAR ORBITER	-3000 USED FOR "SHORT" OR MAX HEAT RATE DESIGN TRAJ ONLY	± 5 USED FOR BOTH "SHORT" OR MAX HEAT RATE, AND "LONG" OR MAX HEAT LOAD TRAJ'S		3	ESTIMATED TO ACCOUNT FOR G&C, TEMP SENSING, AND LONGITUDINAL RANGE PERTURBATIONS ONLY
NAR ORBITER	(1) -3000 (2) -10000			4	(1) G&C, TEMP SENSING ONLY (2) ALL EFFECTS
GAC INT TANK HCR ORBITER (CONFIG G3A)	-5000	± 2		5	ESTIMATED, CONSIDERING DISPERSION ANALYSIS FOR GAC LCR ORBITER
X-20	-4000	+3 -2.4	± 2 , NO ROLL ± 6 , WITH ROLL	6,7	MAXIMA FROM STEADY STATE, TRANSIENT AND MANUEVER TOLERANCES AT APPROPRIATE α , FROM SIMULATOR STUDIES
SELECTED FOR PRESENT STUDY DESIGN TRAJECTORY					
REPRESENTATIVE HCR DELTA WING ORBITER (GAC G3A)	-3000	± 5	± 5	---	ESTIMATED, ON BASIS OF ABOVE NOTES, TO ACCOUNT FOR G&C, AERO COEF, ENTRY ANGLE, WIND DISPERSIONS, ATMOS VARIATIONS TO BE ACCOUNTED FOR SEPARATELY

Trajectory Dispersions

The expected deviations from a nominal trajectory arise from random variables such as atmospheric properties over which the designer has no control, and other characteristics such as guidance and control system errors determined by the characteristics of that system. Limit trajectories for design which make the risk of exceeding limit design acceptably small without imposing excessive weight penalties are desired. Rational determination of limit trajectories requires knowledge of the probability distributions of random variables, maximum values of controllable variables, and correlations, if any, between all significant variables. Thus, in order to establish a viable and characteristic limit trajectory, the effects of trajectory and atmospheric dispersions at a number of points through the critical loads and heating part of the reentry trajectory must be examined.

In normal design practice such an examination would include extensive simulator studies in order to cover all reasonable dispersions and the most critical combinations thereof. At each design point the effects due to the combination of mechanical loads, temperatures, temperature gradients and thermal loads would be assessed. Each study point could be expected to have its own combination of dispersions resulting in the most critical design condition. Since such a detailed approach was beyond the scope of this study, it was decided to use X-20 Development Program information and the data available from the Phase B contractor studies to establish reasonable trajectory dispersions.

The X-20 Development Program included simulator studies that resulted in detailed 3σ dispersions from which were defined interrelated tolerances on altitude, angle of attack, and yaw angle for steady state glide and a number of transient and maneuver conditions. These analyses had the benefit of reasonably well defined guidance and control system characteristics and detailed data on the vehicle's dynamic and aerodynamic characteristics.

The X-20 trajectory dispersions, which incorporated detailed aerodynamic, guidance, sensing, display, and control characteristics, were reviewed in detail and discussed at length with personnel who participated in developing the data. It was found that the particular guidance and control system, which employed the pilot in the loop, reading a cathode ray tube display with overlays, had a significant effect on trajectory dispersions. Many of the guidance and control errors were related to characteristics of specific hardware. Because of these facts the X-20 dispersions were not considered to be directly applicable to the present study in any detailed manner.

A study of the Phase B contractor reports revealed that only NAR showed evidence of some kind of dispersion analysis. The NAR results (ref. 3) expressed aerodynamic, atmospheric, and guidance variations in terms of cross-range loss. The more usual approach, however, to establishing a design trajectory was either to show an envelope of trajectories (NAR, ref. 3) or to use discrete values for dispersions applied to the nominal trajectory (GAC, ref. 8 and MDAC, ref. 1).

A summary of the tolerances used by the Phase B contractors and the appropriate X-20 tolerances is given in table 2.

Trajectory Selection Criteria and Tolerance Application

The selection of the tolerances to be used in this study was based on past X-20 experience and the recommendations found in the Phase B contractor and Grumman documents. The establishment of a limit trajectory by applying tolerances to a defined nominal trajectory was felt to be the most practical and meaningful approach to the present study, as opposed to the alternative, that of fitting a most severe trajectory or trajectories within a corridor determined by TPS temperature limits. It was also recognized, that the present approach could result in violation of allowable temperatures for certain candidate materials for some of the selected study concept. Thus, in addition to sizing the baseline designs, the limit trajectory influences the choice of TPS materials or may even necessitate modification of a particular structural or TPS concept. The tolerances used in this study and applied to the nominal trajectory to account for trajectory dispersions are shown in table 2.

The altitude and angle of attack tolerances selected for the present limit trajectory definition follow closely the values used by the Phase B contractors. The recent orbiter work offers no guidance for selection of a yaw angle tolerance; therefore, the X-20 results formed the basis for yaw tolerance selection. Since the nominal trajectory for the present study employs roll modulation for longitudinal range control, and thus frequent changes in bank angle, a relatively high yaw angle tolerance was chosen.

The stated tolerances for the present study were intended to account for guidance and control, aerodynamic coefficient, entry angle, wind, and vehicle variations, but not atmospheric property variations. Deviations in atmospheric properties from the 1962 standard, however, were included in later sensitivity studies as separate perturbations.

An effort was made not to select extreme tolerances for the baseline limit trajectory since it was intended that perturbations would be made in both directions. The application of limit reentry trajectory tolerances for the baseline design to the specific study points is shown in table 3.

To satisfy the requirement for studying vehicle maneuver capability and associated design criteria, a set of three maneuvers was postulated. These maneuvers were not considered as part of the design limit trajectory, but as separate perturbations in the reentry environment. A major concern was that of defining the maneuver to realistically yield true limit conditions without resulting in temperatures so severe that the existing TPS design would not survive, even on a one time basis, or that a revised design could not be made to work.

The nominal and limit trajectories of figures 3 and 7, respectively, were used as the bases for the maneuver excursion study. Each maneuver was essentially a transfer from the limit to the nominal trajectory, with the time to complete the transfer being the major distinction between maneuvers. The aerodynamic coefficient, reentry weight, and area data used in maneuver trajectory synthesis were obtained from Grumman. A simplified point-mass computer program was used to synthesize the maneuver histories. After initiation of the maneuvers the angle of attack was moduled, on the basis of an assumed realistic

Table 3. - APPLICATION OF LIMIT REENTRY TRAJECTORY TOLERANCES FOR SPECIFIC STUDY POINTS

POINT NO.	LOCATION	ALT TOL ΔZ (FT)	ATTACK TOL $\Delta \alpha$ (DEG)	YAW TOL β (DEG)
1	LOWER MIDBODY	-3 000	+5	5*
2	UPPER MIDBODY SIDE	-3 000	-5	5*
3	LOWER WING	-3 000	+5	5*
4	UPPER WING	-3 000	$\pm 5^{**}$	5*
5	LOWER WING, L. E. BEAM	-3 000	+5	5*
6	WING L. E. STAG LINE	-3 000	+5	5*
7	NOSE STAGNATION POINT	-3 000	0	0
8	FIN SIDE	-3 000	-5	5*
9	LOWER AFT BODY	-3 000	+5	5*

* APPLIED IN A DIRECTION FOR MAXIMUM LOCAL SURFACE ANGLE OF ATTACK OR MINIMUM BOUNDARY LAYER DEVELOPMENT LENGTH

** INVESTIGATE BOTH EXTREMES OF α

guidance law, to achieve equilibrium flight on the nominal trajectory after a certain elapsed time. The three maneuver cases are shown graphically in figure 9. Additional maneuver data are given in table 4.

Case I is a minimum maneuver which, by definition, will not exceed current baseline design loads or temperatures. It begins at 1100 seconds on the limit trajectory and returns to the nominal trajectory in approximately 70 seconds. The 1100 second time point was selected for maneuver initiation since that was near the time of maximum temperature for point number 3, which was selected for maneuver excursion analysis, and the time at which the environment has greatest influence on the design of TPS at point 3. For this case, the orbiter was assumed to somehow arrive at the 1100 second point on the limit trajectory with the design angle of attack. At this point artificial constraints were removed and the vehicle was allowed to begin to seek an equilibrium flight condition.

In the Case II maneuver the vehicle flight history began originally on the nominal trajectory. Through an assumed realistic flight path, the vehicle arrived at 1100 seconds at a point 3000 feet below the nominal trajectory, i.e., on the limit trajectory. Velocity at that point was assumed as the nominal value. At that point a 2.4 g maneuver was initiated to return to the nominal path. This maneuver continued through an overshoot and a $-.673$ g corrective maneuver, returning to the nominal trajectory in approximately 30 seconds.

The Case III maneuver was similar to Case II except that 1.15 g's were applied at maneuver initiation with a subsequent $.063$ g's overshoot recovery, resulting in a return time to the nominal trajectory of approximately 60 seconds.

All maneuver trajectory computer simulations were carried to approximately 1200 seconds to ascertain that a match with the nominal altitude-time line had been achieved and to permit examination of the ensuing velocities. The maneuver trajectories were synthesized in such a manner that a return to the exact velocity history of the nominal trajectory was not possible. The execution of the maneuver dissipated energy, resulting in a velocity deficiency, relative to that of the nominal trajectory, when the nominal altitude-time line was reached. This velocity deficiency, in turn, resulted in a higher required angle of attack to maintain flight along the nominal altitude-time line.

In the Case I maneuver the excess energy dissipated by the maneuver was so slight that the resulting final angle of attack increment above nominal was not even detectable (see table 4). The velocity deficit became stable at 152 ft/sec soon after completion of the maneuver and was assumed to be constant throughout the remainder of reentry.

The Case II maneuver resulted in a 24° angle of attack to maintain the nominal altitude-time line from maneuver completion to 1218 seconds. At this time (the last computer simulated time point), however, the velocity deficiency, relative to the nominal, was still increasing (table 4). It is likely that a continued increase would have been seen had the trajectory synthesis been carried further. The growing velocity deficiency would eventually result in the need for a further increase in angle of attack, leading to further velocity deficiencies, and so on until it would no longer be possible to follow the nominal altitude-time line. It is seen that a severe maneuver could easily prevent achieving the required mission range.

Table 4: - MANEUVER EXCURSION DATA

(a) Case I Maneuver, $\alpha_i = 25^\circ$

t (sec)	α (deg)	Normal Load Factor (g)	Deviation From Nominal Trajectory	
			ΔZ (ft)	ΔV (ft/sec)
1098	25	.861	-3000	0
1106	↓	.861	-2721	- 45
1114	↓	.853	-2181	- 90
1122	↓	.838	-1374	-133
1130	↓	.816	- 381	-171
1131	10	.190	- 217	-164
1138	↓	.189	511	-139
1146	↓	.191	727	-105
1150	25	.829	646	- 72
1154	↓	.840	416	- 89
1160	22	.723	250	-121
1162	↓	.727	213	-120
1170	↓	.742	98	-133
1178	↓	.755	53	-147
1180	20	.666	89	-152
1186	↓	.676	86	-151
1190	↓	.682	82	-151
1194	↓	.690	80	-151
1202	↓	.705	57	-152
1210	↓	.721	31	-152
1218	↓	.737	31	-152
> 1218	↓	—	~0	-152

Table 4:—MANEUVER EXCURSION DATA (Cont.)

(b) Case II Maneuver, $\alpha_i = 50^\circ$

t (sec)	α (deg)	Normal Load Factor (g)	Deviation From Nominal Trajectory	
			ΔZ (ft)	ΔV (ft/sec)
1098	50	2.40	-3000	0
1106	↓	2.27	-2179	- 410
1112	-12	-.673	- 620	- 798
1114	↓	-.663	- 251	- 693
1122	↓	-.654	- 207	- 695
1125	42	1.62	- 112	- 140
1130	↓	1.63	46	- 810
1133	25	.750	25	- 811
1138	↓	.756	- 8	- 812
1146	↓	.766	- 27	- 939
1150	24	.731	- 23	- 953
1154	↓	.736	- 21	- 963
1162	↓	.747	- 19	- 984
1170	↓	.759	0	-1004
1178	↓	.772	0	-1025
1186	↓	.786	0	-1046
1194	↓	.802	0	-1067
1202	↓	.817	0	-1089
1210	↓	.833	0	-1111
1218	↓	.848	0	-1133
> 1218	↓	—	0	-1150 (Assumed)

Table 4.—MANEUVER EXCURSION DATA (Cont.)

(c) Case III Maneuver, $\alpha_i = 31^\circ$

t (sec)	α (deg)	Normal Load Factor (g)	Deviation From Nominal Trajectory	
			ΔZ (ft)	ΔV (ft/sec)
1098	31	1.15	-3000	0
1106	↓	1.13	-2573	-104
1114	↓	1.10	-1609	-202
1120	7	.0645	- 508	-245
1122	↓	.0640	- 183	-261
1130	↓	.0631	737	-212
1138	↓	.0642	859	-162
1141	29	.971	610	-169
1146	↓	.988	335	-184
1151	23	.746	195	-212
1154	↓	.752	83	-233
1162	↓	.766	- 16	-274
1170	21	.646	- 41	-274
1178	↓	.657	0	-274
1186	↓	.671	0	-273
1194	↓	.687	0	-273
1202	↓	.705	0	-273
1210	↓	.725	0	-274
1218	↓	.744	0	-273
> 1218	↓	—	0	-273

Since the computer runs were terminated after 1218 seconds, the long-term effects of the Case II maneuver upon velocity can only be estimated. For purposes of design analysis in this study, a velocity deficit somewhat greater than the last computed value for the Case II maneuver was assumed constant through the remainder of the trajectory. It is pointed out that the period of peak heating was covered with accurate trajectory data and that any discrepancies between assumed and true velocities later in the trajectory have little effect on TPS design or survivability.

In the Case III maneuver, a 21° angle of attack (1° higher than nominal) was required to maintain the altitude-time line after maneuver completion. The velocity deficit was 273 ft/sec, stable after 1180 seconds, and as in Case I was assumed to continue at this value thereafter (see table 4).

The design considerations and the assessment of the effects of the maneuver excursions are described in later paragraphs.

Late Reentry and Transition Trajectory Definition

Data for the Grumman G3A nominal reentry trajectory, which was used as a basis for the limit design trajectory for the current study, end at a point 2346 seconds after reentry initiation. Trajectory variables supplied by Grumman began to deviate from a flight history useable for this study at a somewhat earlier time, probably due to approximations in computer modeling of vehicle characteristics at low Mach numbers.

For the purpose of thermal analysis the orbiter landing was assumed to occur at 3600 seconds. The particular flight path assumed between 2000 and 3600 seconds has little impact on TPS design since both positive and negative heating rates are very low at the low velocities involved. For reentry loads on hot structure points, however, the late reentry and transition to full lifting flight is quite important. The maximum reentry dynamic pressure occurs during this period and the 2.5 g to -1.0 g maximum maneuver load factor capability is imposed during this period. Furthermore, parts of the vehicle employing hot structure may retain high temperatures with resulting degraded structural capability during the period when such maximum loads occur.

Thus, in order to provide a basis for hot structure load prediction it was necessary to extend the limit trajectory well beyond the originally defined history, and to do so realistically. For this purpose, a McDonnell Douglas Design Transition Trajectory was employed. It was found that the altitude and dynamic pressure values of this transition trajectory at a particular time early in transition closely matched the 2250 second values from the current limit trajectory. Normal load factors at these points also closely agreed and angle of attack histories could be faired together without difficulty. The McDonnell Douglas trajectory includes a 2500-ft-altitude margin and so is similar in concept to the current limit reentry trajectory. Thus, the adoption of the MDAC transition trajectory provided all the necessary data to a time well beyond maximum dynamic pressure and maximum load factor.

Figures 10 and 11 show the late reentry and transition trajectory that resulted from fairing the MDAC transition trajectory into our limit trajectory based on the Grumman G3A nominal reentry trajectory. The fairing was done in such a way that Mach number, dynamic pressure, altitude, and velocity are all consistent at each time point. The fairings of load factor and angle of attack used to join the traces of these variables were not analyzed for compliance with exact vehicle aerodynamic characteristics because these fairings occupy a period when load factors are low. The maximum load factor and maximum dynamic pressure conditions, which potentially influence the hot structure design, are entirely from the MDAC trajectory, which was assumed to be well founded.

A final addition to the late reentry and transitional design requirement definition was the adoption of the rule expressed in reference 8, section 8.3.6.2.1, that the 2.5 g maximum normal load factor capability from a pull out in lifting flight be required only after the dynamic pressure has dropped below 300 lb/ft². (This rule was waived to permit carrying out the reentry maneuver excursion study.) A summary of the design requirements affecting reentry loads is included in figure 11.

Transition to airplane type flight was assumed to be completed with the passage of the minimum angle of attack condition at approximately 2325 seconds (fig. 11). Subsequent to that time, the trajectory was assumed immune to the altitude and angle of attack perturbations considered for the purpose of weight sensitivities. Thus, any study points employing a TPS or structural design critical to reentry maximum q or post-reentry maneuver conditions were affected by altitude or angle of attack perturbations only through residual temperatures.

THERMAL-STRUCTURAL COMBINED LOADS ANALYSIS

The detailed thermal-structural combined loads analysis provided the required inputs for weighing the designs and for determining the weight sensitivity of the TPS and the hot structure. It consisted of loads, thermal and strength analyses using generally accepted methods and techniques for entry vehicle designs, as well as alternate methods selected for this study.

Loads Analysis

Structural loads were considered to consist of quasi-steady loads due to dispersions and deviations established for the limit and maneuver trajectories plus incremental loads due to angle of attack perturbations from turbulence, gusts, and corrective maneuvers. Preliminary design techniques assuming a rigid airframe were used in determining external loads for the detailed thermal-structural analysis. This analysis considered aerodynamic and inertia loads with structural dynamic effects accounted for by means of dynamic magnification factors estimated or determined from the results of more detailed dynamic response analyses of the baseline configuration available from Phase B contractor reports.

As part of the review of the Phase B loads and environment data, the entire ascent trajectories for both MDAC and NAR systems were examined. These trajectories are shown in nominal form in figure 4. In addition, work from the Grumman-Boeing Alternate Design Concept Study was examined, and it was found that no complete set of loads data needed for the present study existed in any single reference. The NAR Phase B Technical Summary (ref. 3) gave load distributions for the wing and fin, which is the form of load data required for study points number 4 and 8. The MDAC report (ref. 1) gave only the wing root and fin root loads, but the slightly greater similarity between the MDAC orbiter and the present study baseline configuration made it desirable to utilize the MDAC orbiter loads. On the other hand the maximum ascent $q\alpha$ (dynamic pressure-angle of attack product) values for the MDAC orbiter were considerably lower than the NAR design value, the Grumman-Boeing value, or values computed in current Boeing IR&D studies. Ascent maximum $q\alpha$ values from MDAC were +1672 and -1794 lb/ft²-deg, while the stated NAR design value was 2800 lb/ft²-deg and both Grumman-Boeing and Boeing independent analyses have yielded nearly 5000 lb/ft²-deg before and 3300 lb/ft²-deg after load alleviation.

The approach selected for the determination of wing and fin ascent loads for points number 4 and 8 was therefore to use a maximum $q\alpha$ and $q\beta$ value of 3300 lb/ft²-deg, from Boeing IR&D analyses. This value of $q\alpha$ and $q\beta$ represented a limit value and as such included the effects of ascent trajectory dispersions. Then the MDAC wing and fin root loads were scaled to the above $q\alpha$ and $q\beta$ value. Thereupon, the NAR wing and fin load spanwise distributions were scaled to the above root loads. Hereby, the appropriate distributions for positive and negative (headwind and tailwind) angle of attack conditions were used.

Ascent body loads for the purpose of designing the hot structure at point number 2 were drawn exclusively from the MDAC data (ref. 1) since the body structure and the local panel concept are similar to those of the MDAC orbiter.

Table 5 summarizes the loads obtained for flight conditions other than reentry, such loads having a potential for determining the choice of structural or TPS materials and gages at the indicated locations. Whether these loads were actually critical to the designs was determined upon a comparison of stress analyses at these conditions with stress analyses based on the loads and the elevated temperatures of reentry. Care was taken to make these non-reentry loads as realistic as possible in order not to preempt any sensitivity of the structure to reentry environment perturbations by overly conservative and thus possibly design-critical non-reentry load condition. The normal, bending moment, and torsion loads were generated as described above. The ascent local net pressures on panels with metallic TPS (points 1, 3, 5 & 9) were taken directly from a Boeing IR&D study of boost panel pressures. The ascent pressures at points 6 and 7 were computed from standard swept cylinder and hemisphere stagnation external values, respectively, and internal pressures from a 10-second lag rule.

The loads for reentry and for the 2.5g to -1.0g subsonic maneuver condition were computed directly for the conditions shown in figures 10 and 11. The reentry and post-reentry maneuver loads were obtained using the assumption of a rigid airframe with a panel grid such as shown in figure 12. The vehicle planform was divided into a finite number of panels. The panel airloads were determined from Newtonian theory supplemented by pressure coefficients computed during the present study for the particular study points. A rigid body trimmed flight condition was assumed. Panel inertia loads were determined from mass distribution and load factors. The shears, moments, and torsions at the required locations were computed by summation of appropriate panel loads, with the computations being carried out by means of a computer program in use for the Grumman-Boeing program.

Differential pressures for TPS design were computed and varied parametrically, reflecting the effects of various assumed leakage, venting and purge rates.

Table 6 summarizes the loads obtained and used at the various study points during reentry and post-reentry. A more detailed description of the loads analysis is presented in Appendix B.

Thermal Analysis

The thermal analysis consisted of predicting the aerothermodynamic environment, including the local pressure, at the chosen point locations and then computing the resulting indepth temperature distributions. These data were then used for selecting the structural and thermal protection materials and for sizing the designs at the various study points.

Table 5: - SUMMARY OF LOADS FOR FLIGHT CONDITIONS OTHER THAN REENTRY
(ALL LOADS ARE LIMIT)

POINT NO.	LOCATION	FLIGHT CONDITION	NORMAL LOAD (1000 LB)	BENDING MOMENT (10 ⁶ IN-LB)	TORSION (10 ⁶ IN-LB)	LOCAL NET PRESS. (LB/IN ²)	METHODS OR DATA SOURCE
1	LOWER MIDBODY	ASCENT MAX $q \alpha$				-4.84	SHOCK-EXPANSION, 10 SEC LAG
2	BODY SIDE	ASCENT MAX $q \alpha$ LANDING		260 -25			MDAC DATA
3	LOWER WING	ASCENT MAX $q \alpha$				-4.84	SHOCK-EXPANSION 10 SEC LAG
4	UPPER WING	ASCENT MAX $q \alpha$	± 113	-17.1	± 1.77		MDAC ROOT LOADS, DELTA WING DISTRIB, SCALED TO GAC MAX $q \alpha$ FOR ASCENT COND
5	LOWER WING, L E BEAM	ASCENT MAX q				-4.84	SHOCK-EXPANSION 10 SEC LAG
6	WING L E S L	ASCENT MAX q				-0.58	NORMAL COMPONENT STAGNATION, 10 SEC LAG
7	NOSE STAG PT	ASCENT MAX q				1.18	STAGNATION, 10 SEC LAG
8	FIN SIDE	ASCENT MAX $q \beta$	± 37	± 3.55	± 1.3		SIMILAR TO PT NO. 4
9	LOWER AFT BODY	ASCENT MAX $q \alpha$				-4.84	SHOCK EXPANSION, 10 SEC LAG

Since the objective of the present study included the investigation of the influence of criteria and method selection on orbiter vehicle structural and TPS design, it was necessary to establish baseline thermal analysis methods. Subsequent variations of the various thermal analysis parameters were then treated as perturbations. The effects of these perturbations were then assessed and used in determining the design weight sensitivities to the varying design parameters, as described in later paragraphs.

Generally, different baseline methods and criteria were used for the various vehicle locations because the latter often experience different flow regimes. Locations on the lower surface lie in an attached three dimensional flow region, experiencing high pressures and heating rates. The effect of surface roughness due to TPS panel mismatch and thermal distortion is more important at lower surface locations, while effects of interference are generally absent. Acceptable pressure and heating prediction methods are available for the windward surface of a delta wing. The heat transfer rates were computed using inviscid flow prediction methods without viscous interaction effects for obtaining boundary layer edge properties. Boundary layer transition and overshoot in heating were considered.

Locations on the upper or side surface of the vehicle were generally considered to lie in separated flow. It was recognized that the upper surface flow was probably complicated by vortices forming as the flow expanded over the nose, leading edges and chines. The upper surface pressure and heat transfer were obtained from analytical estimates and by using empirical predictions based on similar bodies.

The procedure adopted for reentry aerodynamic heating computations can be summarized as follows:

1. From the limit reentry trajectory, histories of reference laminar and turbulent heat transfer coefficients and recovery enthalpies were computed. From examination of these results, specific time points along the trajectory were selected at which to perform detailed local heating calculations for the nine vehicle locations. The time points were selected from consideration of vehicle attitude, Mach number, Reynolds number, and appropriate temperature histories. The selected time points are shown in table 7.
2. Using the selected time points, the local heating at the vehicle study points was computed. The calculations used the selected heat transfer theory or an empirical technique as appropriate to the local vehicle geometry and the particular aerothermodynamic regime through each portion of the trajectory. These computations included boundary layer transition as predicted by the method being examined. Where required, the time points shown in table 7 were modified in order to include the beginning and end of transition.

Table 6.:- SUMMARY OF LOADS FOR REENTRY
(ALL LOADS ARE LIMIT)

POINT NO.	LOCATION	FLIGHT CONDITION	NORMAL LOAD (1000 LB)	BENDING MOMENT (10 ⁶ IN-LB)	TORSION (10 ⁶ IN-LB)	LOCAL NET PRESS. (LB/IN ²)	METHOD OR DATA SOURCE
1	LOWER MID-BODY	LATE REENTRY (t ≈ 1900 SEC)				0.4	P _{ext} : BMN, P _{int} = 0 FOR t < 2000 SEC
2	BODY SIDE	(NO CRITICAL REENTRY COND.)					
3	LOWER WING	LATE REENTRY (t ≈ 1900 SEC)				0.4	P _{ext} : BMN, P _{int} = 0 FOR t < 2000 SEC
4	UPPER WING	POST-REENTRY 2.5g MANEUVER	92.7	11.5	19.0		▷
5	LOWER WING LE BEAM	LATE REENTRY (t ≈ 1900 SEC)				0.8	P _{ext} : BMN, P _{int} = 0 FOR t < 2000 SEC
6	WING LE SL	q ⁹ MAX				2.08	NORMAL COMPONENT STAGNATION
7	NOSE STAG. POINT	q ⁹ MAX				2.27	STAGNATION
8	FIN SIDE	q ⁹ MAX	40.5	3.99	-1.199		▷
9	LOWER AFT BODY	LATE REENTRY (t ≈ 1900 SEC)				0.4	P _{ext} : BMN, P _{int} = 0 FOR t < 2000 SEC

▷ AERODYNAMIC INFLUENCE COEFFICIENT APPROACH (APPENDIX B)

3. The thus obtained local heating environments at specific times contributed the required input data for the thermal analysis of the TPS or hot structure for the baseline design.
4. In order to investigate the effects of perturbations steps (2) and (3) were repeated for the respective design conditions.

The aerothermodynamic environment prediction methods (heating rates and pressures) used for the baseline design and the perturbations at the various study point locations are presented in detail in Appendix C.

The in-depth temperature distributions for both the heat shield and the hot structure locations were computed by means of transient analyses. The heat balance included the aerodynamic heat input (with inclusion of wall temperature effects on heat transfer coefficients), external and internal radiation, heat conducted through insulation and structural and heat shield members, and heat stored in the components. In addition, the analysis of ablators included the effects of thermochemical decomposition, combustion, and boundary layer blockage. These results were used for the selection of structural and TPS materials and served as inputs for the strength analysis of the hot structure or TPS respectively.

The thermal analyses were recycled as necessary as part of the design iteration process and repeated as required to incorporate the effects of parameters perturbed for the purpose of the weight sensitivity studies. A detailed description of the thermal analysis and the methods used is contained in Appendix D.

Strength Analysis

Stress analyses of the structural elements for the TPS panels and for the hot primary structure, were used to insure the adequacy of structure to withstand the induced environment for the service life of the orbiter. The structure was designed to withstand primary structure loads, local pressures, acoustic environment, temperature and temperature gradients, and to satisfy flutter requirements. The analyses were performed using conventional aircraft and launch vehicle preliminary design stress methods. The effects of local and general component structural instability, eccentric loading, differential thermal expansion, and material property degradation with increasing temperature were included. The analysis of the metallic TPS panels utilized a parametric approach, whereas the hot structure analysis utilized discrete point designs.

The sensitivity of the metallic TPS panels to variations in trajectory parameters, heating and pressure prediction techniques, and structural criteria was established by determining the resulting variation in structural weight. Variations in the foregoing parameters resulted in variations in design temperatures and pressures on the TPS panel. Therefore, one structural concept was selected for each panel material required to cover an anticipated range of temperatures. A parametric study was made to determine the optimum size and weight of the metal components of TPS panels, which would survive the anticipated range of temperatures and pressures. The analysis was accomplished using the

Boeing computer program, "OPTimization by RANdom Search" (OPTRAN). This program optimizes panel dimensions for minimum panel weight. Program input, output, and design constraints are summarized in figure 13. The eight variables shown were optimized simultaneously to provide minimum panel weight for selected panel sizes. Although the OPTRAN program provides no direct constraints on panel design to satisfy flutter and acoustic requirements, past experience has shown that corrugation stiffened panels designed by this program will satisfy criteria requirements. The corrugation stiffened face sheet concept shown in figure 13 was used to size all TPS panels. The results of this study are shown in figure 14 which demonstrates the relationship between the weight of a metallic TPS panel, the maximum temperature, maximum net pressure, and a characteristic temperature difference across the panel.

The stress analysis and sizing of the carbon/carbon composite designs was also accomplished parametrically. A particular layup of .008 inch thick plies of C/C material was selected and integral stiffeners included in a configuration that was roughly optimized for the pressure loads at points 6 and 7. Since the carbon/carbon material was assumed to exhibit full strength up to its maximum use temperature and since thermal stress effects on the designs were found to be insignificant, the sizing of the C/C designs depended only upon pressure loads. Figure 15 shows the carbon/carbon sizing curves for points 6 and 7. The stepped shape of the curves arises from the use of discrete layers (plies) of material, while the slopes between steps are caused by increasing stiffener depth with pressure. It is pointed out that the parametric curves of figure 15, like those of figure 14, do not include the weight of insulation that eventually must be included in the TPS design.

TPS panels using REI were analyzed to assure adequacy of the substrate under all environmental conditions. A titanium honeycomb sandwich panel was assumed for the substrate structure. The design conditions for the substrate are normal pressure during boost and post reentry thermal gradients. For both conditions the panel must provide sufficient stiffness to protect the REI from excessive strain as well as carry the required pressure load. Since insufficient material properties were available for the REI coating material to defined strain limitations, the properties of the REI material alone were used. Thus, the critical design condition for the substrate used in this analysis is the normal pressure load occurring during boost. Consequently, the substrate is not affected by reentry conditions so long as a constant peak bondline temperature is assured.

Discrete design analyses were conducted for the three hot structure design points (body side surface, wing upper surface, and fin surface skin panels) to assure adequacy throughout the flight. In all cases the assumed structure consisted of Inconel 718 skin panels with "Z" stiffeners.

The skin panel on the side of the body was assumed to carry shear and normal pressure only (no body bending). The critical design conditions for this panel were the launch acoustic environment and flutter limitations during boost. Standard analysis methods were employed using the acoustic environment discussed in Appendix B. Flutter criteria from reference 10 were used.

Both the wing upper skin panel and the fin skin panel were analyzed using discrete point designs. The structure at each point was designed to withstand all primary loads occurring on the wings and fin throughout flight as well as those resulting from differential thermal expansion. The baseline design for the wing was critical for post reentry maneuver loads immediately following reentry when the structure was still hot. Subsequent perturbations in some design parameters during reentry resulted in increased structural weight. The baseline design for the fin was critical for the environment occurring at maximum g during reentry. Perturbations in this environment resulted in changing structural weight. Analysis of the wing and fin structures utilized standard preliminary design methods. The structure was designed as wide column compression panels subjected to combined axial load and shear. The skin and stringer proportions were optimized to minimize panel weight.

Table 7. - TRAJECTORY POINTS SELECTED FOR DETAILED BASELINE LOCAL AERODYNAMIC HEATING CALCULATIONS

TIME (SEC)	ALTITUDE (FT)	VELOCITY (FT/SEC)	ANGLE OF ATTACK (DEG)	ANGLE OF YAW (DEG)	MACH NUMBER
0	397 000	24 500	50 ± 5	5	27.7
116	293 624	24 464	50 ± 5	5	27.7
206	239 592	23 590	50 ± 5	5	24.9
214	238 856	23 516	20 ± 5	5	24.8
306	285 576	23 216	20 ± 5	5	24.2
514	230 774	22 458	20 ± 5	5	23.2
802	221 432	21 180	20 ± 5	5	21.4
1346	179 704	16 743	20 ± 5	5	15.6
1754	152 824	10 146	20 ± 5	5	9.45
2074	116 856	4 912	20 ± 5	5	4.85

THERMAL PROTECTION SYSTEM AND HOT STRUCTURE DESIGN

In order to compare the effects of the various parameters, design criteria and methods described in the preceding chapters, baseline designs for each of the study points were required. Thereupon, perturbations were applied to the baseline designs in order to arrive at the final (perturbed) designs as a basis for determining the sensitivity of the designs to the various perturbation parameters. This sensitivity was determined in terms of weight. A reliability assessment was then performed using a grading system based on several grading parameters. A sample computation showing all the steps used in designing the baseline thermal protection system at study point number 3 plus a particular perturbation assessment and the resulting weight sensitivity is presented in Appendix F.

Baseline Designs

The baseline designs were obtained using the various concepts shown in figure 6 at the respective study point locations shown in figure 5. The underlying intent in selecting the particular concepts was to develop designs which would be representative of Phases A and B orbiter designs at the various vehicle locations. At the same time, the designs were intended to be sufficiently realistic to exhibit accurately sensitivities and trends. In all, 14 baseline designs were examined. Some initially conceived baseline designs had to be deleted or changed because of excessive temperatures, other limitations inherent in the particular concept or material system selected, or due to overconservatism of the particular prediction methods applied. Thus, e.g., the design at point 6A based on an empirically modified cylinder heat transfer theory was treated as the baseline at that point in order to permit establishment of weight sensitivities. The originally selected baseline heat transfer prediction technique for point 6A, the simple infinite swept cylinder theory, which was a priori expected to yield conservative predictions, resulted in temperatures exceeding metal TPS capabilities and was deleted.

In order to actually size the selected designs it was necessary to establish their operating environment, to carry out the thermal and structural analyses, and to verify the structural integrity of the particular selection. All baseline designs were sized on the basis of all possible critical design conditions, be it reentry, post-reentry maneuver, ascent or landing, employing as much as possible methods and criteria recommended in reference 10. Where such criteria were deemed to be insufficient, assumptions were made supplementing the available information. The design requirements and analysis methods common to all baseline designs are summarized in table 8.

Guidelines were established for the maximum use temperatures of the various structural and TPS materials as shown in figure 16. Material properties were standard design values from MIL-HDBK-5A, MIL-HDBK-17, MIL-HDBK-23 or equivalent properties based on the latest available data. Properties for carbon/carbon composites, REI and columbium were supplied in part by NASA-Langley Research Center. Where material property information was lacking, assumptions were made

Table 8: – BASELINE DESIGN REQUIREMENTS AND METHODS

1. ATMOSPHERE: 1962 STANDARD
2. TRAJECTORY: LIMIT (SEE TABLE 3)
3. BASIC TURBULENT HEATING THEORY: $\rho - \mu$
4. BASIC HEATING UNCERTAINTY FACTORS: 1.10 LAMINAR; 1.25 TURBULENT
5. SURFACE ROUGHNESS HEATING FACTOR: 1.0
6. INTERFERENCE HEATING FACTOR: 1.0
7. BOUNDARY LAYER TRANSITION ONSET: MDAC CORRELATION (EXCEPT AT POINTS 6 AND 7)
8. TRANSITION REGION LENGTH: $Re_{END} = 2 Re_{BEG}$ (EXCEPT AT POINT 6)
9. TPS PANEL INTERNAL PRESSURES: ZERO PRIOR TO $T = 2000$ SEC
10. ULTIMATE FACTOR OF SAFETY: 1.5
11. ABLATOR ALLOWABLE BOND LINE TEMPERATURE: $600^{\circ}F$
12. ABLATOR DECOMPOSITION RATE PARAMETER (COLLISION FREQUENCY): NOMINAL VALUE FOR MATERIAL CONSIDERED
13. ABLATOR DESIGN THICKNESS MARGIN: 25% OF PREDICTED THICKNESS LOST

NOTE: VARIOUS OTHER AEROTHERMODYNAMIC ENVIRONMENT PREDICTION METHODS WERE APPLIED AS APPROPRIATE FOR THE PARTICULAR POINT LOCATIONS. SEE APPENDIX C FOR DETAILS

based on literature and Boeing experience, allowing reasonable projections beyond current material capabilities.

Columbium C-129Y with a VAC-HYD 109 coating was selected as the metallic TPS material with the highest reuse temperature capability because of its advanced development level. The next metallic material capability level would be represented by tantalum alloys which still need considerable development in both material and coating. The early state of development and the lack of consistent properties led to the decision not to consider tantalum as a candidate material in the present study.

The resulting fully detailed baseline designs (figs. 17 through 21) were used as the basis for weight sensitivity and reliability assessments.

The orbiter maximum surface temperatures for the baseline conditions at the various study point locations are shown in figure 22. For comparison, the figure includes maximum temperatures at the same or similar locations on contemporary GAC, MDAC, and NAR orbiters. The differences seen can be attributed to differences in vehicle geometry, trajectory characteristics, prediction methods and/or design criteria. As with the trajectory comparisons, however, the similarity between the four sets of temperatures gives credence to the current predictions as typical delta wing orbiter values.

Design Parameter Perturbations

The perturbations applied to the baseline designs are associated with system and trajectory parameters on one hand and methods and criteria selection and application on the other. The first group of perturbations is inherent in the vehicle, its systems and the physical limitations of the group of entities connected with reentry in a random fashion. The second group is largely dependent on experience, knowledge and level of technology and can be expected to follow a learning curve with time. The present study has attempted to treat these two types of perturbations separately in order to assess their relative influence on the vehicle weight.

As a special case vehicle maneuvers were added late in the study and also treated as perturbations. A small portion of the system and trajectory perturbations was treated in a "lump" fashion by adopting a certain limit trajectory which formed the basis for the design of the baseline. This included one altitude tolerance value, one angle of attack tolerance and one angle of yaw as shown in table 3. Winds and gusts were included when determining maximum $q\alpha$ and $q\beta$ for the study. Further dispersions, including hot and cold atmospheres, other altitude and angle of attack increments as well as all method and criteria variations were treated as separate perturbations.

The selection of the particular design requirements, criteria, and method perturbations resulted in a matrix of 32 specific design conditions for 14 effective study points in addition to the baseline as shown in table 9. With a few exceptions the perturbations were applied singly, i.e., when one parameter was perturbed, all others were held at their baseline values. For various reasons, not all of the 32 perturbed design conditions were applied to the various study

Table 9: STUDY MATRIX

DESIGN CASE		STUDY POINT (CONCEPT AND LOCATION)															
		METAL TPS						HOT STRUCTURE				C/C		ABLATORS			
		1	3	5	6A	9	3A	2	4	8	6	7	7A	7B	7B1	7C	
CONDITION IMPOSED	LOWER MID-WING BODY	LOWER MID-WING	LOWER WING LE BEAM SL	LOWER WING LE SL	LOWER AFT BODY	LOWER MID-WING	SIDE BODY	UPPER MID-WING	FIN SIDE	WING LE SL	NOSE STAG PT	NASA SILICONE	PNM	PN	APOLLO		
BASE LINE (SEE DESCRIPTION OF BASELINE RQMTS)	A	A	A	A	A	A	A	A	A	A	A	A	A	A	A		
HOT ATMOSPHERE	A	A	A	A		A	A	A	A	A	A						
COLD ATMOSPHERE	A	A	A	A		A	A	A	A	A	A						
$\Delta Z = +3,000$ FT	A	A	A	A		A	A	A	A	A	A						
$\Delta Z = -7,000$ FT	A	C	B	C		A	A	A	A	B	A						
$\Delta \alpha = -5^\circ$	A	A	A	A		A	A	A	A	A	A						
$\Delta \alpha = +5^\circ$	A	C	C	B		A	A	A	A	B	A						
$\beta = 0$	A	A	A	A		A	A	A	A	A	A						
CASE I MANEUVER (70 SEC)	A	A	A	A		A	A	A	A	A	A						
CASE II MANEUVER (30 SEC)	D	D				A	A	A	A								
CASE III MANEUVER (60 SEC)	A	A				A	A	A	A								
NOM TRAJECTORY	A	A				A	A	A	A								
SPALDING-CHI TURB THEORY	A	A	A	E	A	A		A	A	E	E						
ECKERT 1*	D	D	D		D	A		A	A		E						
TURB THEORY								A	A	A							
MODIFIED LOCAL HEATING PREDICT				D				A	A	A							
1.0, 1.0 HEAT TRANS FACTOR	A	A	A	A		A	A	A	A	A	A						
1.2, 1.5 HEAT TRANS FACTOR	A	B	C	B		A	A	A	A	B	A						
1.1 ROUGHNESS FACTOR			B														
1.2 ROUGHNESS FACTOR			C														
INTERFERENCE FACTOR	E	A	D	D						A	E						
NASA BL TRANSITION PRED	A	A	D	E		A	A	A	A	E	E						
MAX OF LAM OR TURB HEAT TRANS	A	A	D	D		A	A				E						

Table 9: STUDY MATRIX (Cont)

DESIGN CASE CATEGORY	STUDY POINT (CONCEPT AND LOCATION)																
	METAL TPS							HOT STRUCTURE				C/C			ABLATORS		
	1	3	5	6A	9	3A	2	4	8	6	7	7A	7B	7C	7D		
	LOWER MID- BODY	LOWER MID- WING	LOWER WING BEAM	WING LE SL	LOWER AFT BODY	LOWER MID- WING	SIDE BODY	UPPER MID- WING	FIN SIDE	WING LE SL	NOSE STAG PT	NASA SILICONE	PNM	PN	APOLLO		
CONDITION IMPOSED	A	A	D	E		A	A	A	A	E	E						
Re 5/3 TRANSITION VARIATION	A	A	A	E		A	A	A	A	E	E						
COS δ FOR LOCAL VELOCITY	A	A	A	E		A	A	A	A	E	E						
NORM SHOCK-EXP FOR LOCAL VEL	A	A	B	E		A	A	A	A	E	E						
LOW INTERNAL PRESSURE	A	A	A	A		A	E	E	E	A	A						
HIGH INTERNAL PRESSURE	A	A	A	A		A	E	E	E	A	A						
UFS = 1.0	A	A	A	A		A	A	A	A	A	A						
UFS = 2.0	A	A	A	A		A	A	A	A	A	A						
LOW BOND LINE TEMPERATURE	E	E	E	E	E		E	E	E	E	E	A	A	A	A		
HIGH BOND LINE TEMPERATURE	E	E	E	E	E		E	E	E	E	E	A	A	A	A		
LOW COLLISION FREQUENCY	E	E	E	E	E	E	E	E	E	E	E	A	A	A	A		
HIGH COLLISION FREQUENCY	E	E	E	E	E	F	E	E	E	E	E	A	A	A	A		

NOMENCLATURE

- A - ANALYSIS COMPLETED AND DESIGN SIZED AS PLANNED
- B - TEMPERATURE EXCEEDS ALLOWABLE. TPS OR HOT STRUCTURE WEIGHT DEFINED BUT REUSE AND/OR RELIABILITY IS DEGRADED
- C - TEMPERATURE EXCEEDS ALLOWABLE. TPS WEIGHT DEFINITION NOT POSSIBLE AT INDICATED CONDITION IMPOSED. LESS SEVERE CONDITION SELECTED TO PERMIT DEVELOPMENT OF WEIGHT SENSITIVITY.
- D - TEMPERATURE EXCEEDS ALLOWABLE. TPS WEIGHT DEFINITION NOT POSSIBLE
- E - CONDITION NOT APPLICABLE AT THIS POINT
- BLANK - CONDITION WAS NOT CONSIDERED FOR THIS POINT BECAUSE OF ITS ANTICIPATED LESSER IMPORTANCE AND SCOPE OF STUDY.

points. Thus, for example, one would generally not expect to study turbulent methods or transition criteria at a nose stagnation point or the effects of collision frequency on non-ablating materials, etc. In most instances, non-applicability or evident reasons for eliminating certain cases from detail analysis could be established by inspection.

Final Designs

The final designs at the various study points constitute changed baseline designs due to the variations from the baseline caused by the particular design parameter perturbations. The final designs were sized as a result of repeating or readjusting the required loads, thermal and strength analyses for each particular study point and the respective weight perturbation and provide the necessary weight information for determining weight sensitivity.

Weight Sensitivity Determination

The sensitivity to design parameter perturbations was determined by examining the change in panel or structural unit weight versus change in various parameters, criteria and/or prediction methods. The approach taken in developing such data was to compute the weight of each final panel or structural design which evolved from the redesign effort due to deviations from the baseline design based on the limit trajectory. Particular emphasis was placed on comparisons of weight sensitivity dispersions that are statistically or otherwise rationally predictable versus sensitivity to uncertainty factors, estimating techniques, and other inexact criteria. By keeping these two types of parameters separate it is possible to see which group is more sensitive and to determine the extent of its leverage on vehicle weight and design.

A difficulty in determining the full range of sensitivities was encountered in the metal heat shield studies because a number of design method or criteria perturbations led to temperatures in excess of the maximum allowable for columbium. Since columbium was the highest temperature metal considered, the theoretical result in these cases would have led to an unrealistic design and invalidated any comparisons. Therefore, a method was devised for permitting comparisons on a partial basis. In cases where the perturbation parameter was continuously variable, e.g., angle of attack, orbiter reentry weight, or surface roughness factor, it was possible to show the weight sensitivity up to the value of the parameter yielding the temperature limit. For these cases, the design weight was shown up to a maximum temperature of 2450°F, i.e., 50° beyond the postulated columbium full reuse limit. Sizing the TPS for any higher temperatures was not considered practical because of the rapidly deteriorating creep capability for C129Y columbium alloy. Although columbium panel designs were thus postulated to withstand maximum temperatures greater than the 2400° established maximum, it should be realized that these designs may be subject to reduced reliability or service life.

For cases where the perturbation was a discrete or "point" change in method, an excess temperature condition could only be identified as such, and no weight associated with the particular method could be stated.

Certain unexpected results appeared in the weight sensitivity relations due to local combinations of effects. These seeming anomalies, seen rather frequently, illustrate the need for caution in drawing general conclusions. In most instances such anomalies were due to the behavior of boundary layer transition causing shifts in transition location with variation in the perturbation parameter. In some cases, the transition shift caused a change in maximum temperature at a point, opposite to the change due to that particular perturbation parameter itself through its effect on laminar or turbulent heating.

The result of this sensitivity analysis formed the basis for assessing the importance of the various design parameters on orbiter vehicle design and for establishing leverage of each parameter or combination of parameters on vehicle weight.

The weight sensitivity relations are summarized in figures 23 through 27. All weights are expressed as percentages of the baseline panel weight per unit surface area. The weights from which these percentages were derived include weights of load-bearing components, surface materials, insulation, bond layers, etc., as detailed in figures 17 through 21. Numbers associated with the individual curves or bars on the bar charts refer to the study points to which those curves or bars apply. Weight sensitivity plots for each point treated individually, showing more details of the results, are included in Appendix E.

Several of the weight sensitivity curves for the metallic TPS points (fig. 23) are affected by the design temperature limitation and the resulting reduced range of the perturbation parameter as discussed on page 27. Specifically, the upper ends of curves for altitude perturbations at points 3, 5, and 6A, those for angle of attack perturbations at points 3 and 5, and for heat transfer uncertainty factor and surface roughness factor perturbations at point 5 should not be extended beyond their present end points. These end points represent the 2450°F maximum temperatures beyond which definition of a columbium panel design is not possible. Where a discrete method perturbation yielded a temperature above 2450°F, the weight bar on the figure is shown open, indicating that no sizing or weighing was possible. The individual point weight sensitivity plots in Appendix E show the values of the continuous perturbation parameters for which the 2400°F allowable for full columbium reuse occurs as well as the 2450° values. Also shown in Appendix E plots are the maximum temperatures for most discrete perturbations regardless of whether the design could be defined.

The maximum temperature entries were omitted from some of the plots where, by inspection or scaling techniques, design weights were derived without the need of detailed temperature histories. It is pointed out that the maximum temperatures alone do not necessarily characterize the thermal environment for design sensitivity purposes. For designs at some of the points lower temperatures occurring at critical load conditions or total heat load effects on insulation requirements were more important than the effects of peak temperature.

In many cases a sharp rise is exhibited by the metallic TPS weight curves as the perturbation parameter varies in the direction of more severe heating, e.g., point number 3 subjected to angle of attack perturbations. These sharp increases are due not so much to the effect of the perturbation parameter on the heating environment, but to the effect of temperature on the weight of the TPS panel metal components. The steep slopes cited derive directly from the steep slopes of the curves of figure 14 in the 2300° to 2450°F region.

The lack of sensitivity of metallic TPS panel weights to panel net pressures above 0.4 lb/in² is consistent with the same characteristic of the curves of figure 14. Panel net pressures were perturbed only up to 0.7 lb/in². It is possible that above this level a sensitivity would again appear.

It is seen from figure 23 that the metallic TPS designs exhibit no sensitivity to ultimate factor of safety. The reason is that all the metallic TPS designs are creep-critical and that creep assessment utilizes limit (yield) stresses, not ultimate stresses.

The sensitivities of the reusable external insulation design, shown in figure 24, are due entirely to thermal effects. The titanium honeycomb panel which supported the REI (fig. 18) was sized by ascent pressure loads, and the REI itself, in all thicknesses required for its insulation function, was found adequate for all ascent and reentry pressure loads. Thus, no design sensitivity exists to perturbations in net pressures or in ultimate factor of safety. The only sensitivity to perturbations in altitude, angle of attack, or atmosphere is through the thermal effects of these parameters on insulation thickness.

The hot structure points, figure 25, exhibit little or no sensitivity to any of the perturbations except those of ultimate factor of safety. The hot structure panel at point number 2 remained critical to ascent load conditions regardless of the perturbations in reentry environment or analysis methods that were applied. Thus, it exhibits no sensitivity at all to those perturbations.

The panels at points 4 and 8 were found to be critical to conditions of the post-reentry 2.5g maneuver and the reentry maximum dynamic pressure (actually occurring in the transitional flight phase), respectively. At the times of these conditions the effects of perturbations in the reentry thermal environment had largely disappeared, resulting in little variation in the critical design temperatures with the various perturbations. Then, since limit loads were not perturbed at these conditions, only the perturbations of ultimate factor of safety produced any significant design weight sensitivities.

In the case of some of the perturbations, because of the fact that aerodynamic cooling rather than heating existed in the neighborhood of the design conditions, reversals in the usual weight sensitivity trends are seen. Thus, for development of the Rho- μ , Spalding-Chi, Eckert i^* comparisons for point 4 in figure 25, the Spalding-Chi method gave the lowest heat transfer coefficients and the Eckert i^* the highest, as usual. In the cooling environment of the design conditions, however, the lowest heat transfer coefficients led to the highest temperatures and the highest design weight, and the highest coefficients produced the lowest temperatures and weight. A similar departure from the expected trend is seen for the effect of heat transfer uncertainty factor perturbations on point number 4.

The weight sensitivity curves for the carbon/carbon composite points in figure 26 exhibit, in many cases, the stepped character, arising directly from that feature of the sizing curves in figure 15. In the case of the perturbation of heat transfer uncertainty factor, the pressure load and therefore the weight of the carbon/carbon material alone does not change. The slight continuous slope seen in the total weight sensitivity curve is due entirely to the variation in insulation weight. It is evident that the sensitivity of the insulation weight in this case is quite small, and its contribution to the other carbon/carbon design weight sensitivities was likewise quite small.

Ablator weight sensitivities, summarized in figure 27, were evaluated only for perturbations in allowable bond line temperature and for perturbations in the virgin material collision frequency. The latter parameter is a measure of the material decomposition rate in a given thermal environment. A one order of magnitude variation in this parameter was chosen for the purposes of this study for perturbations representing all uncertainties in the ablator decomposition kinetics. The ablation TPS design weights from which the curves of figure 27 were derived include the weight of the titanium honeycomb support panel (fig. 21), the bonding material, and the design margin equivalent to 25% of the predicted thickness lost, in accordance with reference 10. Detailed results and evaluation of ablator studies are given in Appendix D.

It is seen in figure 27 that the sensitivities of ablator design weights to bond line temperatures are greater for variations about the lower baseline allowable bond line temperature. It was also concluded, for some of the material and temperature ranges, that a small margin in design weight (ablator thickness) would yield a substantial margin in actual bond line temperature.

Variations in decomposition rate, as represented by the one-order-of-magnitude range in perturbations of collision frequency, as seen in figure 27, have a relatively minor effect on ablator design weight. This observation adds confidence to the viability of ablator designs even though material decomposition kinetic properties may not be known to great accuracy.

Total surface recession values for two of the candidate ablators studied, the NASA silicone material, and the phenolic nylon with microballoons (PNM) were very near one inch. The design margin, computed according to the design criteria specified in reference 10, accounts for 10% to 12% of the baseline weights of the NASA silicone and the PNM designs, respectively. From figure 27, then, the corresponding margins in bond line temperature are 125°F and 220°F, respectively. For the Apollo ablation material, very little recession is expected. Thus, for this material, the same design criteria would yield only a very small margin in bond line temperature. No margin would be available for non-receding materials. In order to avoid over-conservatism and at the same time provide sufficient design margins the currently recommended (ref. 10) ablator design criteria should be revised. Such revision could specify either sizing the ablator using an arbitrary percentage increase in overall thickness or a specified toleranced bond line temperature.

Combined Thermal-Structural Loads Sensitivities

After determination of the sensitivities of the individual study points to the particular method and criteria perturbations, as shown in figures 23 through 27, a means of analytically combining the sensitivity results was sought. Such a combination was essential to a quantitative comparison of perturbations grouped as specified in the study objectives into categories of trajectory and system parameter perturbations and method and criteria perturbations (table 9). A means of combining the results to permit assessment of the perturbations on the vehicle as a whole, rather than on discrete locations, was also desired.

Three possible means of combining the sensitivities to the various perturbations were considered. The simplest technique, and one often employed in structural design, was the worst-on-worst approach, where the extreme positive weight increments due to each perturbation are summed directly. The second technique was the root-sum-square (RSS) method, where the extreme positive and negative weight increments are, in two respective groups, squared before summation, and the sum raised to the one-half power to yield the combined extreme positive and negative weight increments. The weight increments at any intermediate values of the perturbation parameter, where available, may be treated likewise in order to develop continuous RSS combined sensitivity relations. The third and most sophisticated combination technique is the Monte Carlo method, in which an appropriate sample array of discrete combinations is analyzed by statistical techniques to predict combined sensitivities and probabilities thereof, as influenced by all possible discrete combinations of perturbation effects. Fundamentals of the Monte Carlo approach are described in reference 11 and an application to a problem similar to the present one, the analysis of combinations of lunar landing load components, was reported in reference 12.

The worst-on-worst approach was eliminated as unrealistically conservative considering the number and extent of the perturbations treated in this study. Its use implies a 100% correlation coefficient between each pair of dispersion parameters, which is certainly not the case for the perturbations studied here.

The Monte Carlo method was the ideally preferred method and the one that, had the required data base existed, was appropriate for the present purpose. Its use would have permitted proper accounting for probability distributions of the various perturbation parameters and for correlations between the parameters. The lack of these probability distributions and correlations, however, was the reason for eliminating the Monte Carlo method as a means of combining the weight sensitivities from this study.

The root-sum-square method was selected as the only practical, although far from ideal, technique for the present study. Its use implies the existence of zero correlation coefficients among all dispersion parameters whose effects are combined. This condition was probably satisfied by some of the parameters. However, among other parameters, such as trajectory, attitude, and atmosphere dispersion, correlations, although undefined, undoubtedly existed. Also implicit in the application of the RSS technique is a knowledge of the probability distributions of the parameters so that the effects thereof can be

combined at a common probability level (σ factor). The results of the application of the RSS method must therefore be tempered with the recognition that these conditions were not entirely satisfied and the application itself should be viewed primarily as an illustration of a sensitivity combination technique. Results from the RSS combination exercise, shown in table 10, should be interpreted with extreme caution and with recognition of the limitations that will be pointed out in the following paragraphs.

For the purpose of exercising the root-sum-square combination technique, only the primary design concepts at the nine orbiter study point locations were included. Thus, study points 3A (REI), 6A (metallic TPS on the wing leading edge), and points 7A, 7B, 7B1 and 7C (ablaters) were eliminated. Also, only those method and criteria perturbations that were considered realistic and were extensively examined were included. Thus, the Eckert i^* turbulent heat transfer theory was eliminated as not comparable to the Rho- μ or Spalding-Chi methods from a standpoint of realism. The maneuver excursions, the modified local heating predictions, and the maximum of laminar or turbulent heat transfer conditions were eliminated since they were applied at only a limited number of points.

Even with the reduction in scope of the sensitivity combination exercise as described in the preceding paragraph, a complete set of input data did not exist, as evidenced by the blank spaces in the matrix of table 9. In order to fill in all the required inputs, estimates were made for the missing sensitivity values and are so identified among the input values in table 10.

An additional problem encountered in carrying out the combination operations was the fact that for certain study point - perturbation parameter combinations design weights were undefined (see figure 23). In the case of the continuously varying parameters, e.g., ΔZ and $\Delta \alpha$, this problem was circumvented by reducing the range of the perturbation parameter to a level where a weight value was defined. This reduced value of the parameter was then treated as the extreme for the purpose of sensitivity combinations. Such parameter range reductions were made symmetrically so that the parameter was assumed to vary equally above and below the baseline value. Also, the range reduction, as necessitated by the most restrictive point, was then applied for evaluating the sensitivity of all study points to that parameter. The resulting ranges for the perturbation parameters selected for the purpose of this exercise are shown in table 10 and can be construed to represent the 2σ values of the parameter distributions.

When an application of a particular analysis method or technique as a perturbation parameter resulted in an undefined weight, a range reduction, of course, was not possible and the only recourse was to ignore the particular undefined weight increment. Such was the case, for example, of point number 5 when subjected to the transition prediction perturbation, as indicated in table 10.

The reduction of parameter ranges and the approximation or dropping of particular conditions in order to avoid undefined design weights imposed a certain bias upon the results. This simplification reduced or eliminated,

Table 10.
 ROOT-SUM-SQUARE COMBINATIONS OF THERMAL STRUCTURAL
 DESIGN CRITERIA PERTURBATIONS

CATEGORY	DESIGN CASE		STUDY POINT INCREMENTAL WEIGHT, FRACTION OF BASELINE WEIGHT PER UNIT AREA																	
	PERTURBATION PARAMETER	PARAMETER RANGE	POINT 1		POINT 2		POINT 3		POINT 4		POINT 5		POINT 6		POINT 7		POINT 8		POINT 9	
			HIGH	LOW	HIGH	LOW	HIGH	LOW	HIGH	LOW	HIGH	LOW	HIGH	LOW	HIGH	LOW	HIGH	LOW	HIGH	LOW
TRAJECTORY & SYSTEMS	ΔZ	-3000 FT. +3000 FT.	.03	-.015	0	0	.18	-.05	0	-.005	.10	-.11	.015	-.080	.015	-.065	0	-.005	.03	-.015*
	$\Delta \alpha$	+3° -3°	.04	-.015	0	0	.22	-.030	0	0	.30	-.075	0	0	0	0	0	0	0	-.04*
	$\Delta \beta$	0 5°	0*	0	0	0	0	0	0	0*	0	0	0	-.09	0*	0*	0	0	0	0*
METHODS & CRITERIA	ATMOS.	HOT COLD	.035	-.02	0	0	.155	-.05	0	0	.055	-.14	.02	-.09	.01	-.085	0	0	.035*	-.02*
	TURB. HT	RHO-MU S-C	0*	-.01*	0	0	0	-.01	.005	0	0	-.068	0*	0*	0*	0*	0	0	0.025	0
	TRANS. PRED.	NASA MDAC	0	0	0	0	.023	0	0	-.01	X	0	0*	0*	0*	0*	0	0	0	0*
	TRANS. VAR.	RE 5:3	0	0	0	0	.006	0	0	0	X	0	0*	0*	0*	0*	0	0	0	0*
	F	1.14, 1.35, 1.06, 1.15	.022	-.015	0	0	.055	-.035	.003	0	.140	-.065	.002	-.002	.002	-.002	0	-.003	.022*	-.015*
	R	1.1 0.9	.22*	-.08*	0*	0*	.22*	-.08*	0*	0*	.22	-.085	0*	0*	0*	0*	0*	0*	.22*	-.08*
	v_e PRED.	ALL 3 METHODS	0	-.017	0	0	.021	-.065	0*	0*	.19	-.035	0*	0*	0*	0*	0*	0*	0*	0*
	Δp	1 ± .75) × BASELINE	0	-.005	0	0	0	-.03	0*	0*	0	-.10	.12	-.085	.130	-.095	0*	0*	0*	-.005*
	UFS	2.0 1.0	0	0	0	0	0	0	.260	-.105	0	0	.02	-.10	.03	-.10	.22	.183	0*	0*
	T&S	ROOT-SUM-SQUARE COMBINATION	HIGH & LOW Δ WEIGHT COMBINATIONS OF THE ABOVE, RESPECTIVELY	.061	-.029	0	0	.324	-.077	0	-.006	.321	-.193	.025	-.150	.018	-.1165	0	-.0112	.061
M&C			.221	-.084	0	0	.229	-.113	.260	-.106	.323	-.165	.122	-.1315	.1335	-.138	.22	-.183	.223	-.083
STUDY POINT DESIGN WEIGHT, % OF BASELINE																				
T&S	COMBINED EFFECTS	HIGH & LOW Δ WEIGHT COMBINATIONS OF THE ABOVE, RESPECTIVELY	106.1	97.1	100	100	132.4	92.3	100	99.5	132.1	80.7	102.5	85	101.8	88.4	100	98.9	106.1	97.1
M&C			122.1	91.6	100	100	122.9	88.7	126	89.5	132.3	83.5	112.2	86.8	113.4	86.2	122	81.7	122.3	91.7
ORBITER SURFACE AREA REPRESENTED BY STUDY POINT, % OF TOTAL AREA																				
			5.0	31.0	25.0	27.0	1.0	1.0	1.0	0.5	6.5	3.0								

* ESTIMATED
 X WEIGHT UNDEFINED

respectively, effects which, had they been definable in terms of design weight, could have altered the combined weight sensitivity values.

The results of the RSS combinations of design perturbations in table 10 show no consistent trends with regard to the relative effects of trajectory and systems perturbations versus those of method and criteria perturbations. It is recognized that some general trends may have been obscured by the limitations of this exercise. However, some general conclusions are still possible and deserve attention.

The metallic TPS points (points 1, 3, 5 and 9) appear to be more sensitive to both categories of perturbations than the carbon/carbon (points 6 and 7) or the hot structure points (points 2, 4, and 8). The hot structure points would universally show almost no sensitivity were it not for the contribution of the ultimate factor of safety perturbation. The same perturbation was a strong but not the exclusive determinant of combined sensitivities for the carbon/carbon points. It can also be seen that the RSS approach results in lower combined structural weight sensitivities than a worst-on-worst approach.

A basis does not exist for determining whether the results of table 10 are applicable to lifting reentry vehicles in general or only to the particular orbiter configuration, reentry trajectory, and design concepts. Characteristics of individual sensitivities observed during their formulation led to the tentative conclusion that the combined sensitivity trends seen in table 10 should be considered as pertinent only to the conditions of this study.

In order to gain the proper perspective of the sensitivity assessment and to relate it to the entire vehicle a further step in the combination of design sensitivities can be accomplished by applying the estimated orbiter surface area percentages represented by each study point as shown in table 10. Had a more comprehensive data base been available, permitting a more rigorous approach to combining sensitivities, a weighted average of the sensitivities at each study point, formed by use of appropriate area percentages as weighting factors, would have provided a proper measure of the overall vehicle sensitivity. The area-averaged sensitivities could be developed for individual perturbations or perturbations in any desired combination. The suggested computation of overall vehicle sensitivities was not carried out here since a complete set of perturbation and sensitivity data for all study points was not available. However, it is felt that given this full matrix of data, valuable conclusions could have been established.

The further assessment of the broader effects of the sensitivities on shuttle system and mission capability would require an additional weighting operation, wherein the contribution of TPS or hot structure weight to the vehicle total inert weight would be accounted for. Application of trades between payload, propellant weight, orbital capability, and reentry cross range could then indicate the final impact of the perturbation parameters on mission capability.

The results of an RSS combination of sensitivities may be used, within the qualifications of the RSS technique, to gain some insight as to the degree of

conservatism inherent in the approach used to develop the baseline designs for this study. The baseline designs at the various study points were determined on the basis of simultaneous application of the trajectory and systems dispersions as listed in table 3. These criteria resulted in a design, at each particular point, whose weight is approximately that represented by a worst-on-worst combination of individual sensitivities to those dispersions. The resulting design is over-conservative since, in general, the probability of simultaneous occurrence of the dispersion extremes is less than the probability of occurrence of each dispersion extreme taken independently.

In order to illustrate the assessment of the degree of conservatism in the baseline designs, point number 3 was examined as an example. For the purpose of this illustration the sensitivities of point 3 to altitude, angle of attack and angle of yaw, as shown in figure 23, were assumed to be mutually independent. Then the percentage weight increases associated with variations of ΔZ from +3000 feet to 0, α from -5° to 0, and β from 0 to 5° could be interpreted as representing the contributions of the respective dispersions to the weight difference between a nominal design, i.e., one based on conditions of the nominal trajectory, and the baseline design. The existing weight sensitivity curves of figure 23 were thus used to supply data for table 11, where comparisons between the worst-on-worst and RSS combinations of weight effects from the limit trajectory dispersions are illustrated. From table 11 it is seen that the design incorporating the desired degree of conservatism, (represented by the RSS combination of limit trajectory dispersions) is 6.1% heavier than a design satisfying the conditions of the nominal trajectory. The worst-on-worst combination design, equivalent to the baseline design, is 8.5% heavier than the nominal, i.e., 2.4% heavier than actually necessary to satisfy an independent-dispersion limit trajectory criterion.

The lower section of table 11 shows a possible distribution of study point design weights whose worst-on-worst combination equals the RSS combination of limit dispersion effects. Associated with these reduced perturbed weights are trajectory dispersion parameter values defining a modified limit trajectory. The use of such a modified limit trajectory is a possible means of retaining the practical approach of designing to a simultaneously applied set of trajectory dispersions without incurring excessive design conservatism.

In the simplified example of table 11, the RSS combination of dispersion contributions was used to arrive at an indication of the desired degree of conservatism. In a more rigorous effort to establish design requirements, the Monte Carlo or other more sophisticated techniques could be used in the same way to arrive at a modified limit or design trajectory, providing a higher degree of confidence in the validity of such an approach.

Table 11:

COMPARISON OF TRAJECTORY DISPERSION EFFECTS
POINT NUMBER 3 NOMINAL DESIGN

TRAJECTORY DESIGNATION	DISPERSION PARAMETER	PARAMETER VALUE	STUDY POINT DESIGN WEIGHT, % OF NOMINAL
NOMINAL	ΔZ	0	100
	$\Delta \alpha$	0	
	$\Delta \beta$	0	
LIMIT	ΔZ	-3000 FT	105.0
	$\Delta \alpha$	+5°	103.5
	$\Delta \beta$	+5°	100.0
	Worst-on-Worst Combination		108.5
	Root-Sum-Square Combination		106.1
MODIFIED LIMIT	ΔZ	-2000 Ft	103.6
	$\Delta \alpha$	+1.7°	102.5
	$\Delta \beta$	+5°	100.0
	Worst-on-Worst Combination		106.1

TPS Design Margins

Metallic TPS design during reentry was governed by limit loads because of limitations on thermal distortions and creep. Thus, the use of the ultimate factor of safety in defining ultimate loads did not assure the metallic TPS the usual ultimate factor of safety margins during reentry. Because of this fact there was concern over the possible lack of margins in the TPS design to accommodate possible overload (limit-exceeding) flight conditions.

The quantitative results of this study do not provide a comprehensive assessment of TPS design margins because of the multitude of ways and times that overload conditions could occur and the different failure modes possible. The maneuver excursion study, however, provided data that could be examined as a single hypothetical assessment of metallic TPS design margin.

It was found for this hypothetical case that a design margin for the metallic TPS could be construed to exist, primarily by virtue of the TPS being designed for multiple missions. Even this single-point, hypothetical margin cannot be defined precisely, since, toward the end of the vehicle life, the cumulative effects of creep and oxidation will have consumed some part of the margin.

The baseline metallic TPS design at point number 3 was actually sized by a peak temperature occurring at $t = 1350$ seconds, a peak pressure at $t = 2000$ seconds, and a temperature gradient occurring at $t = 60$ seconds. The maneuver excursion study, however, was conducted for maneuvers, i.e., potential overloads, initiated at $t = 1098$ seconds. Therefore the TPS margin assessment could be performed only for a hypothetical metallic TPS design, located at point number 3 but sized for the temperature and pressure conditions existing at $t = 1098$ seconds and immediately thereafter.

Figure 28 shows the relationship between metallic TPS surface temperature and surface pressure for the range of the maneuvers studied. These data were taken directly from the results of the maneuver aerothermodynamic and thermal analyses. The ultimate external pressure indicated on the figure was found by multiplying the limit design pressure by an ultimate factor of safety of 1.5. The 2395°F temperature associated with the ultimate pressure, by virtue of some inferred maneuver, consistent with the curve, was then read from the graph.

Referring to the C129Y material properties of figure 95, it is seen that the creep allowable at the above described "ultimate" temperature of 2395°F is approximately one-third the allowable at the limit temperature of 2172°F. With an allowable reduced to one-third the design value and an applied load increased to 1.5 times the design value, assuming linear creep behavior, the creep for a single maneuver excursion could be estimated as 4.5 times the amount expected for a single normal (limit) flight. Thus the effect of the excursion would be to reduce the life of the TPS by approximately 5 normal missions. An estimate of the effect of actual creep behavior indicated a greater reduction in TPS life.

Obviously, the TPS has a greater margin than the preceding exercise indicates, provided a further reduction in TPS life is acceptable. It is seen from figure 95, however, that the C129Y creep allowable approaches zero at approximately 2600°F, indicating the possibility of experiencing more than the entire lifetime allowable creep in a single overload excursion. Also, at temperatures in this neighborhood for C129Y, accelerated oxidation or coating degradation occurs, introducing an additional failure mode.

It is clear that a detailed assessment of metallic TPS design margins would require a comprehensive evaluation of failure modes, including more details on material properties and property degradation than currently exist. Furthermore, a complete definition of the metallic TPS reentry margins would require examination of all possible flight condition excursions at frequent time points throughout reentry. It is also evident that the margins are not constant but vary through the life of the vehicle.

The practice of designing TPS to limit conditions apparently results in some capability to survive overload conditions. Since the consequence of experiencing an overload condition is, in all probability, an excessive deformation or local coating failure and not catastrophic failure, such an occurrence should not jeopardize the safety of the crew or the completion of that particular mission. For this objective to be met it is important that postflight inspection procedures ensure the detection of damaged TPS panels prior to the development of a dangerous condition. It is also important that the TPS be designed so that deformation does not result in catastrophic failure.

Reliability Assessment

Determination of reliability involves definition of acceptable risk. In an actual design development acceptable risk levels depend on trades between the value of what is risked against the penalties for reducing the risk. It is obvious that designing of the vehicle to extremely severe loads criteria would virtually eliminate the probability of having to change the flight plan to avoid the risk of loss of the vehicle or mission due to contingencies. However, such extremely conservative criteria would be acceptable only if the weight penalty involved were small, which, also quite obviously, is not the case. Thus, definition of risk levels for design criteria on a rational basis is both a selective and an iterative process, since the final selection is generally influenced by risk assessment weighed against the potential penalties involved.

In establishing a reliability assessment philosophy, it was decided to use the form of a word chart with a grading system, where the grading was based on a scale of one to five representing the consensus of experience of advanced vehicle design personnel. The reliability assessment was guided by considerations which, although somewhat lacking in precision, relate back to aircraft, spacecraft, and reentry vehicle design experience. Thus, the assessment can at best be considered qualitative.

The factors considered in the evaluation relate directly to the current state of the art of reentry vehicle design, including the sensitivity of the various designs to trajectory and system parameters, and method and criteria perturbations, and reflect the experience obtained from various reentry flight programs. Another set of evaluation parameters deals with the amount of development required for the various design concepts and ties in with the problem of component and materials integrity of the various point designs. Finally, operational problems affecting reliability were included in the rating chart even though these problems were not examined in the course of the present study. It was assumed for the purpose of this study that enough familiarity with the entire problem of Space Shuttle design and operation existed for assessing the degree of familiarity with the problems of design at the selected study points. A set of weighting factors was chosen, indicating the relative importance of the various problem areas to the overall reliability.

The results of the reliability assessment are shown in table 12. A more detailed quantitative reliability assessment was lacking the required data base and was considered beyond the scope of the present program.

The ratings of reliability with regard to insensitivity to trajectory and systems parameters and to analysis methods and criteria were based on a review of the weight sensitivity summaries, figures 23 through 27. Weight insensitivity was felt to be a valid indicator of design reliability since a high insensitivity (low sensitivity) to a particular parameter indicates the possibility of achieving a large capability margin, hence reliability, with a small weight penalty. It is seen from table 12 that there are no significant differences between sensitivity to trajectory and system parameters and sensitivity to analysis methods and criteria.

From the total weighted reliability figures in table 12, it is seen that the hot structure points received ratings of significantly higher reliability than the other concepts. In making such comparisons, however, it must be recognized that differences arise from the particular points' locations and local environments on the vehicle studied, as well as from characteristics inherent in the design concepts. The ablators showed poorer reliability than the hot structure points and were followed by the metallic TPS and C/C points, with REI receiving the lowest rating.

- KEY:**
 1 . VERY-HIGH
 2 . HIGH
 3 . MODERATE
 4 . LOW
 5 . VERY LOW

Table 12
RELIABILITY ASSESSMENT — ORBITER REENTRY

WEIGHTING FACTOR	PROBLEM	STUDY POINT																
		METAL TPS						HOT STRUCT			C/C		ABLATORS					
		1	3	5	6A	9	REI	2	4	8	6	7	7A	7B	7B1	7C		
		LOWER MID BODY	LOWER MID WING	LOWER WING BEAM	WING LE SL	LOWER AFT BODY	LOWER MID WING	SIDE BODY	UPPER MID WING	FIN SIDE	WING LE SL	NOSE STAG PT	NASA SILICONE	PNM	PN	APOLLO		
2	Inensitivity to: Traj. & Sys. Parameters Analysis Meth. & Crit.	2	4	4	4	2	2	1	1	1	2	2	2	2	2	2		
1		2	3	5	4	2	2	1	1	1	2	2	2	2	2	2		
1	Confidence in Analysis	3	3	3	2	3	5	2	2	2	4	3	3	2	2	3		
2	Confidence in Design	3	3	3	3	4	5	2	2	2	4	4	3	3	3	3		
2	Concept Inherent Forgiveness	4	4	4	4	4	3	3	3	3	3	3	1	1	1	1		
2	Concept Dev. Status (Materials and Fabrication)	4	4	4	4	4	5	2	2	1	4	4	3	4	4	3		
1	Design Application Experience	4	4	4	4	4	5	3	2	2	4	4	3	3	3	2		
2	Ground Test Confidence	3	3	3	3	3	4	1	1	1	2	2	3	3	3	3		
5	Handling	4	4	4	4	4	5	1	1	1	3	3	2	3	2	3		
3	Inspection	3	3	3	3	3	4	1	1	1	3	3	4	4	4	4		
4	Maintainability (Repair and Refurbishment)	3	3	3	3	3	2	1	1	1	4	4	2	3	3	3		
TOTAL WEIGHTED RELIABILITY*		82	87	89	87	88	95	36	35	33	80	79	62	72	67	70		

* IDEAL SCORE IS 25

CONCLUSIONS AND RECOMMENDATIONS

The present study used as a guideline the recommended practices and criteria outlined in reference 10. Where this guideline was insufficient, assumptions were made to supplement the recommendations therein. On this basis a vehicle design study was undertaken using characteristic point designs for Space Shuttle orbiter vehicles to assess the effects of the assumed design parameters, methods and criteria on the thermal structural combined loads environment and the resulting design concept weight sensitivities. The major work items included in the present program were the determination of the thermal and pressure environment, calculation of design loads, computation of structural design temperatures, and definition of structural designs.

It was concluded that the variation in vehicle systems and trajectory parameters showed comparable sensitivities to those produced by perturbing methods and criteria.

Although the conclusions reached in this study were influenced by the initial assumptions, the selected configuration and trajectory, as well as the methods and criteria employed, some general conclusions were reached. The findings of this study although intended to supplement NASA SP-8057, by virtue of their subject matter, also impact on NASA SP-8062, "Entry Gasdynamic Heating" and NASA SP-8014, "Entry Thermal Protection." (For details see also Appendices C and G.)

The most important conclusions are summarized in the following paragraphs.

Aerothermodynamic Environment

The vehicle trajectories used in this study were not obtained by a rigorous optimization procedure, but were selected with the assumption that the thermal and load limits of the conceived structure would not be exceeded. Nevertheless, some of the conditions studied resulted in environments too severe for the metallic TPS employing columbium, which was the highest temperature candidate metal considered. This result, however, may be overly pessimistic since in actual practice the designer would exhaust all possibilities of modifying and refining the vehicle trajectory in order to alleviate thermal loading before resorting to more exotic TPS materials (such as tantalum) or employing columbium beyond its established reuse temperature capability.

The boundary layer transition criteria selection has a very strong influence on location of peak heating. The total heat load is influenced to a lesser degree. Since thermal and pressure environment predictions are dependent on the selected configuration, trajectory, methods and criteria, conclusions and extrapolations cannot be readily generalized. In some cases contradictory trends were observed due to various combinations of the above factors.

The present study indicated that either the Rho-mu or Spalding-Chi heat transfer prediction methods are acceptable for prediction of turbulent heat

transfer to a Space Shuttle orbiter. The difference in TPS design weights resulting from use of these two methods was not significant.

Roughness effects on heating and on transition cannot be accurately predicted without more experimental information. Roughness, while increasing heating in the immediate vicinity of the roughness, may act to reduce heating over some areas of the vehicle by moving the transition point and, thereby the point of peak heating (turbulent overshoot), forward on the vehicle and earlier in the trajectory. To assess the effect of this phenomenon heat rates for this case can be approximated by using the maximum of the laminar or turbulent heating approach. This results in higher heating to forward regions and reduces heat transfer to aft portions of the vehicle where turbulent overshoot conditions would have occurred according to the predictions based on more advanced boundary layer transition criteria. The differences in heating distribution with differences in transition location are illustrated in figure 29. Because of this phenomenon and the fact that some degree of roughness is unavoidable, it would seem that for the cases where a serious weight penalty on forward areas of the vehicle can be avoided, turbulent flow may be a preferable mode. The question of physical viability of this situation merits further investigation.

It should also be realized that the preceding finding shows that the approach employed in some past design practices of using the maximum of the predicted laminar or turbulent heating does not necessarily represent the worst case condition on a vehicle.

It can be seen from the above that the presence of surface roughness and its effects can significantly alter the conclusions of this study.

No special abort considerations were found to be critical for the vehicle environment, assuming no loss in orbiter main engine power and assuming orbiter capability to abort into orbit exists. Preliminary studies by Grumman (reference 8) also indicated that orbiter sub-orbital and/or fly-back return from early booster failure would impose no environmental conditions on the structure more severe than those of normal reentry.

Loads and Stresses

The various design concepts exhibited widely varying degrees of sensitivity to load level perturbations and to the particular type of load considered.

The metallic TPS panels were found to be critical for both boost and reentry load conditions. Ultimate loads during boost were found to influence the design of the panels even though temperature-critical design conditions existed during reentry. At the lower temperature ranges during reentry, thermal distortion limitations governed detail structural design. At the higher temperatures of reentry creep limitations governed sizing. Optimization procedures used for the TPS design accounted for these varying requirements, resulting in a balanced design, equally critical for the governing conditions.

Among the study points examined in the course of the definition of baseline and perturbed designs no thermal stresses acting to alleviate load-induced stresses at a critical design condition were found. Thus, a selection of criteria for combining stress components of opposite signs was not necessitated during the design exercises of this study.

Ideally, a probabilistic approach should be followed for predicting all design loads and resulting stresses. On this basis, the load-induced and thermally-induced stresses should be combined at the dispersion levels appropriate to satisfy the required design success probability regardless of the signs of the components. Thus, if thermal stress acts to aggravate the load-induced stress, the $(\text{mean} + n \sigma)$ * level of thermal stress is added to the $(\text{mean} + n \sigma)$ level of load stress. If the thermal stress acts to alleviate a predominant load-induced stress, the $(\text{mean} - n \sigma)$ level of thermal stress should be subtracted from the $(\text{mean} + n \sigma)$ level of the load-induced stress.

In actual design analyses the dispersions in stresses needed to carry out the combination approach described in the preceding paragraph may not be adequately defined. Usually, conservative methods and uncertainty factors employed in thermal analysis lead to a design thermal stress that exceeds the mean of the possible dispersion by some unknown amount. Where thermal and load stresses have the same sign the undefined conservatism in the thermal stress introduces no problem and it is recommended that the two components be added to obtain the combined design stress. Where thermal stress acts to alleviate the load stress, combining the two components according to their signs could result in an unconservative estimate of net stress. For this case it is therefore recommended that the thermal stress be ignored. Similarly, if the thermal stress is the predominant component and the load stress is alleviating, the latter should be ignored in arriving at the design stress.

It is further recommended that the factor of safety used to arrive at ultimate load or stress be applied only to the mechanical load or mechanical-load-induced stress and not to the thermally-induced component, regardless of how they are combined. The reason for this recommendation is that thermal stresses, unlike mechanical-load-induced stresses, tend to be self-relieving once the yield stress is reached. Thus it is unlikely that thermal stresses could be responsible for the total stress approaching or exceeding the ultimate allowable for the material.

The ultimate factor of safety was found to be a significant driver for orbiter structural weight.

Temperatures and Heat Loads

In general, higher peak temperatures were obtained in the present study than have been shown by the Space Shuttle Phase A and B contractors. This result was due to the adoption of a relatively severe nominal trajectory plus the use

*The factor n indicates the number of standard deviations consistent with the required level of design success probability.

of simultaneously applied tolerances on altitude, angle of attack, angle of yaw, and additionally the use of heat transfer uncertainty factors. This conservative approach to design temperatures was chosen in the absence of detailed data on dispersion distributions and parameter correlations needed for a more realistic statistical combination of tolerances. Later in the study a technique for probabilistically defining a design trajectory was examined, as described under "Combined Thermal Structural Loads Sensitivities."

The selected nominal trajectory was used as a basis for the design or limit trajectory. The nominal trajectory was tailored to minimize peak heating, but produced a long period of nearly constant heating. This trajectory was characterized by the absence of sharp heating peaks (except during the early 50° angle of attack condition, which was important to only a few designs) but resulted in a relatively high total heat load.

The trajectory, as described, was near optimum for metallic TPS concepts, for which avoidance of high peak temperatures, even those occurring over very short time periods, yields significant weight benefits. The high total heat load, on the other hand, did not cause serious insulation weight penalties.

The impact of trajectory character on carbon/carbon, REI, or hot structure concepts was not as clear as that on metallic TPS. Properties of material candidates for these concepts were assumed to deteriorate catastrophically above the specified maximum use temperatures. Thus, trajectories producing sharp heating peaks may force weight-increasing material changes or may invalidate concepts entirely if those allowable temperatures are exceeded. On the other hand, within the concepts' allowable temperature range, the heat sink and insulation capabilities, and therefore weights, were affected primarily by the total heat load.

The ablator concepts were at a disadvantage under the conditions of the selected trajectory. The long period of moderately high heating produced significant recession of most of the ablators and dictated the use of considerable thickness of material for insulation. The poor suitability of ablators for the selected trajectory would result in an even greater penalty for an allowable bond line temperature less than the 600°F baseline value.

The relative inefficiency of ablators subjected to the conditions of the present study limit trajectory is illustrated by the baseline design thickness for the Apollo material (point 7C), which approached the thickness required on the Apollo command module for lunar return.

Care should be observed in comparing ablation TPS with hot structure or carbon/carbon concepts. The lack of significant lateral conduction or available heat sink qualities of ablators makes them particularly susceptible to spatial or temporal variations in heating (such as from interference effects). This effect was observed on the X-15 vehicle, as pointed out by reference 13. This implies that a direct comparison is not always possible because of inherent differences in design.

From observations described in the preceding paragraphs it was concluded that for total vehicle optimization, the selection of the reentry profile should be considered concurrently with the selection of the various TPS and structural concepts. This consideration would, in all probability, result in different optimum trajectories for different TPS concepts. Thus, the use of a single baseline trajectory throughout this study undoubtedly resulted in some bias among the various concepts. The influence of this bias on the results of the study cannot be established without a broader study of TPS and structural concept sensitivities for a variety of trajectories.

Many of the internal temperatures which influence design definition reached maximum values late in reentry or were still increasing at landing. In the case of critical temperatures still increasing at landing, external ground cooling was assumed and the TPS was sized to meet thermal design requirements only up to time of landing. For cases of late-occurring peak temperatures, a reduction in TPS weight may be possible through the use of a simple on-board cooling scheme, such as by collecting and circulating ambient air. This possibility warrants further investigation.

Combinations of Weight Sensitivities

In order to assess the combined effects of the various design parameters on the study point designs, the weight sensitivities were combined using a root-sum-square approach. Although this technique was considered only a substitute for an appropriate statistical method, and was intended primarily as an illustration, certain tentative conclusions could be drawn from the results.

The results of the root-sum-square combinations were examined for relative weight sensitivities to the variation of the trajectory and system parameters and to the methods and criteria. No consistent trends relative to the two groups of perturbations could be seen. The metallic TPS points generally showed greater sensitivity to both groups than did the carbon/carbon or hot structure points because of the greater temperature sensitivity of the metallic TPS points.

It is not known whether the combined sensitivity results may be considered applicable to lifting reentry vehicles in general, or should be restricted to the configuration, concepts, and environments of this study. It was therefore concluded that in the absence of a broader data base, the results should not be extended beyond orbiters, design concepts, and trajectories similar to those covered by this study.

As an illustrative example for reducing conservatism in defining limit trajectories, a modified set of trajectory and systems dispersions (limit trajectory) was defined, using the individual sensitivity relation. These modified dispersions were determined such that when their extremes were applied simultaneously to define design conditions, the resulting design would satisfy a root-sum-square combination of the true dispersions. The resulting design would thus have a probability of meeting its design requirements consistent with

the probability of the individual trajectory and systems dispersions. In order to achieve a more rigorous probabilistic treatment, it is recommended to investigate the feasibility of using the Monte Carlo technique as a means of combining the effects of the various trajectory, systems, methods and criteria perturbations.

Maneuver Excursions

Three maneuvers from the nominal trajectory to conditions of the limit trajectory and back to the nominal trajectory were evaluated for effects on TPS design at two of the study points. It was found that only the most severe return maneuver, the case involving $n = 2.4$ g and a 30 second return to the nominal trajectory, had any significant impact on metallic TPS design (point number 3). For this case a temperature exceeding the columbium allowable was encountered, with the probable consequence of excessive creep deformation and reduced reliability of the panel. The baseline insulation was adequate to protect the internal structure for all maneuvers studied.

It was concluded that the metallic TPS designed for the baseline (limit trajectory) environment has capability to withstand moderate excursions from the nominal to the limit trajectory and return without jeopardizing its integrity. It was further concluded that the metallic TPS, designed for limit conditions only, has some margin for withstanding overload and over-temperature (beyond limit) conditions, provided a reduction in service life is acceptable. A definition of this margin would require a thorough examination of the possible overload conditions, TPS failure modes, and the prior load-temperature history.

None of the maneuvers had any significant impact on the REI design (point number 3A). Temperatures for all cases were within the limits for the REI material, and backwall temperatures were less for all maneuvers than for the baseline environment.

The maneuver excursion study results indicated that the REI concept, provided the assumptions regarding coating survivability and REI temperature capability are valid, affords greater maneuver capability than the metallic TPS.

Recommended Practices and Criteria

The recommended practices and criteria are intended to provide a design methodology reflecting the state of the art of reentry vehicle design. The recommendations are presented in detail in Appendix G where they are organized to form the basis for a supplement to NASA SP-8057, and are summarized here as follows:

Use available and applicable design criteria available from airplane and space vehicle design including NASA SP-8057, "Structure Design Criteria Applicable to a Space Shuttle," as updated by recommendations from the present study. Frequent updating is recommended as a broader data base becomes available.

Where the above criteria are inadequate, generate a sufficient data base to cover areas of special interest using a methodology and design philosophy consistent with the intent of NASA SP-8057.

Avoid over-conservatism, but pursue design realism by using safety and uncertainty factors in proper rational combinations to assure reliable vehicle operations. When adequate definition of dispersions exists, employ a suitable statistical technique such as the Monte Carlo method (if feasibility is established) for combining the effects of such dispersions, thereby arriving at a set of design requirements consistent with the desired probability of mission success.

Pay special attention to potential material degradation due to excess thermal-structural loading associated with thermochemical and loads phenomena.

Update prediction methods and criteria as new data become available, particularly concerning extrapolation to flight from ground test information.

Allow appropriate detail in analysis nodes concerning trajectory-time and body location in order to determine peak load and temperature conditions and to determine accurate trends in trade-off analyses.

In computing the ultimate load or stress condition, apply the ultimate factor of safety to the mechanical load or mechanical-load-induced stress only. No factor of safety is to be applied to temperatures, temperature gradients, or thermal stresses.

Compute combined stresses on a probabilistic basis, satisfying the required level of design success probability, where adequate stress dispersion data are available. When insufficient data exist to apply the above recommendation, the following rules should be used: where thermal stress acts to aggravate the load-induced stress (limit or ultimate), add the components to arrive at the total design stress. Where thermal (load) stress acts to alleviate a pre-dominant load (thermal) stress, ignore the alleviating component.

In order to provide capability margins for TPS, in the absence of those usually provided by the ultimate factor of safety, two objectives should be pursued in TPS design. First, degradation due to overload or over-temperature conditions should be detectable by practical inspection procedures before continued use endangers the vehicle. Second, the TPS should be designed to prevent the above-described incipient degradation from becoming a self-aggravating or catastrophic failure.

APPENDIX A

GEOMETRY DEFINITION

Selection of study points and definition of the vehicle geometry at the chosen study point locations were prerequisites for the present study. Since the scope of the study precluded a complete vehicle analysis, the judiciously selected study points were intended to represent the most characteristic and critical areas on the vehicle. By this approach, it was hoped to obtain meaningful trends and sensitivities permitting conclusions to be made applicable to the entire vehicle and as much as possible to the entire category of high cross-range delta wing Space Shuttle orbiter vehicles. Historically, the vehicle windward surfaces, including the stagnation point and stagnation lines, commanded the prime attention of entry vehicle designers, followed in importance by fins, control surfaces and finally by leeward surface regions.

For the present study nine study point locations were chosen to include regions requiring thermal protection systems (TPS), as well as those using a hot structure concept. A list of vehicle study points is given in table 1. The study point locations include the stagnation point, the wing stagnation line, two points each at the windward side of the body and the wing, and one point each on the upper wing, the side of the body and the fin. The exact geometric definition of the study point locations is given in figures 30 through 38. Figure 39 shows the airfoil sections used in the wing and fin analyses.

Figure 30 defines the location of point number 1, on the lower surface of the body. A location well aft of the nose was desired for this point, so that it would typify the lower surface of the body in general. On the other hand, it was desired to avoid influence of the wing on flow at this point. The chosen longitudinal location at exactly half the body length is very near the wing leading edge body side intersection. A lateral location off the vehicle centerline for point number 1 was chosen in order to provide a study point where the TPS was in close proximity to an aluminum cryogenic tank wall (see fig. 2).

Point number 2 was located, as shown in figure 31, so as to satisfy the desire for a hot primary structure study point on the body upper or side surfaces. The possible choices for such a point were rather limited. Large areas of the upper portion of the body are covered by payload compartment doors, which are not primary structure, and the crew compartment, which was expected to experience local heating effects not typical of the body upper or side surfaces in general. The nose cone, likewise, was expected to experience heating not typical of the majority of body hot structure areas. The selected location, on the body side, above and forward of the wing but below the payload door hinge line, is expected to lie in a region of separated or near-separated flow but to be reasonably free of interference or other unusual and difficult to predict heating effects.

Point number 3, whose location is defined in figure 32, was selected to typify the entire lower surface of the wing, except for leading edge areas. It was located at one half the semi-span (measured from vehicle centerline to wing tip) and at the mid-point in the chord at that wing section. In addition to the coordinates of the point shown in figure 32, computation of the flow field and boundary layer at point 3 required knowledge of the wing section geometry, which is shown in figure 39.

Point number 4 was selected to satisfy the requirement in the study plan for a study point on the upper surface of the wing, where hot primary structure could be used. The x,y coordinates of point number 4, as shown in figure 33, are the same as those for point number 3. Point 4 is representative of the upper surface of the wing in general.

Point number 5 was located so as to satisfy a study requirement for a TPS study point where sensitivity to surface discontinuities would be exhibited. Point 5 was also an appropriate addition to the study of the wing lower surface since it represented a significant portion of the wing area where heating was considerably higher than at point 3 and thus not accurately represented by point 3. The location of point number 5 is defined in figure 34.

A study point on the wing leading edge, point number 6, shown in figure 35, was selected in order to include in the study one of the most critical heating areas on the orbiter. The inclusion of point 6 presented the opportunity to examine the sensitivities of leading edge TPS design concepts, which differ from TPS design concepts at other locations.

Point number 7, on the orbiter nose cap, like point 6, was chosen because of its potential heating criticality and the opportunity it offered for studying design concepts differing from those in other areas. The exact location of point 7, shown in figure 35, was that of the aerodynamic stagnation point determined by the vehicle angle of attack and yaw at the time when peak stagnation point heating occurred.

Point number 8, whose location is defined in figure 37, was selected as representative of the hot structure area of fin or fin-rudder combination. The mid-span, mid-chord point was chosen as a typical location. Like the points on the wing, the computation of local flow and boundary layer properties at this point required definition of the section geometry, which is shown in figure 39.

Point number 9, near the aft end of the lower surface of the body, as shown in figure 38, was selected for limited studies supplementing those at point number 1. The intent was to include a study point having all characteristics, except boundary layer transition time, similar to those at point 1. The comparison of aerothermodynamic and thermal analysis study results at two such points was expected to contribute to the evaluation of transition effects on the vehicle in general. Point 9 was located as far aft as possible but still in a region of aluminum internal structure (the hydrogen tank aft skirt). The later condition, and the offset from the vehicle centerline, were imposed in order to maintain similarity of designs at points 1 and 9.

APPENDIX B

LOADS ANALYSIS

by B. E. Clingan and A. L. Brown

Ascent Loads. - Loads at selected hot structure points were obtained by scaling from available data on similar configurations. In reviewing available orbiter data (ref. 1 and 3, and Grumman-Boeing work) it was found that no complete set of loads data needed for the present study existed in any single reference. The NAR Phase B Technical Summary (ref. 3) gives load distributions for the wing and fin, which is the form of load data required for study points number 4 and 8. The MDAC report (ref. 1) gives only the wing root and fin root loads, but the slightly greater similarity between the MDAC orbiter and the present study baseline configuration led to a desire to utilize the MDAC orbiter loads. On the other hand, the maximum ascent $q \alpha$ (dynamic pressure-angle of attack product) values for the MDAC orbiter are considerably lower than the NAR design value, or values computed in current Grumman-Boeing studies. Ascent maximum $q \alpha$ values from MDAC (ref. 1) are +1672 and -1794 lb/ft²-deg, while the stated NAR design value is 2800 lb/ft²-deg, and Grumman-Boeing analyses have yielded values of approximately 3300 lb/ft²-deg.

The method used for obtaining wing and fin ascent flight loads (for points number 4 and 8, respectively) was as follows:

- (1) Use ascent maximum $q \alpha$ and $q \beta$ value of 3300 lb/ft²-deg, from Grumman-Boeing analyses. This value of $q \alpha$ and $q \beta$ is a limit value and as such includes the effects of ascent trajectory dispersions.
- (2) Scale MDAC wing and fin root loads to the $q \alpha$ and $q \beta$ value, above.
- (3) Scale NAR wing and fin load spanwise distributions to the root loads from (2). Use the appropriate distributions for positive and negative (headwind and tailwind) angle of attack conditions.

The resulting ascent loads for the wing and fin are tabulated in tables 13 and 14, respectively.

The launch acoustic environment used in design of the body side panel is shown in figure 40. The acoustic pressure spectral density was derived using data for clustered LOX/H₂ engines in the 550 000 lb thrust regime, obtained from reference 9.

Reentry and Post-Reentry Maneuver Loads. - Analysis of entry and post-entry maneuver loads was performed using a CDC 6600 computer program based on the aerodynamic influence coefficient approach. The theory underlying the development of the aerodynamic influence coefficient matrices is presented in references 16 and 17. This method is applicable in the Mach number regime from zero to approximately $M = 3.0$.

Table 13. - WING BASELINE DESIGN LIMIT LOADS AT POINT NO. 4

CONDITION	M	n _Z	LRA	SHEAR	BENDING MOMENT	TORSION
				LB x 10 ⁺³	IN-LB x 10 ⁺⁶	IN-LB x 10 ⁺⁶
ASCENT	(qα = 3300 PSF-DEG)			113.0	17.1	-1.77
REENTRY & POST-REENTRY	11.6	1.07		21.5	2.52	.86
	1.18	1.80		60.5	7.47	15.67
	.94	1.13		41.8	5.20	8.60

 SEE FIGURE 41

Table 14: - FIN BASELINE DESIGN LIMIT LOADS AT POINT NO. 8

CONDITION	M	β	θ _R	g	LRA	SHEAR	BENDING MOMENT	TORSION
		DEG	DEG	PSF		LB x 10 ⁺³	IN-LB x 10 ⁺⁶	IN-LB x 10 ⁺⁶
ASCENT	(qβ = 3300 PSF-DEG)					37.0	3.55	-1.30
REENTRY & POST-REENTRY	6.4	5.0	0	177		.87	.10	-.029
	1.18	5.0	0	318		40.5	3.99	-.199
	.94	5.0	0	255		25.5	2.45	.248

 SEE FIGURE 42

For the hypersonic regime pressure coefficients based on Newtonian theory must be input. The flight vehicle planform is divided into a finite number of panels. Mass distribution is input. The program computes airloads and inertia loads on the panels, as well as shears and moments for specified load reference axes.

Separate loads analyses were performed for the symmetric wing/body and the vertical tail.

Symmetric Wing Loads. - The symmetric wing load cases analyzed are summarized in table 15. The airloads, net loads and inertial loads were obtained on the panel grid shown in figure 41 and integrated along the load reference axis system also shown in figure 41. The wing panel weights are given in table 16. The airframe was assumed to be rigid. The camber and twist were assumed to be zero. The resulting parametric loads data are given in table 15. Loads for the actual baseline design loading conditions are given in table 13.

Vertical Tail Loads. - The analytical method used in establishing the vertical tail airload distributions was the same as that used for the wing-body as were the principal assumptions. The inertial loads were neglected, since their contribution is generally small on vertical tail surfaces. Unit sideslip load distribution (L_β) and unit rudder deflection load distribution (L_{θ_r}) were calculated for several parametric load cases. A summary of these load cases and the resulting load distributions is shown in table 17. The panel grid used in the analysis is presented in figure 42, along with the load reference axis definition used to integrate the panel loads.

The actual baseline design loading cases were constructed as follows:

$$\{L\} = \frac{q}{144 \beta_{\text{unit}}} \left\{ \{L_\beta\} \beta + \{L_{\theta_r}\} \theta_r \right\}$$

where L = panel loads matrix in lbs.

Analogous equations were used to determine the shear, moment, and torsion. The resulting loads are given in table 14.

Table 15:--WING LIMIT LOADS AT POINT NO. 4

CONDITION	M	nZ	q	α	GW	LRA	SHEAR	BENDING MOMENT	TORSION
		g	PSF	DEG	LB		LB x 10 ⁺³	IN.-LB x 10 ⁺⁶	IN.-LB x 10 ⁺⁶
REENTRY & POST-REENTRY MANEUVER	.5	2.5	288	9.84	247 550		95.2	12.0	16.7
	.85			9.50	247 550		94.3	11.8	17.9
	1.2			9.74	247 550		83.8	10.3	21.9
	1.5			11.10	247 550		84.7	10.5	20.7
	2.0			12.61	247 550		91.8	11.9	18.7
	3.0			15.64	247 550		86.7	9.6	10.2
	5.0	1	148	20.00	247 550		20.0	2.35	.80

 DUE TO THE ASSUMPTIONS IN THE ANALYSIS, THE α AND q ARE INTERCHANGEABLE, THE $q\alpha$ PRODUCT BEING THE ONLY PARAMETER DETERMINING THE LOAD LEVEL

 SEE FIGURE 41

Table 16. - EXPOSED WING PANEL WEIGHTS

COMPONENT	PANEL		TOTAL	WEIGHT DISTRIBUTION (LB)										
	NO.	AREA-FT ²		WEIGHT (LB)	GROWTH	STRUCTURE	TPS	MAIN GEAR	DOORS, INSUL ETC	AUX. PROPUL	HYDR C&D	SURFACE CONTROLS	ELEVON SUPT/MECH	
	(TOTAL)	(1100)	(18,150)	(1410)	(5100)	(4050)	(4335)	(1550)	(200)	(500)	(645)	(360)		
	18	47.47	396	31	190	175								
	19	47.47	396	31	190	175								
	20	47.47	3335	260	190	175	2000	600		110				
	21	47.47	3678	278	190	175	2335	600						
	22	47.47	515	40	300	175								
	23	47.47	970	75	300	175		50		90	175	105		
	27	39.83	332	26	159	147								
	28	39.83	332	26	159	147								
	29	39.83	332	26	159	147								
	30	39.83	332	26	159	147								
	31	39.83	421	33	241	147								
	32	39.83	648	50	241	147		50		80	80			
	36	32.98	274	21	132	121								
	37	32.98	274	21	132	121								
	38	32.98	274	21	132	121								
	39	32.98	274	21	132	121								
	40	32.98	378	29	228	121				70	140	105		
	41	32.98	774	60	228	121		50						

Table 16. - EXPOSED WING PANEL WEIGHTS (Cont)

COMPONENT	PANEL		TOTAL WEIGHT (LB)	WEIGHT DISTRIBUTION, (LB)												
	NO.	AREA-FT ²		GROWTH	STRUCTURE	TPS	MAIN GEAR	DOORS, INSUL ETC.	AUX. PROPUL.	HYDR C&D	SURFACE CONTROLS	ELEVON SUPT/MECH				
BOX (CONT)	45	26.13	218	17	105	96										
	46	26.13	218	17	105	96										
	47	26.13	218	17	105	96										
	48	26.13	218	17	105	96										
	49	26.13	256	20	140	96										
	50	26.13	576	45	140	96		50		60	110			75		
	54	19.29	160	12	77	71										
	55	19.29	160	12	77	71										
	56	19.29	160	12	77	71										
	57	19.29	160	12	77	71										
	58	19.29	181	14	96	71										
	59	19.29	344	27	96	71		50		50	50					
	63	12.44	104	8	50	46										
	64	12.44	104	8	50	46										
	65	12.44	104	8	50	46										
	66	12.44	104	8	50	46										
67	12.44	112	9	57	46											
68	12.44	388	30	57	46		50		40	90			75			
72	8.39	70	6	34	30											
73	11.19	230	18	45	42							100				
74	11.19	230	18	45	42							100				

Table 17.- FIN LIMIT LOADS AT POINT NO. 8

CONDITION	M	β DEG	θ_r DEG	q PSF	LRA	SHEAR LB x 10 ⁺³	BENDING MOMENT IN.-LB x 10 ⁺⁶	TORSION IN.-LB x 10 ⁺⁶
REENTRY & POST-REENTRY MANEUVER	.5	10	0	144		22.2	2.16	276
	↓	0	10					
	.85	10	0			25.9	2.50	.356
	↓	0	10					
	1.2	10	0			36.6	3.62	-.206
	↓	0	10					
	1.5	10	0			30.4	3.25	-.407
	↓	0	10					
	2.0	10	0			20.8	2.36	-.578
	↓	0	10					
3.0	10	0	12.2		1.36	-.398		
↓	0	10						
5.0	5	0	.7	.08	-.024			
↓	0	5						

SEE FIGURE 42

LOADS AT POINT NO. 8 NOT CALCULATED.

APPENDIX C

AEROTHERMODYNAMIC ANALYSIS

by C. L. Jaeck

INTRODUCTION

The design of TPS for hypersonic vehicles is dependent upon the aerothermodynamic environment. The inability to simulate this environment in ground facilities requires analytic methods and procedures to estimate the local flow field and boundary layer condition which introduces inherent uncertainties in the TPS design. In order to overcome the uncertainties, often conservative methods as well as safety factors are applied, with subsequent increase in TPS weight.

The major objective of this study was to determine the sensitivity of the TPS weight at nine vehicle locations to perturbations in the prediction techniques for the local inviscid flow field, turbulent heating rates, location of boundary transition and "overshoot" in heating at the end of transition.

The heat transfer coefficients for each of the nine locations (see Appendix A) were obtained using analytical predictions, semi-empirical relations, empirical results for simple geometries, and data from tests of more closely representative geometries.

The approach used in this study was to generate heat transfer coefficients at each location as a function of time and at a nominal wall temperature. The heat transfer coefficient and adiabatic wall enthalpy histories were then fed into the CHAP program (ref. 15) for determination of surface and internal temperature histories (see Appendix D).

The following discussion describes the methods and procedures for calculation of the heat transfer coefficient history at each of the nine vehicle locations. The description is in four parts:

1. Basic methods.
2. Specific methods, windward surface locations.
3. Specific methods, upper surface locations.
4. Concluding remarks.

BASIC METHODS

Flow Field Analysis Methods

The ability to predict aerodynamic heating rates and local transition parameters depends upon knowledge of the Space Shuttle vehicle flow field. Aerodynamic heat transfer calculations can be separated into two parts: the calculation of the inviscid flow properties and calculation of the viscous boundary layer. The inviscid flow calculations provide a description of the conditions at the boundary layer edge including pressure and velocity. Other fluid properties, such as temperature, density, viscosity, etc., can be obtained from the freestream properties, local surface pressure and edge velocity. A general method for calculating the inviscid flow properties does not exist. Several different methods based on knowledge of flow fields about basic shapes must be used.

The flow field surrounding a vehicle traveling at hypersonic speeds and the heating rate to its surfaces are influenced by the shape. A blunt shape reduces the boundary layer edge velocity and increases the static temperature.

The heating rate on a blunt body downstream of the nose can be predicted for two limiting cases. The maximum or upper limit is predicted by assuming an oblique shock and using the velocity and enthalpy of a corresponding sharp body. The lower limit is obtained by assuming that all the fluid in the boundary layer has entered through a normal shock. The local flow properties are then obtained by assumption of isentropic expansion from the stagnation pressure to the local pressure.

The actual heating on shuttle vehicle models usually follows the normal shock calculations in the nose region and gradually approaches the oblique shock predictions farther aft. With increasing angle of attack, the effect of the nose decreases and the oblique shock calculations become more appropriate. At very high angles of attack, however, the sharp body (oblique shock) predictions approach the normal shock predictions for all windward areas, and therefore either technique can be used.

Prediction of heating rates to vehicles at angle of attack requires the prediction of:

- (a) surface pressure,
- (b) boundary layer edge velocity,
- (c) streamline divergence due to body geometry, and
- (d) streamline divergence due to crossflow pressure gradients.

The latter two items are of particular importance at the lower surface centerline, and at points 1 and 9.

Pressure Predictions. - Three possible pressure prediction methods are

- (a) Cone and Wedge (ref. 16)
- (b) Delta Wing (ref. 17)

$$C_p = \frac{2 \sin \alpha \sin(\alpha + \epsilon)}{\cos(\alpha + \epsilon)} \quad (C1)$$

- (c) Modified Newtonian

It should be noted that the cone and wedge relationships fail above $\delta = 57^\circ$ for the cone and above $\delta = 44^\circ$ for the wedge because of shock detachment. For high Mach numbers and the angles of attack being considered, method (b) reduces to $C_p = 2 \sin^2 \delta$ since the shock wave lies close to the body.

Since the vehicle under consideration flies at $\alpha_{nom} = 50^\circ$ and 20° , the selected pressure relationships must be continuous and applicable for local deflection angles from 0 to 90° . A comparison of all three methods for a Mach number of 20, shown in figure 42, indicates that in the range of applicability the differences are small. For these reasons, the Modified Newtonian pressure prediction was used in both the sharp and normal shock calculations. In the latter case, the hemisphere pressure relationship was faired into the Newtonian distribution at the hemisphere shoulder. (See fig. 43.)

The modified Newtonian relationship (ref. 18) is given by

$$\frac{C_p}{\sin^2 \delta} = 1.05 + \left[1.1025 + \frac{4}{M_\infty^2 \sin^2 \delta} \right]^{1/2} - \frac{1.278 \sin^2 \delta}{M_\infty^6} \quad (C2)$$

Edge Velocity. - The prediction of boundary layer edge velocity is more uncertain than prediction of pressures because pressures are less sensitive to real gas effects. In computing the edge velocity a method must be selected which accounts for the real gas effects on the heat transfer coefficient. Two edge velocity methods are included in this study. In the first method, the velocity is calculated by expansion from a normal shock. The second is a sharp body (oblique shock) method. Two relationships were used to predict the local sharp body edge velocity;

the parallel shock method, where

$$\frac{u_e}{u_\infty} = \cos \delta \quad (C3)$$

and an X-20 delta wing windward surface method, where

$$\frac{u_e}{u_\infty} = 1 - \frac{\delta^2}{5600} \quad (\delta \sim \text{Degrees}) \quad (C4)$$

Application of equation (C4) to bodies, other than delta wings, has in the past led to reasonable heating predictions. This equation, however, indicates a local velocity of zero for a local flow deflection angle of 75°.

A comparison of the two sharp body methods is shown in figure 44.

Heat Transfer and Transition

Laminar Heating Method. - The Boeing Reference Density-Viscosity (Rho-mu) momentum integral method was used to make all laminar heating predictions during this study. A detailed description of this method is provided in references 18 and 19.

Effects of streamwise and crossflow pressure gradients, as well as stream-line divergence due to body geometry on heat transfer coefficient, shear and momentum thickness are considered in the Rho-mu method. In addition, the boundary layer displacement thickness (δ^*) is determined for use in the transition calculation discussed in the next section. The laminar displacement thickness was calculated using the flat plate form factors (δ^*/θ) given in references 20 and 21, modified for real gas effects as given below:

$$\frac{\delta^*}{\theta} = 6.10 \frac{i'}{i_e} - 3.51 \quad (C5)$$

where

$$\frac{i'}{i_e} = 1 + .152 \left(\frac{i_o}{i_e} - 1 \right) + .481 \left(\frac{i_w}{i_e} - 1 \right) \quad (C6)$$

This modification was checked using a finite difference, nonsimilar, real gas boundary layer method described in Appendix C of reference 22. The real gas calculations were in good agreement with results of eq. (C5).

The use of equation (C5) neglects the effect of streamwise and crossflow pressure gradients on form factors. The primary effect of these variables was included in the calculation of the momentum thickness which is also used in determining transition location.

Boundary Layer Transition Criteria. - The effects of two boundary layer transition criteria on TPS weight were investigated during this study. The two prediction methods are presented graphically in reference 25, and will be referred to as the MDAC and NASA criteria in this report. The results shown in figures 7 and 9 of reference 25 were curve fitted and the following relations obtained:

MDAC Criteria

$$\frac{R_{e,\theta}}{M_e} \frac{1}{(R_e/ft)^2} = 10 + .11e^{.077\delta} \quad (\delta \sim \text{Degrees}) \quad (C7)$$

NASA Criteria

$$\log_{10} \frac{R_{e,\delta^*}}{(R_e/ft)^{.25}} = .7 \left(1 + \frac{M_e}{2} \right), \quad M_e \leq 4.6 \quad \text{(Modified Beckwith and Stainback)} \quad (C-8)$$

$$= 1.78 \left(1 + \frac{M_e}{15.5} \right), \quad M_e > 4.6 \quad \text{(Beckwith and Stainback)} \quad (C-9)$$

The edge Mach number (M_e) appearing in equations C7 through C9 was obtained using the speed of sound for dissociated air, evaluated at the local enthalpy and pressure.

Virtual Origin of the Turbulent Boundary Layer. - The virtual origin for the turbulent boundary layer was selected at the beginning of transition. This approach is in agreement with recommendations of reference 24, but gives a maximum heat transfer coefficient at the end of transition that may be low. Recent unpublished work of Cary and Bertram of NASA-Langley indicates that the virtual origin should be approximately 18% upstream of the end of transition, which is taken as the point of peak heating.

Heating in Transition Region. - For this study, except at point 6, only the case of gradual transition was considered, that is, transition occurring over a finite region. The extent of this region is a function of geometry, Reynolds number and vehicle attitude.

Two methods were used during this study to define the extent of the transition region and the heating distribution in the transition region. The first assumes that the end of transition is located at twice the onset Reynolds number. A linear fairing for variation of heat transfer coefficient with distance on log-log graph paper was employed in the transition region between onset at the laminar condition and end of transition at the turbulent flow condition. The notation "2:1" was used to signify the use of this method on various figures and tables in this report.

The second prediction method consists of using a power law variation of heating rate with Reynolds number. Such a relationship was developed by the authors of reference 25, and is given as follows:

$$\frac{\dot{q}}{\dot{q}_{L, \text{beg}}} = \left[\frac{R_{e,x}}{R_{e,x, \text{tr}}} \right]^{5/3} \quad (C10)$$

or

$$\frac{h}{h_{L, \text{beg}}} = \left[\frac{i_{aw,L} - i_w}{i_{aw} - i_w} \right] \left[\frac{R_{e,x}}{R_{e,x, \text{tr}}} \right]^{5/3} \quad (C11)$$

If the variation in enthalpy is assumed to be small this expression reduces to:

$$\frac{h}{h_{L, \text{beg}}} = \left[\frac{R_{e,x}}{R_{e,x, \text{tr}}} \right]^{5/3} \quad (\text{C12})$$

The use of equation (C12) also determines the end of transition by the intersection of the graph of equation (C12) and the turbulent theory line with its origin located at the beginning of transition.

The notation "Re^{5/3}" was used to signify the use of the power law variation on the figures and tables of this report.

Turbulent Heating Methods. - Three prediction methods were used for this study to calculate turbulent heating rates, the Boeing Rho-mu, the Spalding-Chi, and the Eckert Reference Enthalpy (i*) method. In a sense, the calculation procedures for these three methods all use the same methodology. Each method requires

- (a) An Incompressible Skin Friction Relationship
- (b) A Reference Enthalpy
- (c) Relations to establish transformation between skin friction and Reynolds number for compressible and incompressible boundary layers.
- (d) A Reynolds Analogy Relationship

The calculation methods all assume that the skin friction coefficient as a function of Reynolds number for a compressible boundary layer is given by the same relationship when transformed to an equivalent incompressible case. The transformation is of the form

$$C_f = f(R_{e,x}) \quad \text{Incompressible} \quad (\text{C13})$$

$$F_c C_f = f(F_{rx} R_{e,x}) \quad \text{Compressible} \quad (\text{C14})$$

For the purpose of this study, equation (C13) is assumed to be the modified Schultz-Grunow equation (ref. 18).

$$C_f = \frac{.37}{\left[\log_{10} (R_{e,x} + 3000) \right]^{2.584}} \quad (\text{C15})$$

There is very little difference between C_f relationships except at very low and very high Reynolds numbers.

The compressible transformations for each of the three turbulent prediction methods are:

METHOD	F_c	F_{rx}
$\rho_r \mu_r$ (Rho - mu), (Ref. 18)	$\left(\frac{\rho_e \mu_e}{\rho_r \mu_r}\right) \left(\frac{\mu_o}{\mu_e}\right)$	$\left(\frac{\rho_r \mu_r}{\rho_e \mu_e}\right) \left(\frac{\mu_e}{\mu_o}\right)^2$
SPALDING - CHI (Ref. 26)	F_c	F_{rx}
ECKERT 1* (Ref. 27)	$\left(\frac{\rho_e \mu_e}{\rho^* \mu^*}\right) \left(\frac{\mu^*}{\mu_e}\right)$	$\left(\frac{\rho^* \mu^*}{\rho_e \mu_e}\right) \left(\frac{\mu_e}{\mu^*}\right)^2$

or, in terms of equivalent $\rho_r \mu_r$ and μ_o (See ref. 18 for definition of two parameters).

METHOD	$\rho_r \mu_r$	μ_o
$\rho_r \mu_r$ (Rho - mu)	$\rho_r \mu_r$	μ_o
SPALDING - CHI	$\frac{\rho_e \mu_e}{F_c F_{r\theta}}$	$\frac{\mu_e}{F_{r\theta}}$
ECKERT 1*	$\rho^* \mu^*$	μ^*

Where

$$F_{r\theta} = F_{rx} F_c$$

(C16)

The basic Spalding-Chi method was developed to calculate skin friction coefficients for an ideal gas. For this study the ideal gas relations were modified for a real gas by substitution of enthalpy for temperatures in the definitions of F_c and F_{rx} given in reference 26.

The heat transfer coefficients for each of the three methods were obtained from the skin friction coefficient using a Reynolds analogy factor equal to the Prandtl number raised to the .645 power. This analogy factor is only slightly different from the Colburn factor of $\sigma_r^{2/3}$. The partial Prandtl number (σ) was evaluated at the enthalpy corresponding to the Rho-mu conditions discussed earlier or at i^* for the Spalding-Chi and Eckert methods.

In order to verify the above procedures and estimate the errors introduced into the calculations by the previously discussed assumptions, comparisons were made between calculations of reference 28 and results from the Boeing aerodynamic heating computer program which includes the three turbulent prediction methods. The results of this comparison are shown in table 18.

Table 18:

TURBULENT HEATING COMPARISONS ON FLAT PLATE, $\alpha = 27^\circ$, $X = 100$ FT, $T_w = 2200^\circ$ R

FLIGHT CONDITION	PARAMETER	METHOD							
		SPALDING-CHI			ECKERT		RHO-MU		
		GAC DATA ①		BOEING	GAC	BOEING	BOEING	PROGRAM ②	
ALT = 210 KFT, V = 18 294 $\frac{FT}{SEC}$	C_f	-	-	-	1.72x10 ⁻³	-	-	2.54x10 ⁻³	1.73x10 ⁻³
	REYNOLDS ANAL FAC	-	-	-	-	-	-	-	1.185
	\dot{q} , $\frac{BTU}{FT^2-SEC}$	6.78	9.50	-	9.82	13.53	14.58	14.58	9.94
ALT = 200 KFT, V = 15 199 $\frac{FT}{SEC}$	C_f	1.53x10 ⁻³	1.87x10 ⁻³	1.78x10 ⁻³	1.72x10 ⁻³	-	-	2.41x10 ⁻³	1.68x10 ⁻³
	REYNOLDS ANAL FAC	1.099	1.087	1.087	1.178	-	-	1.178	1.179
	\dot{q} , $\frac{BTU}{FT^2-SEC}$	5.28	6.40	6.10	6.58	9.20	9.21	9.21	6.41

① SPALDING-CHI INCOMPRESSIBLE C_f VS Re ; VON KARMAN REYNOLDS ANALOGY FACTOR (REF.28)

② MODIFIED SHULTZ-GRUNOW INCOMPRESSIBLE C_f VS Re ; COLBURN REYNOLDS ANALOGY FACTOR

The effect of real-gas considerations is shown in table 17 to increase the heating rates predicted by Spalding-Chi by as much as 40 percent. The partial real-gas corrections used in the present study, that is, substitution of enthalpy for temperatures, results in a maximum error of 5 percent. The error involved with using the Modified Schultz-Grunow Skin Friction Law is approximately 2 to 4 percent. These two errors tend to counteract each other, such that the total error introduced into the Spalding-Chi calculations by the two assumptions is negligible.

Maximum of the Laminar and Turbulent Heat Transfer. - The effect of surface roughness on both heating and transition location was not evaluated in this study. Roughness effects on transition during reentry cannot be accurately predicted without information on manufacturing tolerances, thermal deformation and more detailed experimental studies of the relation between transition, roughness configuration and boundary layer characteristics.

The effect of surface roughness will tend to move the transition point forward to the nose and leading edges. A severe heating situation could occur when the transition point is moved up to or near the nose and leading edge. This situation can be simulated by the case of the maximum of the laminar and turbulent heating. The turbulent heat transfer for this case is predicted by assuming that the transition point is located at the nose or leading edge, and thus there is no overshoot in heating. Therefore, this heating prediction method does not necessarily represent a "worst case".

The heating rates were determined for four locations on the vehicle, points 1, 9, 5 and 3. The heat transfer was maximum for laminar flow only during the first 100-150 seconds of the trajectory.

SPECIFIC METHODS

The heating level depends on the local boundary layer conditions of pressure, temperature and velocity. The complex three dimensional flow field that exists over the vehicle under consideration does not allow one to make an exact prediction of these parameters. The aerodynamic heating prediction methods are themselves a function of vehicle location and attitude.

The particular trajectory selected for this study enters strongly into the method selection process. The vehicle angle of attack during reentry is held at a nominal 50° for the first 206 seconds, and then is modulated down to 20°. Thus, in some areas, different prediction methods are required for each of the two angles of attack periods.

The prediction of aerodynamic heating rates at each of the nine vehicle locations can be divided into two groups as shown in table 19. There are those amenable to analytical techniques, such as the lower surface or windward location, and those not amenable to purely analytical techniques, such as the upper surface locations.

The wing leading edge, point number 6, is included in the second group since the purely analytical prediction method applicable at that point, the isolated infinite cylinder theory, is overly conservative.

Table 19 also presents a summary of aerothermodynamic method perturbations. The details of the heat transfer calculations and the procedure will be discussed in the next two sections. Point number 7, the nose stagnation point, is not shown since no method perturbations were considered. The starred items refer to the prediction methods used for the baseline design of the TPS at each location. The baseline prediction methodology is described separately in table 20. Included in the baseline heating predictions are uncertainty factors, and altitude and attitude uncertainties.

The heating predictions performed during this study include certain common basic assumptions and simplifications summarized in table 21. Items 1 through 7 were discussed earlier, while 8 through 11 are self-explanatory.

Windward Surface Locations

Stagnation Region, Point No. 7. - The heating at the stagnation region was predicted using the Rho-mu hemisphere stagnation point theory. A sphere effective radius for the three dimensional nose was calculated using the theory of Reshotko, reference 29

$$\begin{aligned} R &= 40 \text{ inches} \\ R^x &= 72 \text{ inches} \\ R^z &= 50.6 \text{ inches} \\ R_{\text{eff}} & \end{aligned}$$

Table 19.-SUMMARY OF AEROTHERMODYNAMIC METHOD PERTURBATIONS

LOCATIONS AMENABLE TO ANALYTICAL TECHNIQUES

	OBLIQUE SHOCK (SHARP)	NORMAL SHOCK
LOCATION	LSCL; 1; 2, $\alpha_{eff} = 0$; 3; 4, $\alpha = 0$; 8, $\beta = 5^\circ$ ($\alpha = 0$); 9	LSCL; 1; 2, $\alpha_{eff} = 0$; 3; 5
PRESSURE	BOEING MODIFIED NEWTONIAN * (BMN)	BMN PLUS CYL OR HEMISPHERE DISTRIBUTION
VELOCITY	(1) * $U_e/U_\infty = 1 - \delta^2/5600$ (2) $U_e/U_\infty = \cos \delta$ (PARALLEL SHOCK)	ISENTROPIC EXPANSION FROM STAGNATION CONDITIONS
TURBULENT HEATING	RHO-MU *; SPALDING-CHI; ECKERT REFERENCE ENTHALPY	
TRANSITION LOCATION	MDAC *; NASA-LANGLEY; MAX OF LAM OR TURB HEATING POINTS 1, 2, 3, 5, 9	
HEATING IN TRANSITION REGION	GRADUAL * $\left\{ \begin{array}{l} \text{a. LINEAR FAIRING OF HT IN TR REGION } R_{e, END} / R_{e, BEG} = 2^* \\ \text{b. } h \sim R_{e,x}^{5/3} \end{array} \right.$	

LOCATIONS NOT AMENABLE TO PURELY ANALYTICAL TECHNIQUES

LOCATION	TECHNIQUE
2	(1) * $\alpha = 15-25^\circ$, $\alpha_{eff} \approx 0$; ANALYTICAL $\alpha = 45-55^\circ$, $\alpha_{eff} \approx -20^\circ$; ANALYTICAL WITH EMPIRICAL CORRECTION (2) ALL ANALYTICAL $\alpha_{eff} = 0$.
4	(1) * $h = h$ AT $\alpha = 0$ (2) $h = h$ AT $\alpha = 0$, WITH EMPIRICAL CORRECTION
6	(1) * INFINITE SWEPT CYL THEORY (2) EMPIRICALLY MODIFIED SWEPT CYL THEORY
8	(1) * $h = h$ AT $\beta = 5^\circ$, $\alpha = 0$ (2) $h = h$ AT $\beta = 5^\circ$, $\alpha = 0$, WITH EMPIRICAL CORRECTION

* BASELINE TECHNIQUE

Table 20.

BASELINE HEATING PREDICTIONS AND PROCEDURES

1. BMN PRESSURES
2. FLOW FIELD PREDICTION $\frac{U_e}{U_\infty} = 1 - \frac{\delta^2}{5600}$
 - POINT 6 USE CYL THEORY
 - POINT 7 USE MODIFIED HEMISPHERE RELATIONSHIP
3. RHO-MU TURBULENT HEAT TRANSFER THEORY
4. MDAC TRANSITION CRITERIA (AT POINT 6 USE $R_{\infty,D} = 200\,000$)
5. GRADUAL TRANSITION: $R_{e,x,END} = 2 R_{e,x,BEG}$ ASSUMES A LINEAR FAIRING FOR HEATING PREDICTION IN TRANSITION REGION
6. UNCERTAINTY FACTORS ON HEATING PREDICTIONS; 1.1 LAMINAR FLOW, 1.25 TURBULENT FLOW
7. $\Delta \alpha = \pm 5^\circ$
8. $\beta = 5^\circ$
9. ALTITUDE MARGIN 3 000 FEET BELOW NOMINAL
10. 1962 STANDARD ATMOSPHERE

Table 21:

BASIC ASSUMPTIONS COMMON TO ALL AERODYNAMIC HEATING CALCULATIONS

1. LAMINAR HEATING THEORY: $\rho H_0 - \mu$
2. REYNOLDS ANALOGY FACTOR: MODIFIED COLBURN
3. C_f VS REYNOLDS NUMBER: MODIFIED INCOMPRESSIBLE SCHULTZ-GRUNOW CORRELATION
4. VIRTUAL ORIGIN OF THE TURBULENT BOUNDARY LAYER AT BEGINNING OF TRANSITION
5. GRADUAL TRANSITION
6. BOUNDARY LAYER δ^* OBTAINED FROM FLAT PLATE VALUES FOR δ^*/θ
STREAMWISE OR CROSSFLOW PRESSURE GRADIENTS ON θ ARE INCLUDED BUT
ARE NOT INCLUDED ON δ^*/θ
7. SPALDING-CHI METHOD: F_c, F_{rx} OBTAINED FROM IDEAL GAS RELATIONS MODIFIED BY SUBSTITUTION OF
ENTHALPY FOR TEMPERATURES
8. CONTINUUM FLOW
9. AIR IN CHEMICAL EQUILIBRIUM
10. SMOOTH BODY, EFFECT OF ROUGHNESS NOT INCLUDED ON EITHER HEATING OR TRANSITION PREDICTIONS
11. ELEVON AND RUDDER SURFACES ARE UNDEFLECTED

The location of the study point was taken as the stagnation point at the low angle of attack ($\alpha_{\text{nom}} = 20^\circ$). The heating at this location, when the vehicle is at $\alpha_{\text{nom}} = 50^\circ$ was determined from the hemisphere distribution as $h_{\alpha=50^\circ}/h_{\alpha=20^\circ} = 0.86$.

The heating prediction at the stagnation point neglected the effect of vorticity interaction.

Lower Surface Centerline and Point No. 9. - In order to obtain the heating rates at points 1, 2 and 9, the simplest prediction method was to relate them to the lower surface centerline value. The heating rate along the lower surface centerline on the forward fuselage is influenced by the three dimensional flow field.

The forward fuselage is a flat bottom cylinder with rounded edges or chines, while the aft part is a delta wing. These variations in geometry and resulting local boundary layer edge properties were included in the heating calculation through the equivalent distance parameter

$$b_{\text{eq}} = \frac{\int_0^x \rho_r \mu_r u_e (rf \bar{E})^N dx}{\rho_r \mu_r u_e (rf \bar{E})^N \Big|_x} \quad (\text{C17})$$

$N = 2$ for Laminar Flow and $\bar{E} = \bar{E}_L$

$N = 1.25$ for Turbulent Flow and $\bar{E} = \bar{E}_T$

The parameters r and f in equation (C17) account for the three dimensional flow effects, with r accounting for the effect of streamline divergence due to body geometry on heating and f accounting for the effects of streamline divergence due to crossflow or transverse pressure gradients. In the derivation of the momentum equation, r is assumed to be proportional to the body radius of curvature, normal to the streamline. The parameter f is defined in reference 18 by

$$\frac{1}{f} \frac{df}{dx} = \frac{1}{u_e} \frac{\partial v_e}{\partial y} \quad (\text{C18})$$

For a circular cylinder or a hemisphere, assuming a Newtonian pressure distribution, the crossflow velocity gradient becomes

$$\frac{\partial v_e}{\partial y} = \frac{1}{R} \left[\frac{2p}{\rho_e} \left(1 - \frac{p_\infty}{p} \right) \right]^{1/2} \quad (\text{C19})$$

Use of equation (C18) and (C19) to predict the three dimensional parameter f on the forward fuselage requires a correction factor (K) to the velocity gradient to account for the flat bottom and the chine radius R_c . The factor K was obtained from reference 30 based on data from references 31 and 32. Thus, equation (C18) becomes

$$\ln f = \int_0^x \frac{K}{R_B u_e} \left[\frac{2p}{\rho_e} \left(1 - \frac{p_x}{p} \right) \right]^{1/2} dx \quad (C20)$$

The parameter r and the local cylinder radius (R) were taken to be equal to the half body width (R_B).

The three-dimensional parameters r and f on the delta wing centerline were calculated using the method discussed in Section V of reference 18 (Volume I). This method uses sharp leading edge delta wing streamlines to predict the two three dimensional parameters r and f based on the local ratio of specific heats (γ). The flow over the wing over the lower angle of attack portion of the trajectory and during peak heating was calculated to be nearly two dimensional. The origin for delta wing streamlines was assumed to be on the vehicle centerline at the point where the wing intersects the fuselage.

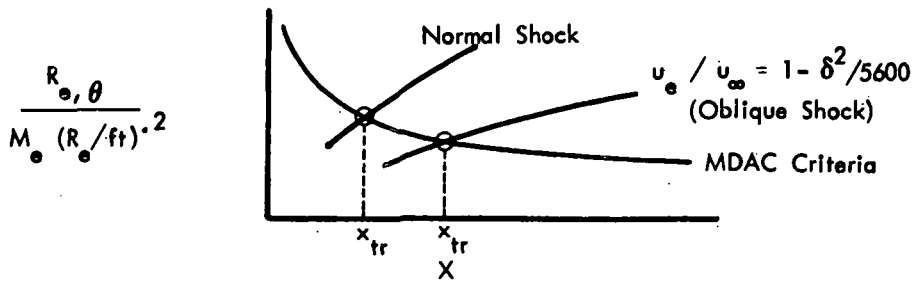
A heat transfer coefficient distribution for the two transition criteria along the lower surface centerline is shown in figure 45. The axial body location of points 1, 2 and 9 are indicated. The heating in the transition region was obtained again by fairing (linear fairing on log paper) between the laminar heat transfer at onset and the turbulent value at end of transition, established where the Reynolds number was twice the onset value.

Point number 9 was selected for the study since it was expected to lie in a region of fully turbulent flow and thus would allow the clearest determination of the sensitivity of TPS to turbulent heating predictions. Heat transfer coefficient histories for the three prediction methods are shown in figure 46. In the time zone of peak heating, near 1300 seconds, the Rho-mu and Spalding-Chi methods give similar results.

The heating rate at point number 9 was assumed equal to the centerline value at the same axial location.

Large differences were observed in the location of boundary layer transition along the lower surface centerline. Presented in figures 47 through 49 are examples of the differences due to flow field prediction methods, transition criteria, and angle of attack variations, respectively.

The normal shock calculations resulted in a substantially earlier onset of transition as a result of the lower unit Reynolds number, larger momentum thickness, and lower edge Mach number. This result is illustrated as follows:



The NASA criteria resulted in the earliest transition during the low angle of attack part of the trajectory ($\alpha = 25^\circ$), while the MDAC criteria give the most forward transition during the high angle of attack portion of the reentry. This difference can be better illustrated by comparing transition locations predicted by the two criteria at one altitude and velocity, as shown in figure 49. The MDAC criteria indicates that the most forward transition location occurs at an angle of attack of approximately 42 degrees. The NASA criteria bottoms out at the significantly lower angle of attack of 13° (shown later with point 3). This variation of location of transition with angle of attack for the NASA criteria is consistent with observations in wind tunnels at hypersonic freestream Mach numbers.

Mid-Body Lower Surface Chine Line, Point No. 1. - The laminar theoretical heating rates at points 1 and 2 were calculated by equating the flow to that on an unyawed blunt slab. The freestream Mach number was taken to be the actual freestream component normal to the vehicle lower surface. The slab was assumed to be at zero angle of attack.

The leading edge of the slab was assumed to have a cross section equal to that of the orbiter vehicle body at the axial location of points 1 and 2. Furthermore, this cross section is similar to that of a flat faced cylinder with a corner radius (R_C) equal to one-half the body radius. The prediction of the heating distribution was then based on the pressure distribution around the flat faced cylinder described in reference 32 and presented in figure 50. The local velocity was obtained by an isentropic expansion from the stagnation line (vehicle centerline).

A laminar heat transfer coefficient distribution for station 1165 is shown in figure 51. The distribution was normalized to the stagnation line value, since the level calculated does not correspond to the centerline values calculated in the previous section.

In order to verify the above method the flight condition calculations were compared with wind tunnel data from the GD delta wing booster of reference 33 which has a fuselage cross section similar to that of the GAC orbiter. This comparison is shown in figure 52 for point 1 and is presented as a function of centerline boundary layer edge enthalpy to account for the difference between flight and wind tunnel real gas effects. The calculations underpredicted the

measured data in the lower enthalpy region due to errors introduced in using the hypersonic pressure distribution ($M_{N,\infty} = 10.5$) in the lower Mach number portion of the reentry trajectory. However, since the error was significant only after peak heating and temperature have occurred, it was neglected for the purpose of the present study.

The actual fuselage spanwise heating distribution with transition at the centerline appears as shown in figure 53. The spanwise transition location, that is, the point where the flow is laminar, was determined by construction of a curve such as shown in figure 54. The transition location was then determined by calculation of η (defined in figure 54) where the numerator is determined from equation (C7), while the denominator became the laminar centerline value of the MDAC transition parameter. This value of η was used in conjunction with figure 54, to locate the spanwise point where the flow becomes laminar. As the orbiter proceeds along the reentry trajectory, the shape of figure 54 changes to that shown in figure 55. At the time shown the spanwise heating distribution is all turbulent. The spanwise variation of transition location with time is shown in figure 56, where distance is measured from the centerline.

When the boundary layer at the centerline and on the complete spanwise distribution was all turbulent, a second method was used to generate the fully turbulent heating distribution. For this case, the local spanwise velocity was calculated using

$$u_{\text{spanwise}} = \left(u_{e,CL}^2 + v_{e, \text{isen. expans.}}^2 \right)^{1/2} \quad (C21)$$

This approach was necessary in order to obtain a reasonable distribution near the stagnation line, and give a definite value to normalize the curve. If one used the same approach for turbulent flow as was used for laminar flow, where

$$u_{\text{span}} \sim y \quad (C22)$$

$$\text{then, } h_{\text{turb}} \sim \frac{u^{\cdot 8}}{y^{\cdot 2}} \sim y^{\cdot 6} \quad (C23)$$

which is a physically impossible result.

However, using equation (C21), (C23) becomes

$$h_{\text{turb}} \sim \frac{u^{\cdot 8}}{y^{\cdot 2}} \approx \frac{u_{e,CL}^{\cdot 8}}{y^{\cdot 2}} \quad (C24)$$

A sample of such a fully turbulent heat transfer distribution is shown in figure 57.

Wing Leading Edge Stagnation Line, Point No. 6. - The basic heat transfer prediction method for a wing leading edge is isolated infinite swept cylinder theory. However, the wing lower surface affects the leading edge heating at angles of attack above 15°, and infinite cylinder theory becomes conservative as is shown in figures 58 and 59. The data shown are from slab delta wings, that is, the lower surface deflection angle is equal to the vehicle angle of attack.

The faired curves of figures 58 and 59 suggest a second heating prediction method for leading edges, that is, an empirically modified cylinder theory. In order to apply the curves to wings with airfoil cross sections, the abscissa is assumed to be the local deflection angle at the leading edge shoulder in the direction of flow. For the orbiter vehicle under consideration, the local flow deflection angle at the shoulder is 61° at 25° angle of attack (see fig. 39). Thus, the modified laminar heating rate prediction on the orbiter leading edge, based on the faired curve of figure 58, is one half that predicted by the basic cylinder theory.

For this study the Rho-mu cylinder theory was used at point 6. In addition, the location of point 6 is defined by the cylinder stagnation line prediction during the lower angle of attack portion of the reentry trajectory. The stagnation line location for the modified cylinder theory was assumed to be at the leading edge shoulder for the lower angles of attack and at the 10-percent chord point for the higher angles of attack. The 10-percent chord location was based on the results of reference 36, where the location of maximum heating at mid-semi-span on the wing lower surface of a delta wing orbiter at 53° angle of attack was shown to be near the 10-percent chord point.

Boundary layer transition on the leading edge was calculated independent of the wing lower surface and was assumed to occur at a freestream Reynolds number of 200 000 based on leading edge diameter. This criterion predicted transition to occur approximately 150 seconds earlier than the calculations at points 5 and 3 based on the MDAC criteria. However, this early onset of transition occurred after the time of peak heating, and thus had no effect on peak TPS temperature. For transition to occur approximately 150 seconds later, a transition Reynolds number of 800 000 would have been a better criterion.

Heat transfer calculations were also made using modified cylinder theory, both with and without an estimate for the effect of the body shock impinging on the leading edge. The heating increment due to shock impingement was based on correlations which indicated

$$\frac{h_{\text{impingement}}}{h_{\text{undisturbed}}} = 2.0$$

Thus, when this factor was applied to the laminar modified cylinder theory the resulting heating predictions were equal to those given by cylinder theory.

Wing Lower Surface Leading Edge Beam, Point No. 5. - The heating rate prediction at point number 5 was a function of the location of the leading edge stagnation line as affected by the angle of attack. In the angle of attack range from 50° to 60° the leading edge stagnation line was assumed to be located at the 10 percent chord line which is the location of point 5, and the heating rate was then predicted using modified cylinder theory.

In the range of $\alpha = 20^\circ$ to 30° , the stagnation line was assumed to be located at the leading edge shoulder. The wing lower surface heating distribution was then calculated using one of the flow field methods, using the stagnation line as the origin of the boundary layer. Streamwise pressure gradient effects on heating in the direction of flow were included, but the flow was assumed two-dimensional (Strip Theory). An example of the heat transfer distribution along the wing lower surface at mid-semi-span at a single altitude and velocity is shown in figure 60. The locations of point 3 and 5 are noted.

The calculation procedure was then repeated at selected time points along the trajectory as shown in figure 61. A comparison of the heat transfer coefficient history for each of two flow field prediction methods is shown in figure 61. The normal shock calculation indicates a higher heating rate during the time span of 900 to 1500 seconds due to earlier onset of transition, than that of the baseline method. The peak temperature for the normal shock calculation occurs at 1350 seconds and is the more severe of the two calculations shown. The higher temperature and heating rate are the result of a higher adiabatic wall enthalpy but a lower heat transfer coefficient than that of the baseline method.

Wing Lower Surface, Mid-Semi-Span, Mid-Chord, Point No. 3. - The heat transfer coefficient at point 3 was calculated as discussed in the previous section. The heat transfer coefficients at point 3 for each of three turbulent heating prediction methods are presented in figure 62. The Rho-mu and Spalding-Chi methods gave nearly the same results. The early sharp peak at 206 seconds is the result of the sudden decrease in the vehicle angle of attack by 30 degrees (fig. 7), and the ensuing dropoff in temperature.

Boundary layer transition began at about 620 seconds as is shown by the increase in heating and divergence from the laminar curve. The variation of the transition location on the lower surface with time is shown in figure 63 for the two transition criteria. The NASA criteria gave the earliest onset of transition during the low angle of attack part of the reentry, while the MDAC criteria indicated the most forward location in the initial high α part of the trajectory. This difference is presented further in figure 64, which shows the variation in transition location with angle of attack at a given altitude, velocity and flow field prediction method. The results are similar to those presented for the LSCL in figure 49. The MDAC criteria indicated the most forward transition location occurred at an angle of attack of approximately 42° , while the NASA criteria bottomed out at an angle of attack of 13° .

Upper Surface Locations

The calculation of upper surface heat transfer of a Space Shuttle orbiter configuration must at present be made using approximate empirical or semi-empirical techniques. The upper surface may have large regions of separated flow, with vortices formed as the flow expands around the nose, leading edges and chines. At present, one cannot predict the vortex formation or the heating increase caused by the vortices.

The upper surfaces are usually inclined at a relatively large negative incidence to the freestream vector such that the usual pressure prediction methods do not apply. For incidence angles less than -15° the pressures tend to reach a constant level which is a strong function of Mach number as shown in figure 65. The pressures can be predicted by the approximation

$$C_p = .01 - \frac{1}{M_\infty^2} \quad (C25)$$

The heat transfer rates to the upper surface locations, where the flow is separated, but away from the vortex regions, decrease as the local surface deflection angle is increased to large negative values. This is shown in figures 66 and 67 for locations on the wing upper surface and fin side of a delta wing booster (ref. 33) whose geometry is similar to that of the orbiter vehicle being used for this study. The heating tends to reach a constant value for angles less than -15° . The constant level, when normalized to the value at zero angle of attack, correlates reasonably well as a function of Mach number as shown in figure 68.

The heat transfer levels shown in figure 68 would be in considerable error if applied in vortex regions. Thus, the approach used for this study was to predict the heating to the three upper surface locations by the following two methods:

1. The value at zero incidence (baseline method) and
2. The separated value given by the method of figure 68.

Dissociation of the air during flight will change effective ratio of specific heats in a manner that the fluid could expand through a larger angle over surfaces at negative incidence. This larger potential expansion angle will result in an increase in the heating over that presented in figure 68.

Forward Fuselage Side Panel, Point No. 2. - Point number 2 is located on the side of the upper mid-body. As the vehicle angle of attack is increased, the effective angle of attack of the side panel decreases as shown in figure 69. For the purpose of this study, it was assumed that the flow during reentry was separated, and that point 2 was in a vortex region. Thus, the heating was predicted using the zero incidence approach to account for the increased heating due to vortices. It was for this reason that the flat faced cylinder pressure distribution was used as the pressure distribution on the fuselage normal to the centerline for points 1 and 2.

The predicted heat transfer rates for point 2 were obtained using the same procedure and techniques as were used to obtain the results for point number 1. The predicted values at point 2 were normalized to the centerline values and compared with wind tunnel data from a delta wing booster (ref. 33) and a semi-cylinder leading edge model as shown in figures 70 and 71. Both models had flat sides ($\alpha_{eff} = 0$). The trends indicated by the data are in agreement with the flight predictions and thus confirm the prediction technique used in this study.

Wing Upper Surface, Point No. 4. - Point number 4 is located on the wing upper surface at mid-span and mid-chord. The heating rate at point 4 was calculated using the semi-analytical (zero incidence) and empirical techniques. Boundary layer transition was included in the zero incidence calculations.

Fin Side, Point No. 8. - The heating on the fin was calculated with the vehicle at zero angle of attack, but included the effect of yaw angle. The flow field ahead of the fin was assumed to be the freestream condition. Boundary layer transition was included in the zero incidence calculations.

CONCLUDING REMARKS

AEROTHERMODYNAMIC METHODS

The aerodynamic heat transfer rate prediction methods used in this study made use of data and techniques which were available when the study began. Thus, many of the techniques presented and used must be looked upon as approximate or preliminary design level techniques. In the actual design study the prediction methods would be modified based on data from wind or shock tunnel tests of models of the actual configuration. However, as a result of this study, conclusions can be drawn and recommendation of methods made.

Heating in Stagnation Regions. - The heating at the nose stagnation point should be calculated using the theory of Fay and Riddell (ref. 41) or the theory of Reshotko (ref. 29) for three dimensional nose shapes. At the stagnation line of delta wings, the maximum heating should be predicted with an empirically modified cylinder theory in order to remove some of the conservatism associated with the purely theoretical isolated swept cylinder prediction method. The predictions should be verified experimentally when applied to airfoil shapes with curved lower surfaces.

Flow Field Predictions on Windward Surfaces. - The effect of flow field prediction method (except normal shock) on aerodynamic heating rates was small. The baseline method or the parallel shock (eq. C3 and C4) prediction for boundary layer edge velocity are therefore recommended. At the angles of attack considered for the present orbiter configurations during reentry, these two flow field methods are more representative of the true case. The pressure should be calculated using the modified Newtonian or an equivalent method.

Boundary Layer Transition. - Boundary layer transition had a strong influence on the time and level of peak heating rate and temperature. The criteria were found to have a small effect on peak temperature and TPS weight at studied locations away from the nose or leading edge or on the aft portion of the vehicle. Point number 5 on the leading edge beam was found to be substantially affected by the criteria selection.

The two transition criteria revealed substantially different trends of transition location with angle of attack. The NASA criteria indicated the most forward transition locations in the angle of attack range of 0 to 35°, while the MDAC criteria indicated the most forward locations between 35 to 60° angle of attack.

This pattern, plus the fact that present data support to approximately equal degrees the validity of the two criteria, makes the recommendation of a single criterion difficult. Therefore, until more verification data become available, it is recommended that location of the beginning of transition be defined as the most forward position predicted by either of the two criteria.

The seeming lack of sensitivity of the TPS temperatures and weight to transition criteria observed during this study is due in part to the assumption of the location of the virtual origin for turbulent flow at the beginning of transition. This assumption yielded an overshoot in heating at the end of transition of approximately 5 percent. Investigations (unpublished) presently being conducted at the NASA Langley Research Center by Cary and Bertram have indicated that the virtual origin should be located at approximately 1.8 the Reynolds number at the beginning of transition. Use of this virtual origin would give an overshoot in heating above the fully turbulent value at the end of transition of approximately 40 percent. This larger overshoot would significantly increase the temperatures and TPS weights predicted during this study. Thus, the findings of this study are highly dependent upon the assumptions used or the state of the art of the methodology at the time of the start of the study.

The effect of surface roughness on both heating and transition location was not evaluated in this study. Roughness effects on transition during reentry cannot be accurately predicted without information on manufacturing tolerances, thermal deformation and more detailed experimental studies of the relation of transition, roughness configuration and boundary layer characteristics.

The effect of surface roughness will tend to move the transition point forward to the nose and leading edges. This situation was simulated by the case of the maximum of laminar and turbulent heating. Of the four points studied, only point number 5, located on the wing leading edge beam was significantly affected by this assumed condition.

Variation of Heating in the Transition Region. - The variation of heating in the transition region had little or no effect on the results of this study. Either of the two methods is therefore acceptable for definition of transition zone heating.

Turbulent Heating Method. - This study has shown that either the Spalding-Chi (Real Gas) or the Rho-mu turbulent heat transfer prediction methods yield nearly the same results for the trajectory and vehicle investigated. Therefore, either of the two methods would be acceptable to predict Space Shuttle orbiter environment.

Uncertainty Factors on Heating. - The recommended uncertainty factors (ref. 12) on heating in regions of attached flow are 1.1 and 1.25 for laminar and turbulent flow, respectively. The laminar factor was based on examination of data at the stagnation point of a hemisphere. The turbulent value was based on a limited amount of data from flat plates and unyawed cones. Thus, these factors should be verified and if necessary reestablished using data from Space Shuttle configurations and for different vehicle locations. In regions of flow field interference and separated flow a factor of 1.5 on heating should be used to account for the increased uncertainty in the prediction methods (primarily empirical) and complex flow field effects such as vortices. The factor of 1.5 should be applied exclusively of the attached flow factors, that is the 1.5 factor should not be used in conjunction with the 1.1 or 1.25 factor.

In the case of flow field interference where sufficient data exist to define the trend of the heating increase with the primary variables, angle of attack, Mach number and Reynolds number, and boundary layer condition, the 1.50 factor should be decreased to 1.25.

Since in separated flow regions the heating may be increased significantly by vortices whose formation cannot be predicted, the uncertainty factor of 1.5 should not be reduced even if data are in existence.

APPENDIX D

THERMAL ANALYSIS by E. W. Brogren

Approach and Methods

Introduction. - The thermal analysis played an important part in defining the baseline and perturbed designs used to develop weight sensitivities at the nine vehicle study points. The effects of many of the method and criteria perturbations on the TPS and structural designs were manifested primarily through the thermal response.

The thermal analysis applied the aerothermodynamic environment data as described in Appendix C to particular designs as represented by the concepts shown in figure 6. The resulting temperatures on the surface and at various points through the TPS or structure were used for selection of materials and gages for heat shield and load-carrying components, for assessment of reliability and reusability, and for determination of thicknesses for insulation blankets and ablaters. In some cases, where the indicated material or thickness was significantly different from the one originally assumed for the analysis, iteration or parametric computation was required.

Computational Techniques. - Most of the thermal analysis was carried out using a Boeing one-dimensional digital program known as the Convective Heating and Ablation Program (CHAP), (ref. 15). This program offers great flexibility with regard to input data, structural modeling, boundary conditions, and output format, and was very well suited for this effort. This program can account for temperature-dependent material properties and can handle radiation and convection across internal spaces, as well as thermal diffusion through a number of different solid layers. Ablation computations employed finite-rate decomposition mathematical models for virgin material pyrolysis and char combustion and sublimation.

All CHAP computations for this study were carried out to $t = 3600$ seconds, the assumed orbiter landing time. In a few instances, internal structural temperatures were still increasing at $t = 3600$ seconds, indicating the need for active cooling or venting in the late phases of flight or on the ground. Thermal protection weights expressed in the results of this study relate only to protection required for $t \leq 3600$ seconds.

Many of the study point-imposed condition combinations for metallic TPS points were analyzed by means of two CHAP computational runs. In one of each of these run pairs the input geometry represented a section through the TPS corrugation ridge (see fig. 13) while the other run represented a section through the corrugation valley. These pairs of runs were initially thought necessary to supply all the temperature gradients needed for stress analysis of the metallic TPS. It was found, however, after examining representative results that, although absolute temperatures varied with the perturbation of imposed

conditions, the gradients were not significantly sensitive. The choice of corrugation ridge or valley resulted in differences of less than 10°F in the maximum surface temperature, which was the primary metallic TPS thermal design parameter. Lateral conduction, which was not included in the one-dimensional analysis, would reduce these differences even further. Later cases, therefore, were analyzed with only one run.

All ablation design cases were analyzed by means of at least three CHAP runs each, with initial ablator thickness varied for the three runs. The results from this approach permitted an accurate interpolation of the initial thickness required to satisfy the required maximum allowable bond line or structural temperature.

Thicknesses of reusable external insulation (REI) and internal insulation for metallic TPS and carbon/carbon designs were sized by means of a simplified technique rather than the three-run and interpolation method used for ablators. A fixed thickness of insulation was input for all cases at a particular point. That thickness was selected to be just greater than that required to satisfy the internal (backwall) structural temperature limit for the worst perturbation case, as established by a preliminary run. Then, for all the actual design analyses the insulation thicknesses were determined by locating the point within the oversized insulation layer where the maximum temperature was the desired insulation-structure interface (backwall) value. This approach is slightly unconservative because of the heat sink effect of the excess insulation. Some of the results were checked, however, against a more exact technique and found to be in error by less than 2% of the insulation thickness.

In spite of the convenience and flexibility of the CHAP program, it was intended at the outset of the study to save effort by substituting simple hand calculations for computer analyses for a large number of cases. Techniques planned included the solution for temperatures by a radiation equilibrium approach, scaling of temperatures on the basis of the fourth root of heating rates, and the sizing of insulation in proportion to total heat loads. It was found early in the study, however, that such techniques often produced inaccuracies that masked the subtle differences between the perturbation methods and criteria, voiding the very results being sought. Consequently, a policy of strict consistency and extensive use of the CHAP program was adopted throughout the thermal analysis to insure validity of the weight sensitivity results.

One of the short-cut approaches remaining was that used to develop weight sensitivities to perturbations of the reentry model atmospheres. It was found that for the significant portion of the reentry trajectory each atmosphere perturbation could be approximated, through the density parameter, by some intermediate trajectory altitude perturbation. Thus, for each study point the effects of the hot or cold atmosphere on TPS or structural temperatures and on local pressures were taken to be those of particular altitude perturbations. TPS or structural weights for these atmosphere perturbations were then read directly from the appropriate points on the altitude sensitivity curves.

Another simplified technique was used to develop the curves of TPS or structural weight sensitivity to total orbiter reentry weight. The use of the lift coefficient versus angle of attack curve (fig. 72), along with the assumption of reentry equilibrium glide, permitted relating orbiter reentry weight variation to angle of attack variation. Through this relation the variation in TPS or structural weight per unit area with orbiter total weight could be derived from the angle of attack sensitivity curves.

Limitations. - Computer-generated thermal analysis results were subject to limitations and inaccuracies from three principal sources; the input data, the mathematical model, and the numerical techniques. Input information consisted primarily of two sets of data; aerothermodynamic environment data (heat transfer coefficients, recovery enthalpies, and external pressures) and material properties (thermal conductivity, specific heat, density, emittance, ablation parameters, etc.).

Because of the effort required in computing a set of aerothermodynamic environment data for each particular case, it was necessary to limit to a reasonable number the time points at which such data were input, (see table 7). Between each of the times at which data were input the CHAP program employed linear interpolation, subjecting the receiving surface to a new heating rate each 0.10 second. The resulting trapezoidal-segment heating histories were approximations of the actual histories, and occasionally it was found necessary to add input data at intermediate times to insure the inclusion of peak points, sudden changes, key points in transition, etc. It is felt that all such points were found and that the resulting heating rate histories accurately represented the actual variations.

No serious difficulties were encountered with regard to material property data. The ranges of thermal data were adequate to cover all cases analyzed. Temperature-dependent properties were input either as polynomial curve-fits to data or as tables of the property versus temperature from which values were linearly interpolated. Surface absorptance and emittance values for some materials were subject to some uncertainty because of the large possible variations in these properties with surface condition. Since material properties were not perturbed in the course of the studies (with the exception of the ablators, which will be discussed later), the slight inaccuracies in material properties cited were felt to have negligible effect on weight sensitivities.

The one-dimensional character of the CHAP program introduced the greatest potential limitation with regard to thermal analytical modeling of the TPS or structure. Lateral conduction in the skin or underlying members; parallel heat paths, such as introduced by TPS standoffs and complex three-dimensional thermal diffusion as near joints, major members, or panel edges could not be detailed in the analysis. Such deficiencies were not felt to significantly affect the results of this study, because a large percentage of the orbiter's surface area is sufficiently remote from major structural members, panel edges, and supports to make the one-dimensional assumption generally acceptable. Heating rate distributions are such that lateral conduction due to impressed variations will be practically non-existent. Even if the model limitations do impact on absolute levels of computed temperature and insulation thickness, the

differences and thus the weight sensitivities should show no significant error resulting from the one-dimensional treatment.

The use of a high-speed machine program permits the use of computer intervals and geometric networks fine enough so that, for all practical purposes, the numerical results duplicate an exact continuous solution. Practical considerations, however, limited the volume of data output that could be printed or examined within the scope of the study. Temperatures were examined at 50 second intervals through critical parts of the reentry trajectory and at 100 second intervals elsewhere. As a result, precise peaks may have been missed. An investigation of this source of error showed resulting surface temperature inaccuracies of no more than $\pm 10^\circ\text{F}$. Some slight differences in temperatures that were the reverse of the relative values expected were seen and are attributed to this effect. It is suggested, therefore, that temperature differences less than 20°F shown in the results of this study not be considered significant.

Results and Application

Metallic TPS Points. - The thermal analysis of the metallic TPS designs supplied three parameters required to size the TPS. These were the maximum surface temperature, a characteristic temperature difference across the TPS, and the location within the insulation layer, as described in page 70, where the maximum temperature equalled the desired value. The maximum surface temperature was used along with the net panel pressure, to determine the weight of the metal components through the use of the parametric curves of figure 14. The characteristic maximum temperature difference between the outer skin and the corrugation valley (see fig. 13), also influenced the weight of the metal components. It was found early in the study, however, that this temperature difference was relatively insensitive to the point location or the various method and criteria perturbations and that variations in its value need not be considered. The selected temperature differences shown in figure 14 can thus be considered applicable for the entire analysis. In addition to the sizing of the insulation as described earlier, the maximum temperatures within the insulation were checked against the maximum allowable for the particular insulation material and were used for selection of material for encapsulating the insulation. For temperatures up to 2200°F the encapsulating material used was Inconel 702 foil, at 0.137 pounds per square foot of vehicle surface area. Above 2200°F the encapsulating material was zirconia cloth at 0.175 pounds per square foot of vehicle surface area. The above weight figures include allowances for edge encapsulation and supports. An actual application of thermal analysis results as described here may be examined in Appendix F.

Point Number 3 Thermal Analysis Results: Point number 3 was the subject of the greatest number of design perturbations in the course of the study and thus was selected for the most extensive presentation of metallic TPS thermal analysis data in this appendix. Figure 73 illustrates some of the thermal analysis data results for point number 3. Shown for the baseline case are the surface temperatures and temperatures at three other locations within the TPS. The early temperature peak, at approximately 200 seconds, appears on many of

the temperature histories and is due to the high (55°) initial angle of attack. The dropoff in temperature is due to the change to 25° at t = 206 seconds.

Figure 74 shows surface temperatures for point number 3 for the altitude and angle of attack perturbations. Changes in the curves with the perturbations occur not only through changes in the general heating levels but also through changes in the time of transition from laminar to turbulent flow as brought about by changes in local Mach and Reynolds numbers. The almost flat portions of some of the curves, in the neighborhood of t = 500 seconds are characteristic of the constant laminar heating for which the corresponding nominal trajectory was originally tailored.

Figure 75 compares point number 3 surface temperature histories for the baseline case, for flight along the nominal trajectory, and for the three maneuver excursions. The maneuver trajectories themselves are described in figure 9 and table 4. It was pointed out in the section on Trajectory Selection Criteria and Tolerance Application that the Case II maneuver resulted in dissipation of kinetic energy to the extent that, upon return to the nominal altitude-time line, a significant velocity deficiency (relative to the nominal velocity versus time) existed. The lower than nominal velocity after maneuver completion led to a higher than nominal angle of attack to maintain the nominal altitude-time line. It is seen in figure 75 that the thermal effect of velocity apparently dominated over the effect of angle of attack and resulted in lower temperatures subsequent to the Case II maneuver. Figure 76 is an expanded-scale plot of the baseline, nominal, and maneuver temperatures for point number 3.

The two more severe maneuvers, Case II and Case III, resulted in peak surface temperatures that exceeded the maximum baseline surface temperature. (See table 22.) The subsequent dips in temperature, caused by the low angles of attack that followed the initial pitch-ups, and the final stabilization on or near the nominal trajectory profile, resulted in total heat loads and internal temperatures that were less than the baseline values.

The thermal effects of the maneuver excursions on the point number 3 TPS design were interpreted using two different approaches. First, the baseline TPS design was held fixed and the effects of the maneuvers on that design examined. The results of this examination are summarized in table 22. In the second approach the point number 3 TPS design was resized, where possible, to satisfy the conditions of each maneuver. Any significant pressure effects, as well as thermal conditions, were reflected in this resizing. The resizing results are summarized in figures 23 and 24.

Figure 77 shows the point number 3 surface temperatures for the baseline and two alternate turbulent heat transfer prediction methods. In the comparison between the Rho-mu and the Spalding-Chi temperatures, the former yields the higher peak temperatures while the latter appears to produce the higher total heat load. This observation is supported by a comparison between the insulation requirements for the two cases, where the thicknesses of 6 lb/ft³ Dynaflex to limit structural temperatures to 600°F were 3.62 in. for the Rho-mu case and 3.63 for the Spalding-Chi case. The effect of maximum surface temperature on

Table 22. MANEUVER EFFECTS

POINTS 3 AND 3A – BASELINE DESIGNS (SIZED FOR LIMIT TRAJECTORY CONDITIONS)

POINT	MANEUVER	MAX SURF T	MAX INS T	MAX STRUCT T	P _{EXT} (PSI)
3	BASELINE ①	2 296	2 282	600	0.40
	I	2,172	2 153	529	0.215
	II	2,580 ②	2 463	519	③ 0.591
	III	2 320 ②	2 265	533	0.266
3A	BASELINE ①	2 290	—	600	0.40
	I	2,177	—	455	0.215
	II	2 515	—	442	③ 0.591
	III	2 298	—	457	0.266

- ① BASELINE CONDITIONS ARE SHOWN FOR REFERENCE ONLY. BASELINE MAX T AND P_{EXT} DO NOT OCCUR AT THE SAME TIME AS THOSE FOR THE MANEUVERS
- ② SURF TEMP FOR WHICH DESIGN IS SIZED IS EXCEEDED. RESULT WOULD BE ACCELERATED CREEP DEFORMATION AND COATING DEGRADATION
- ③ REFERENCE TO FIGURES 23 AND 24, FOR POINTS 3 AND 3A, RESPECTIVELY, SHOWS NO EFFECT FROM INCREASED PRESSURE

sizing the metal components prevailed over the insulation differences, yielding a higher total TPS weight, as seen in figure 23, for the point number 3 Rho- μ (baseline) case.

Figure 78 shows point number 3 surface temperatures for the two extreme sets of factors applied to account for the effects of uncertainties in predicted heat transfer coefficients. The pairs of values shown for the factor, F, were applied to the laminar and turbulent heat transfer coefficients, respectively. Transition was predicted in accordance with the baseline approach and the values of F were varied linearly on a log-log plot from the laminar to the turbulent value across the transition period. The baseline temperatures, incorporating F = 1.1, 1.25, were omitted from the figure for clarity, but would fall between the extreme values shown.

Figure 79 compares point number 3 surface temperatures for the various methods studied for predicting transition onset and heating variation across the transition region. This figure illustrates an important conclusion derived from the aerothermodynamic and thermal analyses of the study. If the 55° angle of attack condition at approximately t = 200 seconds is disregarded, the case of earliest transition onset, i.e., the maximum of laminar or turbulent heating case, results in a lower peak temperature than that obtained using either the MDAC or the NASA transition onset prediction criteria. The obvious conclusion is that there may well be vehicle, location, and trajectory combinations for which an early boundary layer transition is desirable in order to limit peak temperatures. It must, however, be pointed out that the greater total heat load resulting from early transition may cancel a design advantage associated with lower peak surface temperatures by requiring more insulation. In the case of point number 3, however, the early transition retains its advantage over the NASA transition case even when all thermal effects on TPS weight are considered. (See fig. 23.)

Figure 80 shows point number 3 surface temperature histories for the two alternate methods for predicting local boundary layer edge velocity. As on an earlier figure, the baseline case has been omitted for clarity. And, as with the case of altitude and angle of attack perturbations, the temperature curves reflect the effect of u_e variations on transition onset as well as the effects on laminar and turbulent heating predictions individually.

Point 1, 5, 6A, and 9 Thermal Analysis Results: The remainder of thermal analysis results for metallic TPS points is summarized in figures 81, 82, and 83. Figure 81 shows baseline surface temperature histories for the somewhat related points number 1 and 9. Figure 82 gives late time histories for temperatures for the insulation inner face and internal structure at point number 9. The temperature on the aluminum tank skirt, T_2 in the figure, exemplifies the structural (backwall) temperatures examined for the purpose of sizing the insulation layer.

Figure 83 combines the baseline surface temperature histories for points number 5 and 6A, which are near and on the wing leading edge, respectively. The relative insensitivity of the leading edge stagnation line heating to angle of attack can be seen in the very slight dip of the curve for point 6A where

the angle of attack changes at $t = 206$ seconds. The effect of the onset of gradual transition on point number 5 can be seen at approximately $t = 1350$ seconds, in contrast to instantaneous transition on point number 6A at $t = 1920$ seconds.

Carbon/Carbon Composite Points. - Thermal analysis of the carbon/carbon composite designs at points number 6 and 7 consisted mainly of determining the thicknesses of the insulation layers behind the carbon/carbon to protect a titanium structure to 600°F . Maximum insulation temperatures were examined for selection of insulation and encapsulating materials, as for the metallic TPS designs. Maximum carbon/carbon temperatures were also examined for possible exceedance of allowable values, and an investigation of temperature gradients within the carbon/carbon was made to explore the possibility of thermal stress problems.

The limitations of the study led to a compromise in the case of the carbon/carbon backup structure designs. In an actual case, the insulation blanket behind an integral stiffened carbon/carbon composite leading edge or nose cap shell would very likely be placed against the primary structure at the base of the shell, e.g., against the leading edge beam, frame, spar, or against the nose forward bulkhead, respectively. Since the present study dealt with the designs of sections at single surface points, rather than with the design of major components, and since the thermal analysis used the one-dimensional approach, the assumption was made that the insulation blanket followed the inner surface contours of the carbon/carbon shell at the respective study points. This assumption resulted in inefficient use of the insulation and in somewhat questionable absolute weights, but the weight sensitivities thus developed for the carbon/carbon designs are still meaningful.

Figure 84 shows baseline surface temperature histories for points number 6 and 7. The similarity of the temperature history for point number 6 with that for point 6A in figure 83 is evident, but baseline conditions for the two designs were defined in different ways. The point 6 baseline employed the infinite swept cylinder or delta wing leading edge method in order to yield a viable metallic TPS design as a reference for comparisons. While neither the baseline nor any of the perturbation cases resulted in temperatures exceeding the 3200°F maximum for C/C limited reuse, some cases did exceed the full reuse value of 3000°F . Temperatures on the inner surface of the carbon/carbon, and thus on the hot side of the insulation layer, were very near the outer surface temperatures. For point number 6 these temperatures exceeded the 2700°F limit for Dynaflex, which was used at point 7 and at all metallic TPS points. This problem was solved by employing a 0.5 in. layer of zirconia felt insulation between the carbon/carbon and the Dynaflex. This thickness was found adequate for all cases and was kept constant for all perturbations at point 6 while the Dynaflex thickness was varied. The proportions of zirconia felt and Dynaflex therefore were not necessarily optimum for any case examined. Since, however, the densities and thermal conductivities of the two materials are similar, the failure to optimize the insulation composition was not felt to diminish the validity of weight sensitivities.

Thermal gradients through the carbon/carbon composites were examined in detail to assess any possible thermal stress problem. It was found that thermal stresses produced by temperature gradients through the thickness of the material were quite insignificant with respect to those stresses arising from applied loads.

Reusable External Insulation Point. - Thermal analysis of the REI point, point number 3A, was a relatively simple matter, requiring only a check of REI maximum temperatures for material survivability and a determination of the thickness required to limit the bond line temperature to its maximum allowable value. That temperature was taken as the 500°F maximum for unlimited-time exposure of the GE 560 elastomeric bond material.

The REI surface temperatures at point number 3A were very similar to corresponding cases for the metallic TPS at the same location, point number 3. The baseline surface temperatures for point 3A are shown in figure 85. None of the method or criteria perturbations considered resulted in temperatures that exceeded the 2700°F maximum full reuse allowable for the selected REI material.

Since temperatures up to 2700°F have no direct effect on REI weight, the maneuver excursions have no impact on the REI baseline design (table 22). The brief high surface temperatures that exist during the high angle of attack periods in the maneuvers have little effect on bond line temperatures. Thus, REI designs sized specifically for the maneuver excursions are all lighter than the baseline design (fig. 24).

Hot Structure Points. - The thermal analyses of the hot structure study points, 2, 4, and 8, had the objective of predicting the transient temperatures at the possible critical structural design conditions. Since the temperatures at these times could potentially influence material choices and gages, which, in turn, could affect temperatures through heat sink and surface emittance characteristics, the possible need for iterative thermal and structural analyses was recognized.

The hot structure panels were modeled in the CHAP program analyses by use of an effective thickness (\bar{t}) approach. The panel skin and stiffeners were represented, for thermal capacitance purposes, by a single continuous sheet of the panel material, whose thickness was consistent with a uniform distribution of skin and stiffener mass. Any errors resulting from the use of this approach, necessitated by the use of a one-dimensional thermal analysis approximation technique, were expected to affect only the absolute panel weights and not the weight sensitivity trends or comparisons.

Preliminary analysis computer runs were performed to begin the thermal-structural design analysis iterations. The results of these runs showed that the temperatures for a particular material were not sensitive to the \bar{t} for that material within the range of \bar{t} 's expected to be required for the various perturbations. It was found, however, that the temperatures differed significantly between the two primary candidate hot structure materials, Inconel 718 and titanium (6Al-4V). The main reason for the temperature differences was the difference in the surface emittance of the two materials (0.8 for Inconel 718 and 0.3 for titanium).

Reentry Thermal Environment: Reentry thermal-structural design analysis iterations for the baseline cases of all three hot structure points converged with Inconel 718 as the appropriate material (see fig. 19). The baseline temperature histories at these three points are shown in figure 86. Consequently, all criteria and method perturbation thermal analyses were begun using the baseline Inconel \bar{t} .

Among the maximum temperatures resulting from the application of the various perturbed thermal environments to the Inconel hot structure panels, only two values were below 600°F, indicating a possible feasibility of using titanium rather than Inconel. Both cases resulted from the empirically modified local heat transfer predictions, which yielded maximum Inconel temperatures of 487°F at point number 4 and 567°F at point 8.

For the two cases described above, \bar{t} values for titanium hot structure designs were estimated and the thermal analyses repeated using these new \bar{t} 's and the properties of titanium. Although the titanium \bar{t} values were larger than the corresponding Inconel values, the effects of the lower surface emittance and lower density of titanium prevailed and yielded temperatures exceeding 600°F for both cases. The point number 4 titanium maximum temperature was 676°F and the point 8 titanium maximum was 827°F. The hot structure designs for these two cases, therefore, were defined using Inconel 718.

The baseline structural analysis for point number 2 showed that the design at that location, sized for ascent load conditions, had a very wide strength margin at all reentry and post-reentry conditions. This fact, together with the observation that the point 2 reentry temperatures were the lowest of the three hot structure points, led to the conclusion that the point 2 design would be ascent-critical regardless of the planned reentry environment and analysis method perturbations. Inspection of the computed heat transfer coefficient histories led to the conclusion that maximum reentry temperatures for all planned perturbations for point 2 would dictate the use of Inconel for all design perturbations. Therefore, no further thermal analyses were performed for point number 2.

Ascent Thermal Environment: Since points number 2, 4, and 8 carry significant loads during ascent, the possible need for temperature histories at this points in support of ascent stress analysis was considered. A brief thermal analysis study was made to check this need. Point number 8 was selected as the location with greatest potential for ascent criticality. A comparison between certain possible ascent and reentry heating environments, shown in figure 87, showed little likelihood of ascent criticality. Only at relatively low velocities, where heating is of little significance, did there appear any possibility of ascent heating rates exceeding those for reentry. A CHAP program computation of point number 8 temperatures for baseline ascent conditions yielded a maximum ascent temperature of 184°F and a temperature of 76°F at the maximum q α condition. No further ascent thermal analyses were conducted.

Ablation TPS Points. - The study of ablator designs differed from the study of other points on the vehicle in that the ablators were not subjected to variations in design analysis methods or design conditions. Instead, the effects

upon four ablation materials from variations in allowable bond line temperature and in a decomposition rate parameter were examined. The design of the structural panel to which the ablators were bonded was established for the baseline loads environment and was held fixed for all the ablation cases investigated. Thus, the thermal analyses constituted the only perturbation analyses for the ablators.

A total of five ablators was examined in this study. Three of the five were considered as prime candidates and analyzed for Space Shuttle orbiter application. The fourth material, the full density phenolic nylon, was included in order to examine effects of different densities in materials having chemically similar properties. A fifth material, the SLA-561, which was not included in the original study plan, but which has become a candidate material, was examined in a single computer run. The materials studied and references for their basic properties are given in table 23.

For each specific ablator design, such as those whose weights are represented in figure 27, the ablator thickness was sized by interpolation from CHAP program run results for at least three initial thicknesses. The weights shown in figure 27 include the weights of the supporting panel and bond layer, but not that of major frames or nose shell attachment structure. Thus, a reasonably valid basis exists for comparison of ablator weights (points 7A, 7B, 7B1, 7C) from figure 27 with carbon/carbon design weights for the same location (point 7) from figure 26. The ablator weights in figure 27 also include the effect of the added thickness equal to 25% of the predicted receded thickness, as recommended by reference 10.

The results of the parametric ablation studies, as presented in figures 88 and 89, show the weights of the ablation material only. The term "nominal design" indicates that these weights or thicknesses do not include any arbitrary increase beyond the nominally predicted required values.

Figure 88 compares the variation in required ablator weight with allowable bond line temperature in two regions of bond line temperature. It is seen that for all the materials studied (except for the Apollo material at low bond line temperatures) the weight (or thickness) is relatively insensitive to bond line temperature. More importantly, it is concluded that a small change in design weight (such as manufacturing tolerances or an arbitrary added tolerance for uncertainties, etc.) will yield a wide margin in bond line temperature, particularly for designs sized for bond line temperatures in the 600°F region.

Figure 89 shows the effects of the material collision frequency perturbation of one order of magnitude on the design weight - bond line temperature relationships. The collision frequency is the linear coefficient or series of coefficients of an Arrhenius reaction rate equation used to model the virgin material decomposition in the CHAP program (ref. 15). Since decomposition rates are directly proportional to the collision frequency, this parameter was selected for perturbations representing all uncertainties in decomposition characteristics.

From the figure it is seen that for most of the materials studied the ablator thermal protection system weights were not greatly affected by perturbations of collision frequency. The performance of the ablator, i.e., the bond

Table 23. ABLATOR MATERIALS ANALYZED

MATERIAL DESIGNATION OR NAME	MATERIAL DESCRIPTION	VIRGIN MATERIAL DENSITY (LB/FT ³)	PROPERTY DATA SOURCE
NASA SILICONE (POINT 7A)	NASA-LANGLEY SILICONE ELASTOMER IN PHENOLIC HONEYCOMB	15	REF. 43
PHENOLIC NYLON WITH MICROBALLOONS (POINT 7B)	PHENOLIC RESIN, NYLON FIBERS, PHENOLIC MICROBALLOONS	30	
PHENOLIC NYLON (POINT 7B1)	PHENOLIC RESIN, NYLON FIBERS, FULL DENSITY	76	
APOLLO MATERIAL (AVCOAT 5026 - 39 H/CG) (POINT 7C)	EPOXY NOVOLAC IN PHENOLIC HONEYCOMB	34	REF. 44
SLA-561	SILICONE ELASTOMER; CORK, PHENOLIC MICROBALLOON, SILICA MICROBALLOON, AND REFRACTORY FIBER FILLED; IN GLASS-PHENOLIC HONEYCOMB	14.7	REF. 45

line temperature, in some cases was significantly affected by the collision frequency perturbation, but, again, the change in bond line temperature could have been compensated with a small change in design thickness. It was concluded that considerable uncertainty in decomposition rates (whether in the collision frequency or other parameters) could be covered with rather small margins in design thickness or weight.

Further investigation of the effects of collision frequency perturbations disclosed some of the reasons for the relative insensitivity of ablator designs to perturbations in decomposition rates. Variations in decomposition rates have effects that tend to be mutually canceling and the resulting low sensitivity would appear to apply to some degree to ablators in general. For example, a high decomposition rate (high collision frequency) will accelerate the depletion of the material and allow the reaction zone to penetrate closer to the bond line. On the other hand, the high decomposition rate results in greater boundary layer blockage, and the greater thickness of char, if retained, is usually a better insulator than the virgin material.

The effects of collision frequency perturbation on ablator response are shown in figure 90. Results of some of the mutually canceling tendencies can be seen in the figure. The figure includes an additional ablator, SLA-561, which was not studied in detail in this program, but has become a likely candidate for Space Shuttle application. It should be noted that all cases shown in figure 90 are for 2.0 inch initial thicknesses and thus do not satisfy a common design criterion. The $t = 2200$ sec. time was chosen for the sections shown because it is near the end of the applied heat pulse, as shown in figure 91, and thus near the end of ablator thermochemical activity. Temperatures through the materials have begun to relax at this time but for none of the materials has the maximum bond line temperature been reached.

Further studies should be made to show if the one order of magnitude perturbation in collision frequency realistically represents the range of uncertainty for Space Shuttle candidate materials. If the variation can exceed the value assumed here, a further study should be made in order to determine its effect on ablation TPS design.

It is seen in figure 90 that no surface recession is shown for the Apollo material. Although little actual recession is expected for this material, the reason for the predicted zero values lies in the ablation model for this material used in the CHAP program. Ablation of the Apollo material involves a very complex set of reactions, the full modeling of which is beyond the scope of the CHAP program. For best approximation char combustion was eliminated from the mathematical CHAP model. In order to check this approximation the same approach was used to predict the performance of the Apollo material for the Apollo AS-501 trajectory. The predicted temperatures within the material and at the bond line were compared with those measured during that mission and those predicted by the more sophisticated Boeing CHAD program developed especially for Apollo material analysis (ref. 46). The results, shown in figure 92, bear out the adequacy of the simplified CHAP model used for the current study by showing good approximation of the in-depth temperature distributions.

APPENDIX E

STRENGTH ANALYSIS AND DESIGN DEFINITION

by A. L. Brown

The required structure for each of the design points was sized to withstand the load and thermal environments defined in Appendices B, C and D, using the criteria and analysis methods described below. The weight sensitivity of this structure to perturbations from the baseline design conditions was determined either parametrically or by individual point designs. The sensitivities are summarized in this appendix.

Design Criteria

All structure was designed in accordance with the structural design criteria of reference 10, pertaining to load definition, factors of safety, allowable mechanical properties, service life, material design thickness, selected natural and man-made environments, and selected induced environments discussed below. The following criteria were used:

a) Factors of Safety

<u>Load Type</u>	<u>Factor of Safety</u>	
	<u>Yield</u>	<u>Ultimate</u>
Applied (Pressure, Aerodynamic, Inertia, etc.)	1.0	1.5
Induced (Thermal)	1.0	1.0

b) TPS Panel Deflection

<u>Item</u>	<u>Span/Deflection</u>
Overall Panel	100
Local Panel (Skin)	15

c) Service Life - 100 Missions

d) Skin Panel Flutter

The panel shall be free of flutter at all dynamic pressures up to 1.5 times the local dynamic pressure expected to be encountered at any Mach number during normal flight in accordance with reference 10.

Design Conditions

The design environment for each of the study points was derived from data generated in the loads, aerothermodynamic and thermal analyses (Appendices B, C, and D) as described below.

TPS Panels. - The metallic TPS panels were designed to withstand the thermal and pressure environment occurring during boost and reentry. The reentry environment included conditions of maximum temperature and pressure, and maximum positive and negative thermal gradients as shown in figure 93 for a typical panel. Since it was necessary to define TPS panel weights throughout a large range of reentry conditions, panel weights were calculated using parametric reentry environments. The parametric conditions selected for boost and reentry maximum temperatures and pressures are summarized in table 24. The panel net pressures were calculated using the external pressures calculated as described in Appendix C and internal pressures resulting from the requirements shown in table 8.

Design conditions for other TPS panels were calculated using similar methods and are summarized in tables 5 and 6.

Hot Structure. - The wing and fin hot structure points are designed by primary vehicle aerodynamic loads occurring during flight. These design loads for ascent and reentry conditions are summarized in Appendix B. The corresponding thermal environment is given in Appendix D or was calculated using methods described therein. Structural temperatures for the baseline design conditions are summarized in table 25.

The hot structure at body point 2 was critical for the acoustic environment during launch and for flutter during ascent. The acoustic environment is given in Appendix B. The thermal environment existing under the critical flutter condition is shown in table 25.

Material Properties

The material properties used for analysis of the hot structure points were standard values for Inconel 718 obtained from MIL-HDBK-5A. However, similar data were not available for the TPS materials used in this study. Consequently, data from other sources were utilized.

All allowables for annealed Haynes 188 were calculated using data from reference 48. These allowables are summarized in figure 94.

The allowables for Columbium alloy C-129Y (except creep) were based on test data obtained from previous Boeing Company tests and from reference 49. Statistical "A" values were calculated using MIL-HDBK-5A methods including correction for specification minimum values. The creep allowable was estimated from data obtained from many sources. These allowables are summarized in figure 95. In order not to exceed TPS panel deflection limits the creep allowables were deliberately chosen to be conservative. The conservatism was introduced by using creep allowables established for substantially longer exposure times

Table 24. - METALLIC TPS PANEL PARAMETRIC DESIGN CONDITIONS

<u>REENTRY CONDITIONS</u>	MATERIAL	
	HAYNES 188	Cb 129Y
TEMPERATURE (°F)		
1,600	X	
1,800	X	
2,000	X	X
2,200		X
2,400		X
NET PRESSURE (LB/ IN. ²) (POSITIVE IS INWARD)		
0	X	X
0.2		X
0.4	X	X
0.7	X	X
TEMPERATURE GRADIENT (°F)		
+600	X	X
+300	X	
<u>BOOST CONDITIONS</u>		
TEMPERATURE (°F)		
70	X	X
NET PRESSURE (LB/ IN. ²)		
-4.84	X	X

Table 25: — HOT STRUCTURE BASELINE DESIGN TEMPERATURES

CONDITION	LOCATION					
	BODY-PT. 2		WING-PT. 4		FIN-PT. 8	
	M	TEMP (°F)	M	TEMP (°F)	M	TEMP (°F)
ASCENT	1.4	350	(MAX $q\alpha$)	70	(MAX $q\beta$)	70
REENTRY AND POST- REENTRY	—	—	11.60	830	6.40	900
			1.18	510	1.18	550
			0.94	490	0.94	530

than actually existed for the various designs. The analysis of creep accumulation and panel deflection interactions would require a considerable effort, which was considered to be beyond the scope of the present study.

The mechanical properties used in this study for REI material are shown in figures 96 through 102. These data were obtained from references 50 and 51. In some areas the lack of data necessitated extrapolation and reliance on Boeing ceramic material experience in order to provide a basis for designing to temperatures up to 2800°F. It should be noted that all properties available from the references are average values. The lack of adequate quantities of data prevented the formulation of the usual, statistically based, design allowable properties. Because of expected improvements in REI materials prior to Space Shuttle final design, the present average values were taken as representative of future design allowables and were employed as such in this study.

Table 26 contains the available strength data for oxidation protected reinforced carbon material. These data were obtained from reference 52.

Stress Analyses

Stress analyses of the structural elements for the hot primary structure and TPS panels were performed to size the elements and to ensure the adequacy of structure to withstand the induced environment for the service life of the orbiter. Structural designs were formulated for both baseline conditions and perturbed conditions. The structures were designed in accordance with previously stated criteria to withstand primary structure loads, local pressures, acoustic noise, temperature, and temperature gradients discussed in the previous section. The analyses were performed using conventional preliminary design stress methods for aircraft and launch vehicles. The effects of local and general component structural instability, differential thermal expansion, and material property degradation with increasing temperature were included. The material properties used were those discussed previously in this appendix. In combining internal loads the following procedures were established:

Thermal and mechanical stresses were added except thermal stresses, where alleviating, were disregarded.

For buckling analysis thermal and mechanical stresses were added, the resulting stresses remaining under the buckling allowable.

TPS Panels. - Design of metallic TPS panels was accomplished using the Boeing computer program, "OPTimization by Random Search" (OPTRAN). This program optimizes TPS panel dimensions for minimum panel weight. Program input, output, and design constraints are summarized in figure 13. The corrugation stiffened face sheet concept shown in figure 13 was used to size all TPS panels. The eight variables shown were optimized simultaneously to provide minimum panel weight for selected panel sizes. Figure 103 shows the method used to obtain the optimum size panel including the weight of required support structure. This results in a plot defining the optimum panel weight for each parametric design condition as presented in figure 14.

Table 26 .- OXIDATION PROTECTED REINFORCED CARBON MECHANICAL PROPERTIES

TEMP (°F)	PROPERTIES 1			
	ITEM	UNITS	DIRECTION	VALUE
70	TENSION ULTIMATE	LB/IN. ²	WARP	5 100
	↓	↓	FILL	2 700
	↓	↓	INTERLAMINAR	630
	SHEAR ULTIMATE	LB/IN. ²	INTERLAMINAR	3 200
	↓	↓	WARP	1.9
	TENSION MODULUS ¹	LB/IN. ² X10 ⁶	FILL	0.7
ELEVATED	2			2

1 REFERENCE 52

2 STRENGTHS AT ELEVATED TEMPERATURE EXCEED ROOM TEMPERATURE VALUES

Although the OPTRAN program provides no direct constraints on panel design to satisfy flutter and acoustic requirements, past experience has shown that corrugation stiffened panels designed by this program will satisfy criteria requirements.

The design of the ablator TPS panels was accomplished using the configuration shown in figure 21. The ablative material was assumed to be non-structural. Consequently, the titanium honeycomb sandwich support panel was assumed to carry all of the structural loads. The critical design condition, as shown in table 6, is the maximum differential pressure occurring during reentry combined with a panel temperature equal to the maximum bondline temperature of 600°F. The resulting panel design is shown in figure 21.

The design of the carbon/carbon structure for points 6 and 7 was based on the configuration shown in figure 20. A multilayer configuration for the skin layup was assumed in order to be compatible with the combined biaxial bending and shear stresses existing at this location. An integrally bonded stiffener configuration was assumed consisting of uniaxial fibers covered with cross ply layers. The critical design condition at each location is the differential pressure occurring during reentry as shown in table 6. Simple plate and beam theories were used to analyze the skins and stiffeners. Due to the similarity in the design pressure at these locations, the same skin layup was assumed for the baseline design at each point. However, the stiffener spacing and size were varied to fully utilize the capability of the skin under the different pressures. In order to readily determine the effect on sizing due to perturbations in the design conditions, the required number of skin plies and stiffener size was determined parametrically over a range of design pressures. Stiffener spacing was assumed equal to that required for the baseline design. The results of this analysis are shown in figure 104.

The REI TPS panels were designed using the configuration shown in figure 18. Due to the extreme lack of ductility in the M25A7 coating material for the REI, the substrate structural panel must be designed to prevent cracking of the coating under all flight conditions. At point number 3A one critical strain condition occurs when the panel is subject to differential pressure resulting from maximum wind shear conditions at maximum $q \alpha$ during ascent. Another critical condition occurs late in reentry when the substrate is still hot and the coating is cold. In general REI integrity should be determined analytically and verified by extensive tests. In order to analyze adequately the complete material system including coating, bond layer and substrate a finite element analysis is required. Prerequisites for such analysis are complete and consistent material characterization, measured material properties over the entire use temperature range and demonstrated compatibility with adjacent materials such as coatings and bonding compounds. Since sufficient material property data for the coating were not available to conduct such an analysis, only an approximate assessment of the influence of the coating on sizing of either the substrate panel or the RTV adhesive layer could be made. This preliminary analysis indicated a potential problem due to coating failure. The substrate panel was, therefore, sized to carry the ascent loads which were higher than the reentry loads. Then the integrity of the REI material without coating under both ascent and reentry conditions was verified by accounting for the stresses due to extreme loads, substrate deflections and thermal exposure.

Hot Structure. - A conventional three spar, two cell, rib stiffened box structure was assumed for both the wing and fin primary structures. These are shown in figures 105 and 106 together with the assumed location of the elastic axes. The configuration assumed for the wing and fin skin panel structure at points 4 and 8 is shown in figure 19.

Analyses were conducted to obtain individual point designs for both baseline conditions and all perturbations from the baseline. Both ascent and reentry condition primary vehicle loads were investigated to ensure adequate sizing of the structure. The ascent loads used were those resulting from maximum wind shear conditions at maximum $q \alpha$ and $q \beta$ and are shown in table 5. The reentry condition loads analyzed include those occurring at the following times; (1) when the temperature of the structure is at or near the maximum, (2) when the dynamic pressure is a maximum, and (3) when a 2.5 g flight maneuver is first allowed. The loads occurring at these times are shown in tables 13 and 14. The critical design condition for the wing panel is the reentry 2.5g maneuver condition. For the fin it is the condition of maximum dynamic pressure during reentry.

Standard preliminary design analysis methods were used to size the skin and stiffener structure at each location. The primary vehicle loads about the load reference axes were transferred to the assumed elastic axes and the resulting internal loads calculated. The axial compression stresses resulting from spanwise bending were combined with the skin shear stresses resulting from shear and torsion loads carried by the box structure. The failure criterion used is that represented by the interaction formula

$$R_c^2 + R_s^2 = 1.0$$

where $R_c = \frac{\text{applied compression stress}}{\text{allowable compression stress}}$

and $R_s = \frac{\text{applied shear stress}}{\text{allowable shear stress}}$

The allowable compression stress was calculated from reference 53 which optimizes the skin and stringer configuration to provide minimum structural weight. This is accomplished by requiring that local and general instability of the panel structure occur simultaneously. Conventional methods for calculating allowable shear stress were used. Thermal stresses resulting from temperature gradients in the structure were calculated and included in the analysis. Figures 6 and 19 show the detail configuration of the skin and stringer structure required to satisfy the baseline design conditions.

Design of the skin panel at point 2 on the side of the body was based on the configuration shown in figure 19. The structural concept precludes carrying internal loads due to body bending and allows the panel to carry only body shear and normal pressure loads. However, both the shear and pressure loads occurring during ascent and reentry are too small to be critical. Consequently, the critical design conditions are the acoustic noise occurring during launch and the prevention of panel flutter throughout flight. The panel-flutter analytical

method used to size the skin between stiffeners is similar to that given in reference 47. Figure 107 shows the flutter boundary defined in this reference. The resulting skin gage requirements are shown in figure 108 as a function of panel length to width ratio. This figure also shows the corresponding panel stiffener required to withstand the launch acoustic environment resulting from 13 engines as shown in figure 40. The stiffener requirement was established by equating the power spectral density required to the power spectral density capability of a panel. This was accomplished graphically for a range of stiffener depths and panel length to width ratios as shown in figure 109. Standard formulae for panel frequency and panel stress were used together with a material fatigue allowable based on a life factor of 4 (400 flights total). Specific stiffener requirements were then defined from figure 110 including the effect of limiting the minimum stiffener thickness to that of the corresponding skin gage. The resulting minimum average stiffener thicknesses were then added to the required skin gage as shown in figure 108. The minimum total thickness thus occurs at a length to width ratio of 10. Since the slope of the curve at this point is nearly zero, this thickness was used as the true minimum for purposes of this study.

Design Definition

The baseline designs for the fourteen study points, incorporating the results of the structural sizing techniques as described in the preceding paragraphs, plus insulation thickness and material choices discussed in Appendix D, were defined in detail as shown in figures 17 through 21. Similar details are not shown for the perturbed designs, because, in many cases, the use of parametric sizing data permitted a more direct determination of the perturbed design weight. The weights of the baseline and perturbed designs constituted the data from which the individual study point weight sensitivity plots, figures 111 through 125, were drawn.

The weight sensitivity plots show continuous curves for weight per unit surface area versus continuous parameters such as altitude and angle of attack, and bars for weight versus discrete parameters such as atmosphere model and turbulent heating theory. Where maximum surface temperatures were computed in the course of defining perturbed designs, those temperatures are shown on the weight bars for the respective cases. It is pointed out, however, that for some of the study points or design concepts, the maximum surface temperature was not a strong indicator of thermal environment influence on design weight.

Weight sensitivities of the metallic TPS study points are given in figures 111, 113, 116, 118, and 125. Certain metallic TPS designs could not be defined at the originally planned values of perturbation parameters because of temperatures which exceeded the maximum allowable for columbium. Where this problem resulted from the perturbation of a continuously variable parameter, e.g., the altitude perturbation at point number 3 (fig. 113), design weights at intermediate values of the parameter were defined and the sensitivity curve extended as far as possible. For such cases the 2400°F normal reuse maximum temperature conditions are shown as well as the 2450°F limited reuse conditions, which coincide with the highest definable design weight. For cases where a discrete

parameter or prediction method resulted in a maximum surface temperature exceeding 2450°F, e.g., the Eckert i^* turbulent theory for point 3 (fig. 113), the fact could only be so indicated and the design weight left undefined.

The metallic TPS points showed no sensitivity to ultimate factor of safety since the designs were all creep-critical and thus were influenced by limit rather than ultimate stresses.

Weight sensitivities for the single REI point studied, point 3A, are shown in figure 114. The weight variations seen are due entirely to thermal effects on the insulator thickness. The titanium honeycomb support panel was designed by normal pressure loads during ascent and thus was not sensitive to any perturbations during reentry. The REI layer itself, in the thicknesses required for insulation, was also adequate to withstand baseline and perturbed reentry loads.

The hot structure point weight plots, figures 112, 115, and 124 show almost no sensitivity to the perturbed parameters or methods. Point number 2 (fig. 112) is totally insensitive since the concept is designed by ascent conditions regardless of the perturbation studied. Points 4 and 8 (fig. 115 and 124) show very little sensitivity to reentry environment or analysis method perturbations since they are designed by the post-reentry 2.5g maneuver condition and the very late reentry maximum dynamic pressure condition, respectively. At the times of these conditions the effects of reentry perturbations on structural temperatures had virtually disappeared. Perturbation of the ultimate factor of safety had a direct effect on point 4 and 8 weights, however, since the designs were critical to ultimate stresses over much of the range of UFS examined.

Weight sensitivities for the carbon/carbon composite designs at points 6 and 7 are shown in figures 117 and 119. A number of the perturbed designs for point 6 exhibited temperatures in excess of the 3000°F normal reuse maximum but none exceeded the limited reuse maximum of 3200°F. Many of the carbon/carbon weight sensitivity curves exhibit discontinuities (steps) arising from the use of discrete numbers of constant thickness plies of C/C material. (See fig. 15). The carbon/carbon weight sensitivities were generally affected significantly by both the pressure variations, which determined the C/C material weight, and the thermal environment, which affected the weight of the insulation associated with the design.

The ablator weight sensitivity curves, figures 120 through 123 are included in this appendix for completeness of the design definitions, although they were not examined under any perturbations affecting strength analysis. The ablator design weights of figures 120 through 123 include the weight of the titanium honeycomb support panel, the weight of the bond material, and the weight of the ablator design tolerance (a thickness increase equal to 25% of the predicted recession depth), as recommended in reference 10. The titanium honeycomb support panels were assumed to be sized by ascent loads and thus were not resized when maximum allowable bond line temperatures were perturbed.

APPENDIX F

SAMPLE COMPUTATION

The purpose of this appendix is to illustrate the computation procedures used to obtain the TPS weights at the selected orbiter vehicle study points. For this sample calculation point number 3 was selected as the vehicle location, the metallic TPS was selected as the design concept, and the computations will be those for the baseline design definition. In addition, one design perturbation will be included to illustrate a weight sensitivity computation. The discussion will follow the order of application of the technical disciplines used to design the TPS and define the weight.

Aerothermodynamic Analysis

The determination of heat transfer coefficients for point number 3 required the calculation of local pressure and edge velocity along the wing lower surface from the stagnation line to the point 3 location at the mid semi-span line. Local pressure was also required in the computation of panel net pressure loads. The airfoil shape and geometry specified in Appendix A were utilized to define the variation of local flow deflection angle with distance. The local pressure and edge velocity distributions were then calculated using equations (C2) and (C4) of Appendix C at the trajectory points indicated in table 7.

The variation of boundary layer transition location with time was plotted as in figure 62 in order to determine when the beginning and end of transition passed point number 3. This figure also indicates the trajectory points for which point 3 was located in the transition zone. For these cases the heat transfer coefficient and adiabatic wall enthalpy were plotted as functions of the local Reynolds number. The uncertainty factors (table 8) were included with the fully laminar and turbulent heat transfer coefficients. The transitional heat transfer coefficients (including uncertainty factors) and adiabatic wall enthalpy were then obtained by a linear fairing on log-log paper between the laminar value at onset and the turbulent value at the end of transition. The end of transition was assumed to occur at a Reynolds number twice that at the beginning. The resulting heat transfer coefficient and adiabatic wall enthalpy as a function of time are shown in table 27.

Two additional entries were included in table 27, those at 2500 and 3600 seconds. The 2500 second point was obtained by extrapolation from the earlier calculations. The second point is the assumed zero heat transfer coefficient and 80°F ambient condition at landing.

The history of external surface pressures at point number 3 for the baseline environment is shown in figure 126. These pressures were computed using equation (C2) of Appendix C.

Table 27.—BASELINE HEAT TRANSFER PREDICTIONS FOR POINT NO. 3

TIME (SECONDS)	i_{aw} (BTU/LB _m)	$\dot{q}/(i_{aw}-i_w)$ (LB _m /FT ² SEC)
0	11,700	2.77×10^{-5}
116	11,600	2.4×10^{-4}
206.0	11,000	2.1×10^{-3}
206.1	10,000	5.02×10^{-4}
214	10,000	5.02×10^{-4}
308	9,720	5.32×10^{-4}
514	9,120	5.7×10^{-4}
620	8,700	6.2×10^{-4}
802	8,220	9.6×10^{-4}
1,100	6,630	3.0×10^{-3}
1,346	5,320	4.92×10^{-3}
1,756	1,930	5.55×10^{-3}
2,074	540	8.13×10^{-3}
2,500	116	1.45×10^{-2}
3,600	130	0.0

Thermal Analysis

The aerothermodynamic data of table 27 constituted the environmental input to the thermal analysis CHAP run for the point number 3 baseline. The CHAP program performed a linear interpolation between the points of table 27 to compute heating rates at 0.1 second intervals.

The one dimensional model of the metallic TPS represented a section through the panel, shown in figure 17, along the valley of the stiffening corrugation. The details of the section model are shown below:

<u>Layer</u>	<u>TPS Component</u>	<u>Material</u>	<u>Thickness (in)</u>	<u>Number of Nodes</u>
1	Skin	C129Y	.020	4
2	Space		1.0	-
3	Corrugation	C129Y	.015	3
4	Space		1.0	-
5	Insulation Encapsulation	Zirconia cloth	-	-
6	Insulation	Dynaflex	4.0	40
7	Insulation Encapsulation.	Zirconia cloth	-	-

The assumed thickness of the spaces between the skin and the corrugation and between the corrugation and the insulation had no effect on the results since radiation was the only heat transfer mode assumed to take place across these spaces. The mass and thermal conductivity of the insulation encapsulation were ignored in the thermal analysis but the radiant properties (absorbance and emittance) of the encapsulating material (zirconia cloth) were included in the computations.

The initial temperature (at $t = 0$) was assumed to be 80°F throughout the TPS. As a back side boundary condition, the insulation encapsulation inner surface was allowed to radiate to a 80°F background. A 1.0 second compute interval was used for the transient temperature calculations.

The temperature results from the baseline thermal analysis for point 3 are summarized in figure 73. The computer program numerical output was examined in detail to determine the maximum temperature differences between points selected to characterize thermal gradients in the TPS panel. The salient temperature results are listed below:

<u>Parameter</u>	<u>Value (°F)</u>	<u>Time Of Occurrence (sec.)</u>	<u>Use in TPS Design</u>
Skin Maximum Temperature, T_{\max}	2296	1350	TPS panel metal components material selection and sizing.
$(T_4 - T_5)_{\max}$ (see fig. 73)	420	60	TPS panel metal components sizing.
Insulation Maximum Temperature	2282	1350	Insulation and encapsulation material selection.

Temperatures at and near the inner surface of the insulation layer were examined and found to reach peak values in the neighborhood of $t = 2400$ seconds. A plot of insulation temperatures at several specific times and the selection of a thickness meeting the 600°F maximum temperature at the TPS-primary structure interface are illustrated in figure 127. The resulting insulation thickness for the point number 3 baseline design was 3.62 inches.

Strength Analysis and Design Definition

The strength analyses of the metallic TPS designs were actually performed parametrically, as described in Appendix E, yielding the curves of figure 14. Each TPS metal component sizing operation was thus reduced to the reading of the appropriate value from figure 14.

The derivation of the temperature values for sizing the point number 3 TPS was described in the preceding section on Thermal Analysis. A panel maximum net pressure of 0.4 lb/in^2 , consistent with the external pressure history of figure 126 and the internal pressure design requirement, stated in table 8, was applied. It is then seen from figure 14 that at $\Delta p = 0.4 \text{ lb/in}^2$, $T_{\max} = 2296^\circ\text{F}$, and $\Delta T = 420^\circ\text{F}$, a metal TPS panel weight of 2.62 lb/ft^2 was read.

The maximum insulation temperature of 2282°F confirmed the selection of Dynaflex as the insulation material (as used in the thermal analysis) and of zirconia cloth for the insulation encapsulation (see fig. 16). The zirconia cloth, at 8.0 oz/yd^2 basic material weight, when applied to both sides of the insulation layer and supplemented with allowances for edge closures and attachments, had a weight per unit of panel area of 0.175 lb/ft^2 . The weight of the 2.62 inches of 6.0 lb/ft^3 Dynaflex was 1.81 lb/ft^2 .

The total TPS panel baseline weight at point 3 was summed as follows:

Metal Components	2.62
Insulation	1.81
Insulation Encapsulation	<u>.175</u>
Total TPS Weight	4.605 lb/ft ²

PERTURBED DESIGN

In order to illustrate the definition of a perturbed design and the corresponding weight sensitivity value, the development of the TPS weight figures for one particular perturbed design at point number 3 will be briefly described. The perturbation chosen for this illustration is the +3000 ft. altitude perturbation, that is, a reentry environment defined by a trajectory lying 3000 feet above the limit (baseline) trajectory.

For this perturbed trajectory a new set of aerothermodynamic data was computed and input to the CHAP program for thermal analysis, in the same manner as described in the preceding sections. The surface temperature history for this perturbation case at point 3 is shown in figure 74. The key results from the thermal analysis, for TPS sizing purposes, were:

<u>Parameter</u>	<u>Value</u>	<u>Time of Occurrence</u>
Skin Maximum Temperature T_{\max}	2221°F	1350
$(T_4 - T_5)_{\max}$ (see fig. 73)	418°F	60
Insulation Maximum Temperature	2205°F	1350
Insulation Thickness	3.51 In.	-

The increase in altitude, relative to the baseline trajectory, resulted in a panel net pressure of 0.35 lb/in², again following the ground rule of zero internal pressure prior to $t = 2000$ sec. (table 8).

For the indicated temperatures, pressure, and insulation thickness the following TPS panel design weights were determined:

Metal Components (C129Y) (fig. 14)	2.465
Insulation (Dynaflex)	1.755
Insulation Encapsulation (zirconia cloth)	<u>.175</u>
Total TPS Weight	4.395 lb/ft ²

Finally, the weight sensitivity value for this particular perturbed condition was formed by the simple ratio of the perturbed TPS panel weight to the baseline TPS panel weight. For point number 3, $\Delta Z = +3000$ ft:

TPS Design Weight per Unit Area, % of Baseline =

$$100 \times (4.395/4.605) = 95.44\%$$

The above value of non-dimensional TPS design weight furnished one point for the point number 3 curve of the Altitude Perturbation plot of figure 113.

APPENDIX G

RECOMMENDED PRACTICES AND CRITERIA

This appendix contains the recommendations for practices and criteria to be applied supplementary to or in lieu of those in NASA SP-8057, "Structural Design Criteria Applicable to a Space Shuttle," (ref. 10). The recommendations are based on the trends and similarities observed as a result of the present study. Some of the recommendations have also direct bearing on other NASA Space Vehicle Design Criteria monographs such as NASA SP-8014, "Entry Thermal Protection" and NASA SP-8062, "Entry Gasdynamic Heating."

It must be emphasized that, similar to the NASA Space Shuttle Criteria monographs themselves, all recommendations are of a preliminary nature until a firmer data base can be established and the next updating cycle completed.

The recommendations which follow are organized consistent with the format of NASA SP-8057, with the location of the recommended change indicated. The recommended action (addition, deletion, or substitution) is stated and, where appropriate, the revised words and the reason for the recommendation are given.

<u>Section</u>	<u>Page</u>	<u>Para</u>	<u>Action</u>
(NASA SP-8057)			
1.6	1-4	"Limit Load"	Add to existing sentence: "... consistent with a certain accepted probability" value. <u>Reason</u> : Consistent with the approach to limit loads based on probability as discussed in section 4.1.1.
1.6	1-7	THERMAL STRESS	Change to "The structural stress arising from temperature gradients within members or from differential thermal expansion...." <u>Reason</u> : Temperature gradients can cause thermal stresses within monolithic members.
4.2	4-3	"Factors of Safety"	Delete last sentence, beginning with "In addition,...." Add in bold-faced type: "It is recommended that factors of safety be applied only to mechanically induced limit loads and pressures and not to temperatures, temperature gradients, or thermally induced loads or stresses. "Thermal stresses and mechanical load stresses shall be combined as indicated by the respective signs of the components but in a manner that preserves the required design success probability." Continue, in ordinary type: "Ideally, stress components should be computed and combined on a probabilistic basis. When the signs of the thermal and loads stresses indicate addition of stresses the components should be added at the same non-exceedance percentile level. When thermal stress and load stress have opposite signs they should be combined at their individual non-exceedance or non-subceedance levels that result in the most critical design condition." "For many design analyses dispersions in stresses (or loads) required to define the appropriate probability levels described above are not available. For these cases thermal stresses which tend

<u>Section</u>	<u>Page</u>	<u>Para</u>	<u>Action</u>
4.2 (Continued)			to alleviate load stresses shall be considered to be zero." <u>Reason</u> : Means of combining thermally induced and mechanical load induced stresses is not covered.
4.4	4-4	New	Add, following end of 4.4: "The analysis of all structural members shall include consideration of the relative deflection of adjacent members and the resulting loads thereby imposed on all members. In addition, structural deflections of all primary structure and equipment support structure shall be calculated to ensure that the structure is not in interference with an adjacent system, and to ensure that equipment packages are not adversely affected internally by relative movements of their support points. Special consideration shall be given to environmental pressure gradients causing changes in internal flow characteristics due to such relative deflections."
4.6	4-8	2	Delete from first line: "for heat sources or sinks" <u>Reason</u> : Words are unnecessary and imply an incorrect qualification.
4.6	4-8	3, Item 7	Substitute: "...shall be aligned as nearly parallel as possible to the local flow..." or delete (see added section 4.6.1.1) <u>Reason</u> : Local flow angles can change with α , etc. Also, the designer can be allowed some freedom with respect to bead, wave, etc. alignment.
4.6	4-8	8, "Insulation"	Delete, replace with: "Insulation material for use with metallic heat shields must be selected and sized for adequate performance in the total vehicle environment and through the design life of the heat shields. Consideration must be given to possible material degradation due to thermal cycling, noise and vibration environments, and moisture absorption. Adequacy of the insulation

<u>Section</u>	<u>Page</u>	<u>Para</u>	<u>Action</u>
4.6 (Continued)			system shall be demonstrated in ground simulation tests of the environments expected through the service life of the thermal protection system." <u>Reason</u> : Existing paragraph is not constructive. It identifies potential problems but does not tell how to assure design integrity.
4.6	4-8	New	<p>Add, following end of existing 4.6:</p> <p>4.6.1 <u>Allowable Deformation of TPS Outer Surface</u></p> <p>4.6.1.1 General</p> <p>"The design goals for external surface discontinuities shall be aft-facing steps with respect to the local flow at the critical heating condition. All beads, waves or corrugations in skin panels shall be aligned as nearly parallel as possible to the local flow at the critical heating condition.</p> <p>4.6.1.2 Surface Mismatch and Gaps</p> <p>"As an interim requirement, the maximum mismatch between separate surface panels shall be 0.050 in. (aft-facing only). The maximum mismatch between skin sheets on the same panel shall be 0.030 in. (aft-facing only). Protrusions due to fasteners, etc., shall not exceed 0.005 in.</p> <p>4.6.1.3 Surface Deflection</p> <p>"Distortion of the outer surface of the TPS causes an increase in aerodynamic drag and heating. Allowable surface deflections are TBD.</p> <p>"This requirement must be satisfied during the ascent, low cross range reentry and subsonic cruise phases. (For a high cross range entry, reduction of drag is paramount and the surface distortion would be restricted to half the above amount.)</p> <p>"In each case the deflection must include the deflection due to prior creep as well as that due to transverse load and thermal distortion." <u>Reason</u>: Minor surface irregularities can cause very important increases in local heating and can be self-aggravating. Close control of these effects in design is essential.</p>

<u>Section</u>	<u>Page</u>	<u>Para.</u>	<u>Action</u>
4.9.1.6	4-14	New	<p>Add, following end of existing 4.9.1.6:</p> <p>"The thermal protection system flight design conditions shall include, in addition to normal flight, the conditions of aborted flight and emergency maneuvers resulting from a guidance system failure or degradation.</p> <p>"The thermal protection system shall:</p> <p>"Withstand the aerodynamic heating, skin friction and normal pressure under all flight design conditions.</p> <p>"Satisfy the aeroelastic requirements for flutter prevention.</p> <p>"Withstand the acoustic, vibration, and shock loadings associated with the entire design envelope.</p> <p>"Not be functionally degraded during exposure to design environments within the specified limits of reuse and refurbishment.</p> <p>"Withstand the rain, dust, humidity, freezing, etc., requirements of the natural environment (see 5.1.3).</p> <p>"Be compatible with the vehicle structure, in terms of temperature limitations, thermal expansion, deflections, stiffnesses and loads (see 4.6).</p> <p>"Withstand TBD meteoroid/radiation environments (see 4.10.8 and 5.1.3)." <u>Reason</u>: More complete definition of TPS requirements is needed.</p>
4.10.1	4-16	4	<p>Delete last paragraph of 4.10.1, substitute:</p> <p>"The design thickness for ablation materials shall be increased by a selected fraction of the predicted required geometric thickness based on the nominal maximum allowable backwall (bond line) temperature. An interim value for the design thickness of 1.10 times the nominal predicted required thickness is recommended until more detailed characterization of the particular material is available." <u>Reason</u>: The existing criteria may yield excessive conservatism for receding ablators but little or</p>

<u>Section</u>	<u>Page</u>	<u>Para.</u>	<u>Action</u>												
4.10.1 (Continued)			no design margin for those exhibiting little or no geometric recession, respectively, even though such materials may char significantly.												
4.10.4	4-17	New	Add, following end of existing 4.10.4: "All internal compartments of Space Shuttle vehicles shall include provisions for venting such that air can pass from compartments to a base pressure, during all life phases, without exceeding the design strength of floor beams, floor panels, bulkheads, tankage, thermal protection system, spars, ribs, or other structural components. Pending the results of a venting analysis, all structure enclosing compartments shall be designed to carry TBD psi ultimate, in combination with ultimate flight loads and pressures."												
4.10.13	4-19	New	Add, following existing 4.10.13: "The TPS shall be flightworthy for each mission. Evidence of excessive temperature or time-temperature damage shall be easily detectable at least one mission prior to failure."												
5.1.2	5-2	First	Change the sentence beginning: "At least..." to, "Where applicable the following conditions shall be evaluated: (1) gas dynamic heating; (2) solar and planetary thermal radiation; (3) structural conduction, heat capacitance, and reradiation; (4) leakage and internal convection; and (5) internally induced heat transfer." <u>Reason</u> : More complete and more workable requirement. <u>Comment</u> : The words "At Least" imply existence of other conditions whereas a requirement statement should be complete and leave no uncertainties as to what is to be accounted for. On the other hand, not all the stated conditions will always be present and thus need be considered only "where applicable."												
5.1.2.1.1	5-2	3	Change or add following: <table border="0" style="margin-left: 40px;"> <tr> <td>Laminar Heating.</td> <td>Attached Flow</td> <td>1.10</td> </tr> <tr> <td>Turbulent Heating.</td> <td>Region</td> <td>1.25</td> </tr> <tr> <td>Heating in Separated Flow Regions.</td> <td></td> <td>1.50</td> </tr> <tr> <td>Heating in Interference Regions.</td> <td></td> <td>1.50</td> </tr> </table>	Laminar Heating.	Attached Flow	1.10	Turbulent Heating.	Region	1.25	Heating in Separated Flow Regions.		1.50	Heating in Interference Regions.		1.50
Laminar Heating.	Attached Flow	1.10													
Turbulent Heating.	Region	1.25													
Heating in Separated Flow Regions.		1.50													
Heating in Interference Regions.		1.50													

Section Page Para.

Action

5.1.2.1.1 (Continued)

"The 1.10 or 1.25 factors should not be applied in addition to or as a multiplier of the 1.50 factor. Where sufficient data on the type of interference case under consideration exist, permitting definition of trends with the primary variables; angle of attack, Mach number, Reynolds number, and boundary layer condition, the 1.50 factor can be reduced to 1.25."

5.1.2.1.1 5-3 New

Add at beginning of page 5-3:

"The location of the beginning of boundary layer transition shall be defined by the most forward position predicted by:

$$1. \quad \frac{R_{e,\theta}}{M_e} \frac{1}{(R_e/ft)^2} = 10 + .11e^{.077\delta} \quad (\delta \text{ in Degrees})$$

$$2. \quad \log_{10} \frac{R_{e,\delta^*}}{(R_e/ft)^{.25}} = .7 \left(1 + \frac{M_e}{2} \right) \quad M_e \leq 4.6$$

$$= 1.78 \left(1 + \frac{M_e}{15.5} \right) \quad M_e \geq 4.6$$

"The local pressure on windward surfaces should be calculated using the modified Newtonian method. The local boundary layer edge velocity may be calculated using the parallel shock method.

"Either the Spalding-Chi or Rho-mu Momentum Integral Methods may be used to predict turbulent heating to a Space Shuttle orbiter. The Colburn Reynolds analogy factor should be used with both methods.

"The end of transition and the heating in the transition region shall be defined by a linear fairing on a log log plot between the laminar heating at beginning of transition and the turbulent heating of the end, where end of transition is at 2 times the local distance Reynolds number at the beginning of transition."

Reason: Simplicity of application.

<u>Section</u>	<u>Page</u>	<u>Para</u>	<u>Action</u>
5.1.2.1	5-3	New	Add, following existing 5.1.2.1.2: "5.1.2.1.3 LEAKAGE AND INTERNAL CONVECTION. The effects of direct convective heating of internal structural members shall be evaluated for those TPS designs where leakage of hot boundary layer gases to the interior can take place." <u>Reason</u> : This possible mode of structural heating is not mentioned.
5.1.2.5	5-10	4(Last)	Delete, substitute: "The effects of trajectory dispersion shall be determined for all critical external aerodynamic heating areas. Laminar, transitional or turbulent flow shall be considered in accordance with the transition criteria employed for design." <u>Reason</u> : The term, "aero-dynamic-heating indicator" has not been defined. Use of the word "summation" is not clear. Flat plate heating rates are not always adequate indicators of dispersion effects because of response to angle of attack, side slip, and transition different from that of the vehicle configuration. Laminar, transition, turbulent condition needs to be stated.
5.2.10	5-22	New	Add, following Section 5.2.10.2.6: "5.2.10.3 HEAT TRANSFER" "Analysis of aerodynamic heat transfer (cooling), radiation cooling, and structural transient temperatures shall be continued through atmospheric flight that follows reentry or other flight where there has been significant structural heating until such time as can be shown that no thermal contribution to critical design conditions or material degradation can occur" <u>Reason</u> : Critical temperature conditions may occur long after peak heating due to soak - through of stored heat. Critical thermal stress conditions may arise from rapid cooling of outer surfaces while internal structure is still hot.
5.2.11	5-24	New	Add, following Section 5.2.11.2: "5.2.11.3 HEAT TRANSFER" "Analysis of radiant and convective cooling and transient temperatures of the structure shall be continued through and after landing following reentry or other flight where there has been significant structural heating until such time as can be shown that no thermal contribution to

<u>Section</u>	<u>Page</u>	<u>Para</u>	<u>Action</u>
5.2.11	(Continued)		critical design conditions or material degradation can occur. The analysis shall include the effects of the ground cooling system where required" <u>Reason:</u> Critical temperature conditions for some structural components may occur after landing due to soak-through of stored heat. Ground cooling and an analysis thereof may be required.
7.6.6.1 and 7.6.6.2	7-10	All	Combine: <u>Reason:</u> Joints are part of structure and should be covered in 7.6.6.1.
7.6.6.6	7-11	Second	<u>Action:</u> Delete the present paragraph, replacing with: "Frequently tests cannot be performed in completely simulated flight environment. Heating levels which occur as transients in flight can often be produced only as steady state conditions in ground test facilities. For metallic and other inert material TPS, it may be necessary to demonstrate performance at maximum temperature in one test and performance at maximum temperature gradients in a different test. For ablators the additional factors of aerodynamic shear, gas composition, and boundary layer character are important. Tests of ablator TPS usually only approximate the flight environment and must be used to verify analytical predictions rather than to directly demonstrate flight performance." <u>Reason:</u> Greater clarity in recognizing the importance of differing factors as a function of the type of TPS used.
7.6.6.7	7-11	1	After "heating" add "vibration, noise and pressure." <u>Reason:</u> Insulation is potentially degraded by environmental effects other than heating.

APPENDIX H

CONVERSION OF U.S. CUSTOMARY UNITS TO SI UNITS

U.S. CUSTOMARY UNIT	CONVERSION FACTOR*	SI UNIT
foot	0.3048	meter
Reynolds number/foot	3.2808	Reynolds number/meter
inch	0.0254	meter
pound force	4.448	Newton
pounds force/foot ²	47.8803	Newton/meter ²
pounds force/inch ²	6894.757	Newton/meter ²
pound force-second/foot ²	47.8803	Newton second/meter ²
mile (nautical)	1853.25	meter
feet/second	0.3048	meter/second
feet ² /second	0.0929	meter ² /second
°Rankine (°R)	0.5556	°Kelvin (°K)
°Fahrenheit (°F)	°K=(5/9)(°F+459.67)	°Kelvin
British Thermal Unit (btu)	1054.3503	joule
btu/foot ² -second	11348.9310	watts/meter ²
btu/foot ² -second-°R	20428.0658	watts/meter ² -°K
btu/foot ² -second-°R	20428.0658	joules/meter ² -second-°K
btu/pound mass-°R	860.7871	joules/kilogram-°K
btu/pound mass	478.2533	joules/kilogram
pound mass	0.4536	kilogram
pounds mass/foot ³	16.0185	kilogram/meter ³

* Multiply value given in U.S. customary unit by conversion factor to obtain equivalent value in SI unit.

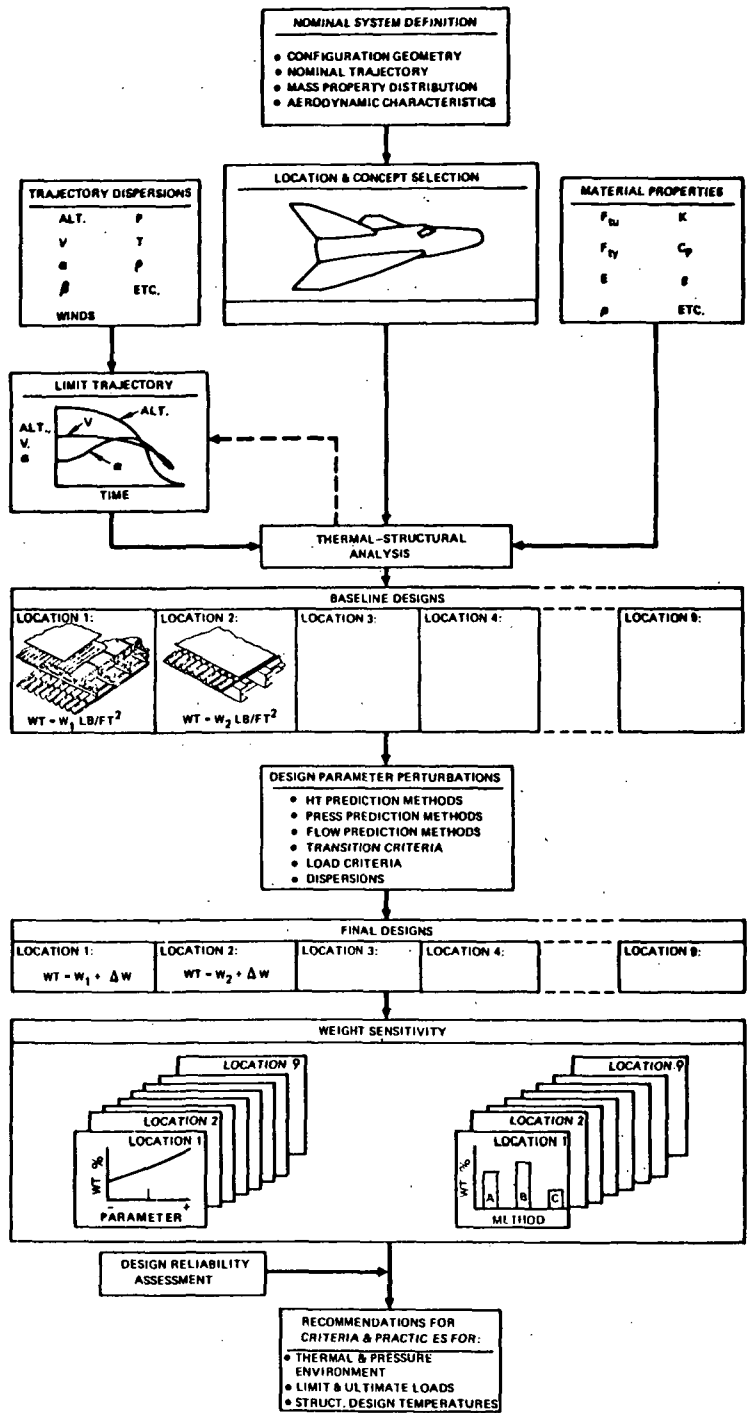
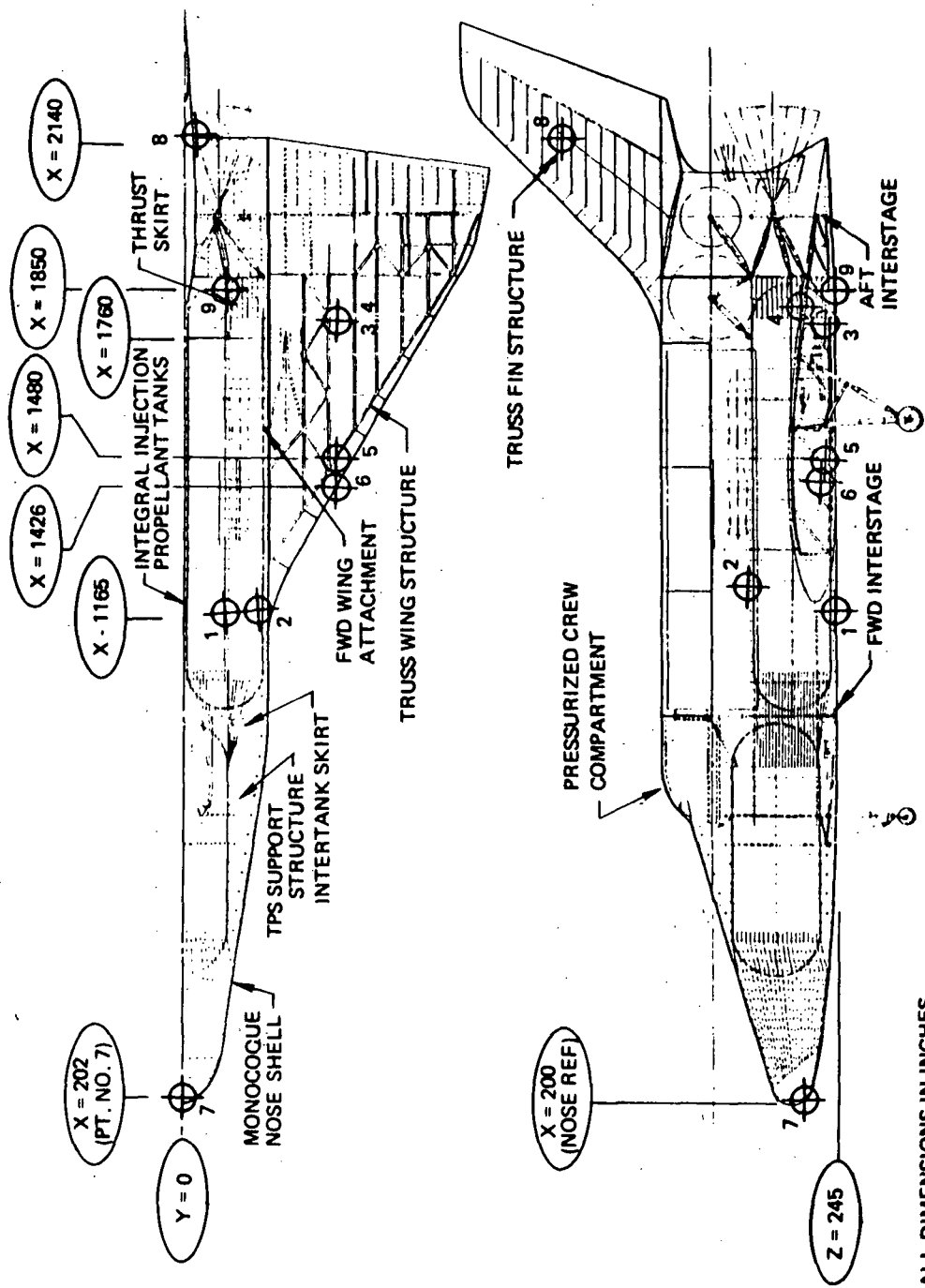


Figure 1. STUDY APPROACH



ALL DIMENSIONS IN INCHES

Figure 2. POINTS SELECTED FOR ANALYSES

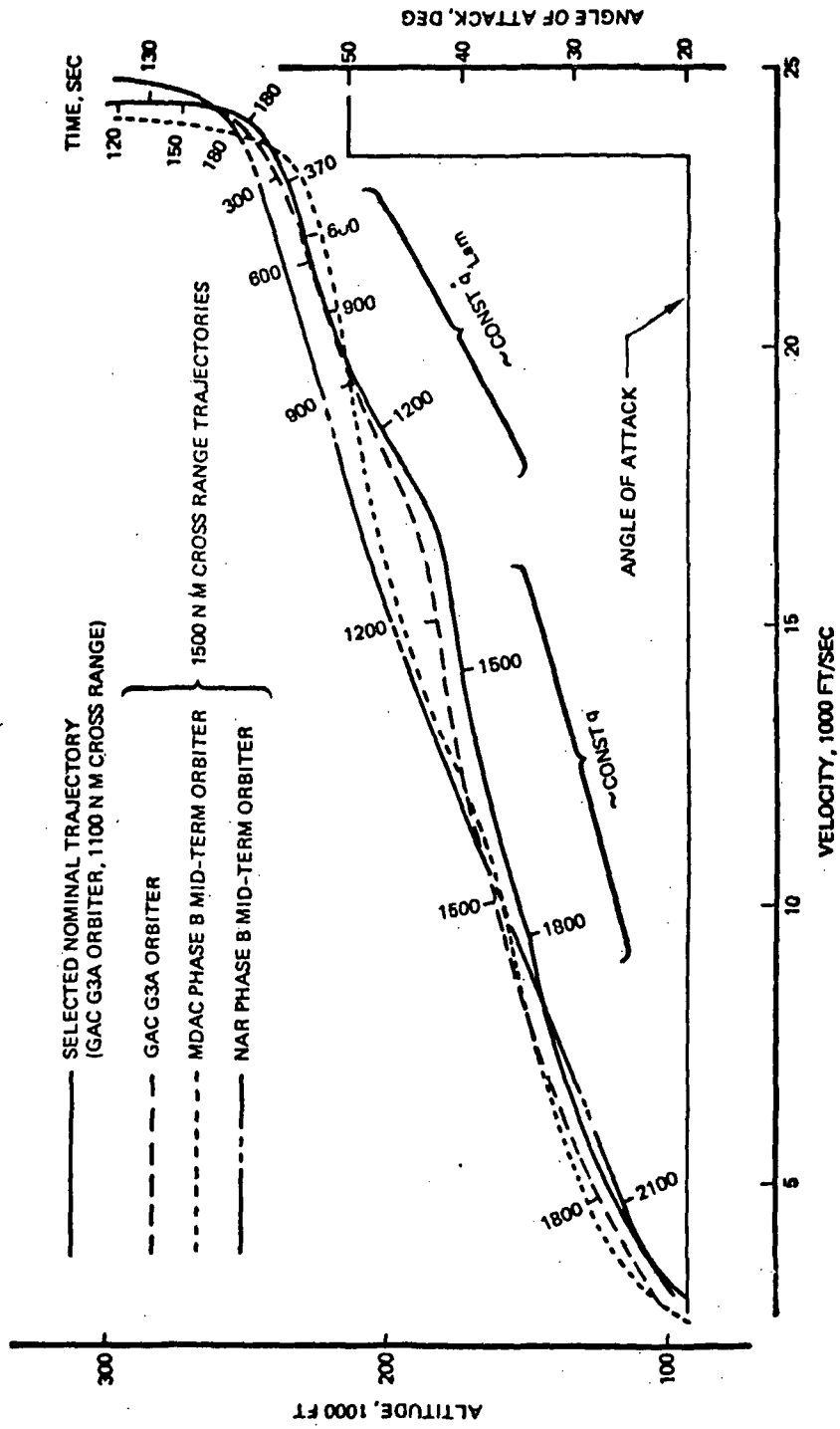


Figure 3: SELECTED NOMINAL REENTRY TRAJECTORY

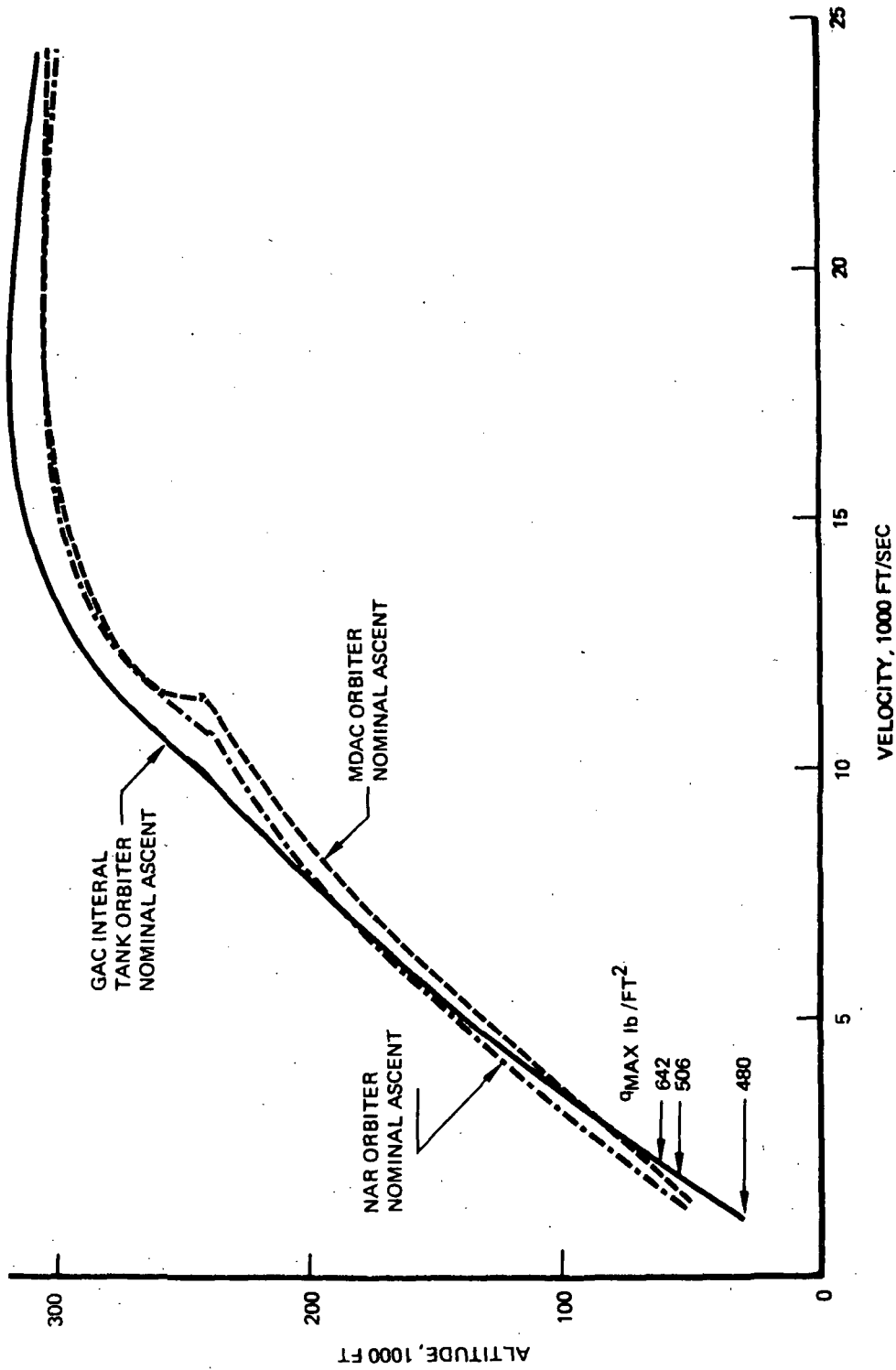


Figure 4: SELECTED NOMINAL ASCENT TRAJECTORY

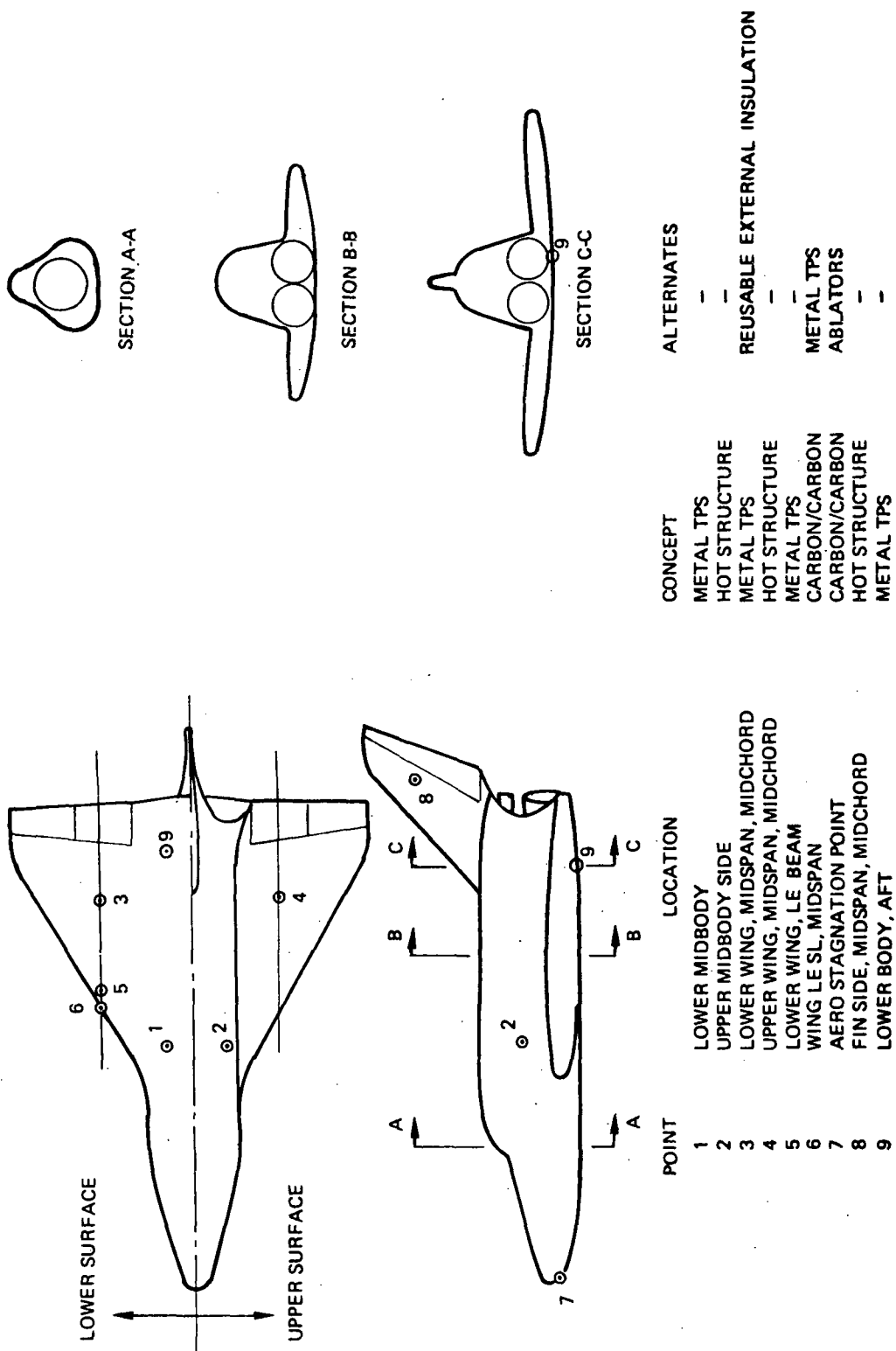


Figure 5: STUDY CONFIGURATION, POINT LOCATIONS, AND CONCEPTS

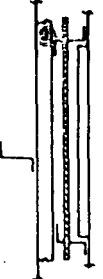
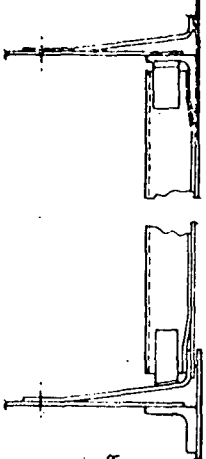
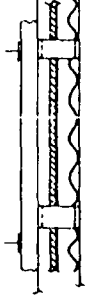
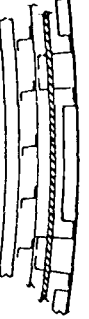
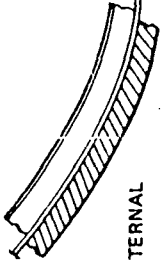
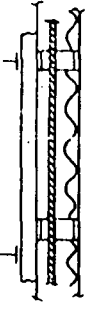
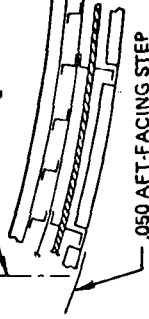
LOCATION	CONCEPT	
	SECTION NORMAL TO ORBITER CL	LONGITUDINAL SECTION
POINT 1 - LOWER MID-BODY		
POINT 2 - UPPER MID-BODY		
POINT 3 - LOWER WING, MID-SEMI-SPAN, MID-CHORD	<p>(1) PRIMARY (METAL TPS)</p> 	
POINT 4 - UPPER WING, MID-SEMI-SPAN, MID-CHORD	<p>(2) ALTERNATE (REUSABLE EXTERNAL INSULATION)</p> 	
POINT 5 - LOWER WING, MID-SEMI-SPAN, L. E. BEAM		

Figure 6. BASELINE DESIGN SECTIONS

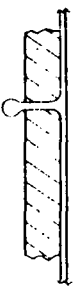
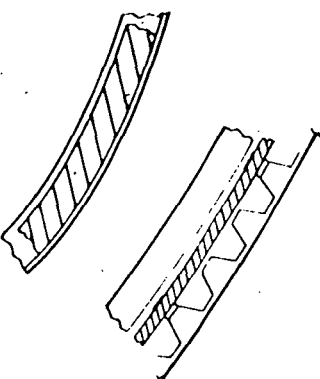
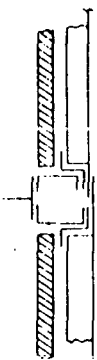
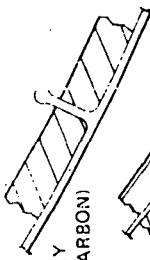
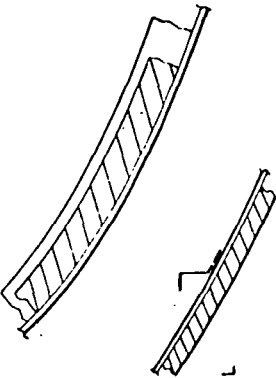
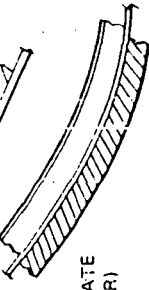
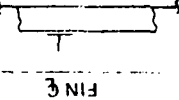
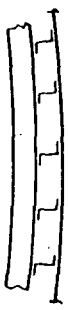
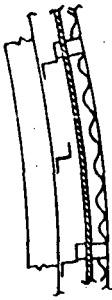
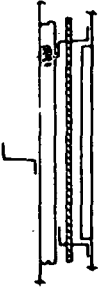
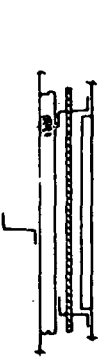
LOCATION	CONCEPT	
	SECTION NORMAL TO ORBITER CL	LONGITUDINAL SECTION
POINT 6 - WING LEADING EDGE STAGNATION LINE MID-SEMI-SPAN	(1) PRIMARY (CARBON/CARBON) 	 INSULATION INTEGRAL SKIN & RIBS RIB INSUL TPS
	(2) ALTERNATE (METAL TPS) 	
POINT 7 - NOSE AERODYNAMIC STAGNATION POINT	(1) PRIMARY (CARBON/CARBON) 	 INSULATION INTEGRAL SKIN AND RIBS FRAME HONEYCOMB PANEL ABLATOR
	(2) ALTERNATE (ABLATOR) 	
POINT 8 - FIN SIDE, MID-SPAN, MID-CHORD		 RIB STIFF SKIN
		
POINT 9 - LOWER AFT-BODY		 FRAME TANK SKIRT, INSULATION TPS (METAL)

Figure 6: BASELINE DESIGN SECTIONS (CONT.)

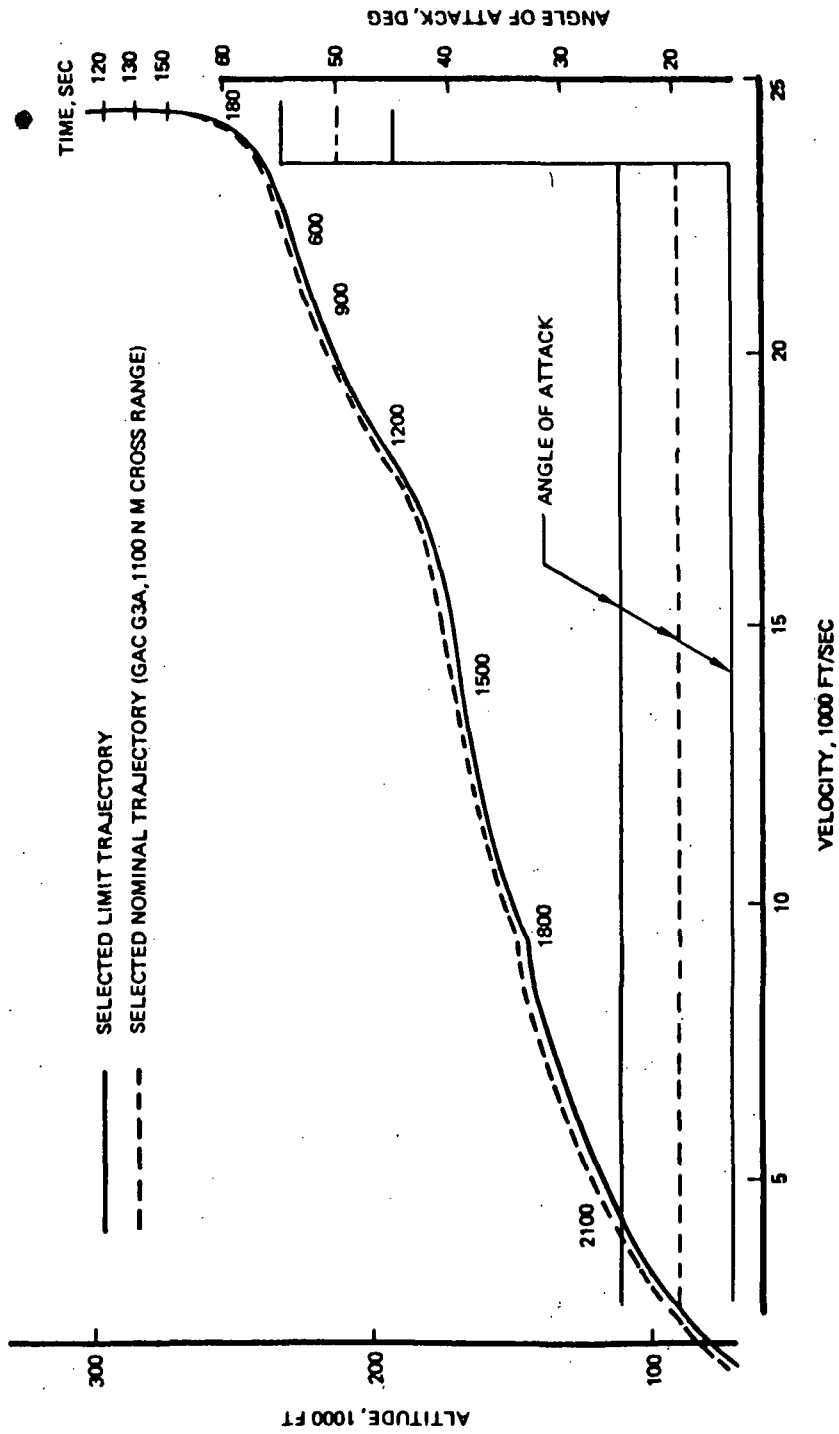


Figure 7: LIMIT REENTRY TRAJECTORY PARAMETERS

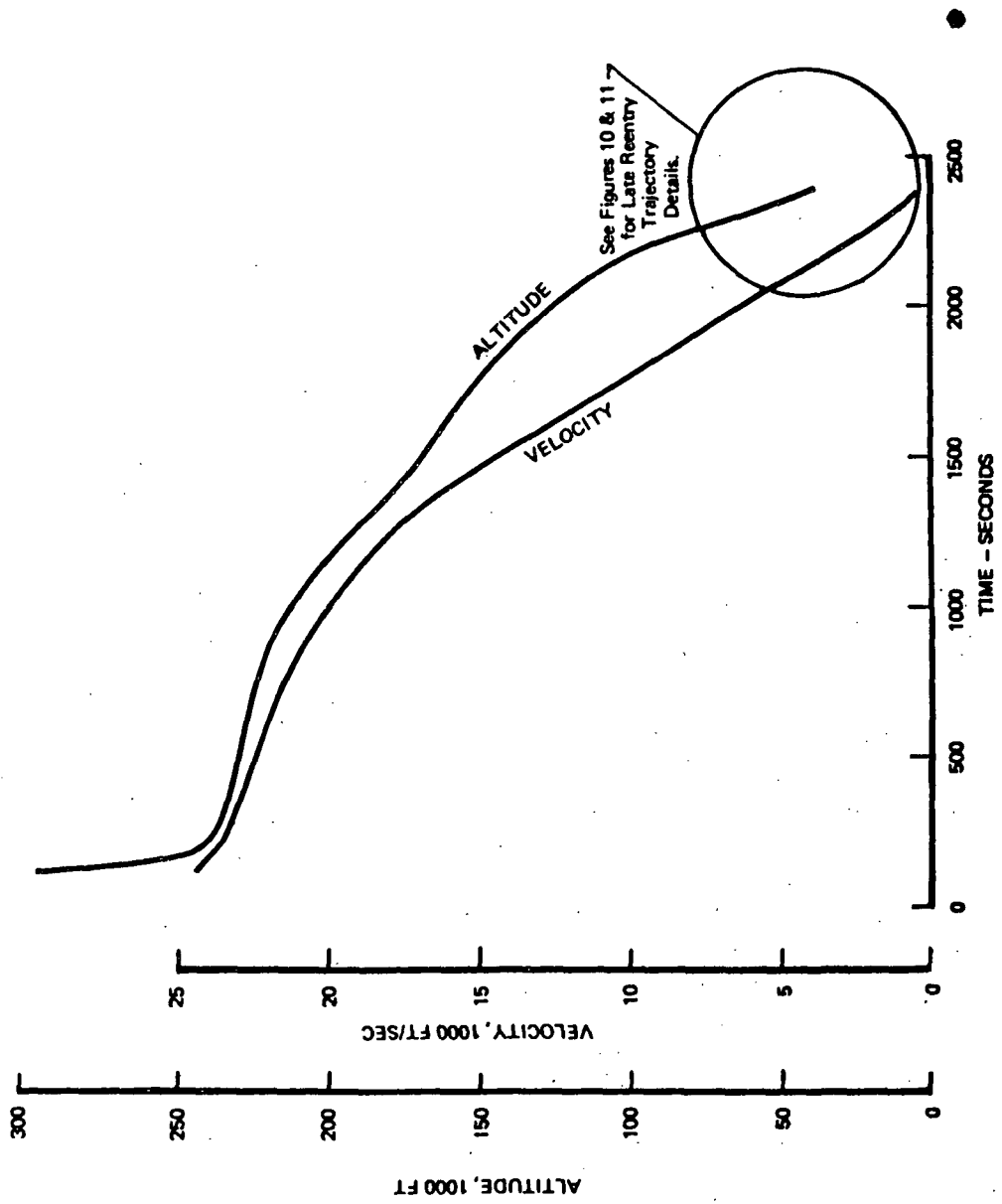


Figure 8: LIMIT REENTRY TRAJECTORY

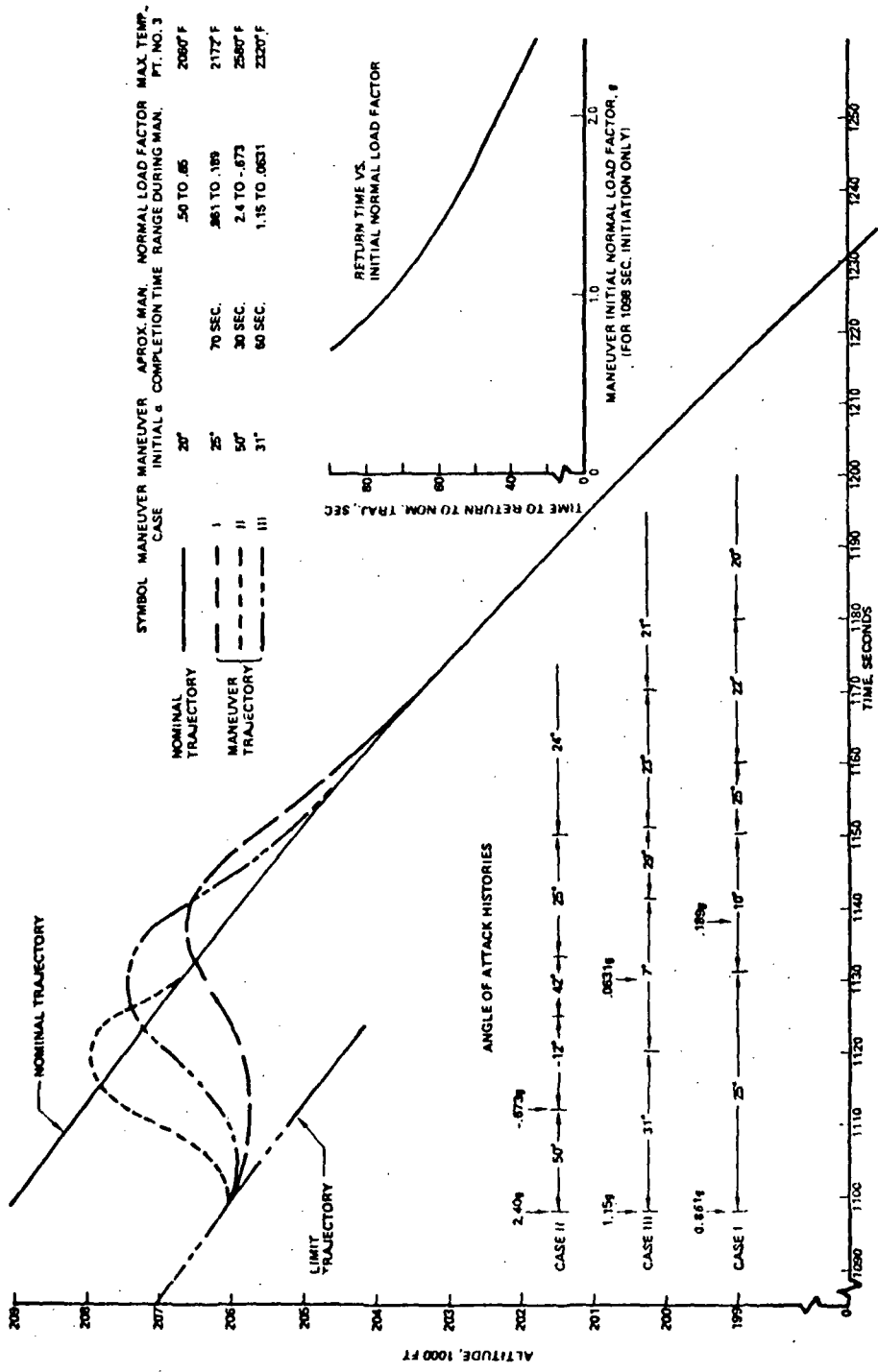


Figure 9. MANUEVER EXCURSION TRAJECTORIES

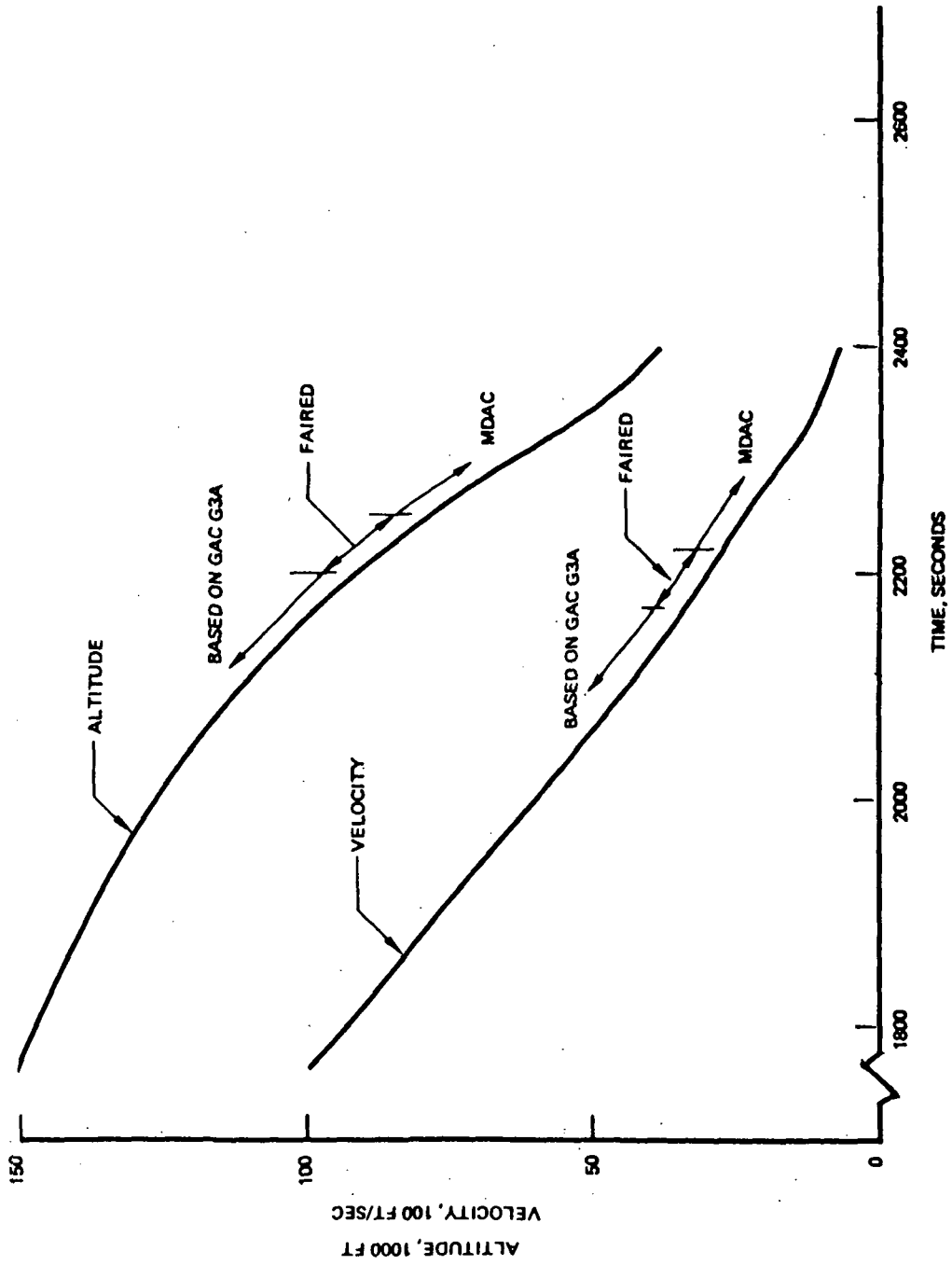


Figure 10. LATE REENTRY & TRANSITION TRAJECTORY

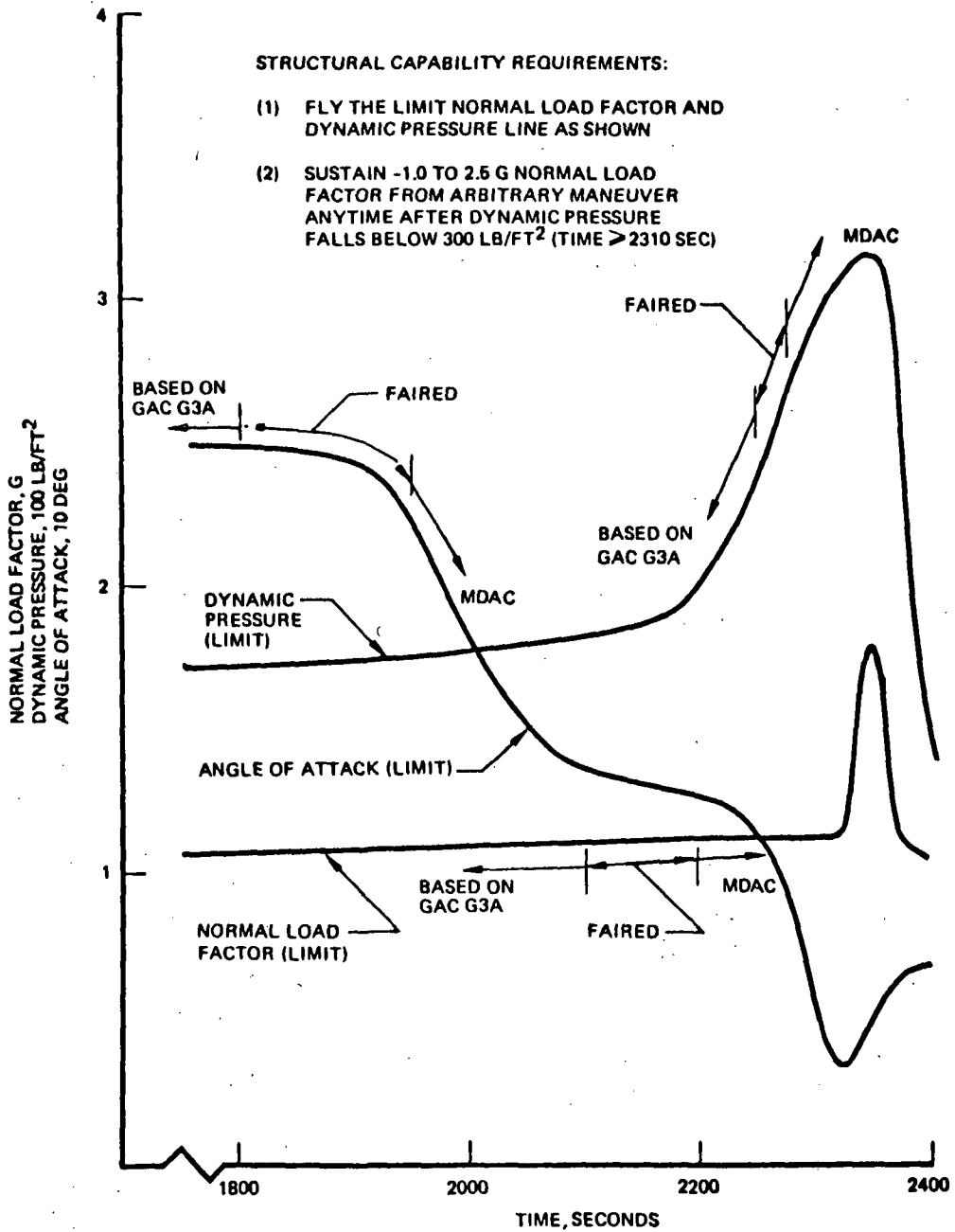
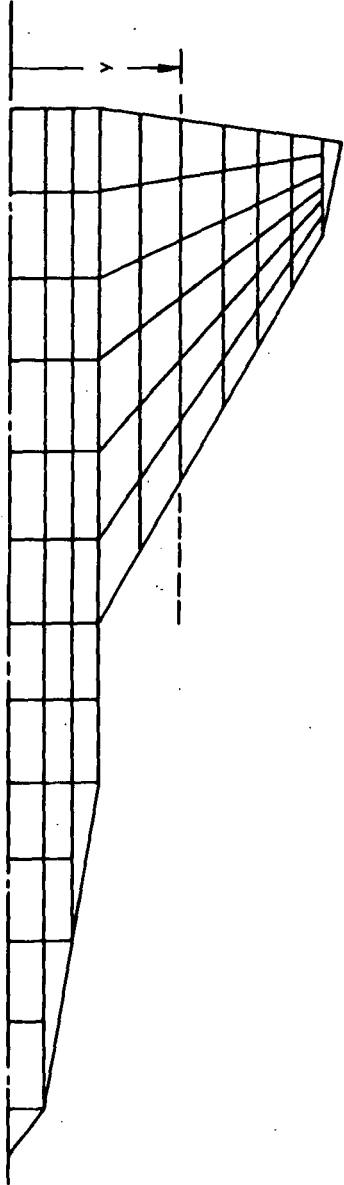


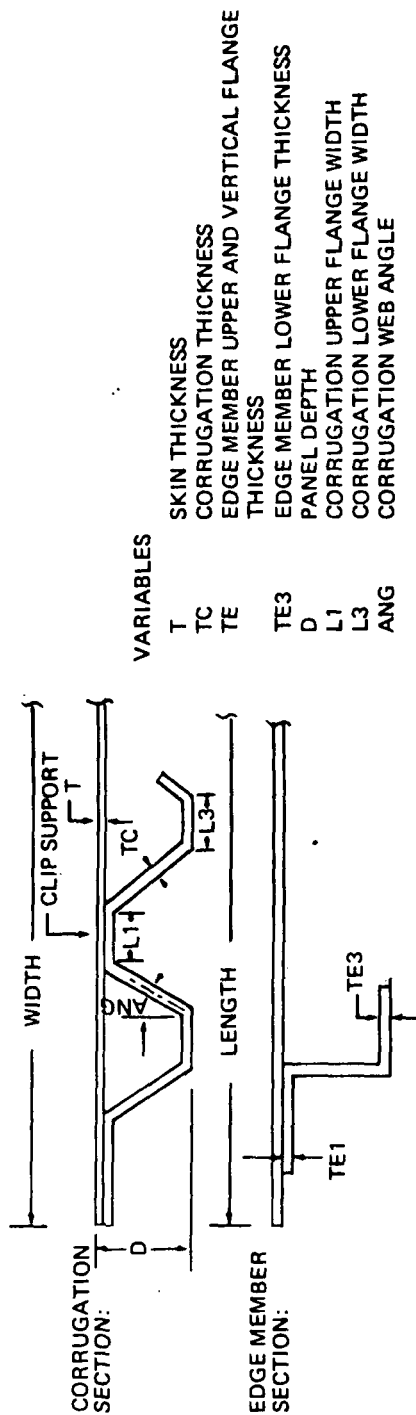
Figure 11: LATE REENTRY & TRANSITION TRAJECTORY PARAMETERS



LOAD (SHEAR, MOMENT, OR TORSION) AT ANY SECTION, y , EQUALS SUMMATION OF CONTRIBUTION OF AIRLOADS PLUS SUMMATION OF CONTRIBUTION OF INERTIAL LOADS ACTING ON INDIVIDUAL PANELS SHOWN

SIMILAR APPROACH FOR LATERAL LOADS USES SIDE VIEW PANEL GRID

**Figure 12: ENTRY LOADS ANALYSIS TYPICAL PANEL GRID
(FOR VERTICAL LOADS)**



INPUT	CONSTRAINTS	OUTPUT
PANEL CONFIGURATION	DEFLECTIONS	MIN WEIGHT CONFIGURATION
LENGTH	OVERALL PANEL	DIMENSIONS OF VARIABLES
WIDTH	LOCAL MEMBER	PANEL WEIGHT
LIMITS FOR VARIABLES		PANEL STRUCTURAL ANALYSIS
MATERIAL PROPERTIES	STRESSES	SECTION PROPERTIES
COEFFICIENT OF EXPANSION	ULTIMATE	STRESSES
MODULUS OF ELASTICITY	YIELD	DEFLECTIONS
ALLOWABLE STRESSES	BUCKLING	
	CREEP	
DESIGN CONDITIONS		
PRESSURE		
TEMPERATURE DISTRIBUTION		

Figure 13: TPS PANEL OPTIMIZATION
 BOEING COMPUTER PROGRAM - OPTIMIZATION BY RANDOM SEARCH (OPTRAN)

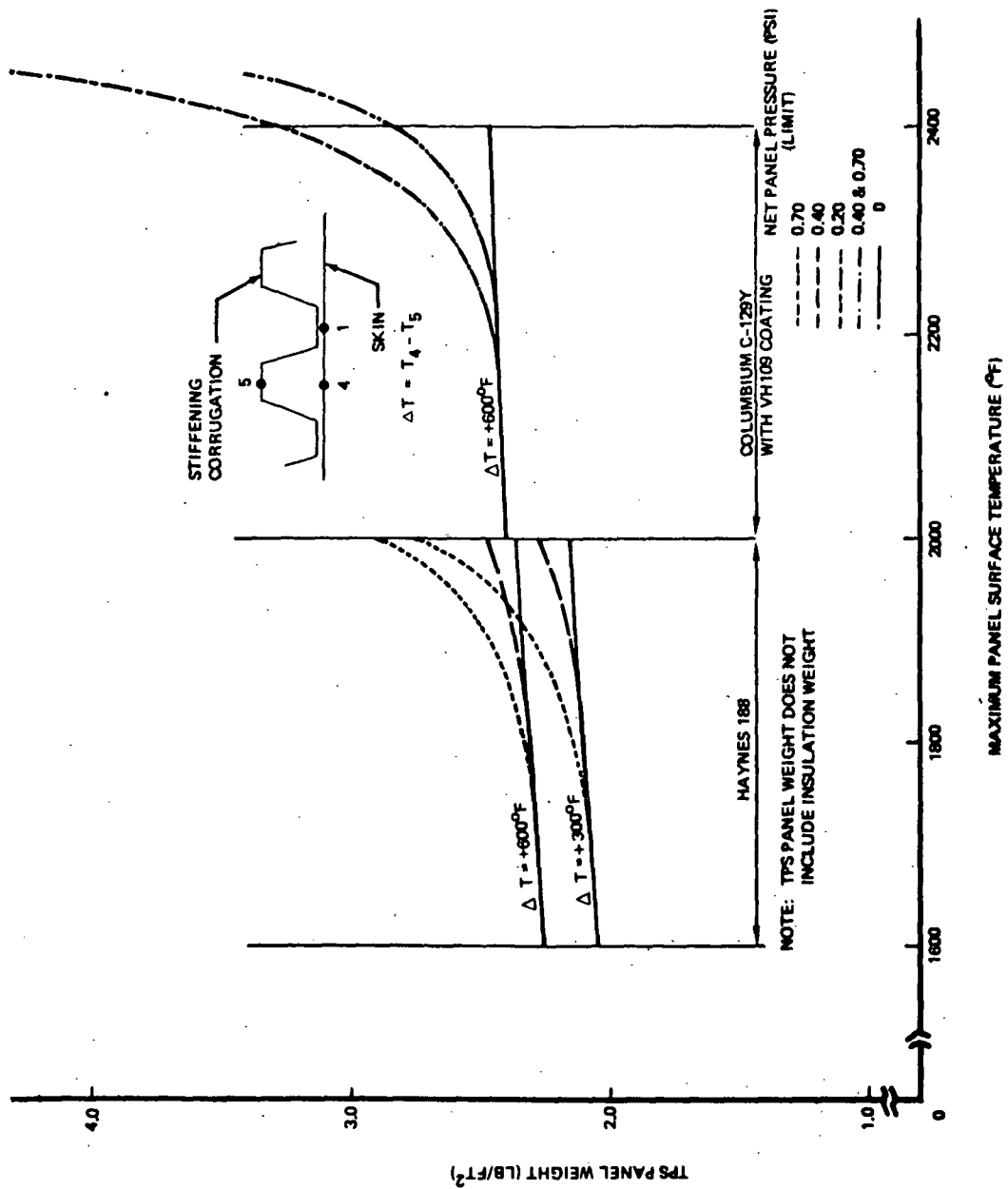


Figure 14. METAL TPS PANEL PARAMETRIC WEIGHTS

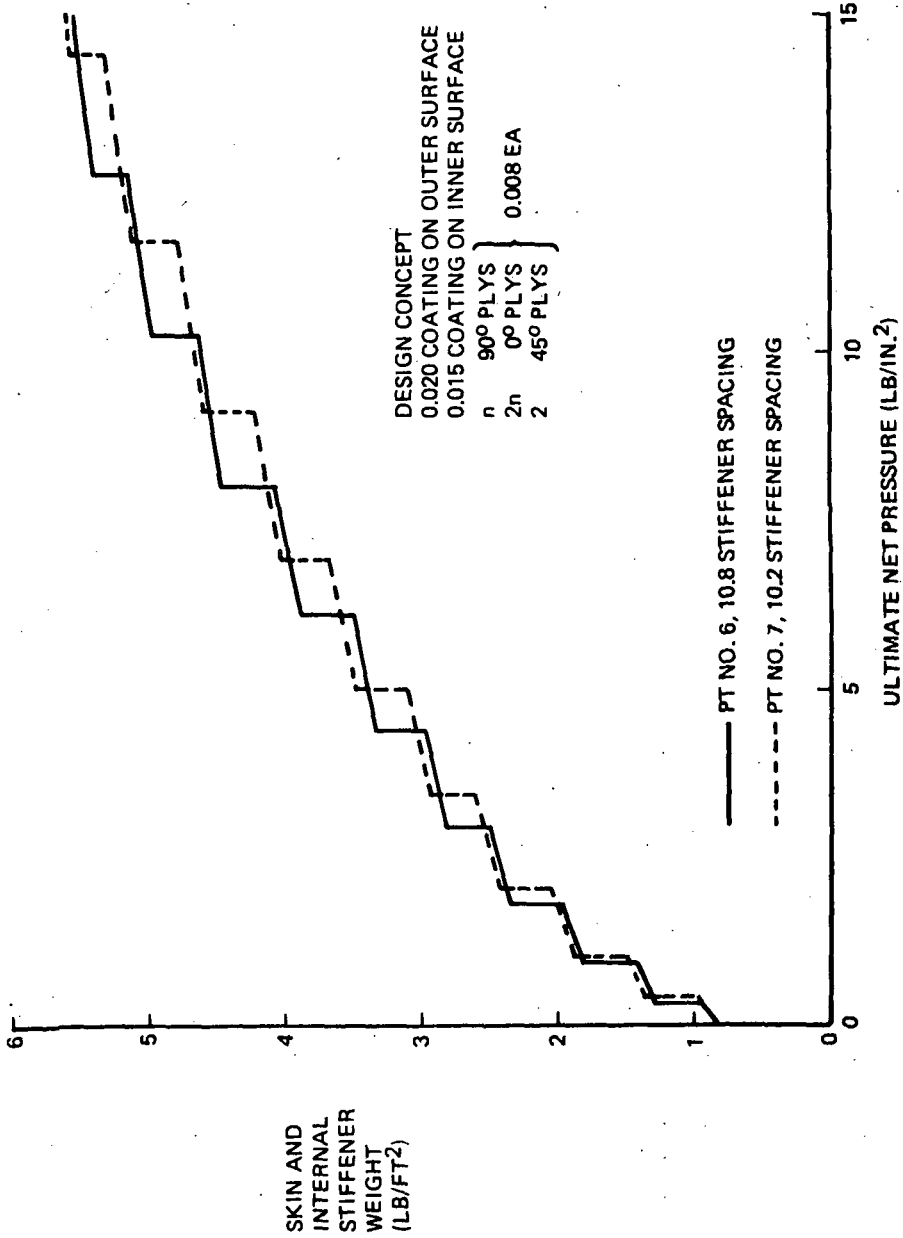


Figure 15. CARBON / CARBON COMPOSITE PARAMETRIC WEIGHTS

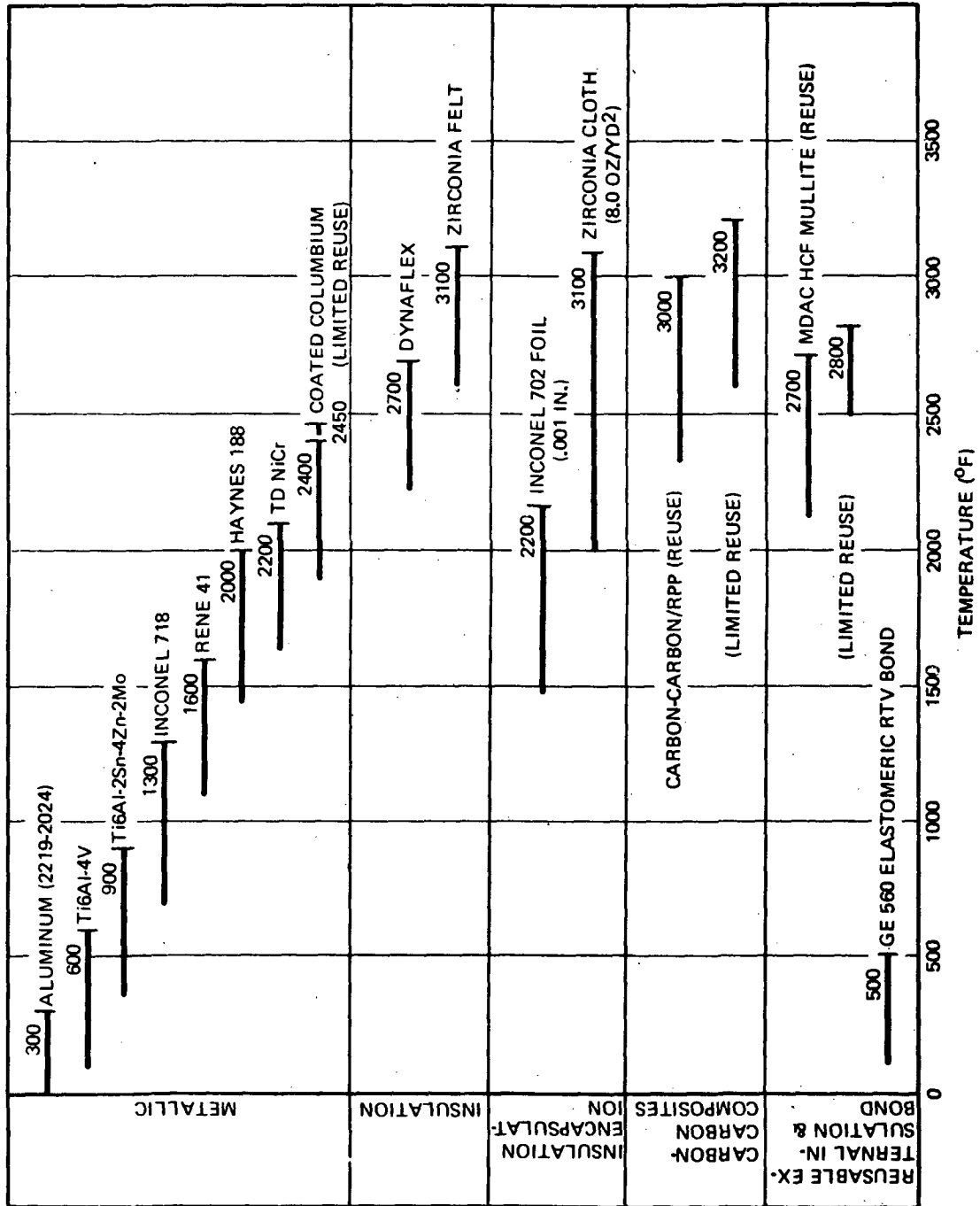


Figure 16. TEMPERATURE USE RANGES CANDIDATE MATERIALS FOR SPACE SHUTTLE ORBITER DESIGN

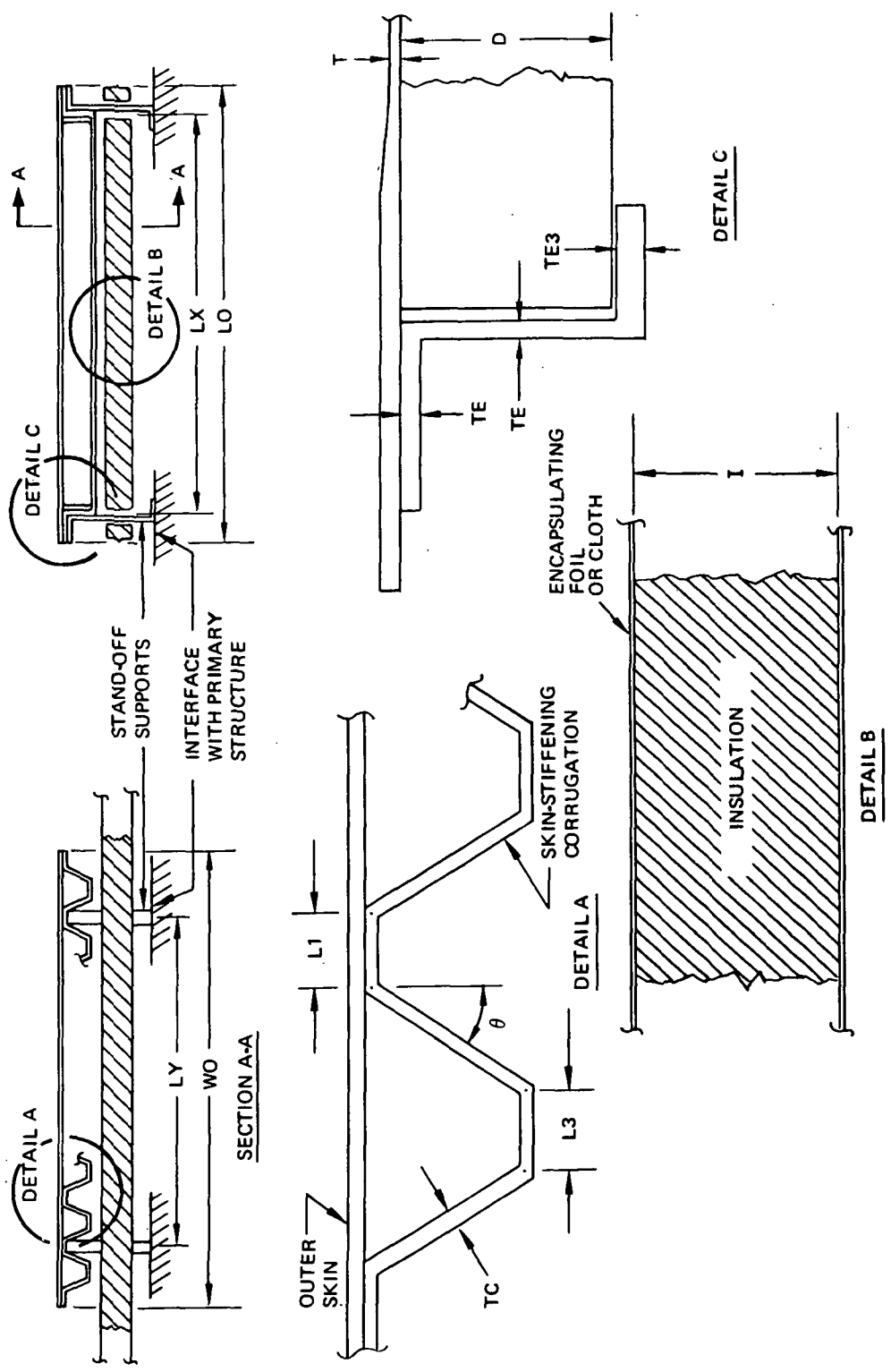
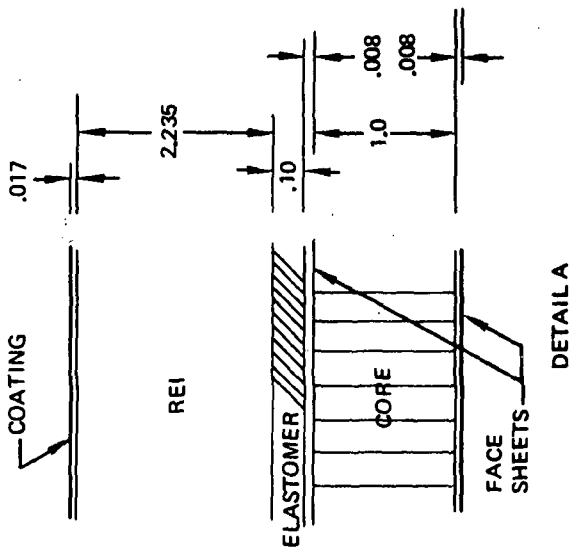
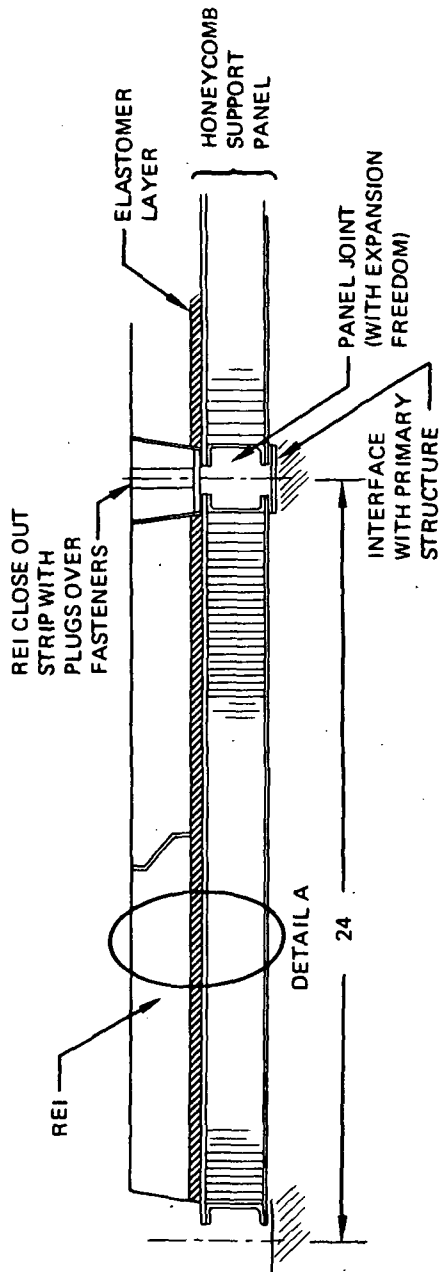


Figure 17. BASELINE DESIGNS-METALLIC TPS

POINT NO.	PRIMARY STRUCTURE	LIMIT DESIGN ΔP (LB/IN ²)	OUTER SKIN T _{MAX} (°F)	PRIMARY TPS PANEL MATERIAL	INSULATION MATERIAL	INSULATION ENCAPSULATION	WEIGHTS, LB/FT ²			
							PANEL W/O INSULATION	INSULATION	INSULATION	TOTAL TPS PANEL
1	ALUMINUM	.4	2211	C129Y	DYNAFLEX (6.0 LB/FT ³)	INCONEL 702 FOIL (.001 IN.)	2.46	1.97	.137	4.57
3	TITANIUM	.4	2296	C129Y	DYNAFLEX (6.0 LB/FT ³)	ZIRCONIA CLOTH (8.0 OZ/YD ²)	2.62	1.81	.175	4.61
5	TITANIUM	.4	2392	C129Y	DYNAFLEX (6.0 LB/FT ³)	ZIRCONIA CLOTH	3.19	1.91	.175	5.28
6A	TITANIUM	.4	2391	C129Y	DYNAFLEX (6.0 LB/FT ³)	ZIRCONIA CLOTH	3.19	1.46	.175	5.83
9	ALUMINUM	.4	2263	C129Y	DYNAFLEX (6.0 LB/FT ³)	INCONEL 702 FOIL	2.54	2.12	.137	4.80

POINT NO.	DIMENSIONS IN INCHES EXCEPT WHERE NOTED												
	T	TC	TE	TE3	L1	L3	D	θ	LX	LY	LO	WO	I
1	.010	.009	.013	.036	.66	.33	.56	23°	9.0	10.6	12.4	16.5	3.94
3	.011	.010	.013	.033	.71	.50	.76	16°	9.0	10.6	12.4	16.5	3.62
5	.013	.010	.017	.038	1.19	.54	1.43	3°	9.0	10.6	12.4	16.5	3.82
6A	.013	.010	.017	.038	1.19	.54	1.43	3°	9.0	10.6	12.4	16.5	2.92
9	.011	.010	.013	.034	.80	.43	.66	18°	9.0	10.6	12.4	16.5	4.24

Figure 17: BASELINE DESIGNS—METALLIC TPS (Cont)

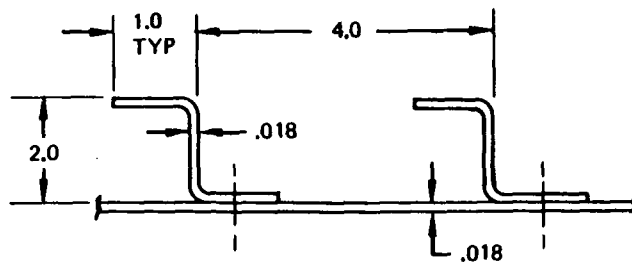


POINT NO. 3A

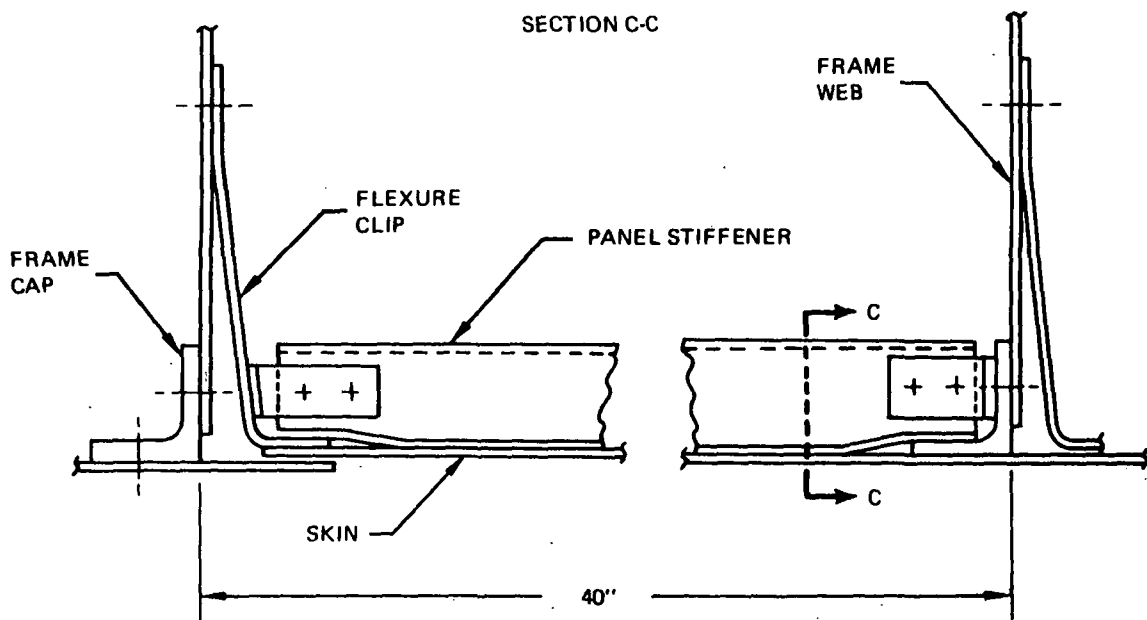
COMPONENT	MATERIAL	DENSITY	WEIGHT
		LB/FT ³	LB/FT ²
COATING	M25A7		.253
REI	MDAC MULLITE	15.0	2.795
ELASTOMER	GE 560	88.6	.739
FACE SHEETS (2)	TITANIUM	276	.618
CORE	TITANIUM	3.0	
TOTAL			4.405

Figure 18. BASELINE DESIGN-REUSABLE EXTERNAL INSULATION

POINT NO. 2



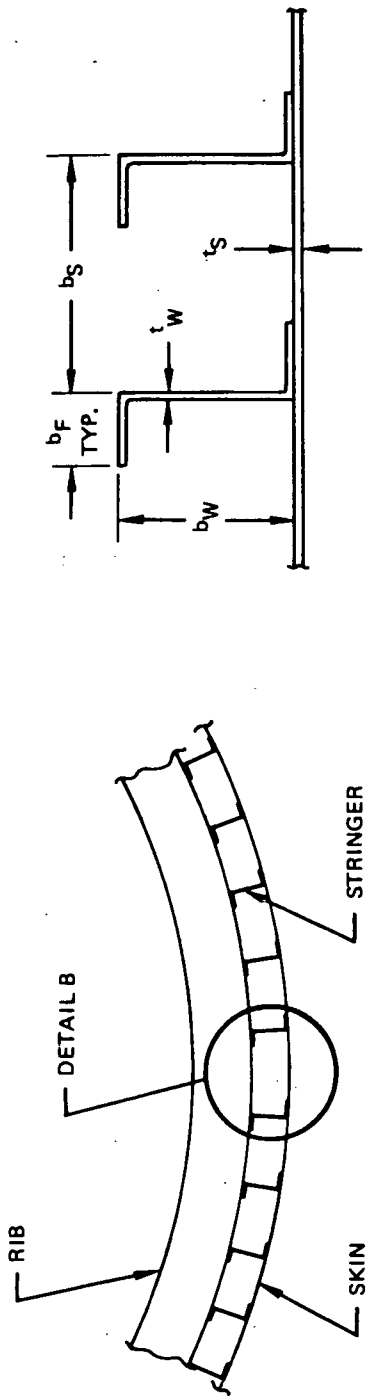
SECTION C-C



NOTES:

1. PANEL SKIN AND STIFFENER MATERIAL-INCONEL 718
2. PANEL WEIGHT = 1.53 LB/FT² (FRAME WEIGHT NOT INCLUDED)

Figure 19: BASELINE DESIGNS – HOT STRUCTURE



POINT NO.	STRUCTURE MATERIAL	STRUCTURE WEIGHT (DOES NOT INCLUDE RIBS) (LB/FT ²)	DIMENSIONS (IN.)					
			RIB SPACING	t_S	t_W	b_S	b_W	b_F
4	INCONEL 718	3.21	24.0	.0302	.0325	.764	.664	.199
8	INCONEL 718	2.60	24.0	.0244	.0264	.798	.694	.208

Figure 19. BASELINE DESIGNS – HOT STRUCTURE (Cont)

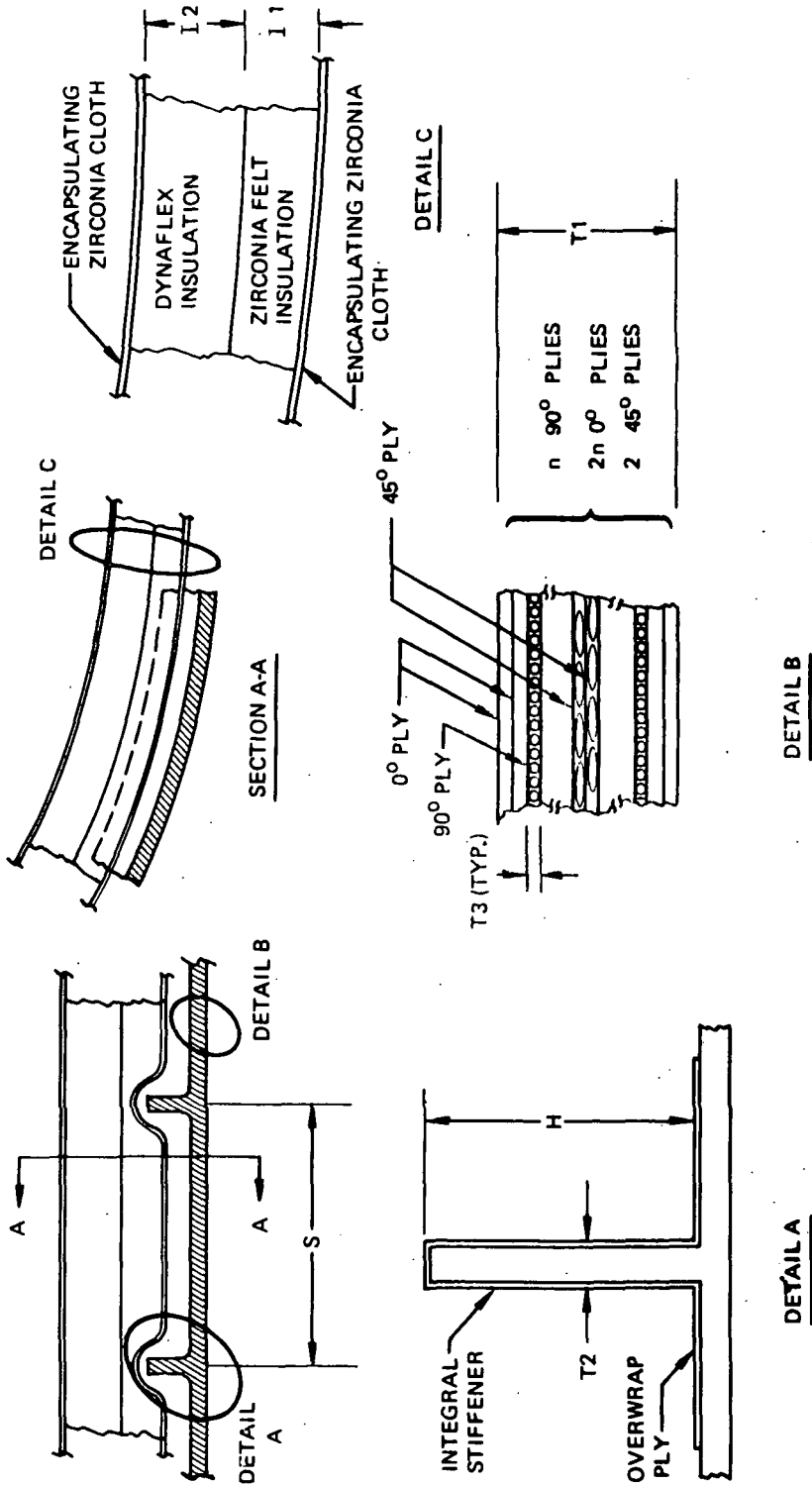


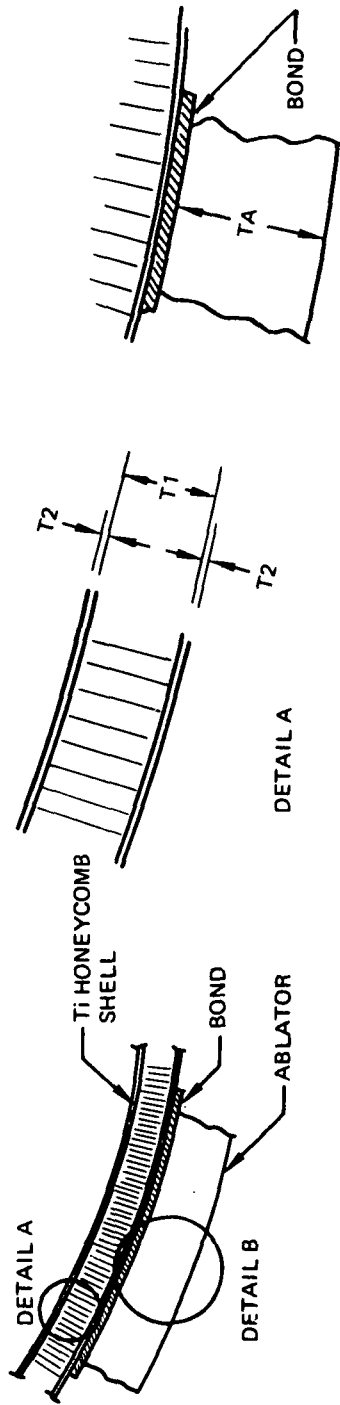
Figure 20. BASELINE DESIGNS - CARBON/CARBON COMPOSITE

POINT NO.	PRIMARY STRUCT (MAX. ALLOWABLE TEMP.)	OUTER SURFACE T _{MAX} (°F)	LIMIT DESIGN STRESS (LB/IN ²)	SHELL MATERIAL	C/C SHELL WT (W/OUT INS.) (LB)	OUTER INSULATION	INNER INSULATION	INSULATION ENCAPSULATION	TOTAL DESIGN WT (INCL. INS.) (LB)
6	TITANIUM (600°F)	2990	2.08	OXIDATION PROTECTED (SILICONIZED) REINFORCED CARBON	2.85*	ZIRCONIA FELT (10 LB/FT ³)	DYNAFLEX (6 LB/FT ²)	ZIRCONIA CLOTH (8.0 OZ/YD ²)	5.12
7	TITANIUM (600°F)	2700	2.27		2.95*	NONE	DYNAFLEX (6 LB/FT ²)	ZIRCONIA CLOTH (8.0 OZ/YD ²)	4.83

POINT NO.	DIMENSIONS (IN.)							SPAN BETWEEN MAJOR FRAMES (NOT SHOWN)	
	T1	T2	T3	H	n	I1	I2		S
6	.208	.264	.008	2.64	8	.50	3.35	10.8	24
7	.208	.270	.008	2.70	8	0	3.41	10.2	24

* — INCLUDES .020 IN. COATING ON OUTER SURFACE, .015 COATING ON INNER SURFACE

Figure 20: BASELINE DESIGNS — CARBON/CARBON COMPOSITE (Cont)



DETAIL B

POINT NO.	NOSE SHELL MATERIAL	LIMIT DESIGN ΔP (LB/IN ²)	ABLATOR	SHELL WT (LB/FT ²)	BOND WT (LB/FT ²)	ABLATOR WEIGHT (LB/FT ²)	TOTAL WT (LB/FT ²)	DIMENSIONS (IN.)				
								T1	T2	CORE DENSITY (LB/FT ³)	TA	SPAN BETWEEN MAJOR FRAMES (NOT SHOWN)
7A	TI HONEYCOMB	2.27	NASA SILICONE IN PHENOLIC HONEYCOMB (15 LB/FT ³)	.518	.001	2.74	3.259	.60	.008	3.0	2.194	24
7B	TI HONEYCOMB	2.27	PHENOLIC NYLON WITH MICROBALLOONS (30 LB/FT ³)	.518	.001	5.06	5.569	.60	.008	3.0	2.025	24
7B1	TI HONEYCOMB	2.27	PHENOLIC NYLON (76 LB/FT ³)	.518	.001	8.57	9.089	.60	.008	3.0	1.356	24
7C	TI HONEYCOMB	2.27	APOLLO MATERIAL (34 LB/FT ³)	.518	.001	3.84	4.359	.60	.008	3.0	1.355	24

Figure 21: BASELINE DESIGNS—ABLATOR TPS

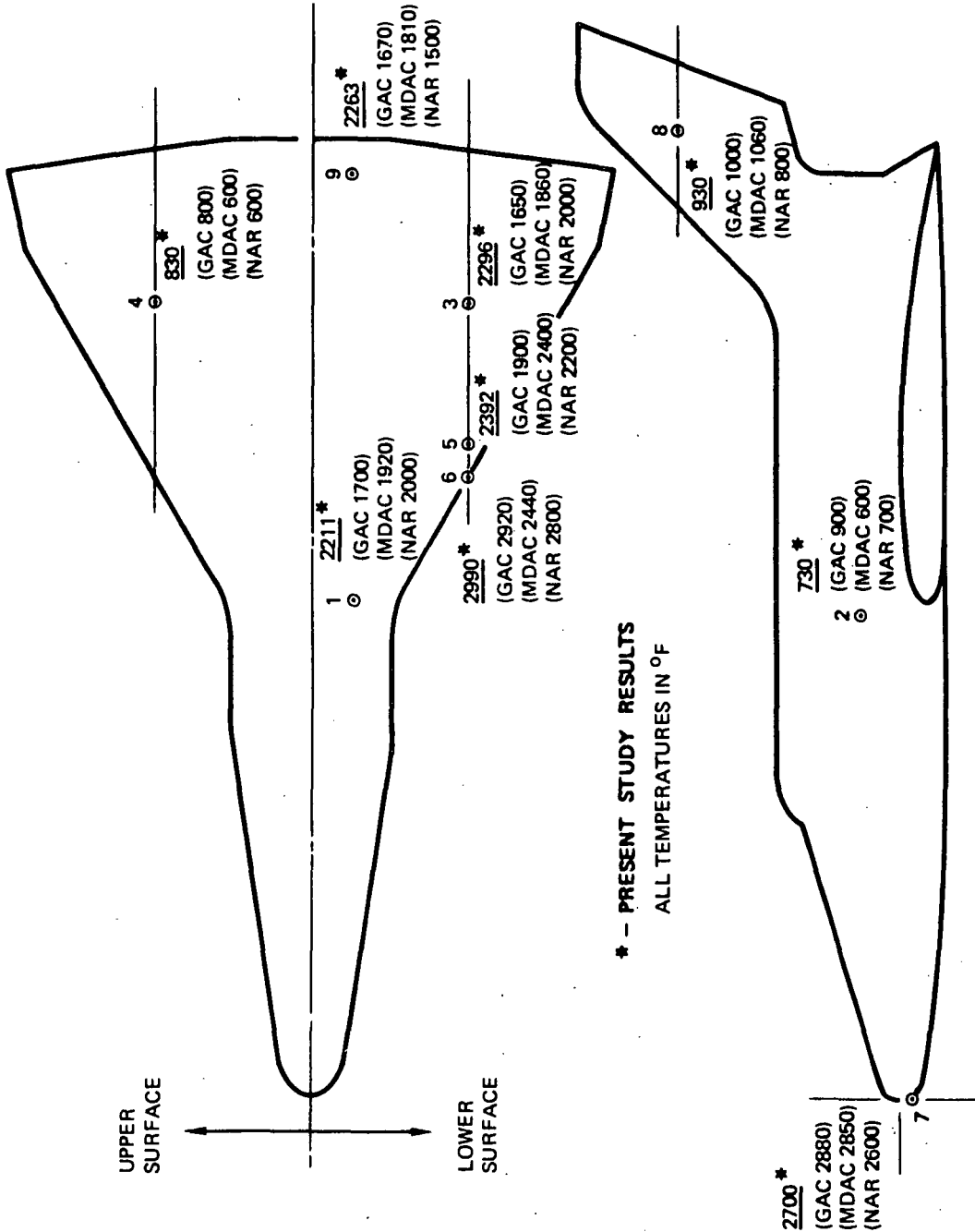


Figure 22. ORBITER MAXIMUM TEMPERATURES (BASELINE DESIGNS, PRIMARY CONCEPTS)

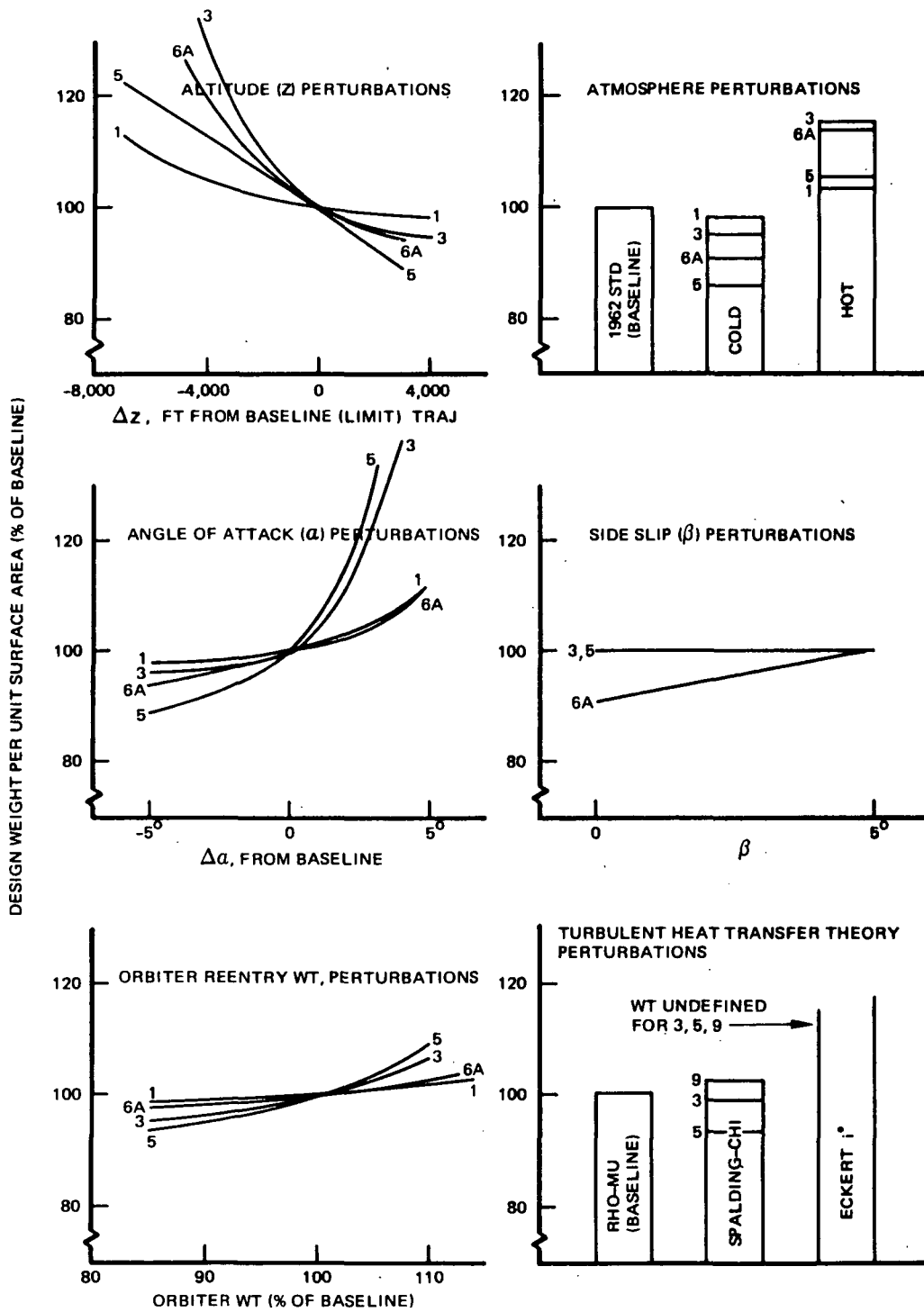


Figure 23: WEIGHT SENSITIVITY SUMMARY - METALLIC TPS POINTS

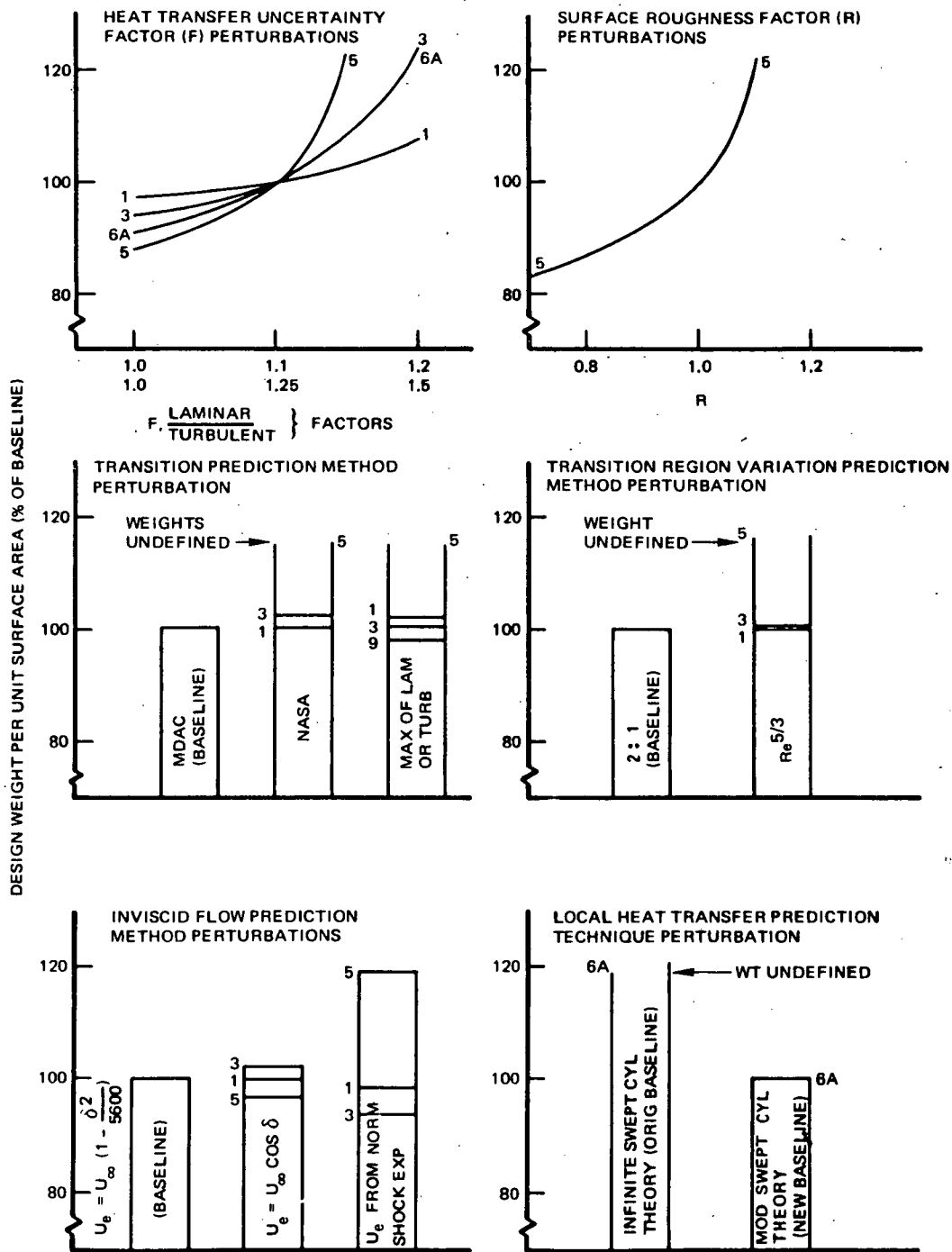


Figure 23. WEIGHT SENSITIVITY SUMMARY — METALLIC TPS POINTS (Cont)

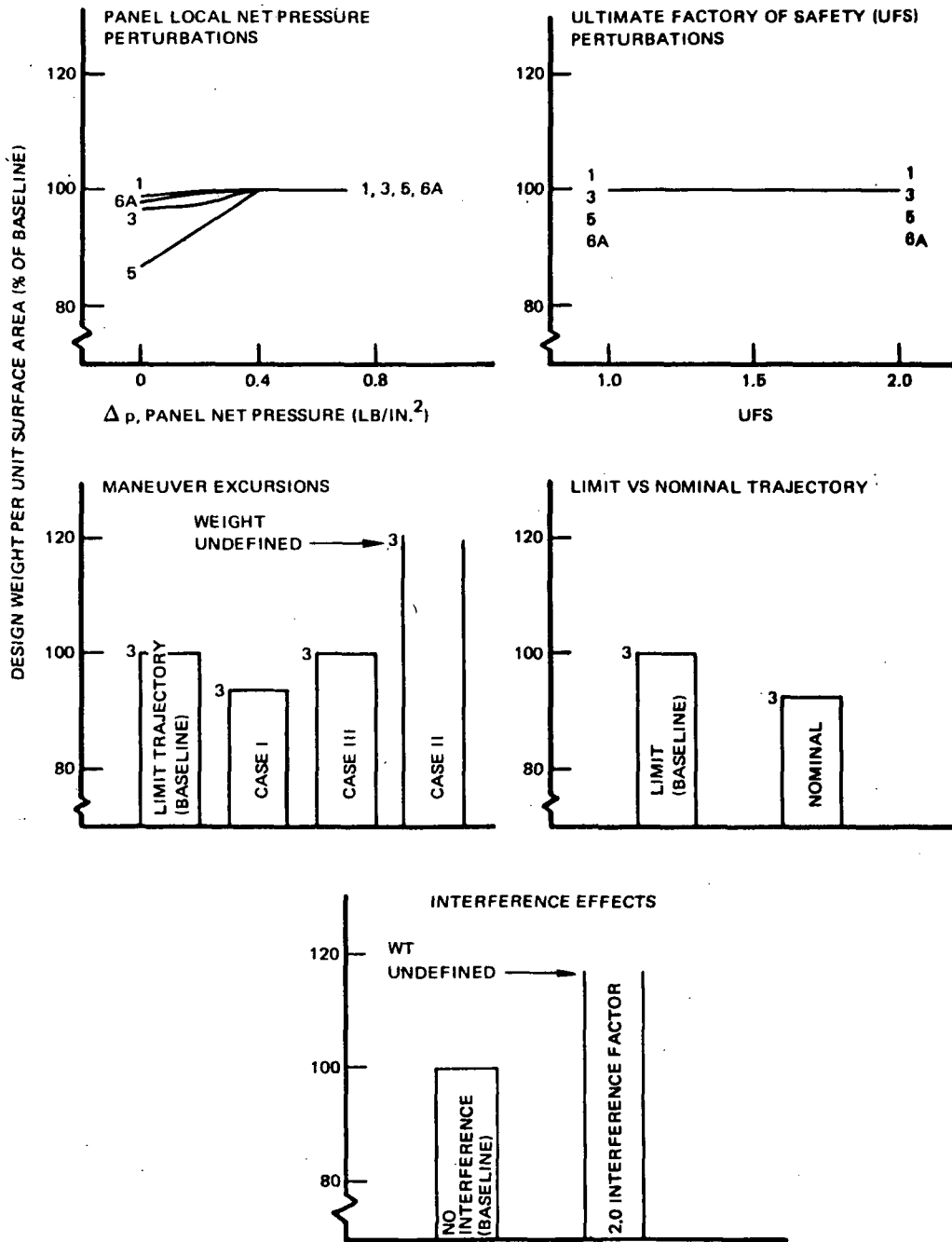


Figure 23: WEIGHT SENSIVITY SUMMARY – METALLIC TPS POINTS (Cont)

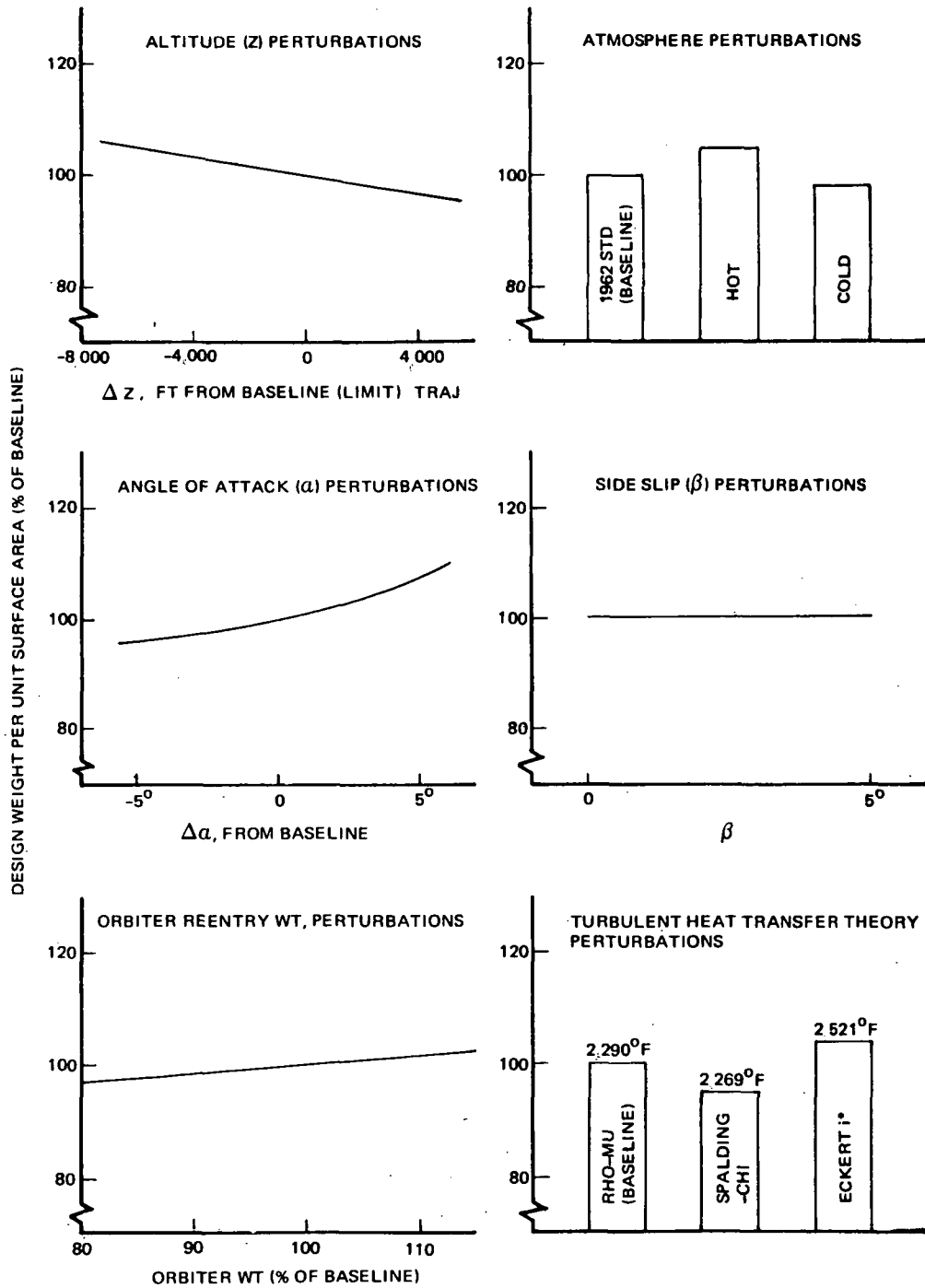


Figure 24: WEIGHT SENSITIVITY SUMMARY--REUSABLE EXTERNAL INSULATION POINT

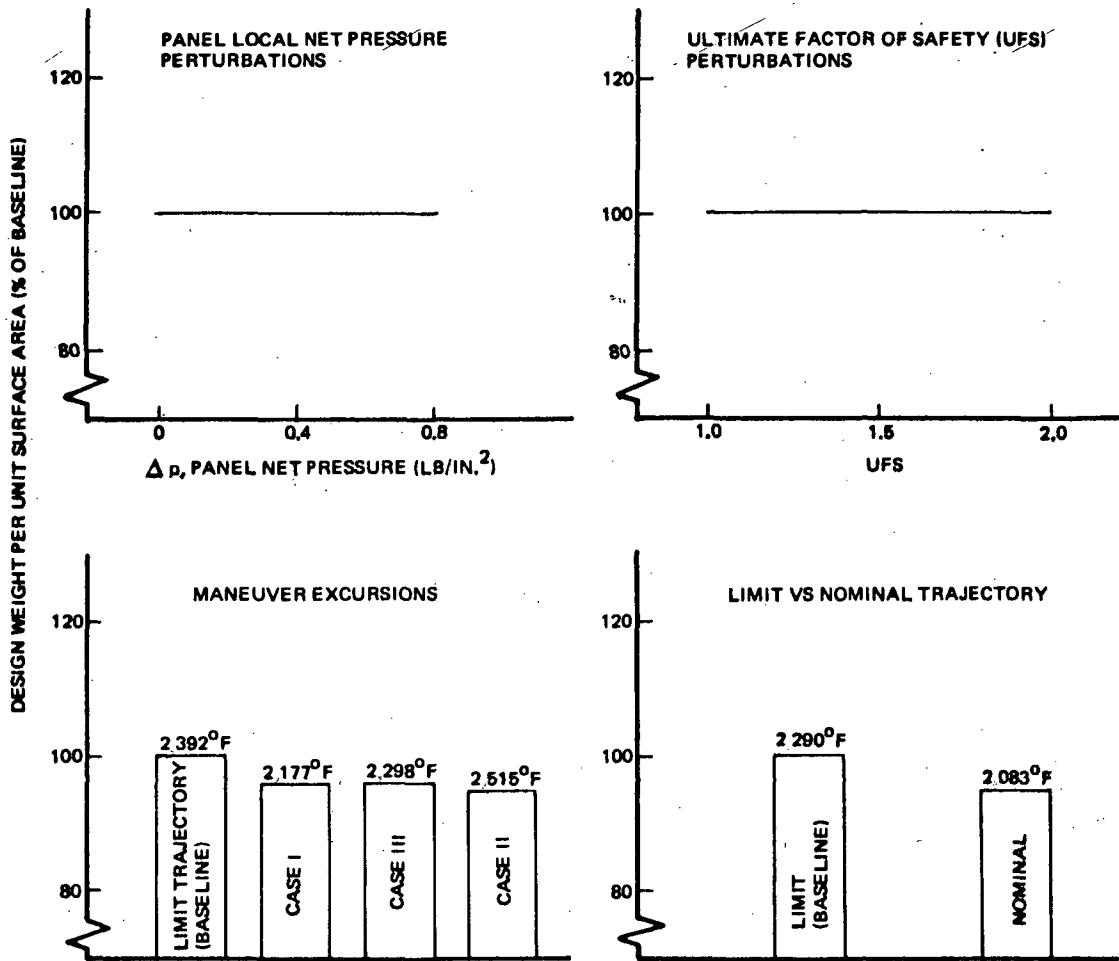


Figure 24. WEIGHT SENSITIVITY SUMMARY-REUSABLE EXTERNAL INSULATION POINT (Cont)

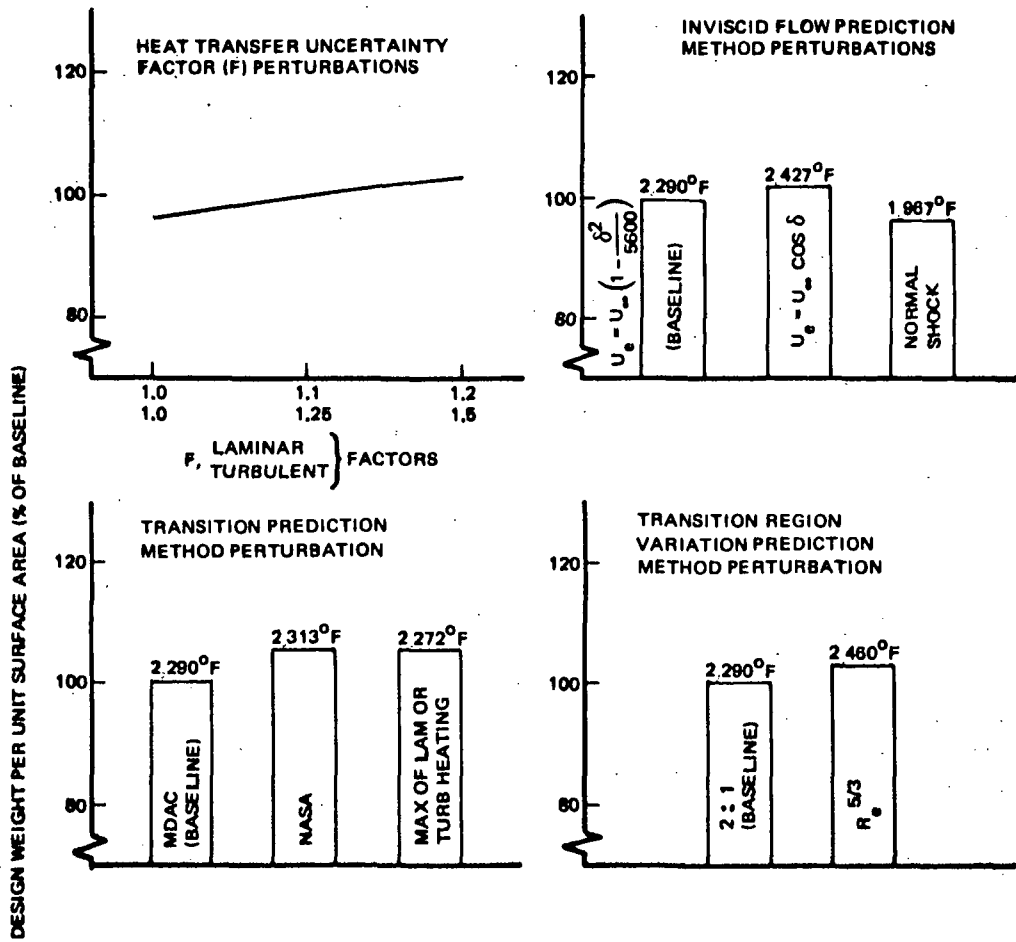


Figure 24: WEIGHT SENSITIVITY SUMMARY-REUSABLE EXTERNAL INSULATION POINT (Cont)

DESIGN WEIGHT PER UNIT SURFACE AREA (% OF BASELINE)

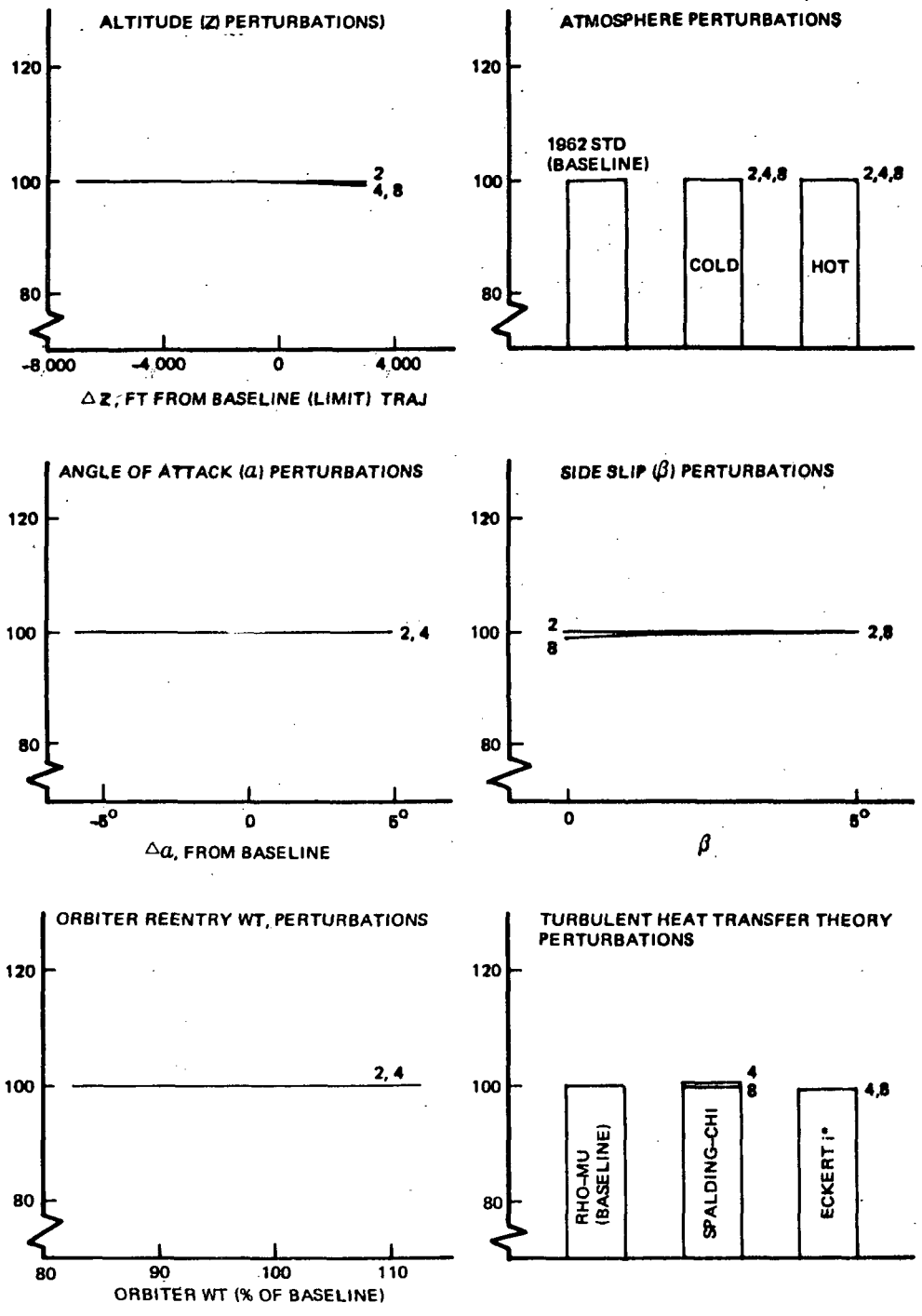


Figure 25: WEIGHT SENSITIVITY SUMMARY-HOT STRUCTURE POINTS

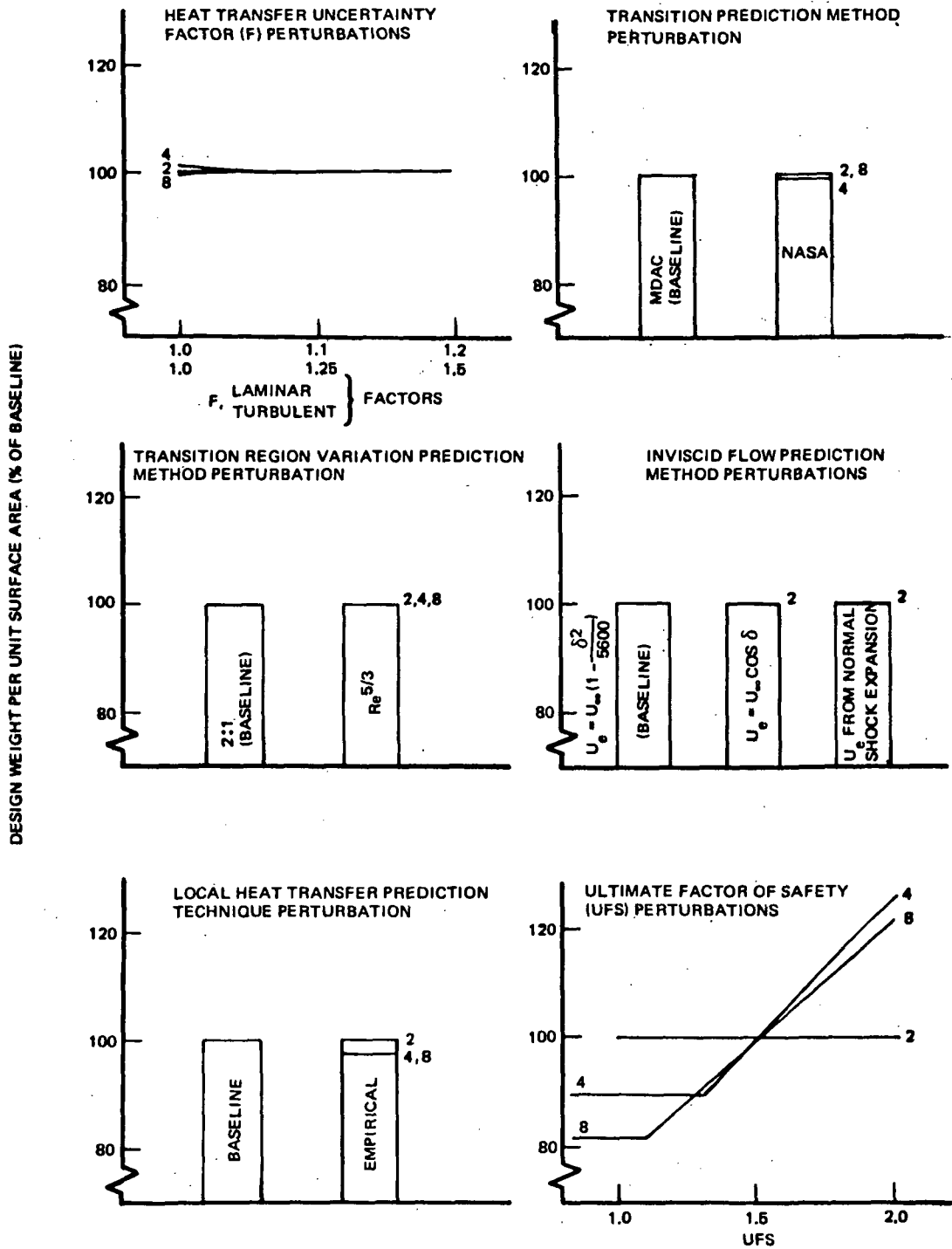


Figure 25: WEIGHT SENSITIVITY SUMMARY-HOT STRUCTURE POINTS (Cont)

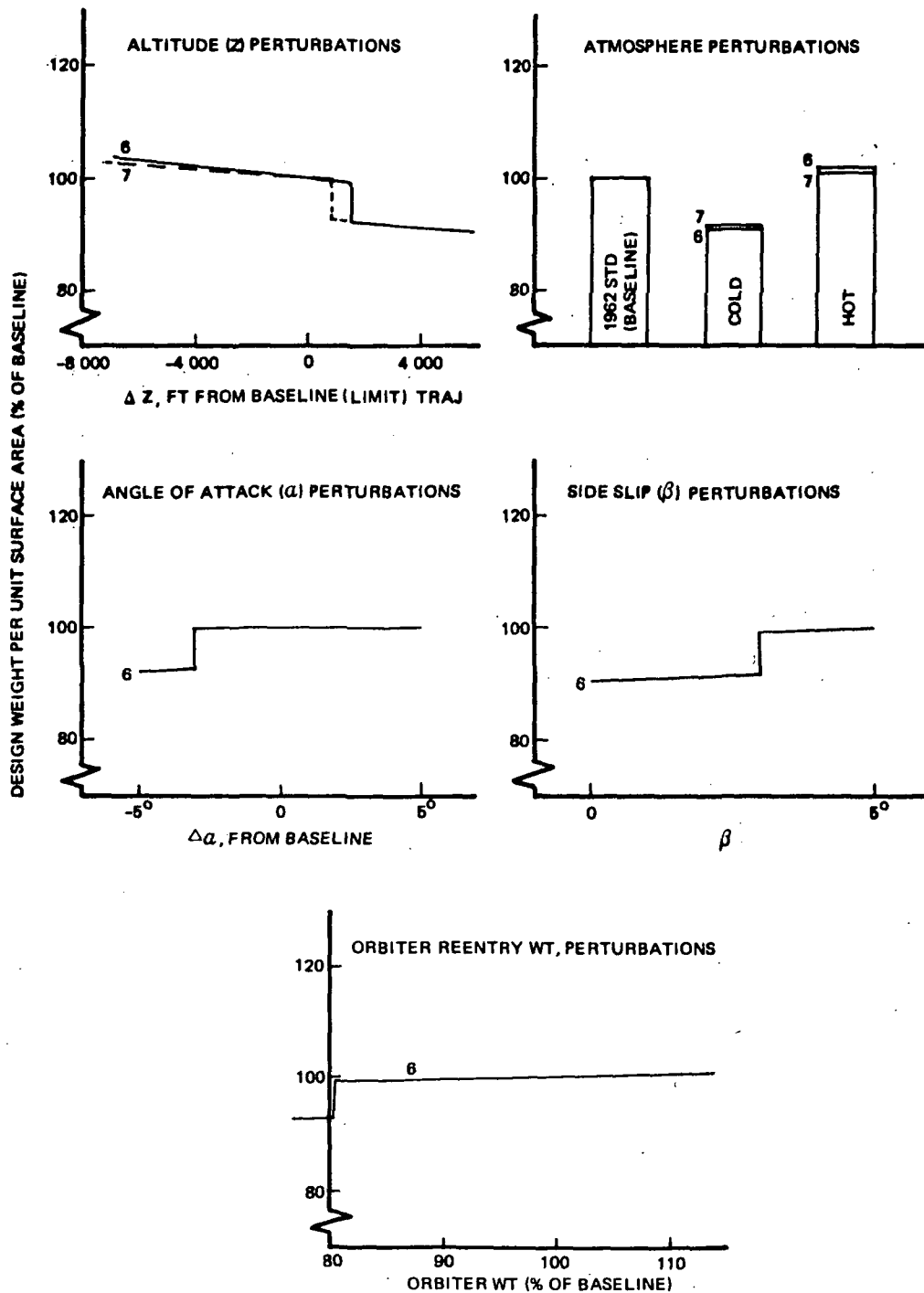


Figure 26: WEIGHT SENSITIVITY SUMMARY-CARBON/CARBON COMPOSITE POINTS

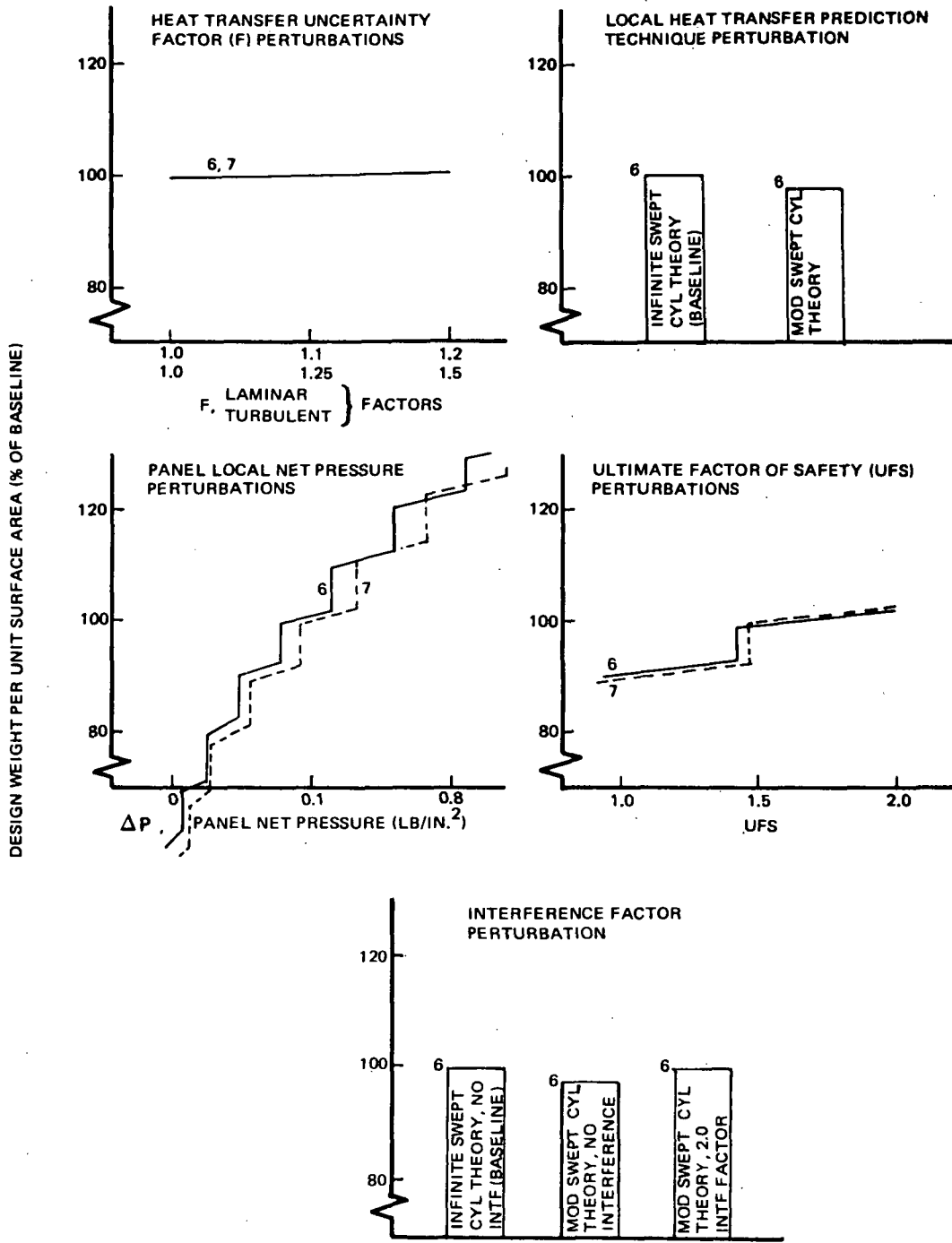


Figure 26: WEIGHT SENSITIVITY SUMMARY-CARBON/CARBON COMPOSITE POINTS (Cont)

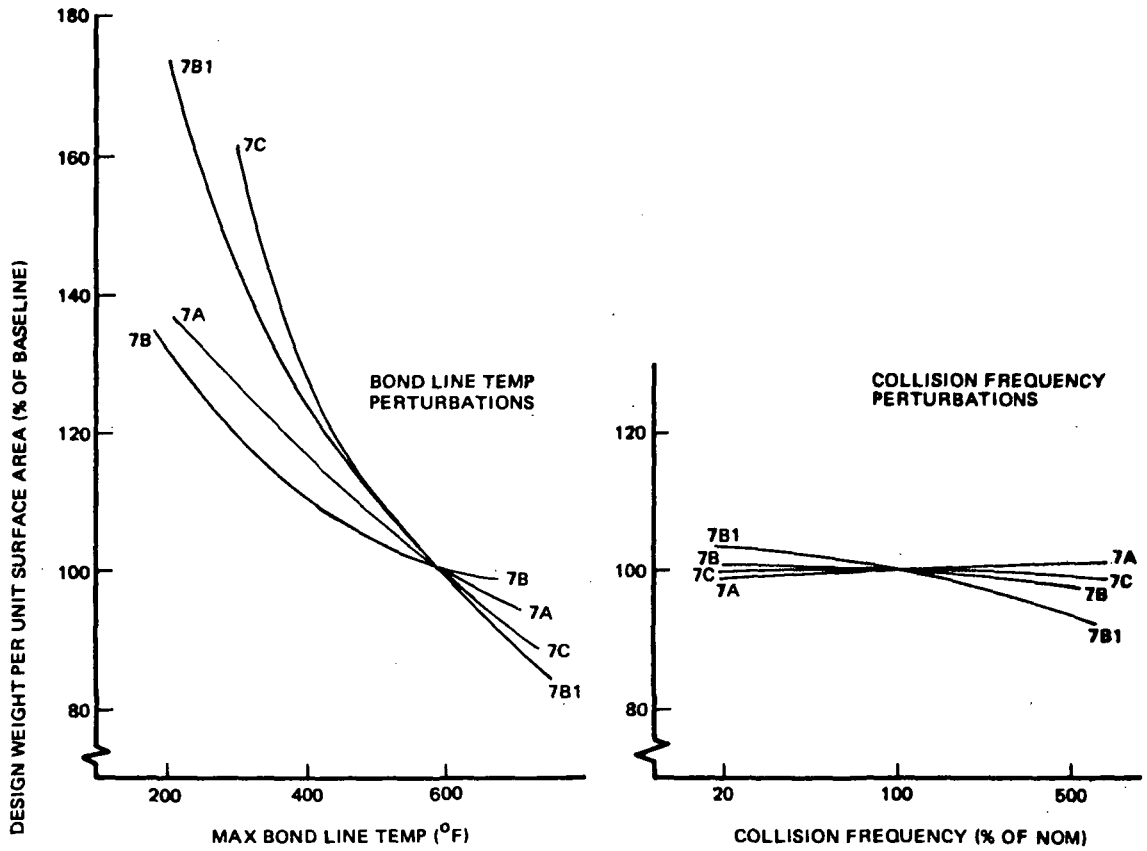


Figure 27: WEIGHT SENSITIVITY SUMMARY-ABLATOR POINTS

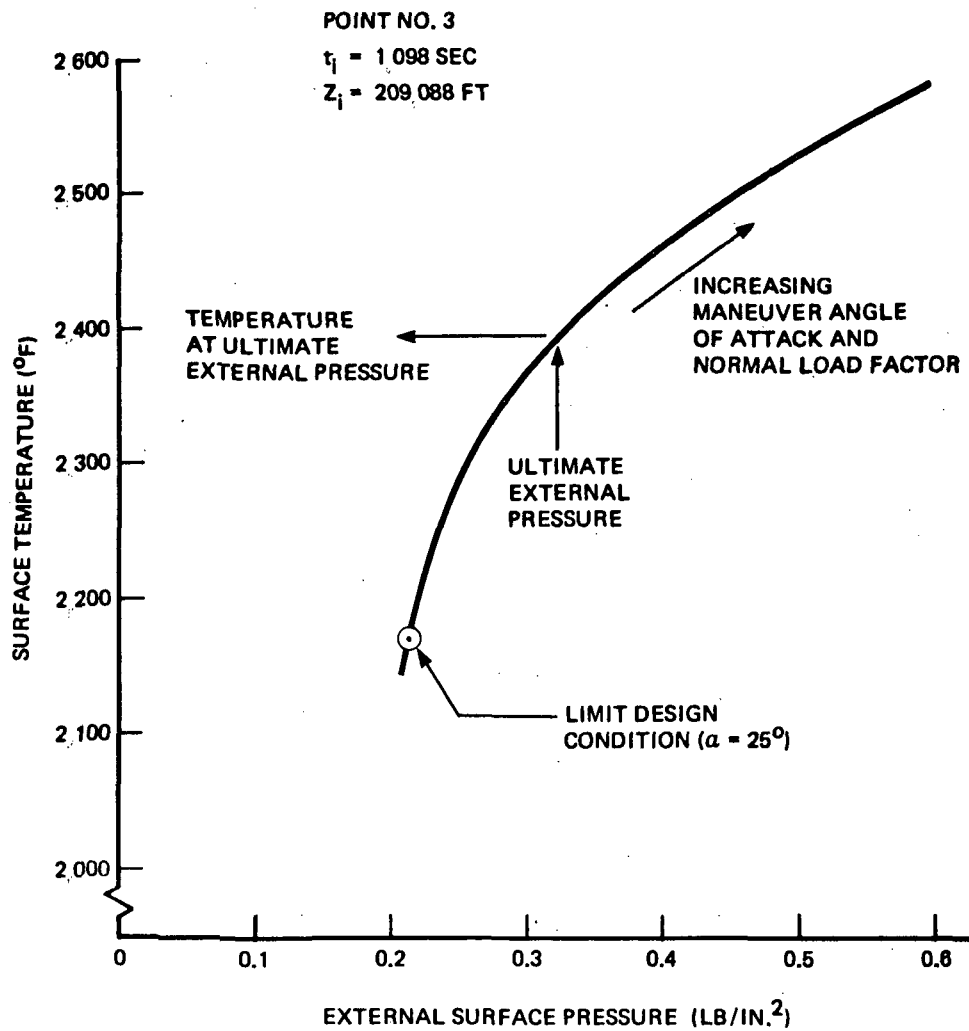


Figure 28: SURFACE TEMPERATURE AND PRESSURE AT MANEUVER INITIATION

NOTE: MAX OF LAM OR TURB CASE YIELDS LOWER PEAK
TURBULENT HEATING AND LOWER HEATING IN
AFT AREAS

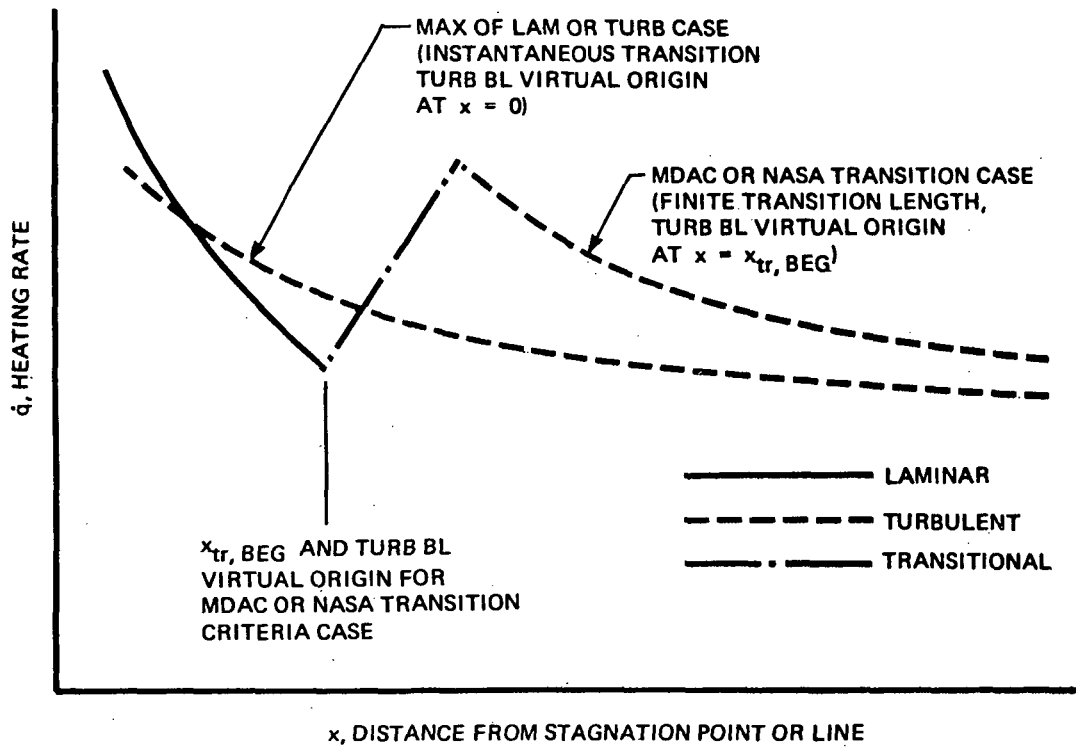


Figure 29: TURBULENT HEATING DISTRIBUTION SCHEMATIC

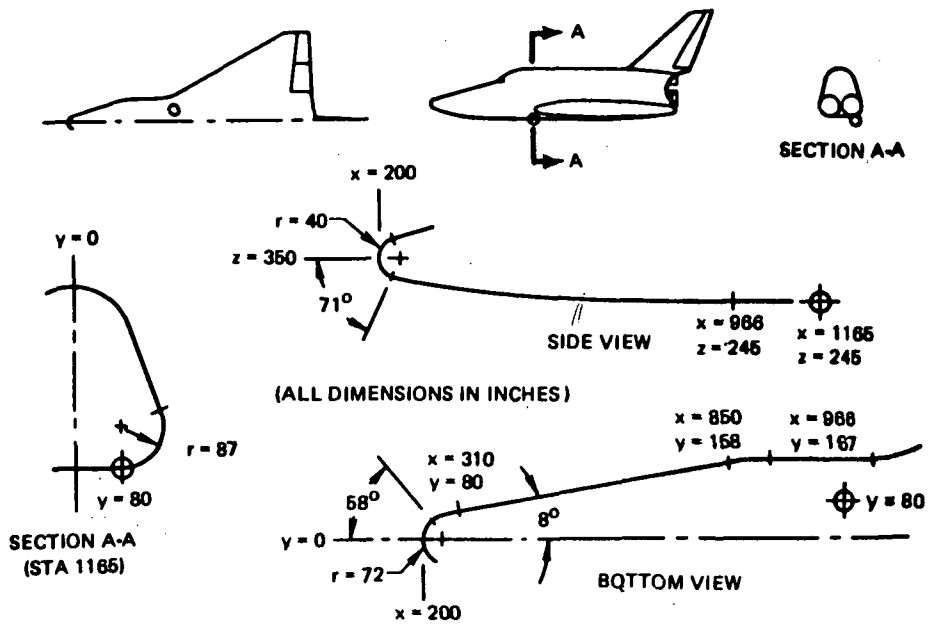


Figure 30: POINT NO. 1-LOWER MID-BODY

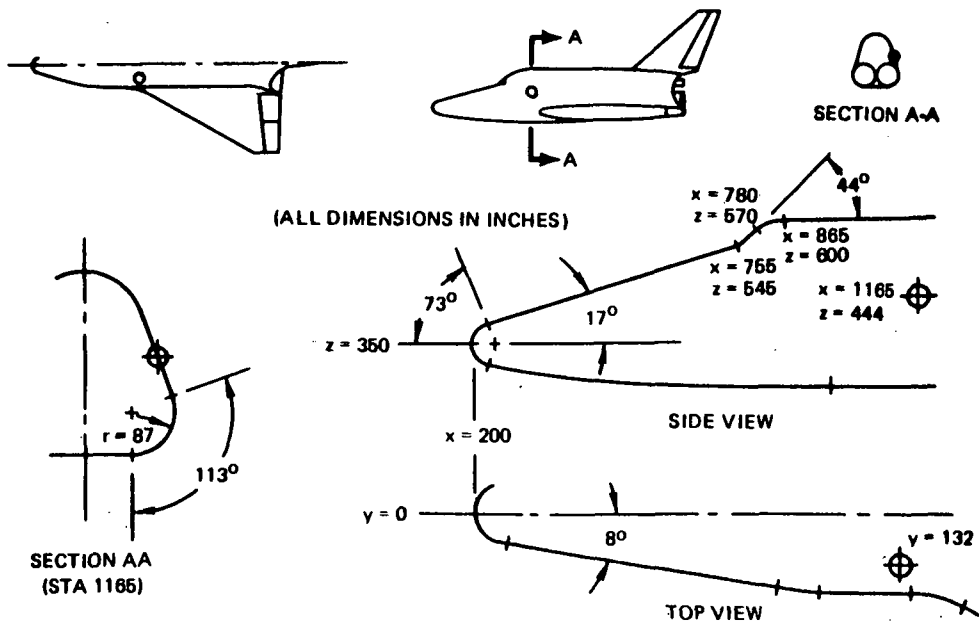
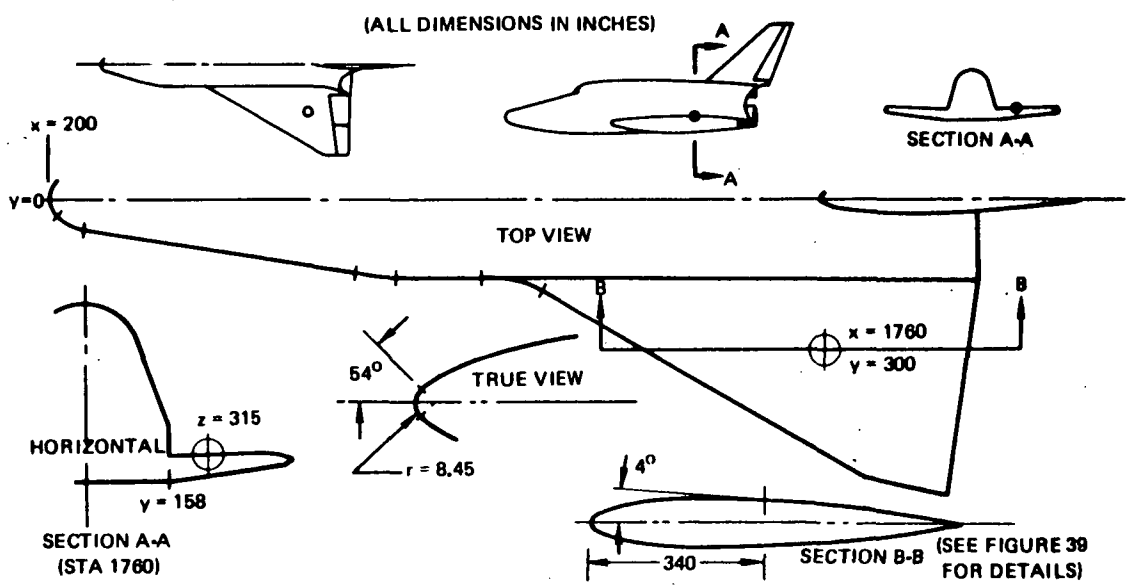
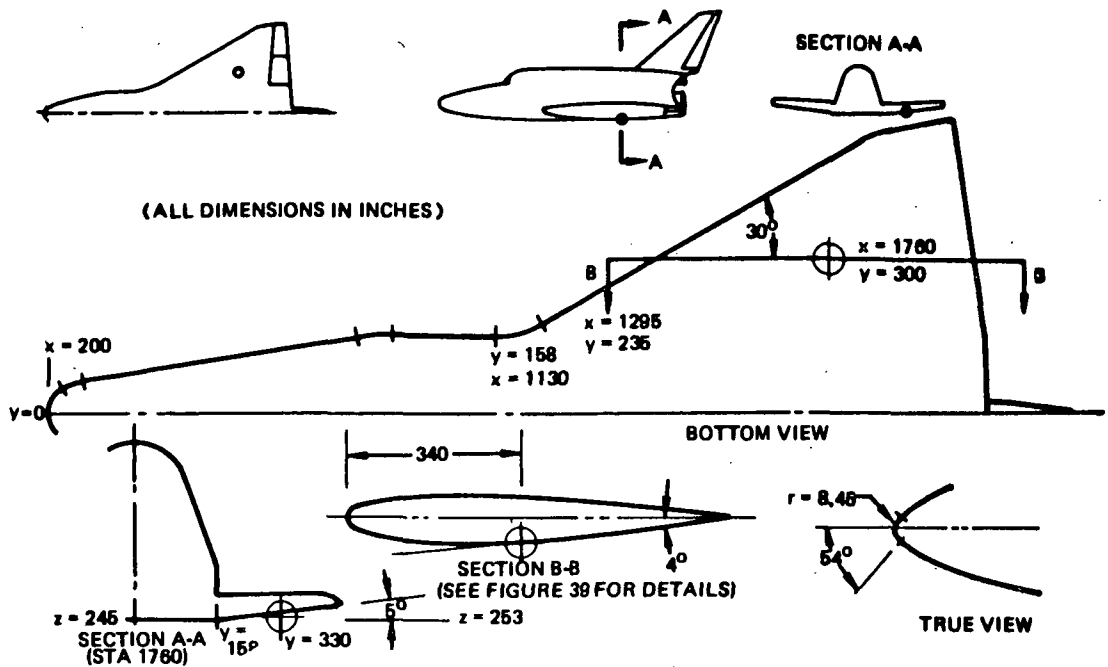


Figure 31: POINT NO. 2-UPPER MID-BODY SIDE



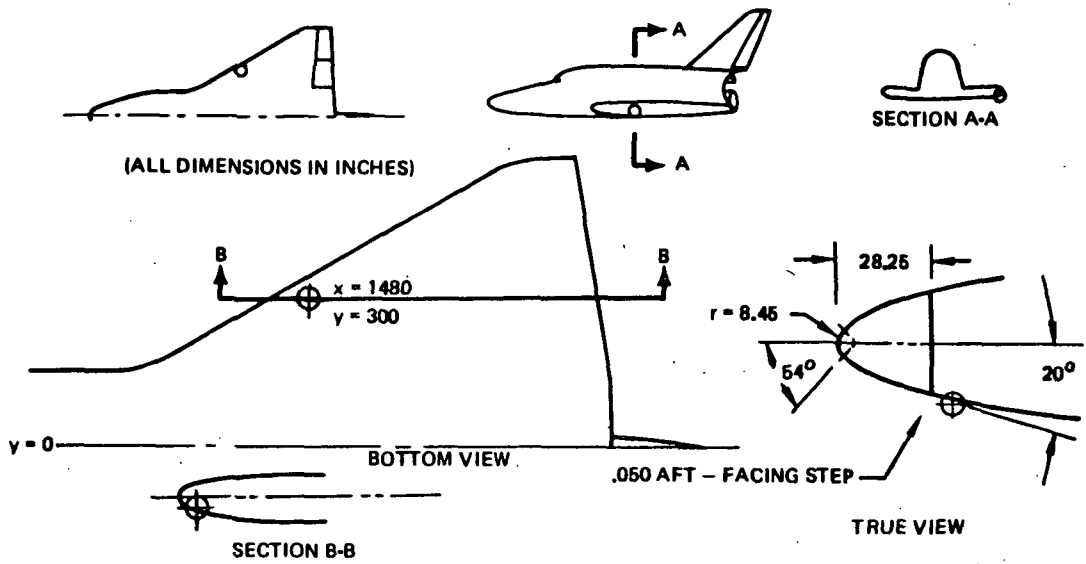


Figure 34: POINT NO. 5--LOWER WING, MID-SEMI-SPAN, L.E. BEAM

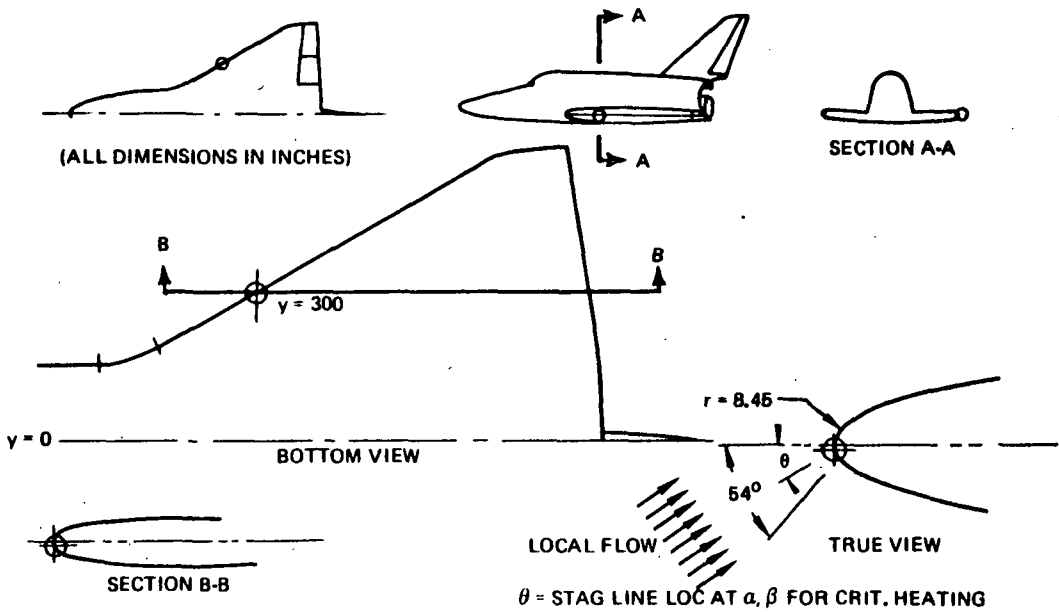


Figure 35. POINT NO. 6--WING LEADING EDGE STAG LINE MID-SEMI-SPAN

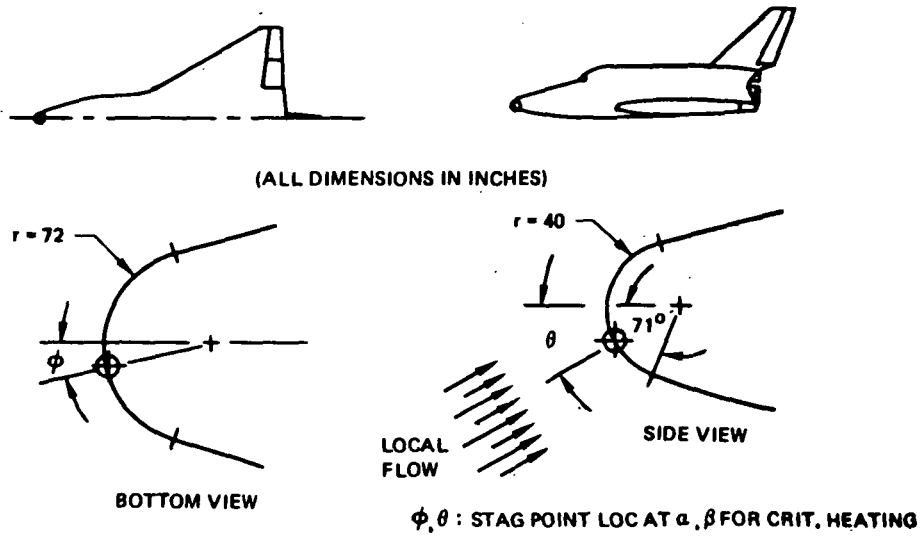


Figure 36. POINT NO. 7--NOSE AERO. STAG POINT.

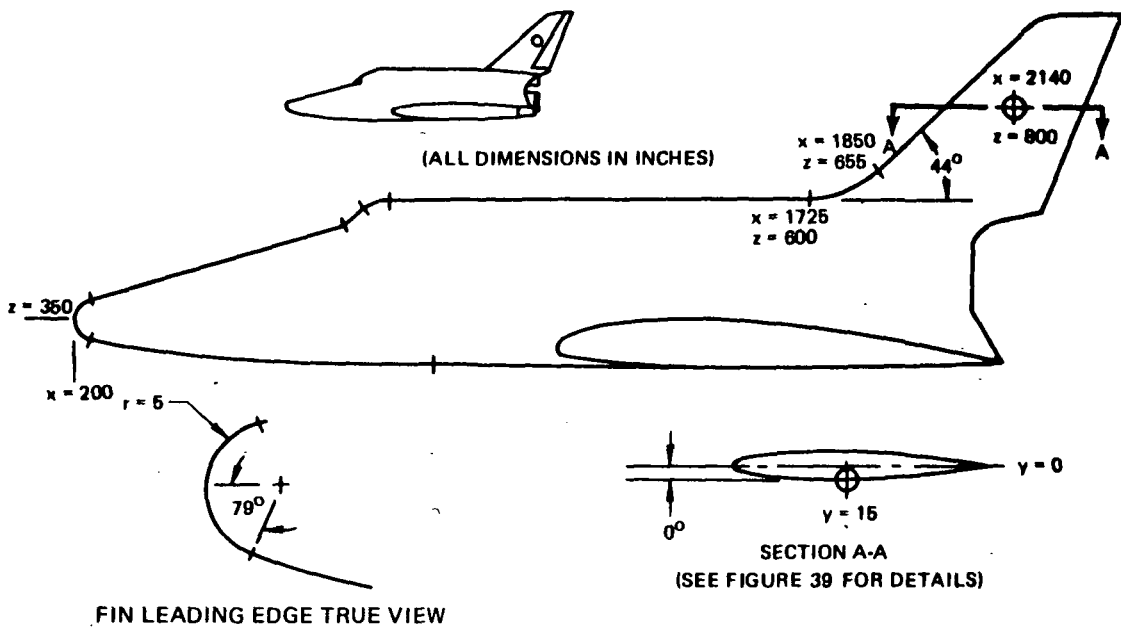


Figure 37. POINT NO. 8--FIN SIDE, MID-SPAN, MID-CHORD



Dimensions are in Inches

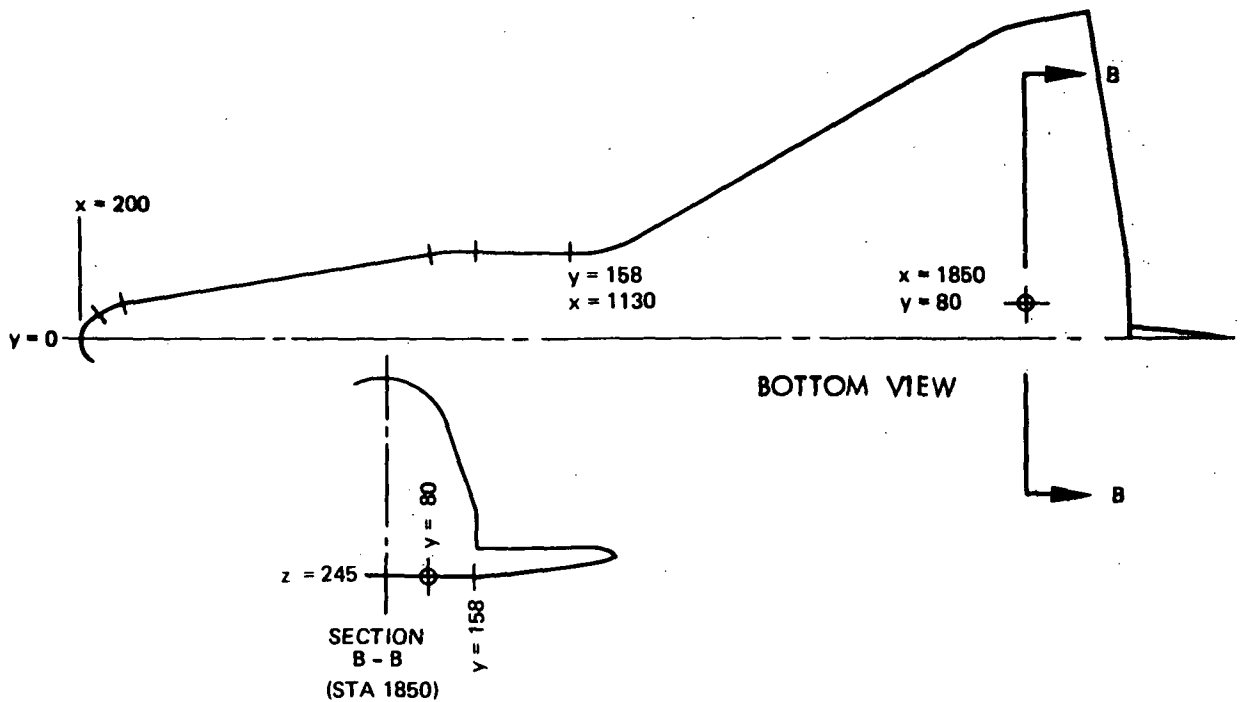


Figure 38: POINT NO. 9--LOWER BODY, AFT

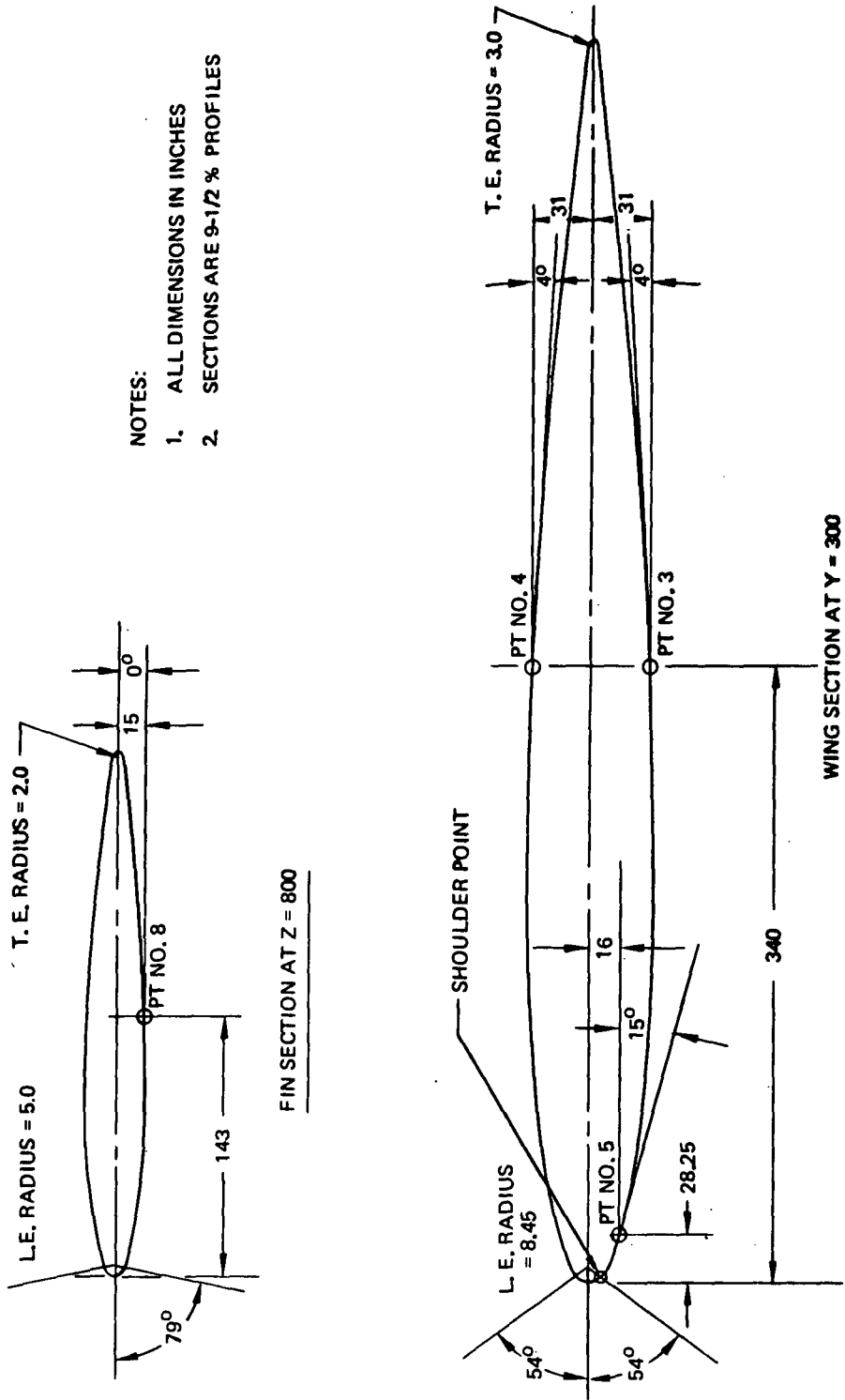


Figure 39. WING AND FIN SECTIONS

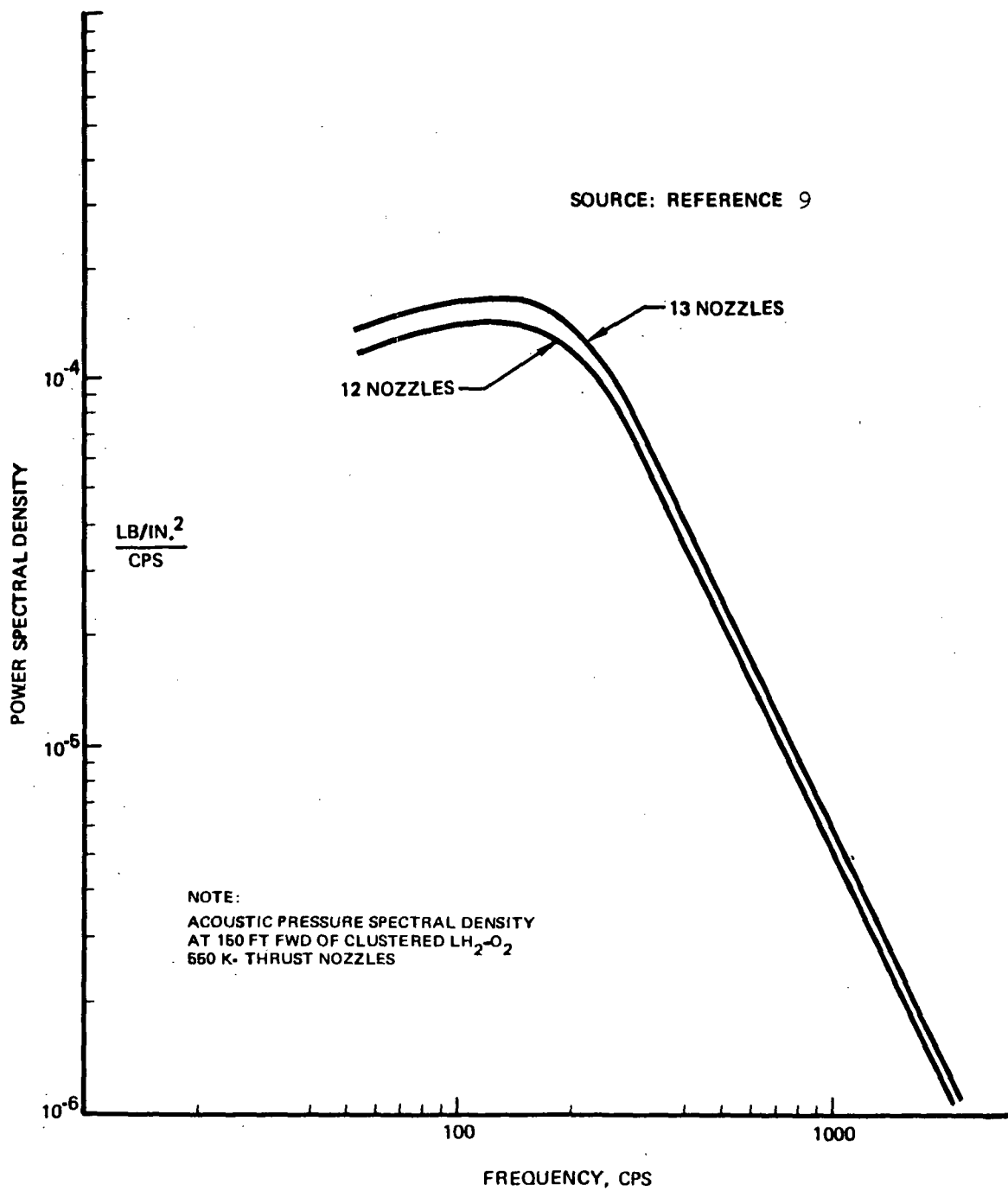


Figure 40: ACOUSTIC ENVIRONMENT

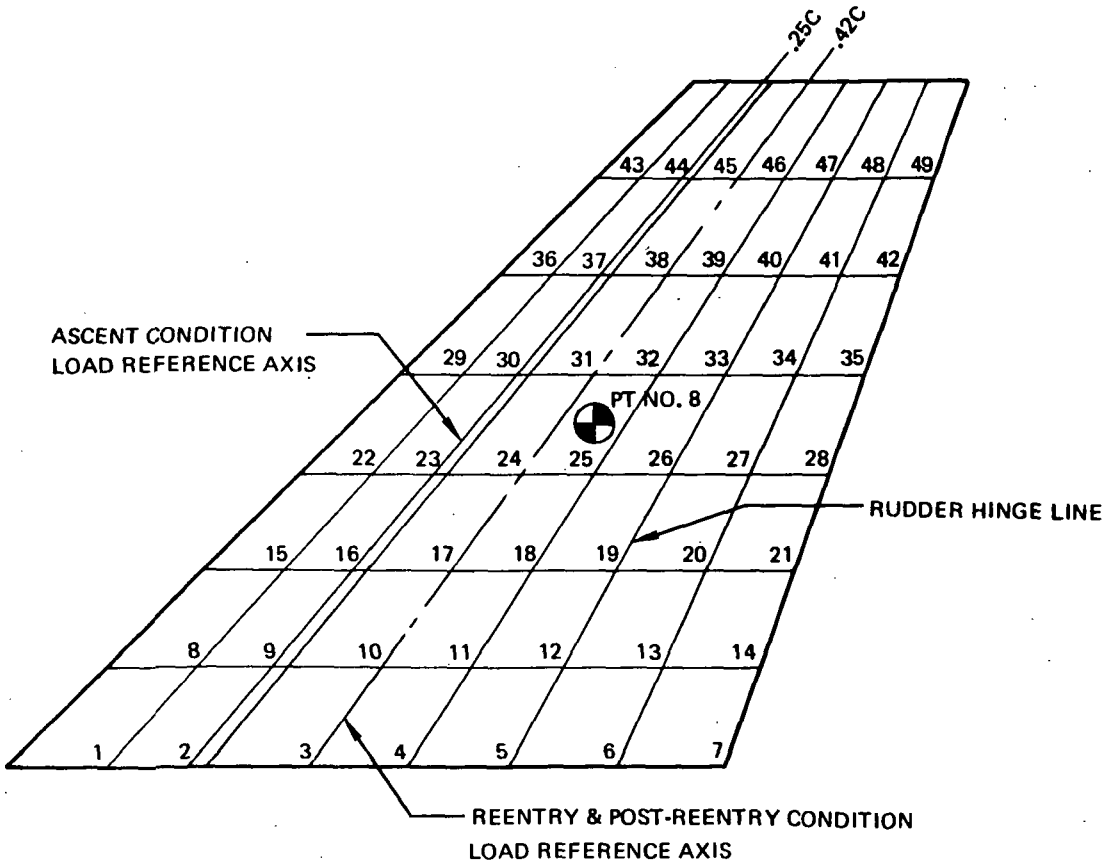


Figure 42: FIN PANEL GRID

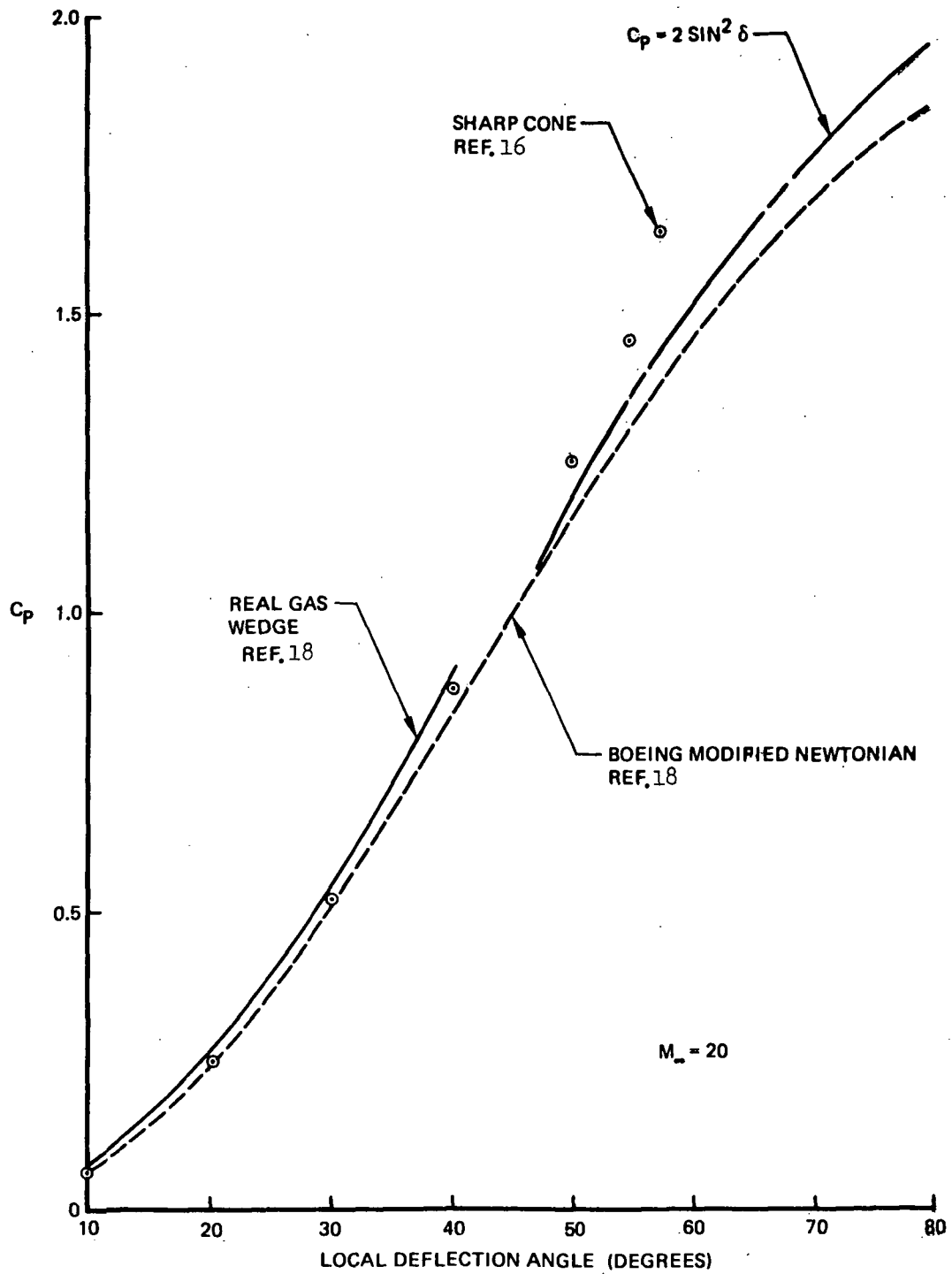


Figure 43. COMPARISON OF PRESSURE PREDICTIONS

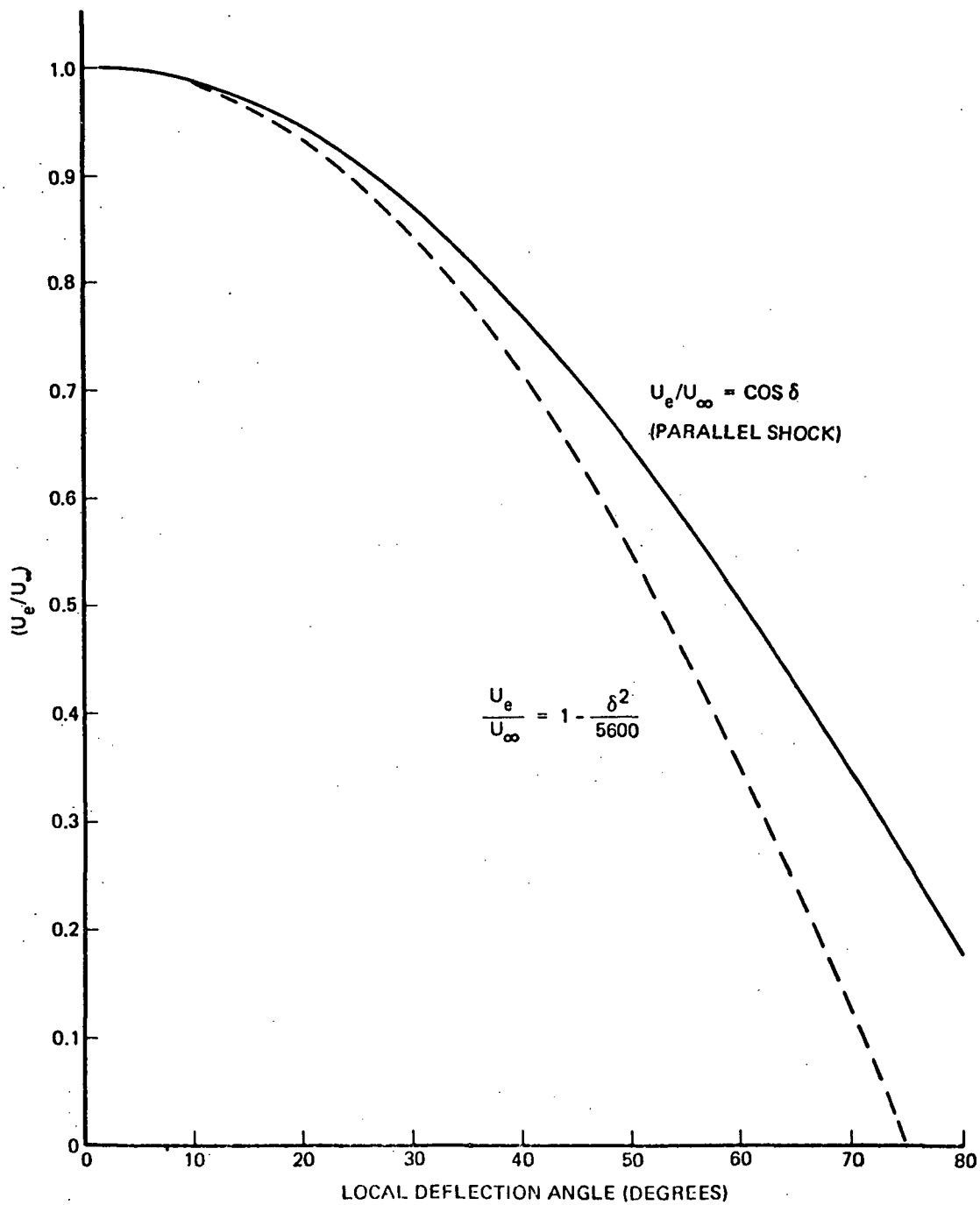


Figure 44: COMPARISON OF BOUNDARY LAYER EDGE VELOCITY PREDICTIONS

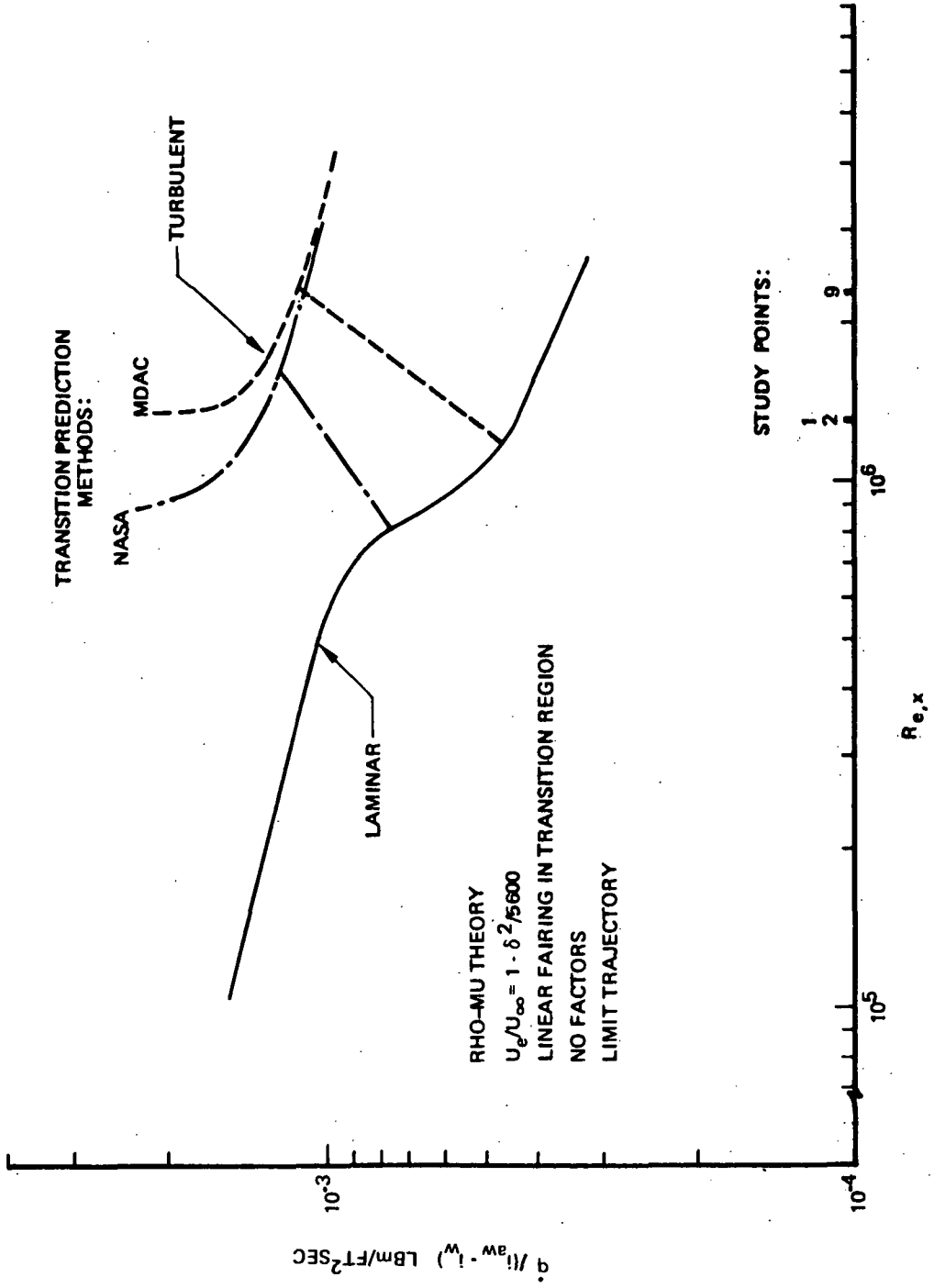


Figure 45: LOWER SURFACE CENTERLINE HEAT TRANSFER COEFFICIENT DISTRIBUTION $t = 214$ SEC

MDAC TRANSITION
 $U_b/U_\infty = 1 - \delta^2/5600$
 1.1, 1.25 FACTORS
 LIMIT TRAJECTORY

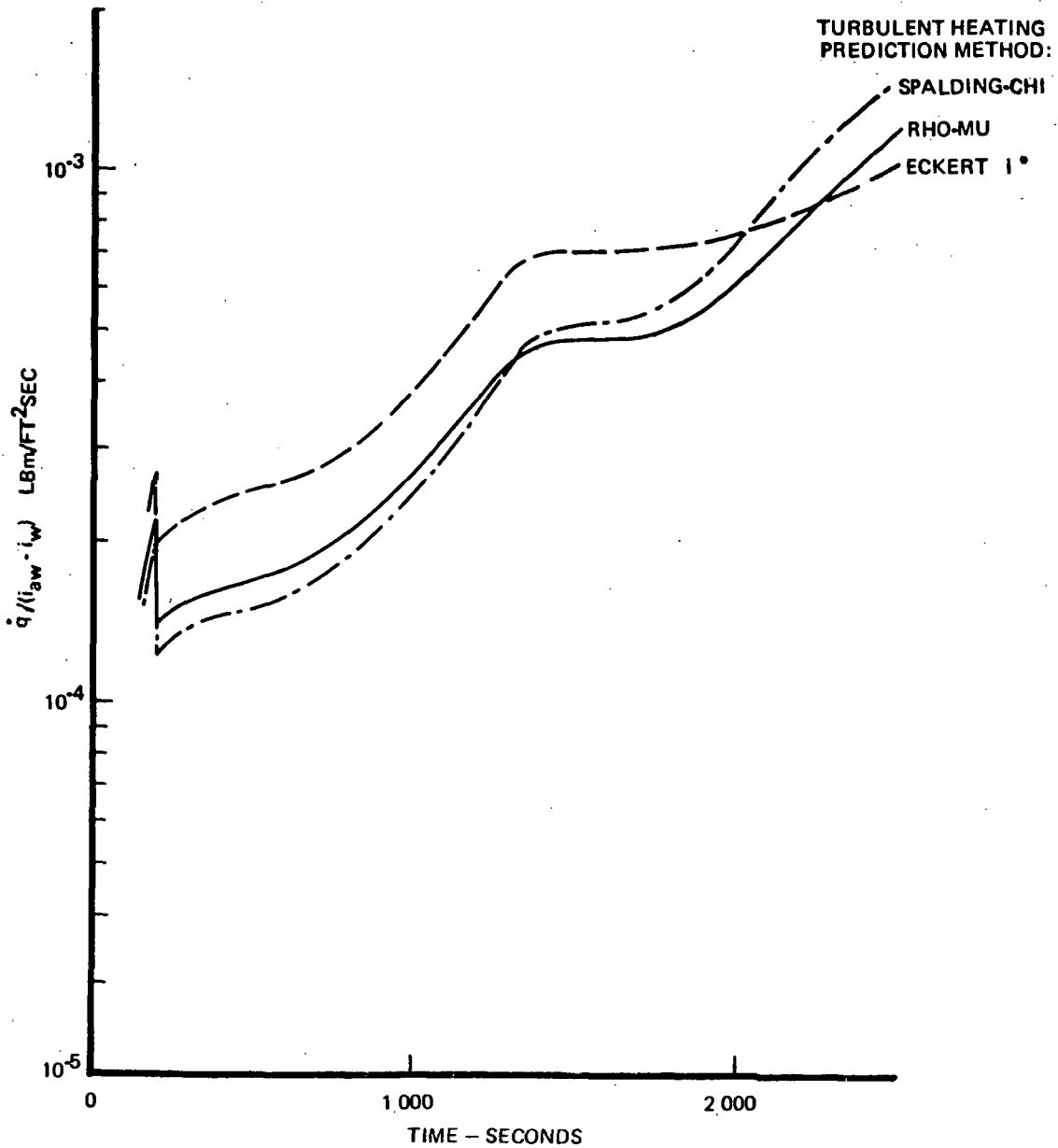


Figure 46: HEAT TRANSFER COEFFICIENT HISTORY AT POINT NUMBER 9

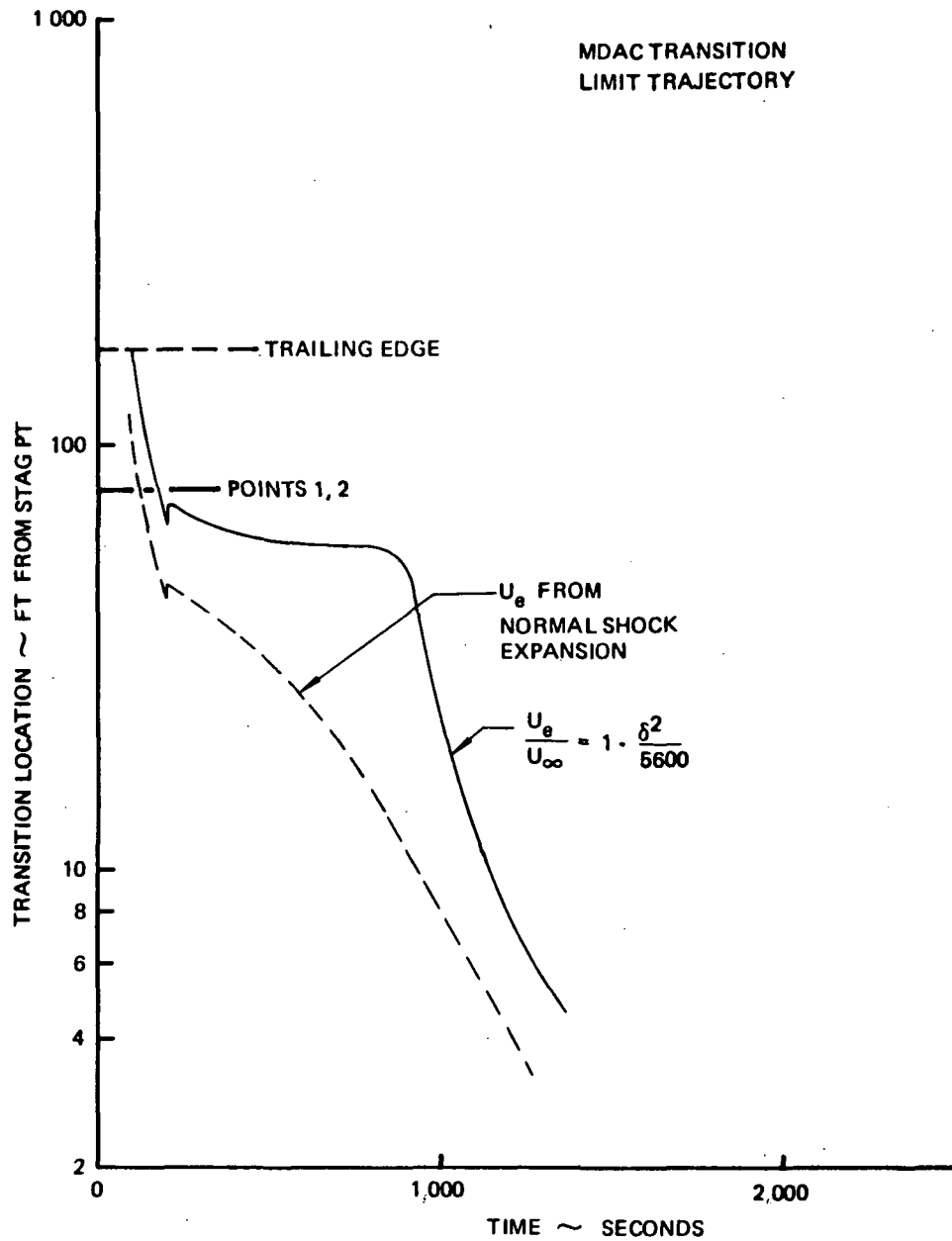


Figure 47: EFFECT OF FLOW FIELD PREDICTION METHODS ON LOWER SURFACE CENTERLINE BOUNDARY LAYER TRANSITION LOCATION

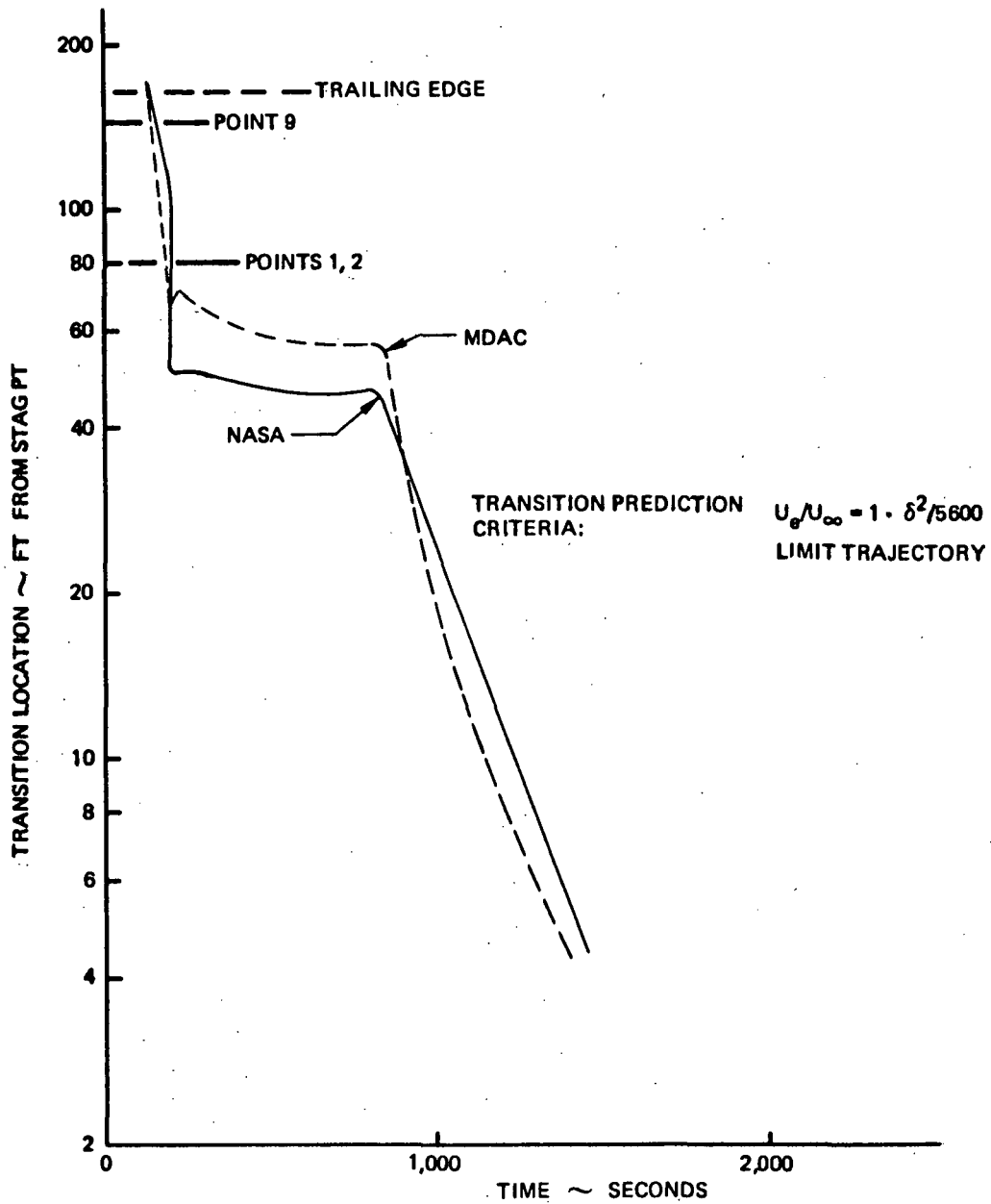


Figure 48: EFFECT OF TRANSITION CRITERIA ON LOCATION OF TRANSITION ON THE LOWER SURFACE CENTERLINE

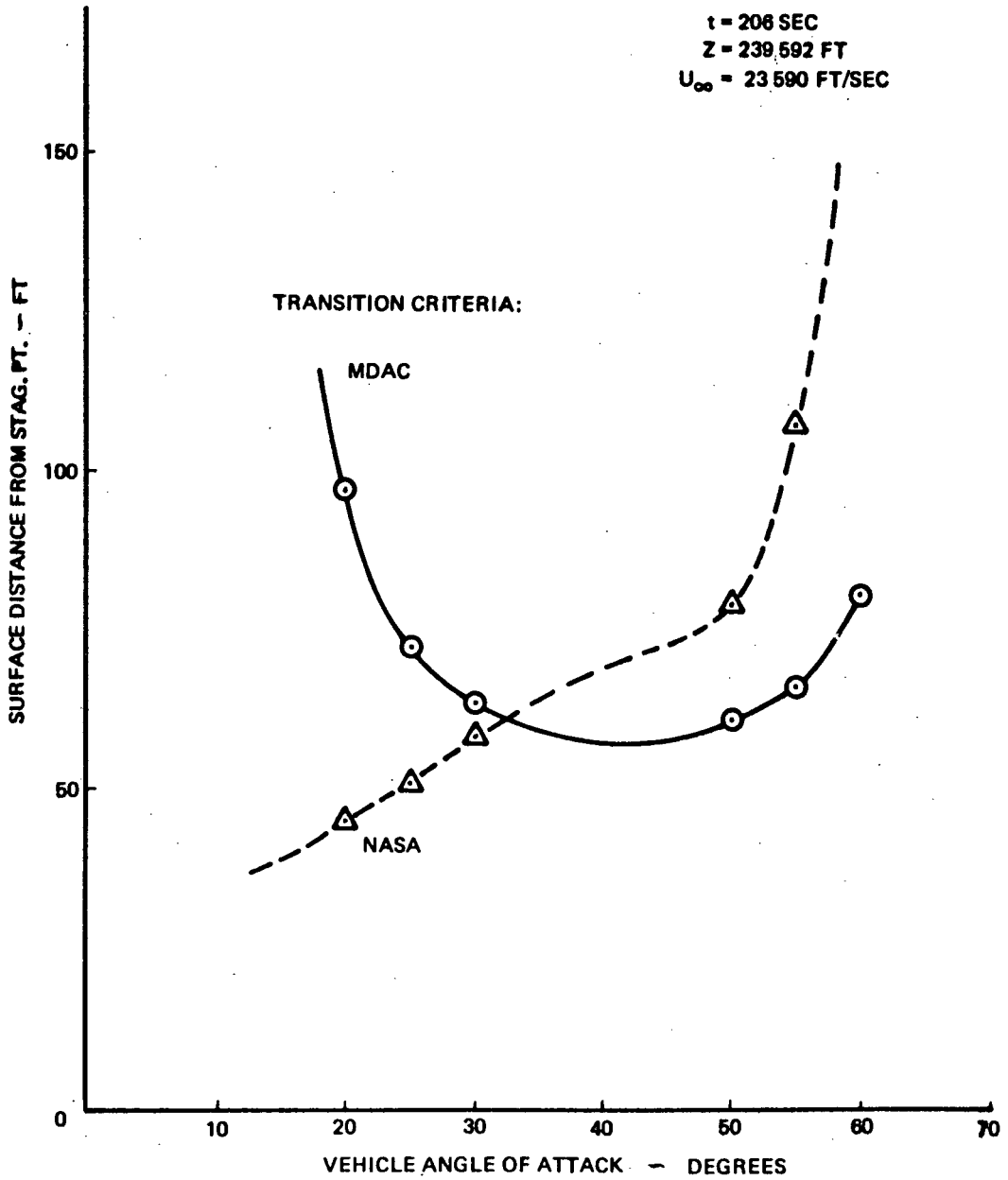


Figure 49. COMPARISON OF TRANSITION CRITERIA ON LOWER SURFACE CENTERLINE AT ONE FLIGHT CONDITION

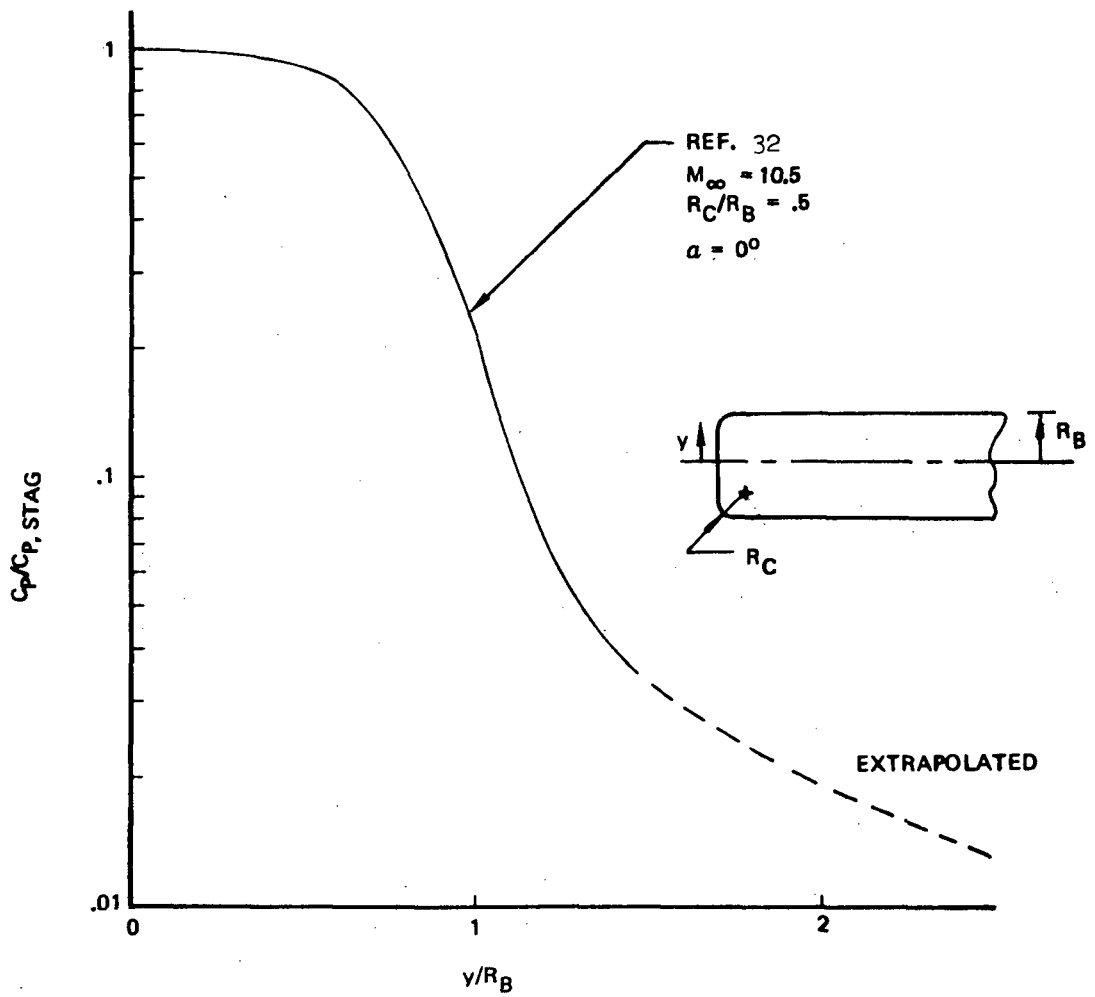


Figure 50: FLAT FACE CYLINDER PRESSURE DISTRIBUTION

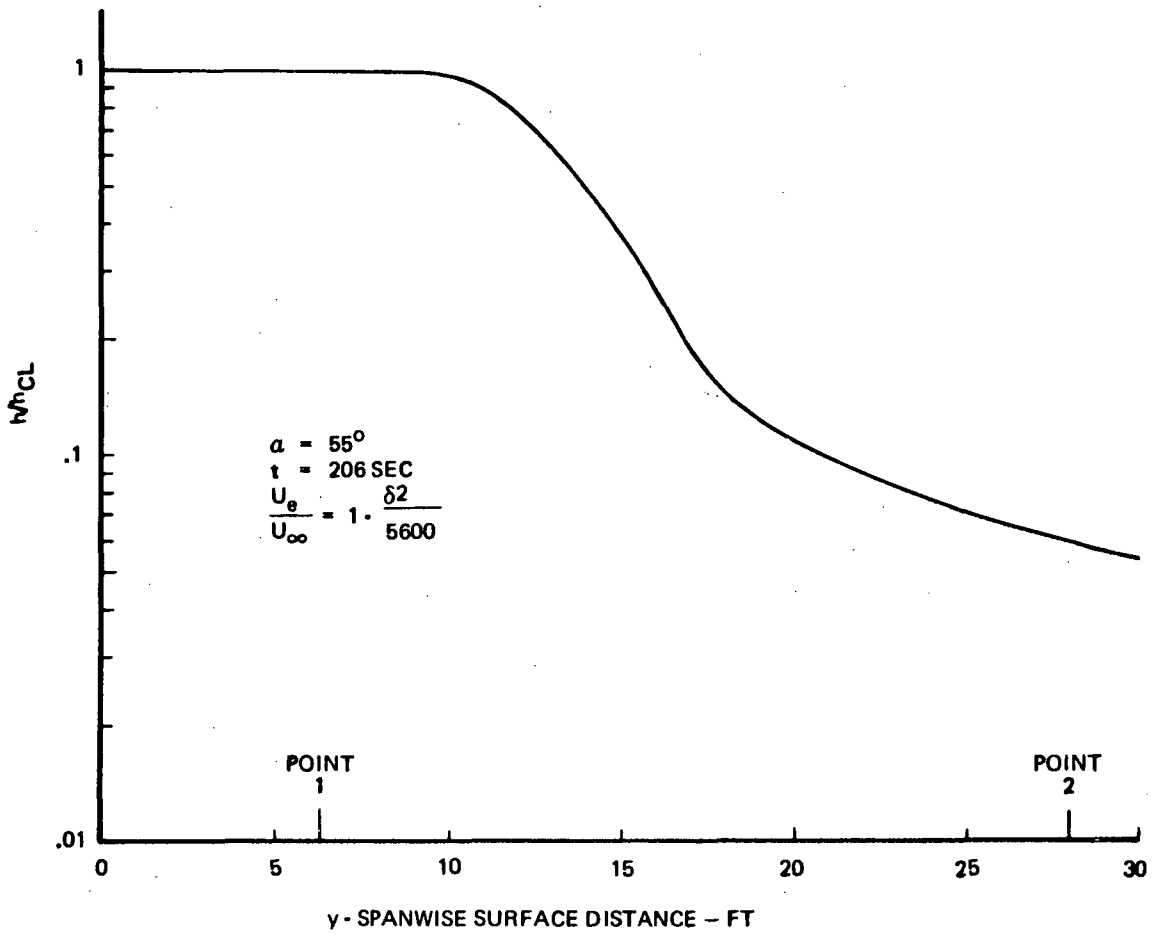


Figure 51. LAMINAR HEATING DISTRIBUTION ON THE FUSELAGE NORMAL TO THE CENTERLINE

$T = 206 \text{ SEC}$ $\alpha = 55^\circ$
 $U_e/U_\infty = 1 - \delta^2/5600$
 RHO-MU TURB. THEORY

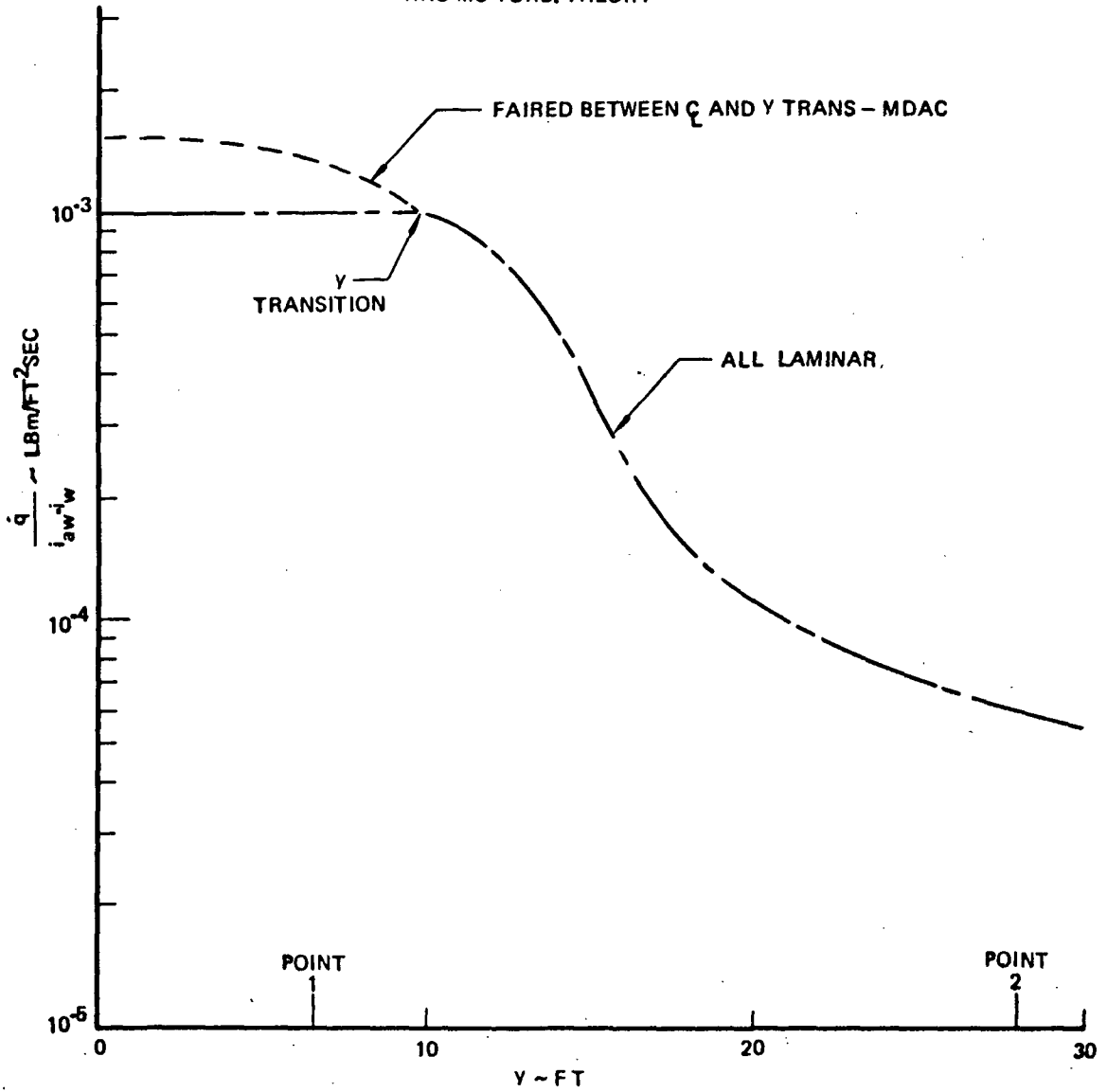


Figure 53. FUSELAGE HEATING DISTRIBUTION

$t = 206 \text{ SEC}$
 $\alpha = 55^\circ$
 $\frac{U_e}{U_\infty} = 1 - \frac{\delta^2}{5600}$

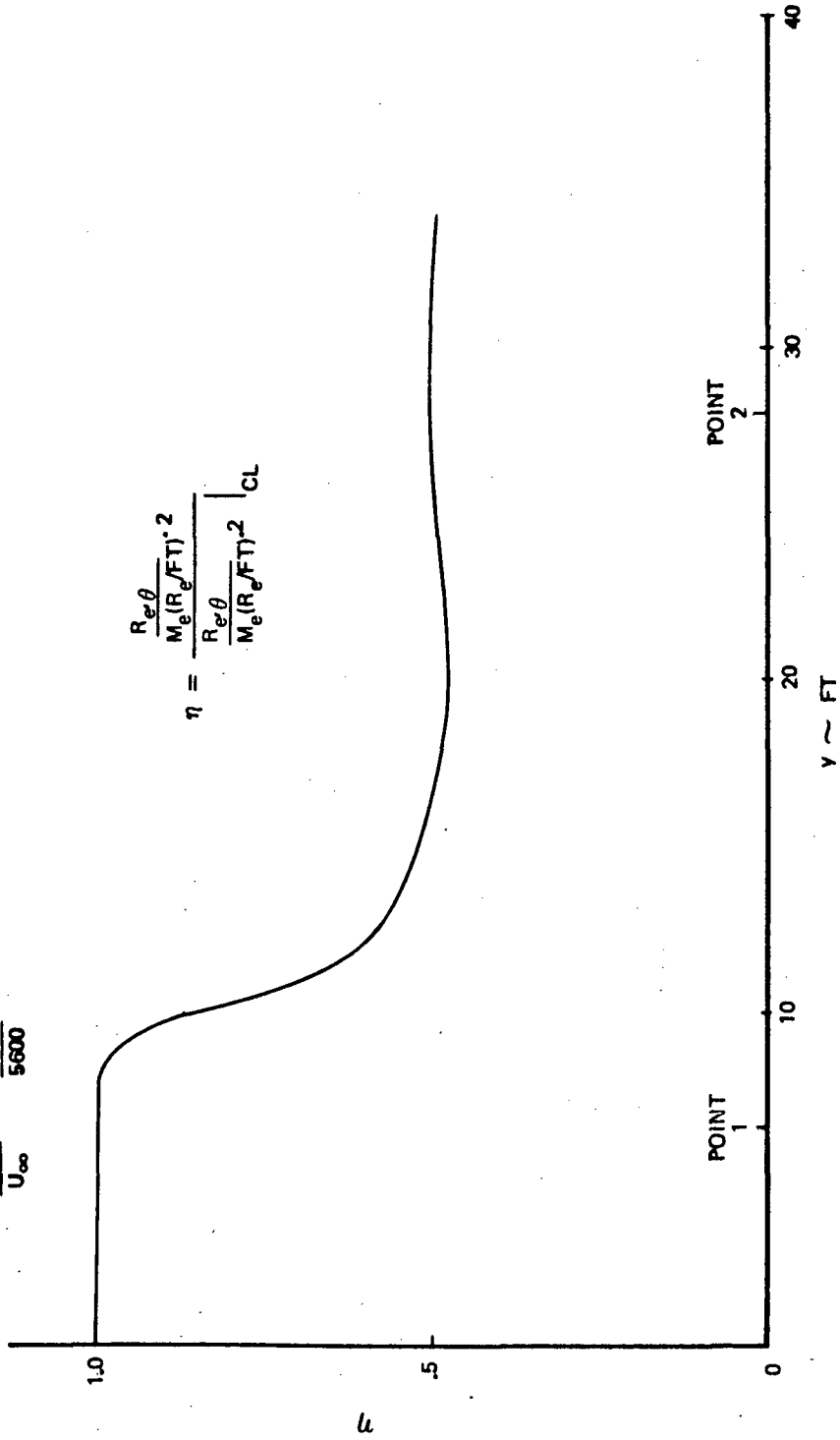


Figure 54. SPANWISE DISTRIBUTION OF THE NORMALIZED MDAC TRANSITION PARAMETER

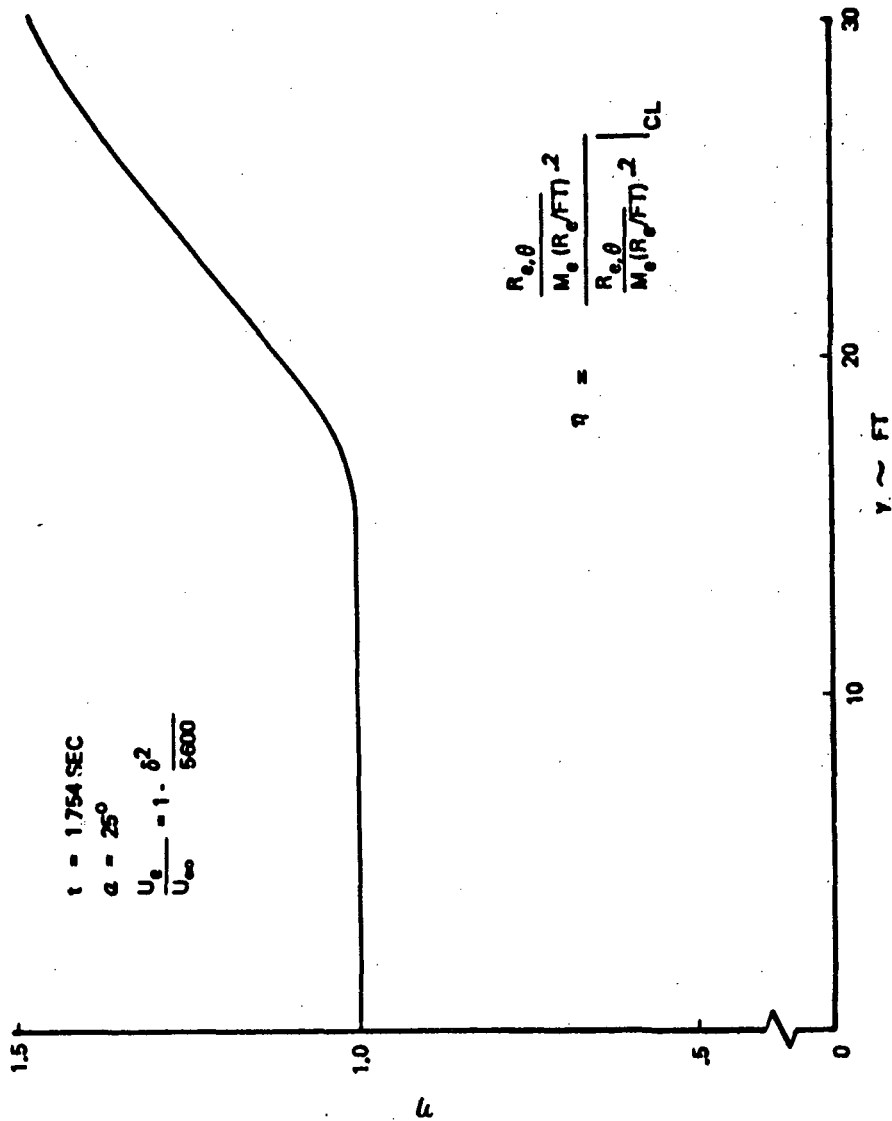


Figure 55: SPANWISE DISTRIBUTION OF THE NORMALIZED MDAC TRANSITION PARAMETER

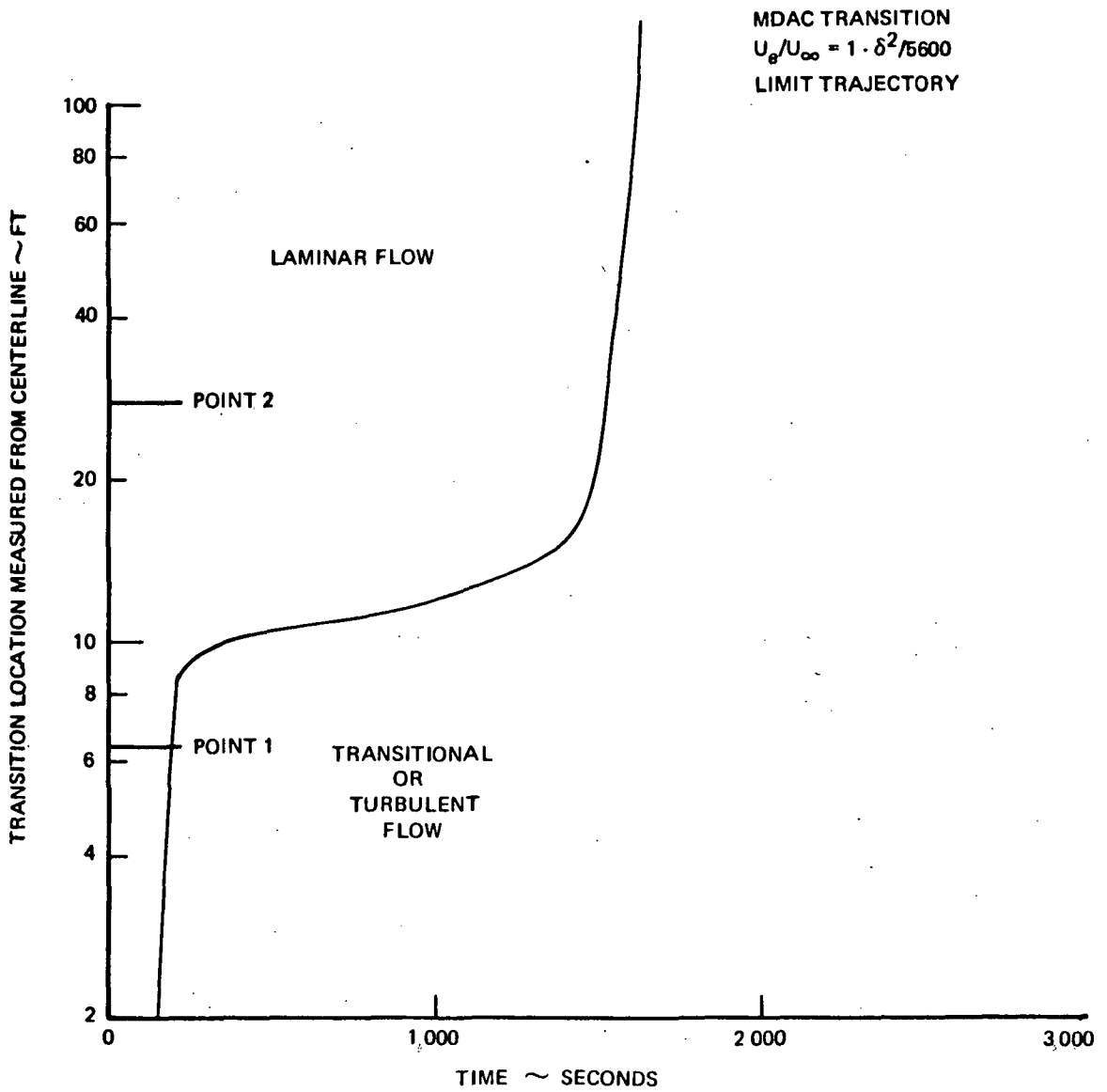


Figure 56: LOCATION OF TRANSITION ON THE FUSELAGE MEASURED NORMAL TO THE CENTERLINE

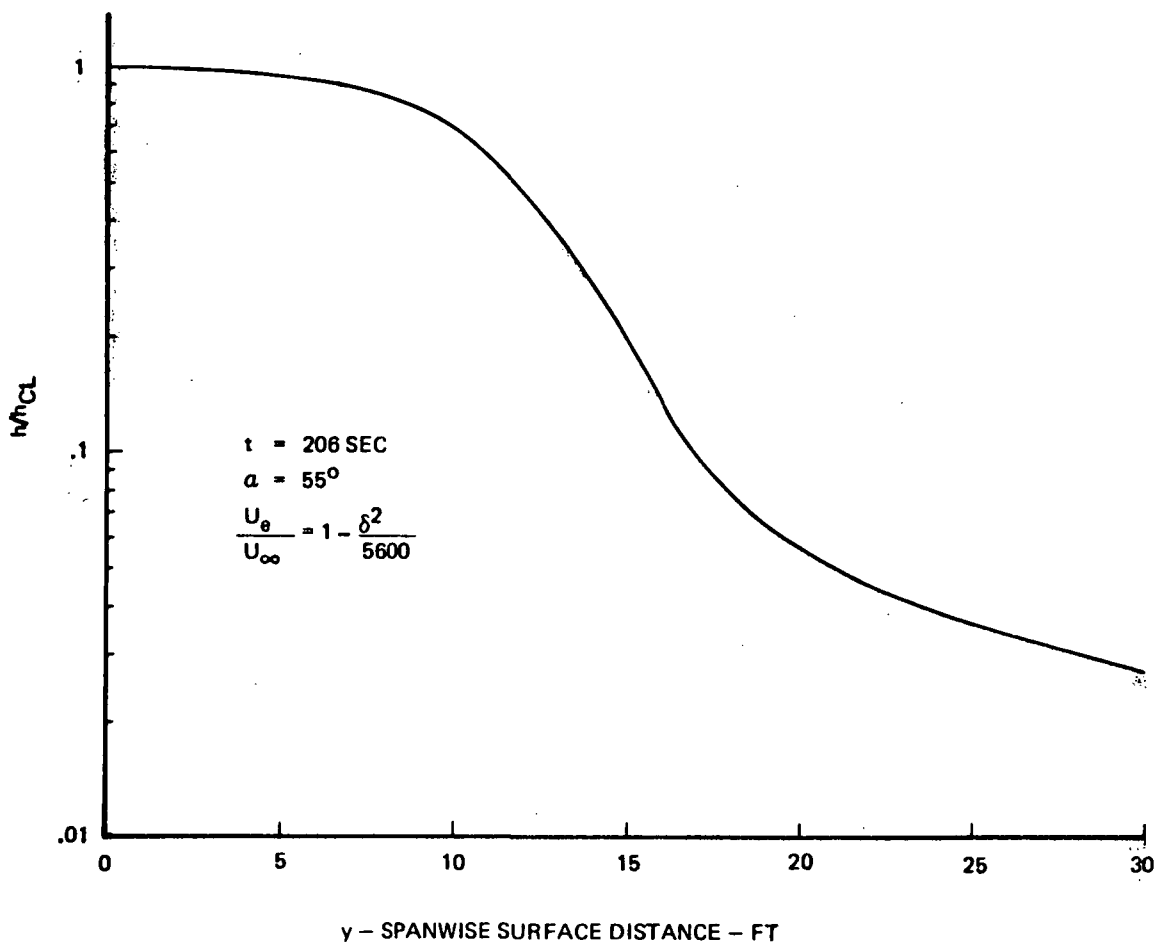


Figure 57. TURBULENT HEATING DISTRIBUTION AROUND THE FUSELAGE NORMAL TO THE CENTERLINE

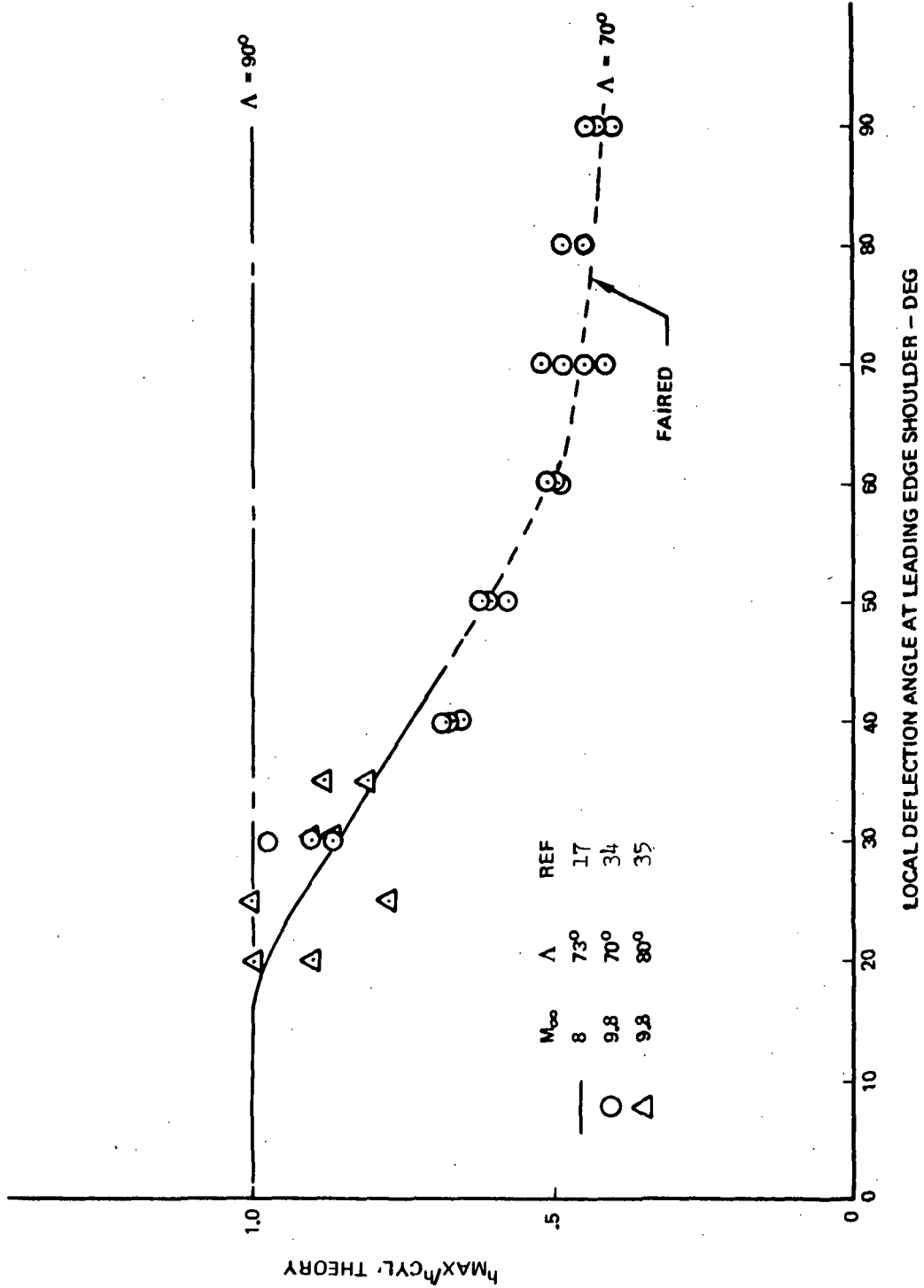


Figure 58. MAXIMUM LAMINAR HEATING ALONG THE LEADING EDGE OF A DELTA WING

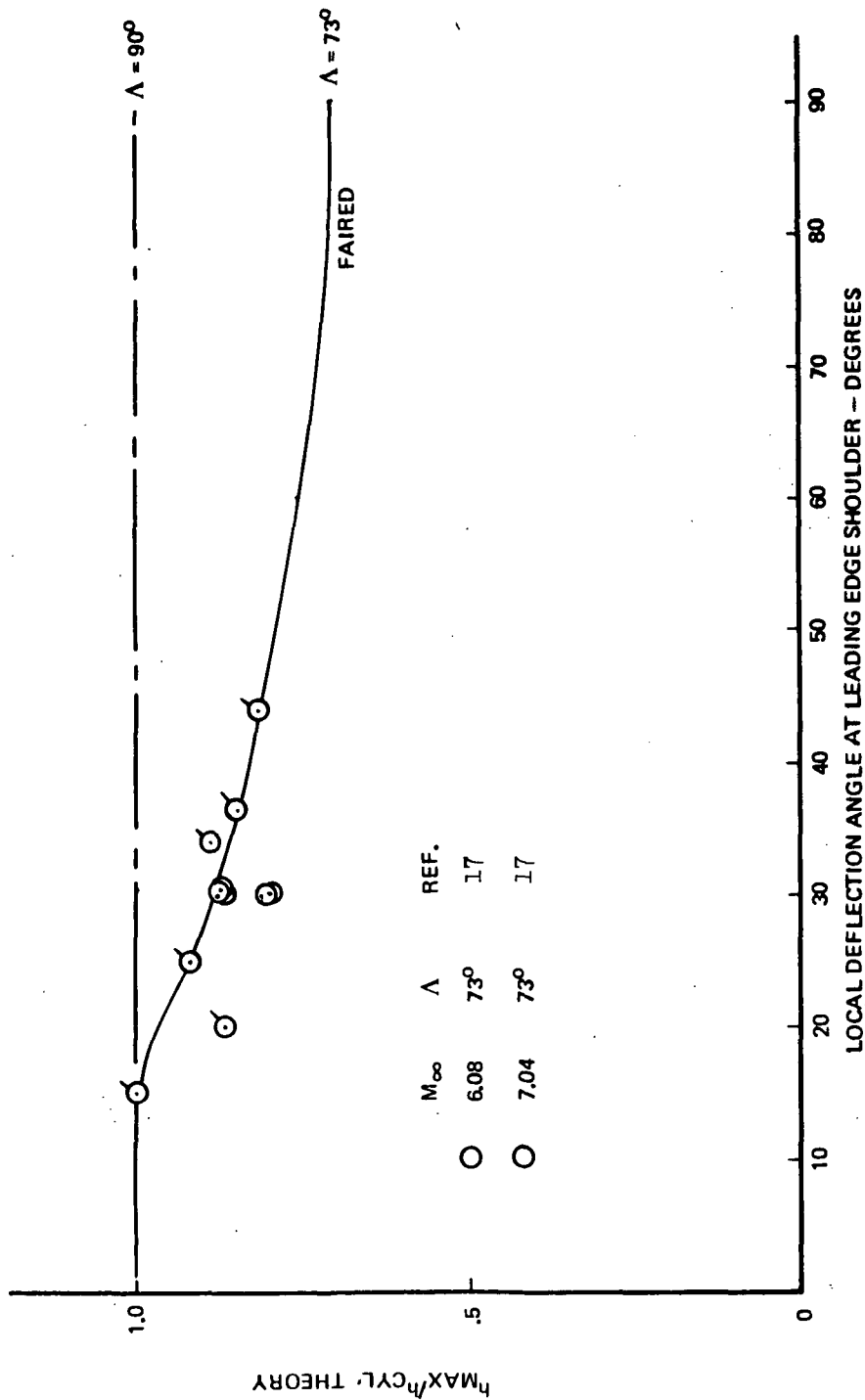
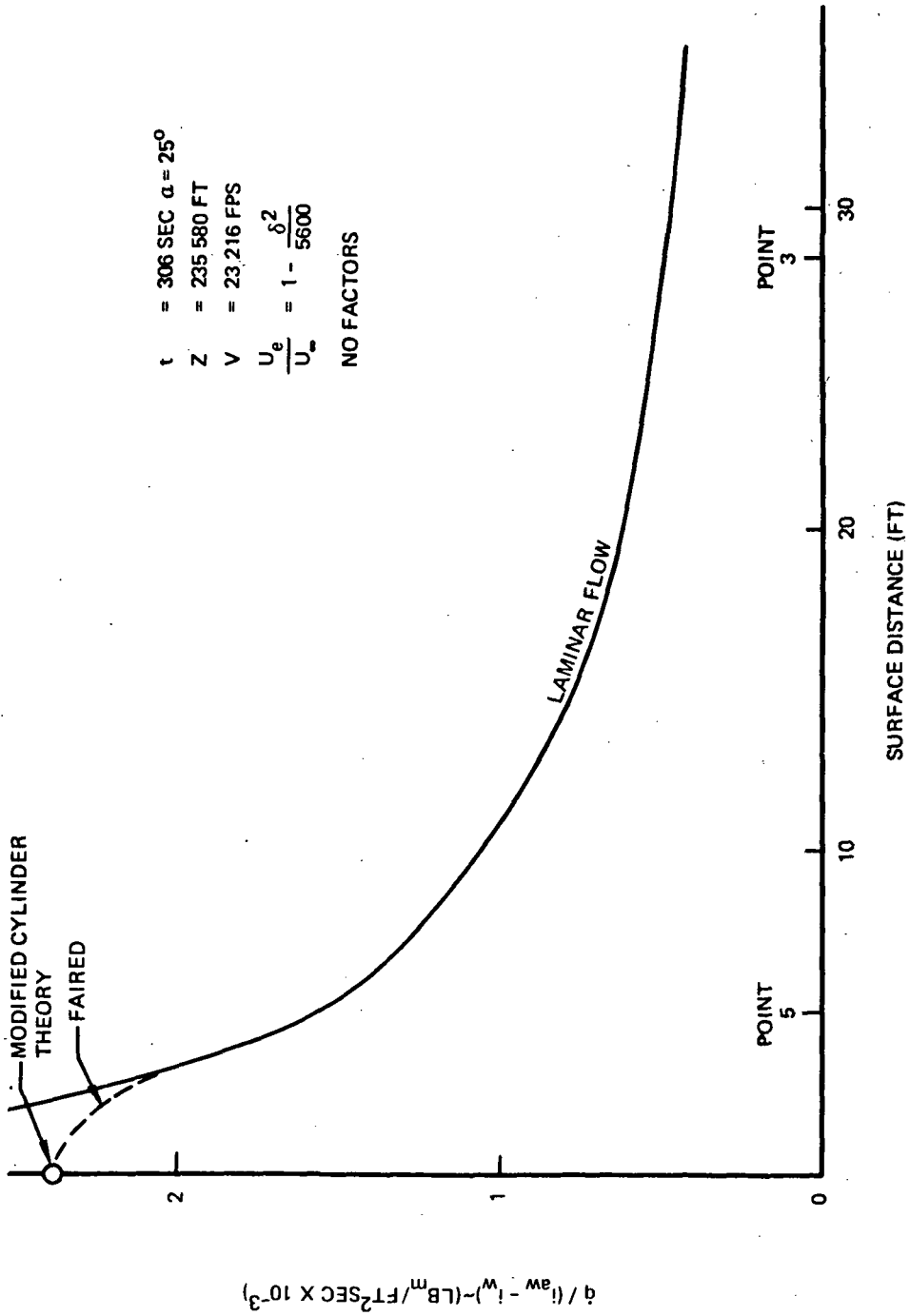


Figure 59: MAXIMUM TURBULENT HEATING ALONG THE LEADING EDGE OF A DELTA WING



$t = 306 \text{ SEC } \alpha = 25^\circ$
 $Z = 235.580 \text{ FT}$
 $V = 23.216 \text{ FPS}$
 $\frac{U_e}{U_\infty} = 1 - \frac{\delta^2}{5600}$
 NO FACTORS

Figure 60: WING LOWER SURFACE HEAT TRANSFER COEFFICIENT DISTRIBUTION

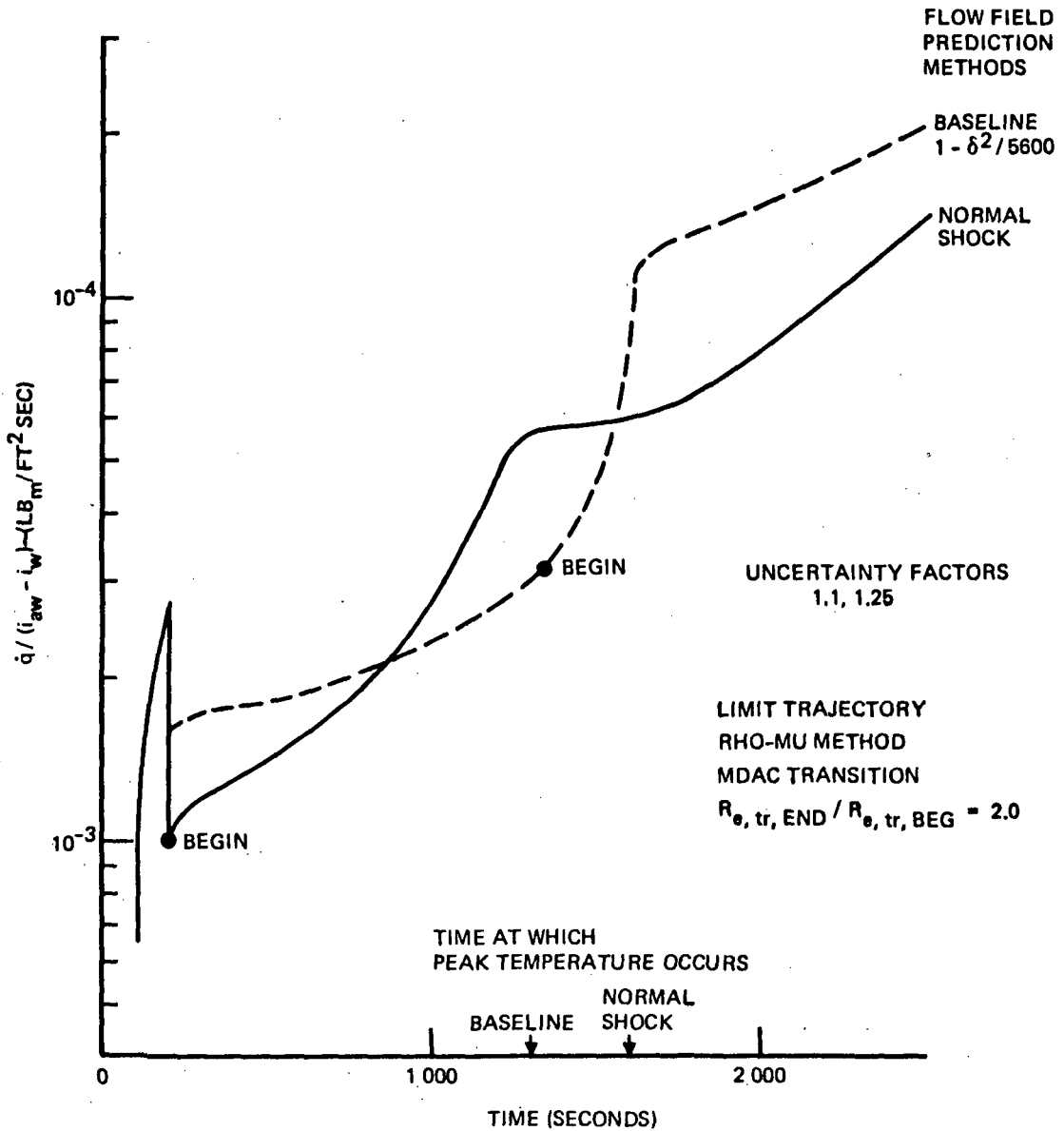


Figure 61. HEAT TRANSFER COEFFICIENT HISTORY AT WING LOWER SURFACE LEADING EDGE BEAM

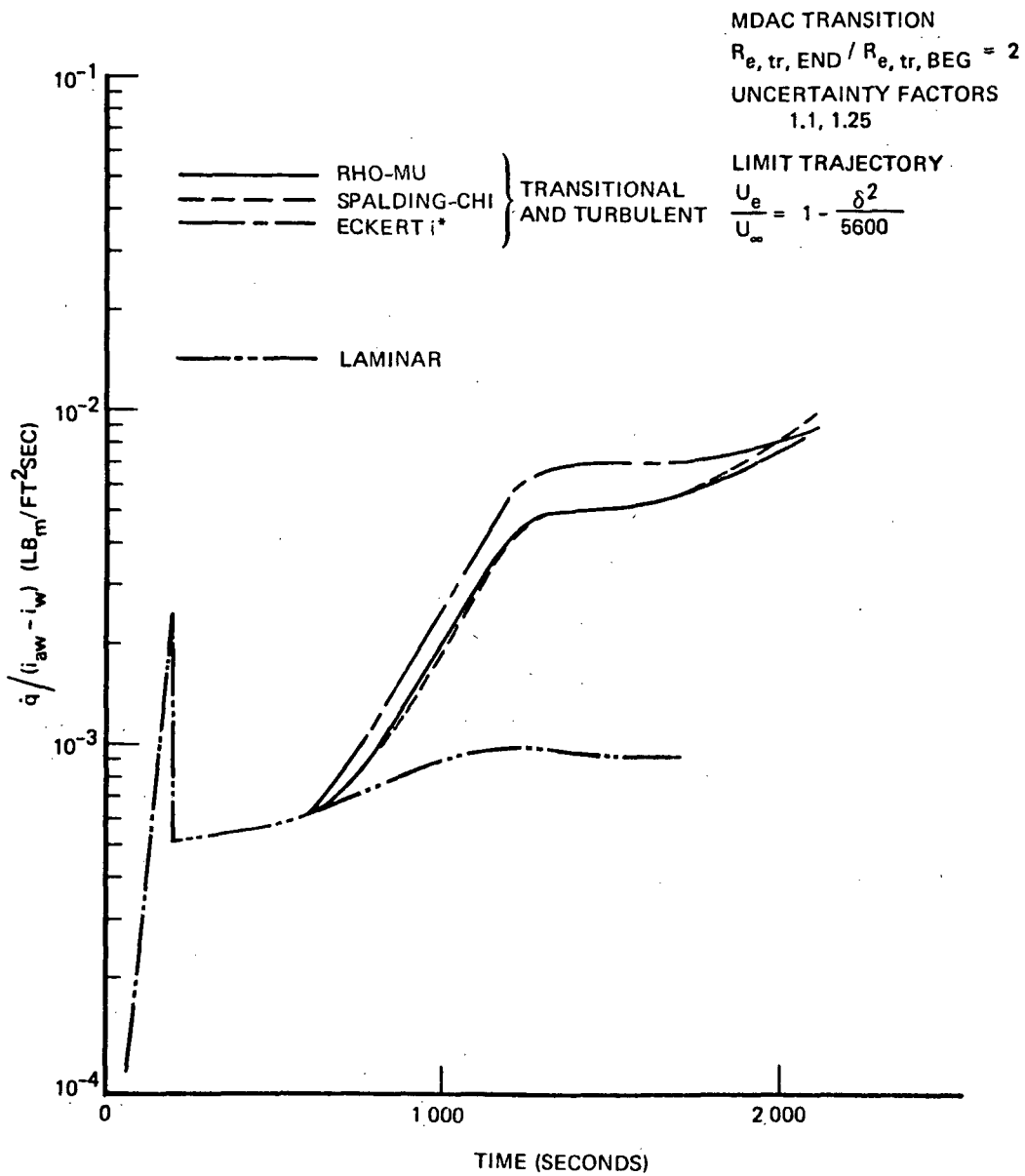


Figure 62: HEAT TRANSFER COEFFICIENT HISTORY AT THE WING LOWER SURFACE MIDSPAN AND MIDCHORD

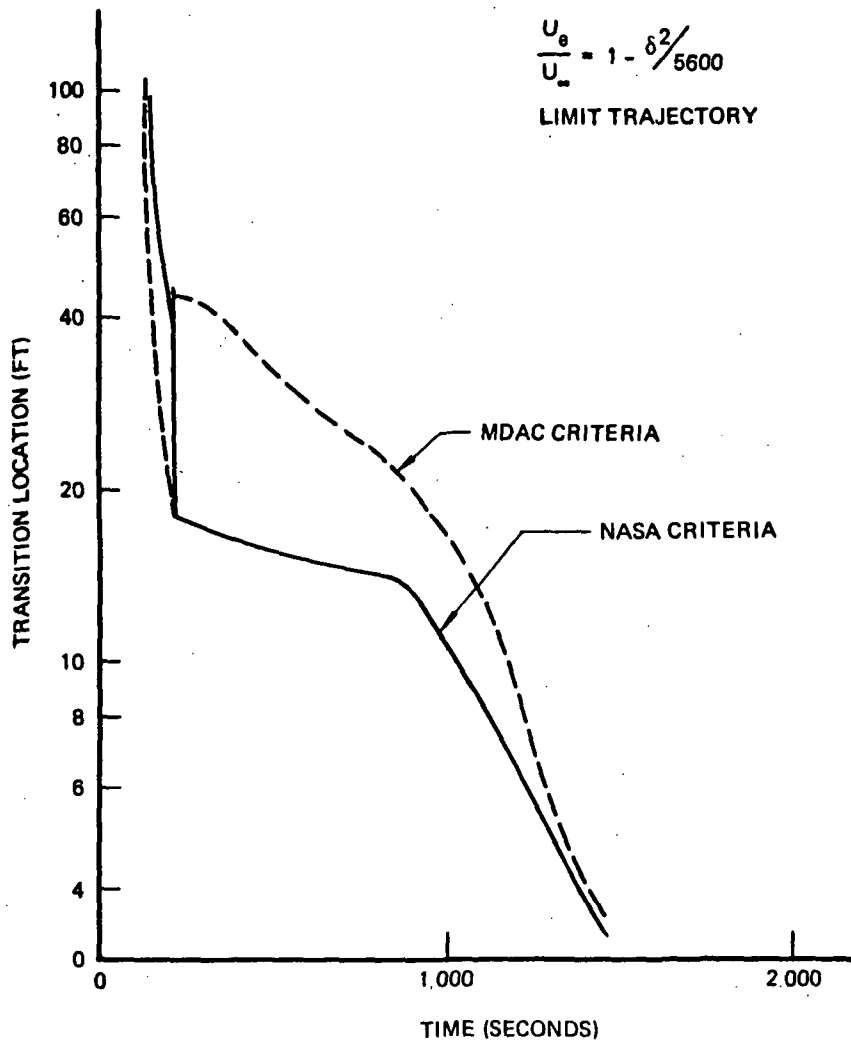


Figure 63. LOCATION OF BOUNDARY LAYER TRANSITION ON WING LOWER SURFACE

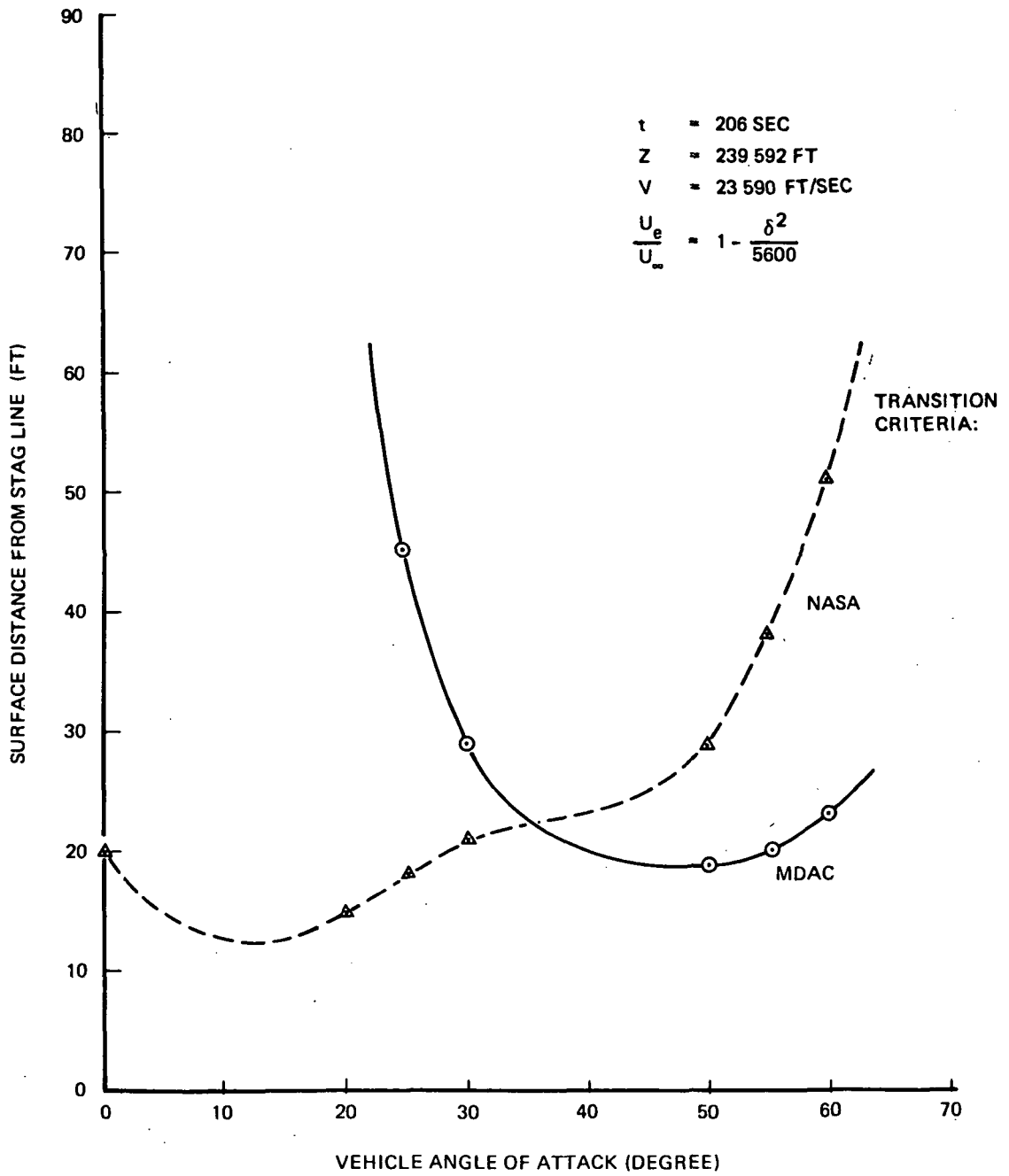


Figure 64. COMPARISON OF BOUNDARY LAYER TRANSITION LOCATION ON THE WING AT MIDSPAN AS A FUNCTION OF ANGLE OF ATTACK

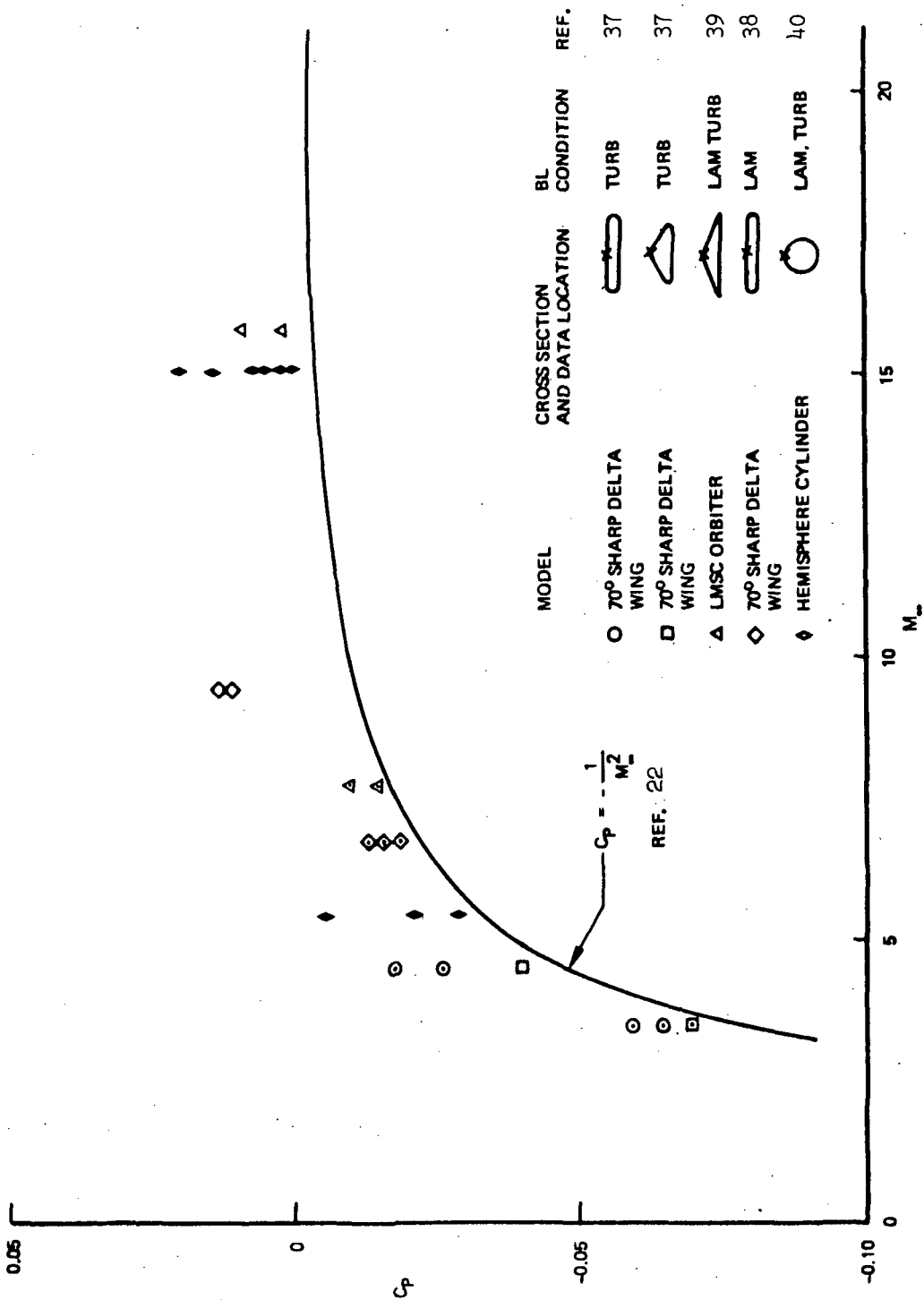


Figure 65. UPPER SURFACE PRESSURE IN SEPARATED FLOW, $\delta < -15^\circ$

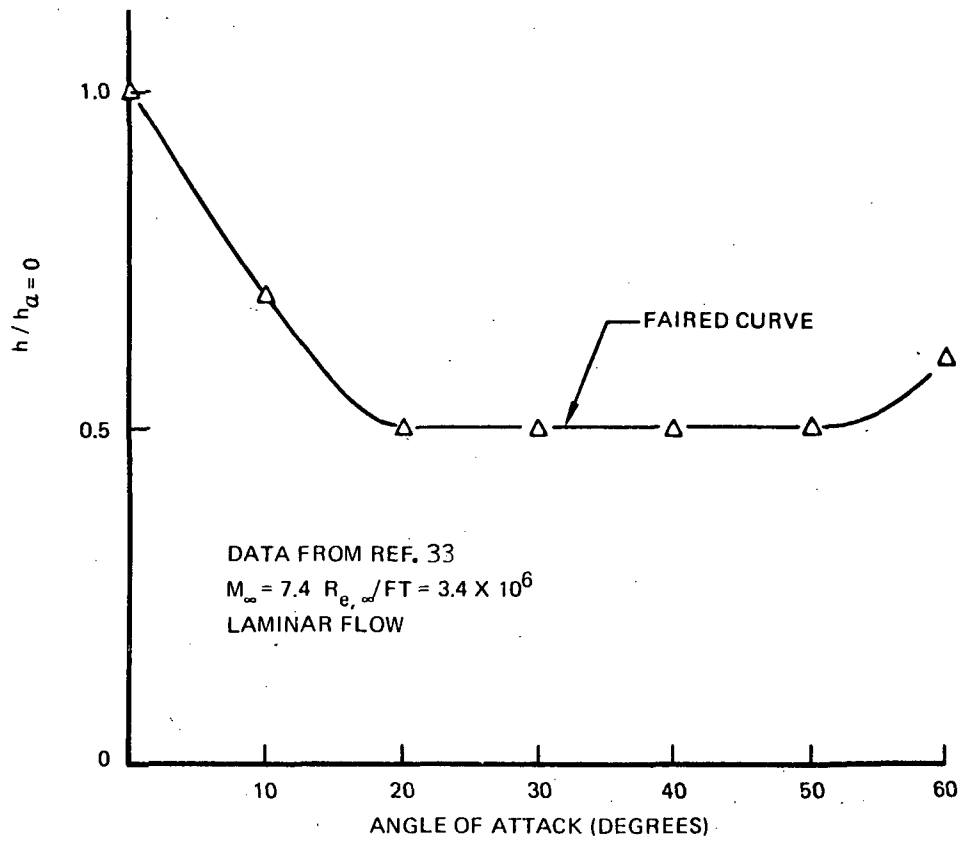


Figure 66. HEAT TRANSFER ON THE WING UPPER SURFACE OF A DELTA WING BOOSTER MODEL, 50% EXPOSED SEMISPAN, 50% CHORD

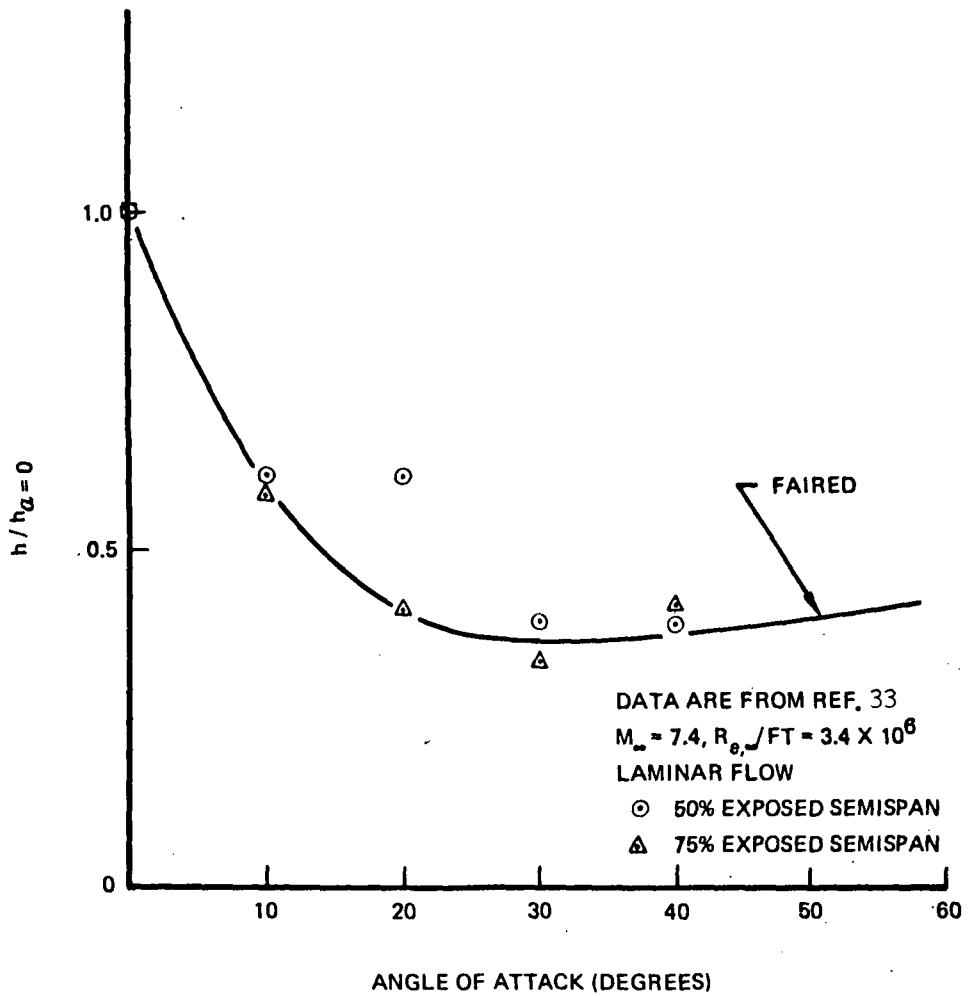


Figure 67. HEAT TRANSFER ON THE SIDE OF CENTER-MOUNTED TAIL FIN ON A DELTA WING BOOSTER, 50% CHORD

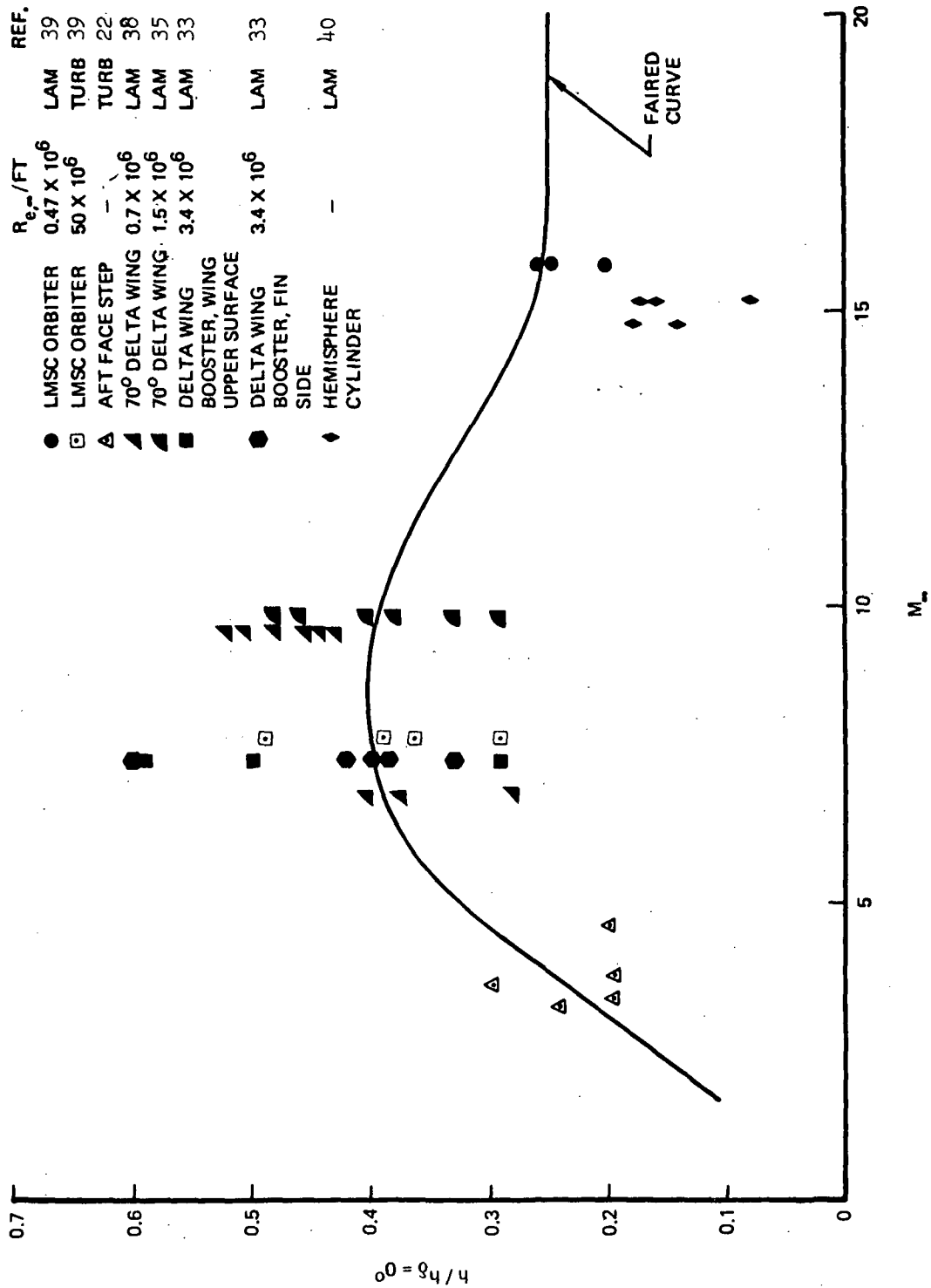


Figure 68. UPPER SURFACE HEATING, SEPARATED FLOW, $\delta < -15^\circ$

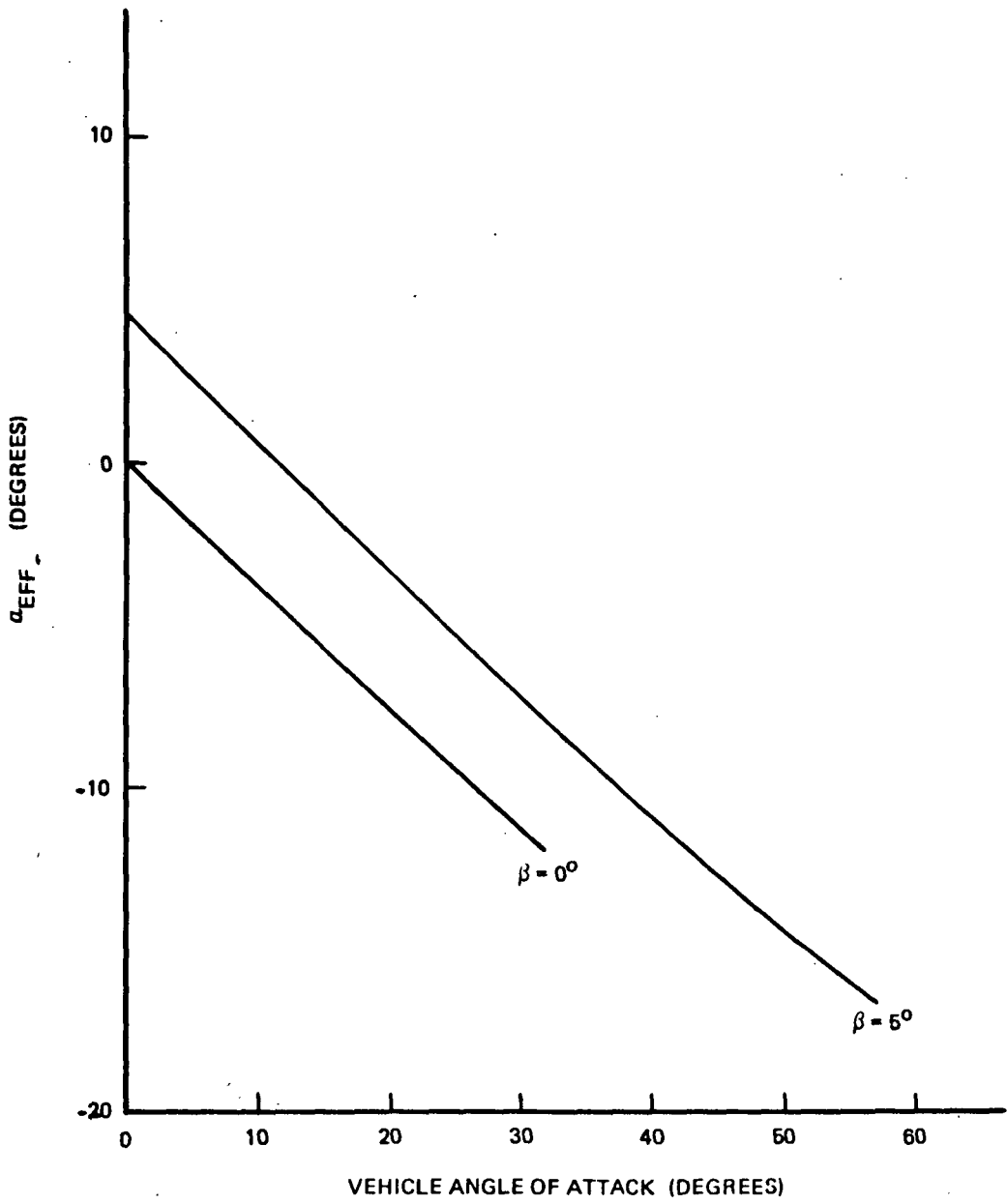


Figure 69: EFFECTIVE ANGLE OF ATTACK OF POINT NUMBER 2

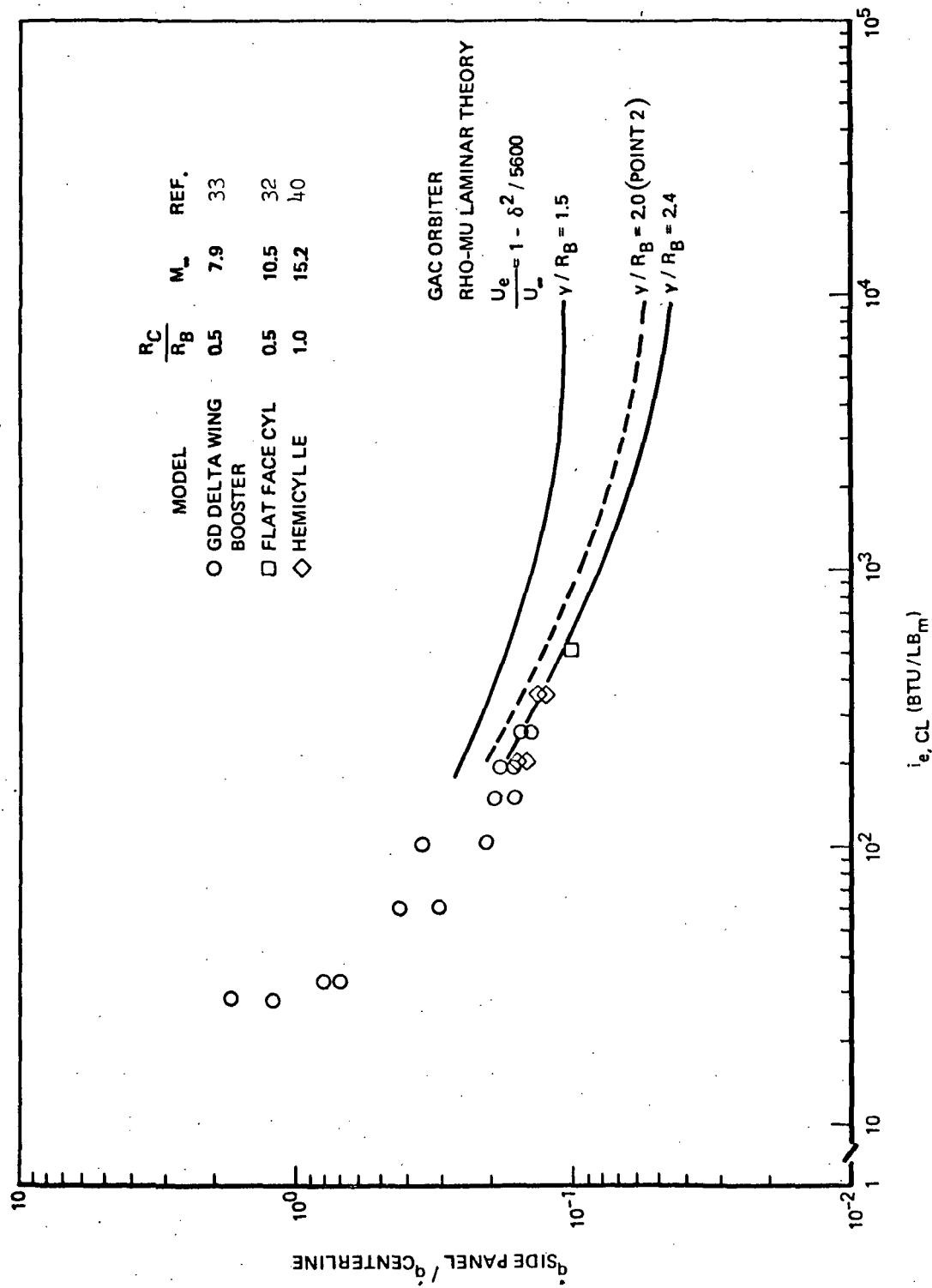


Figure 70: FUSELAGE SIDE PANEL HEATING, $\alpha_{\text{EFF}} = 0^\circ$, LAMINAR FLOW

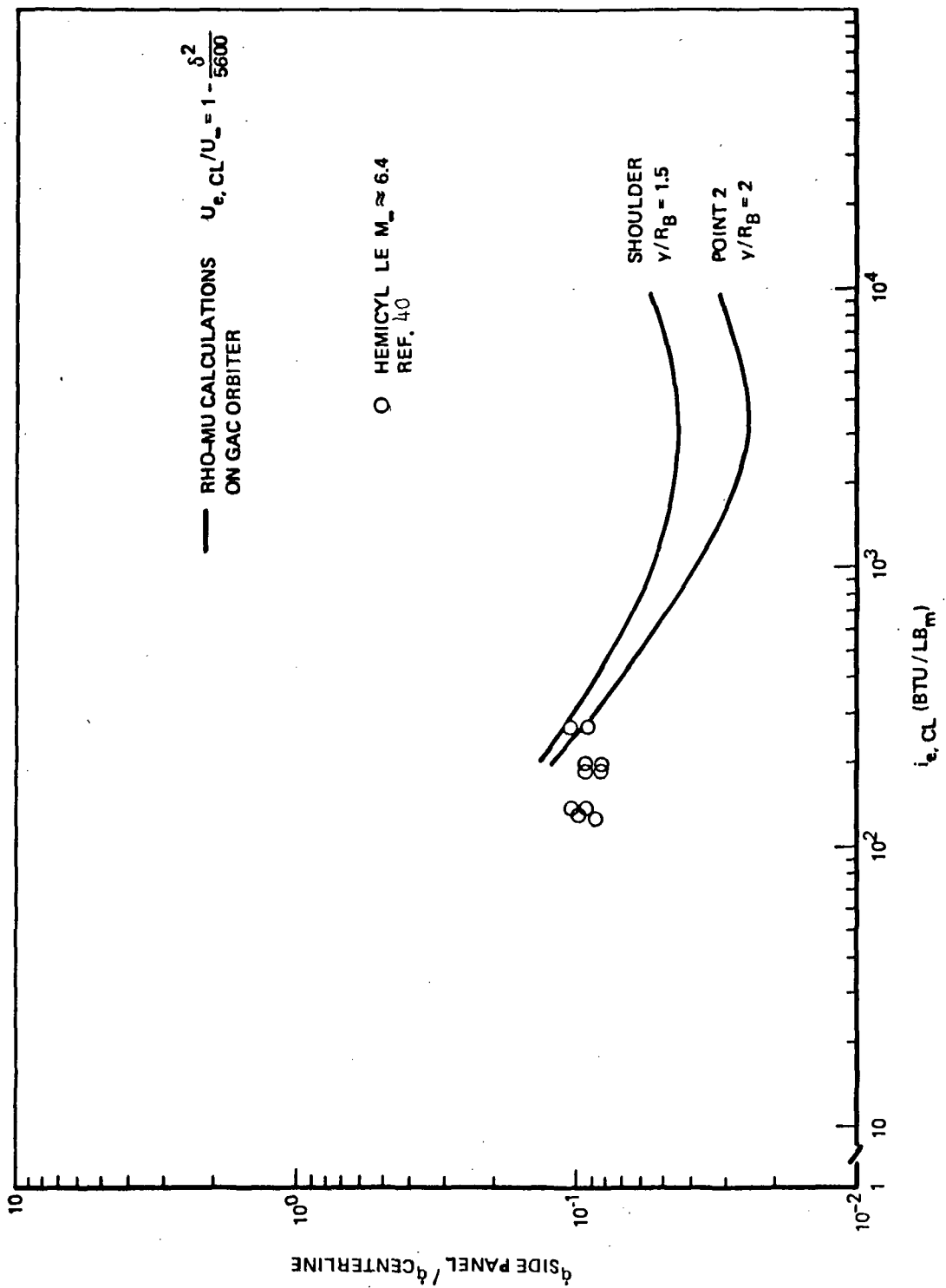


Figure 71. FUSELAGE SIDE PANEL HEATING, $\alpha_{EFF} = 0^\circ$, TURBULENT FLOW

REFERENCE AREA = 5747 FT²
TRIMMED FLIGHT
REF. 42

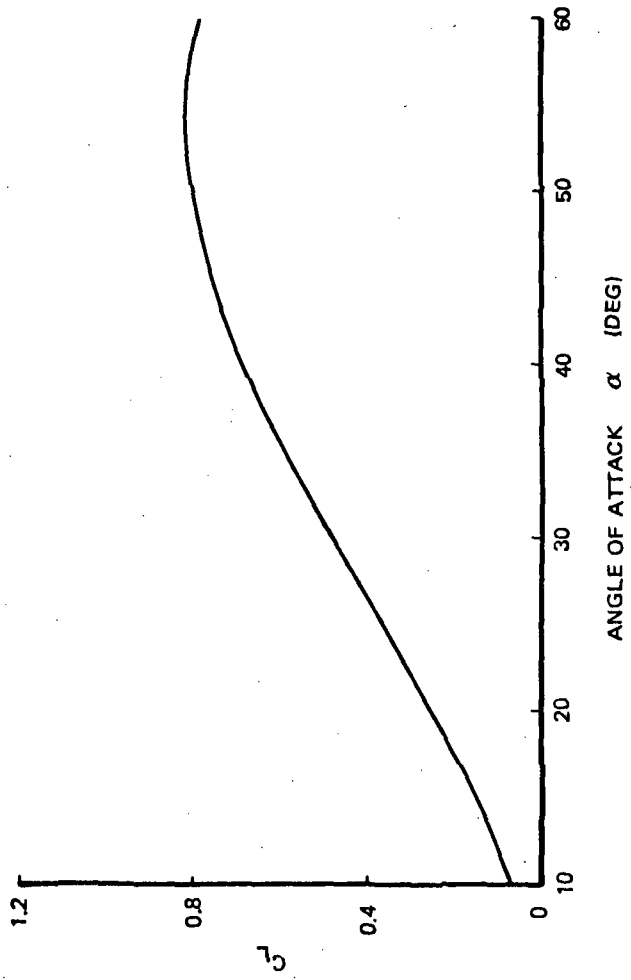


Figure 72. G-3A ORBITER HYPERSONIC LIFT COEFFICIENT

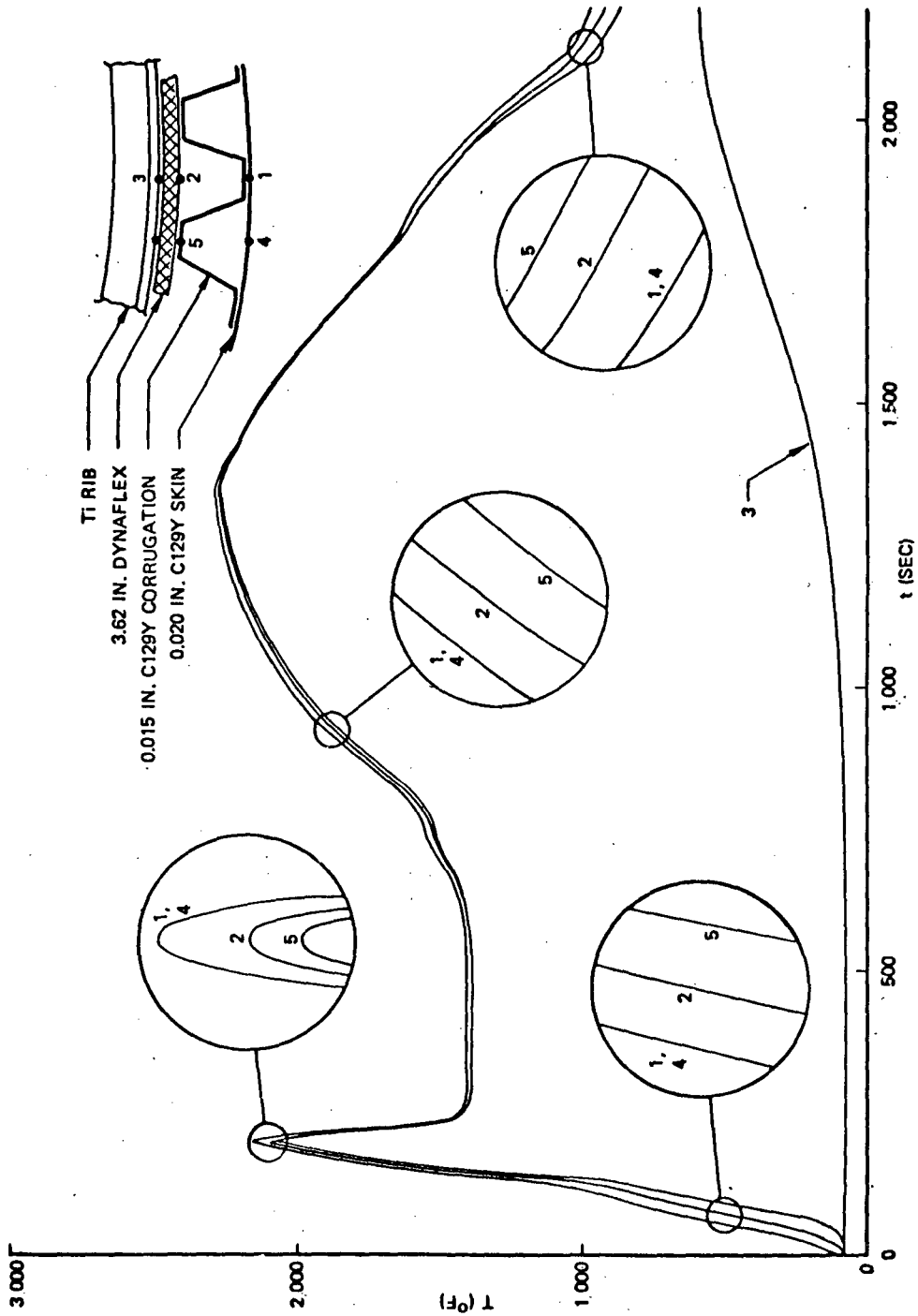
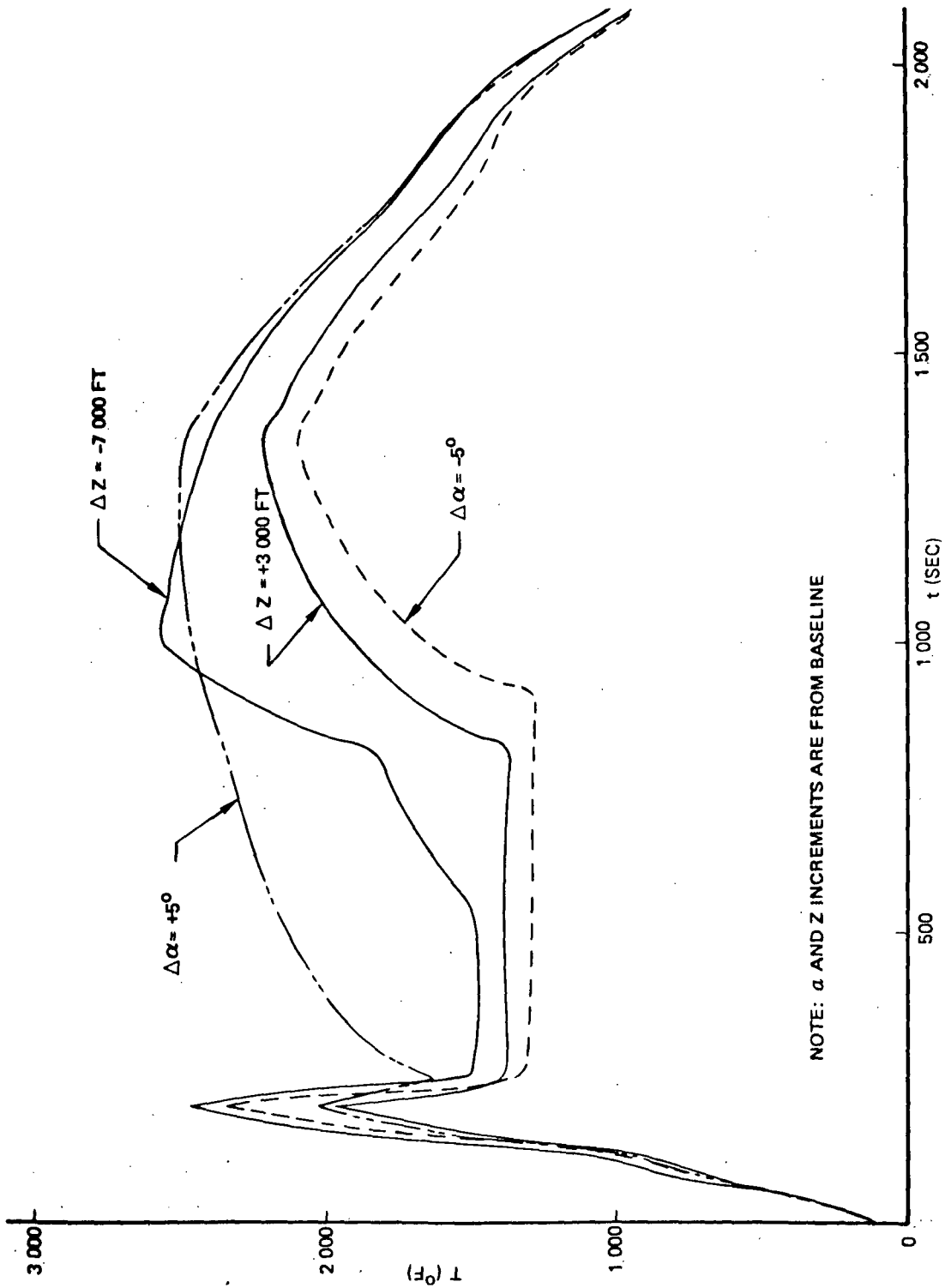


Figure 73: PT. NO. 3 - BASELINE TPS TEMPERATURES



NOTE: α AND Z INCREMENTS ARE FROM BASELINE

Figure 74. PT. NO. 3 - SURFACE TEMPERATURES ALTITUDE AND ANGLE OF ATTACK PERTURBATIONS

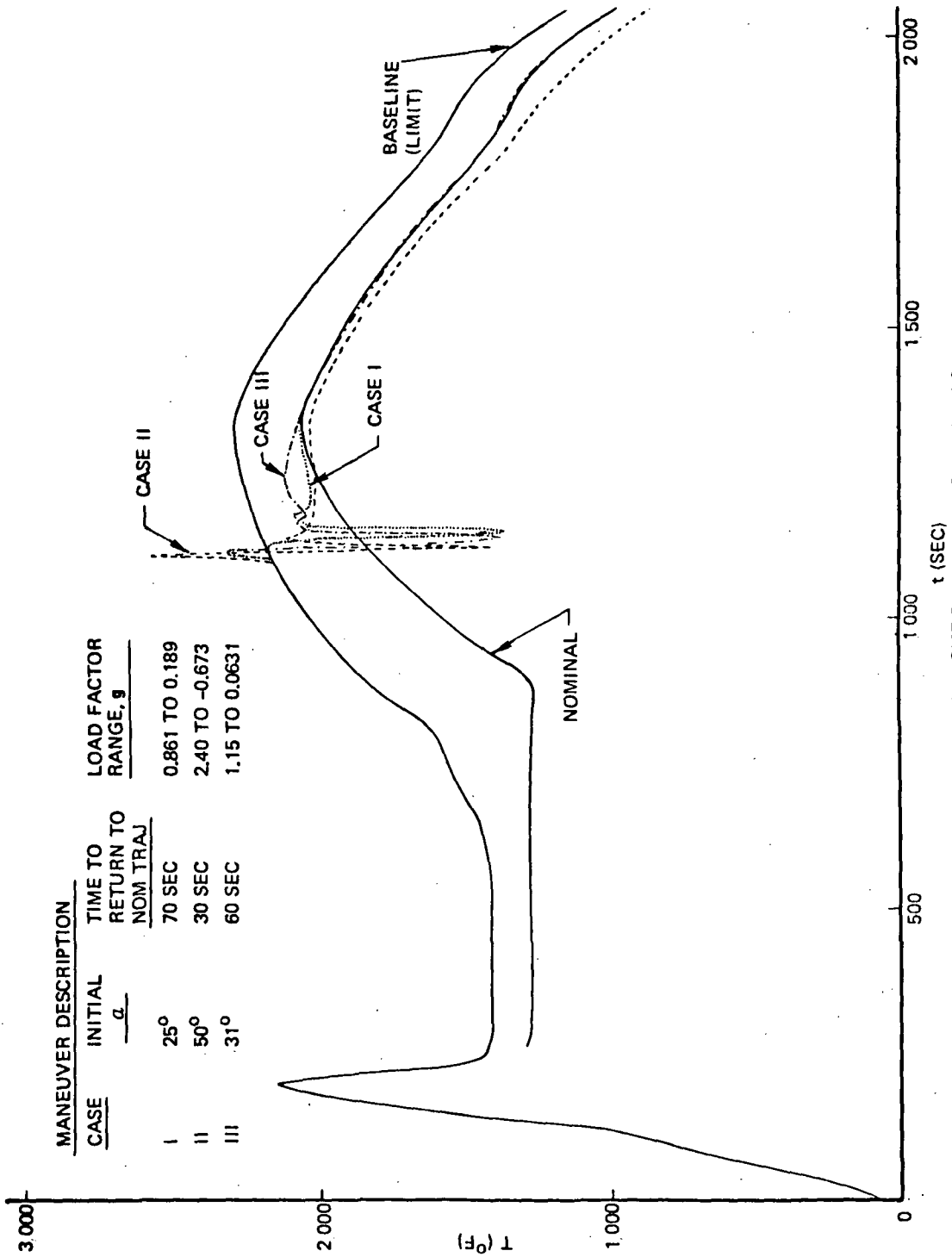


Figure 75. POINT NO. 3 - SURFACE TEMPERATURES TRAJECTORY AND MANEUVER PERTURBATIONS

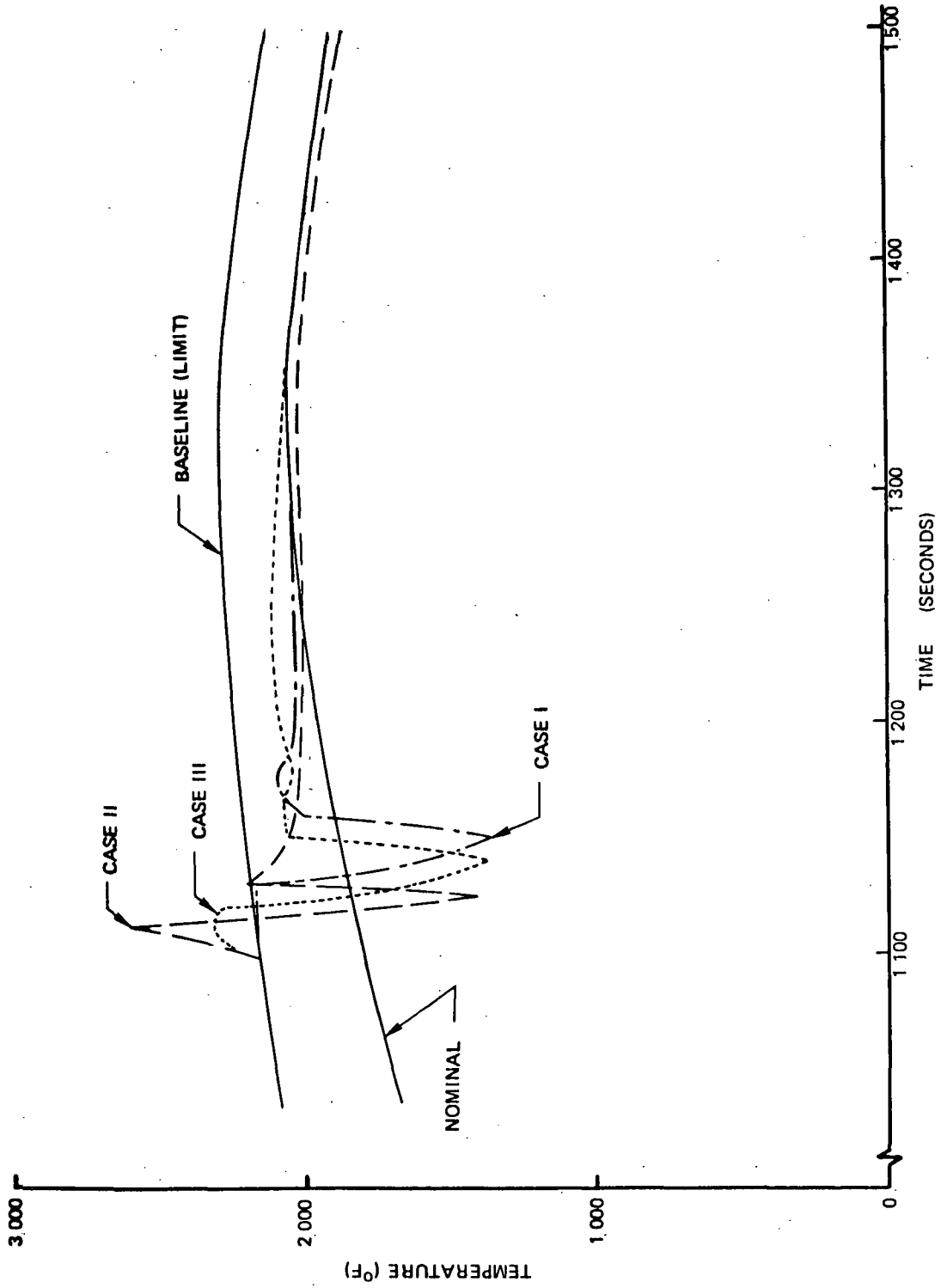


Figure 76. POINT NO. 3 SURFACE TEMPERATURES DURING MANEUVER PERIOD

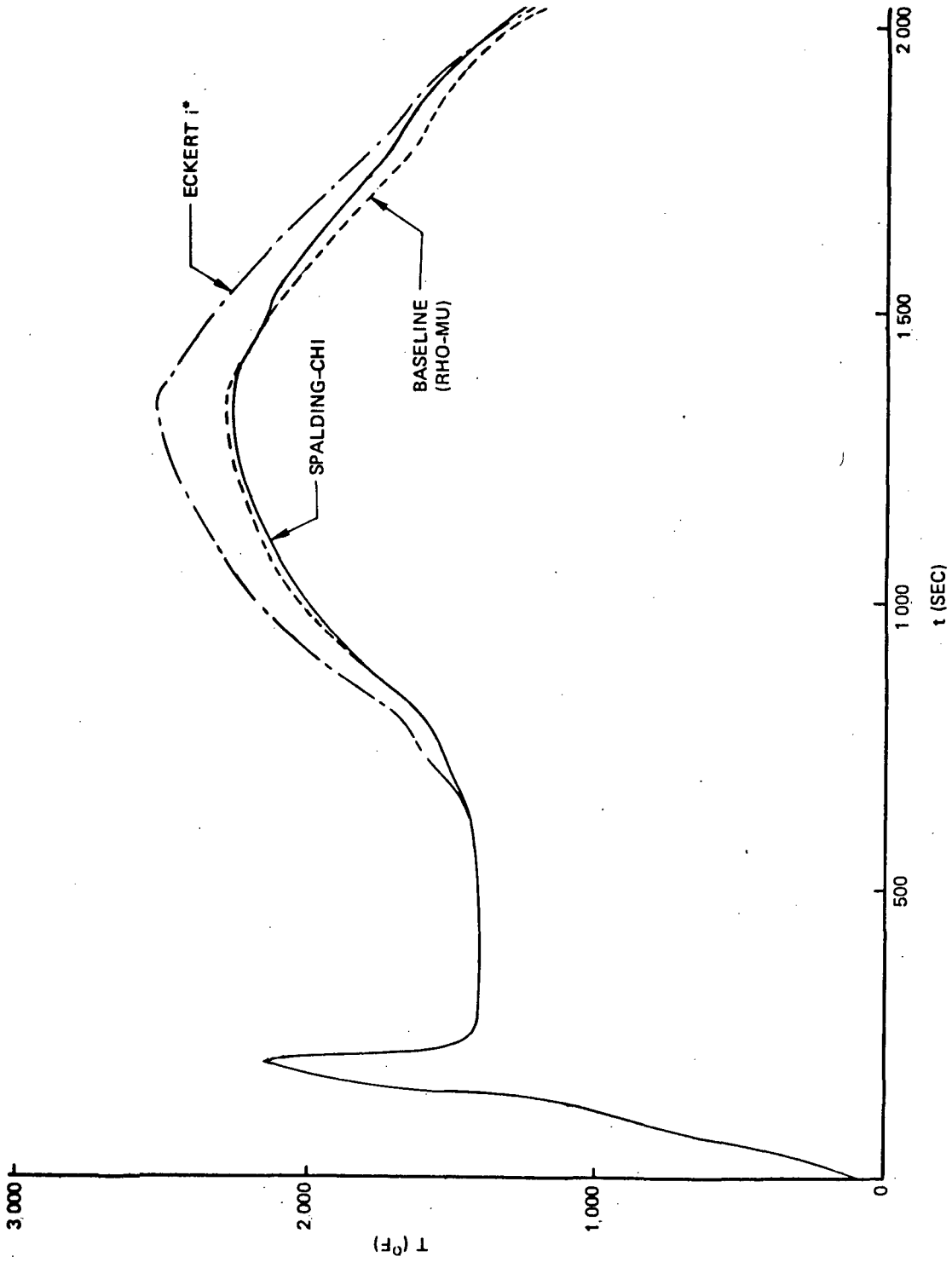
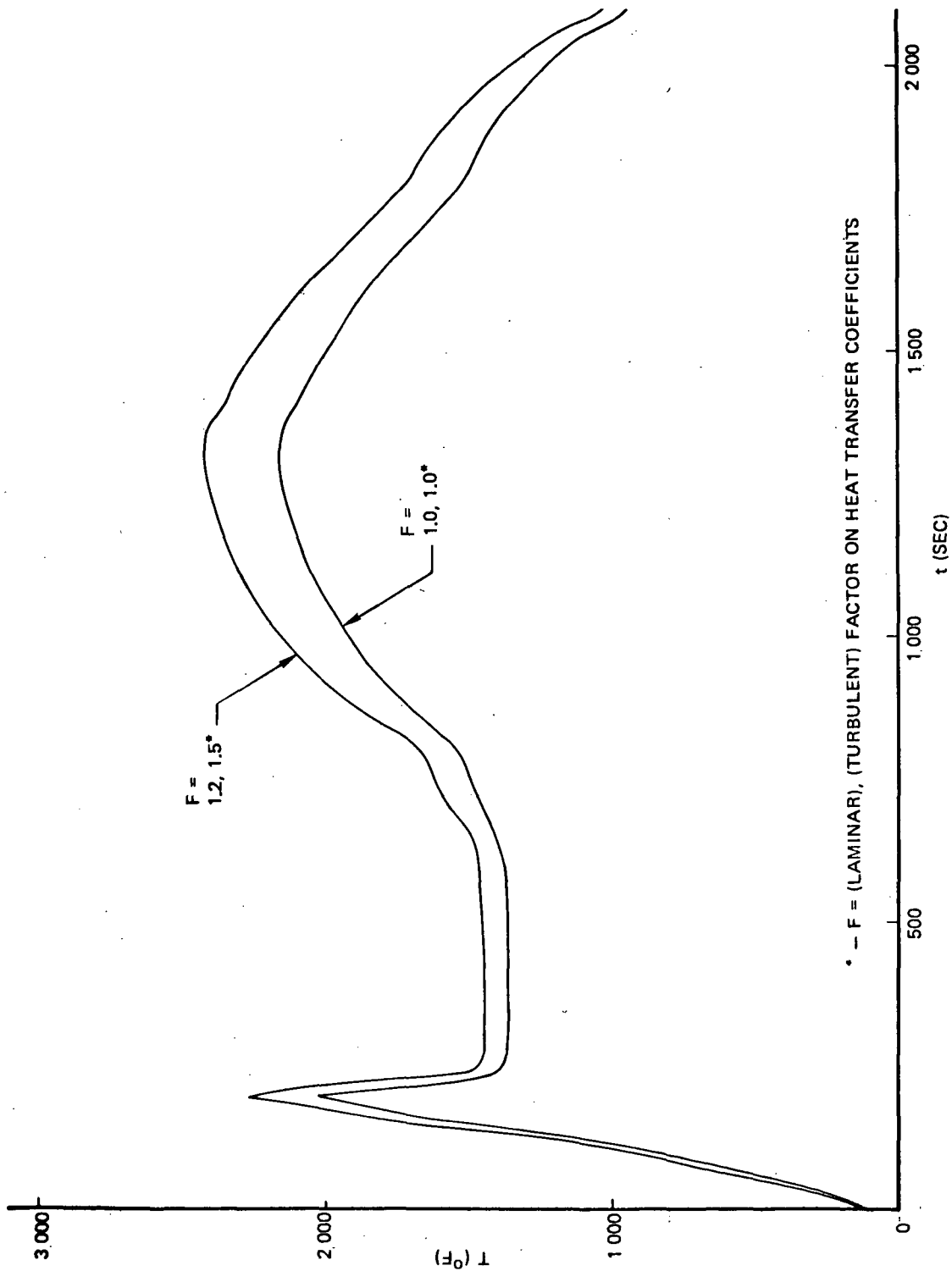


Figure 77: POINT NO. 3 SURFACE TEMPERATURES
TURBULENT PREDICTION METHOD PERTURBATIONS



* -- F = (LAMINAR), (TURBULENT) FACTOR ON HEAT TRANSFER COEFFICIENTS

Figure 78. POINT NO. 3 SURFACE TEMPERATURES
HEAT TRANSFER UNCERTAINTY FACTOR PERTURBATIONS

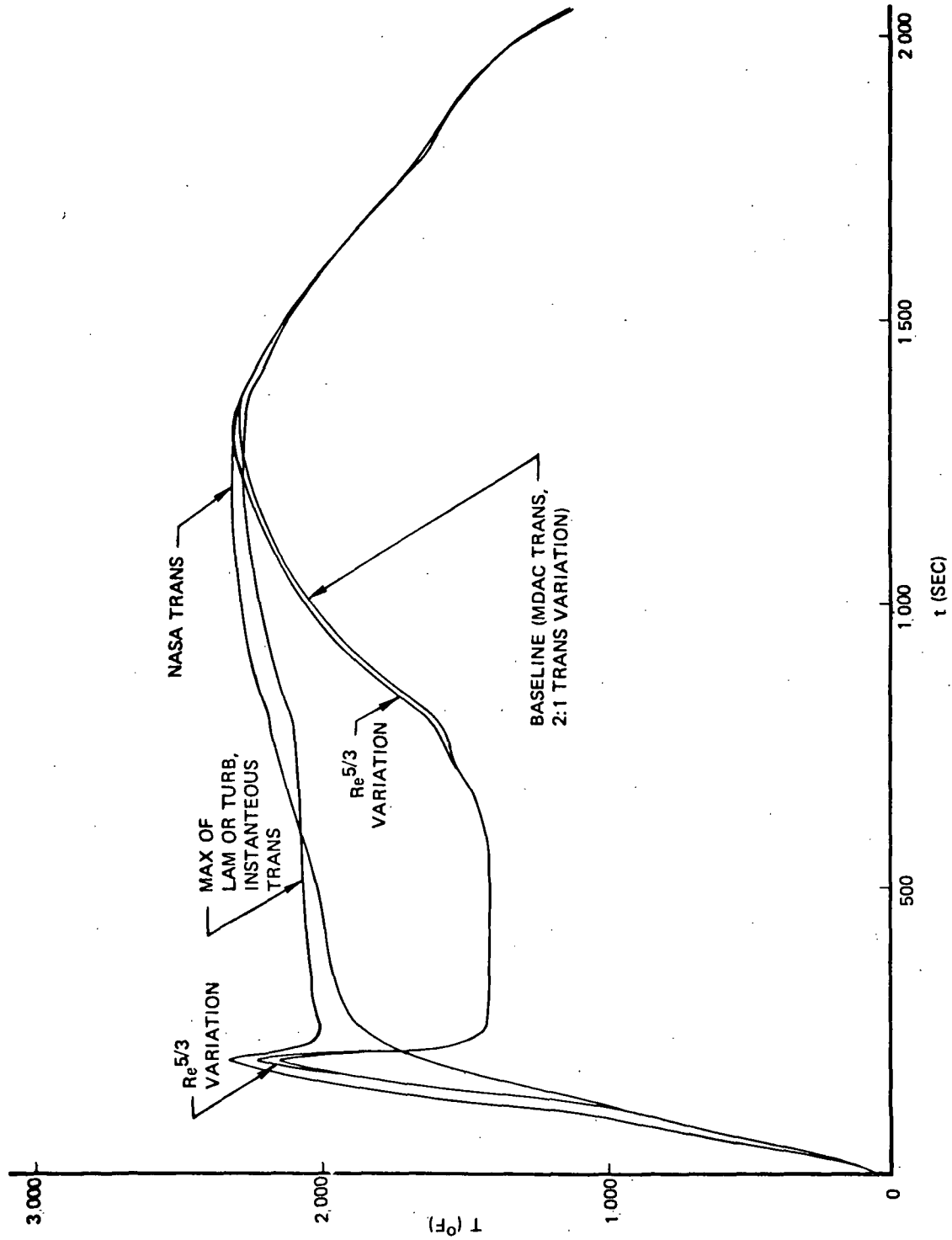


Figure 79. POINT NO. 3 SURFACE TEMPERATURES-PERTURBATIONS IN TRANSITION ONSET AND TRANSITION REGION VARIATIONS

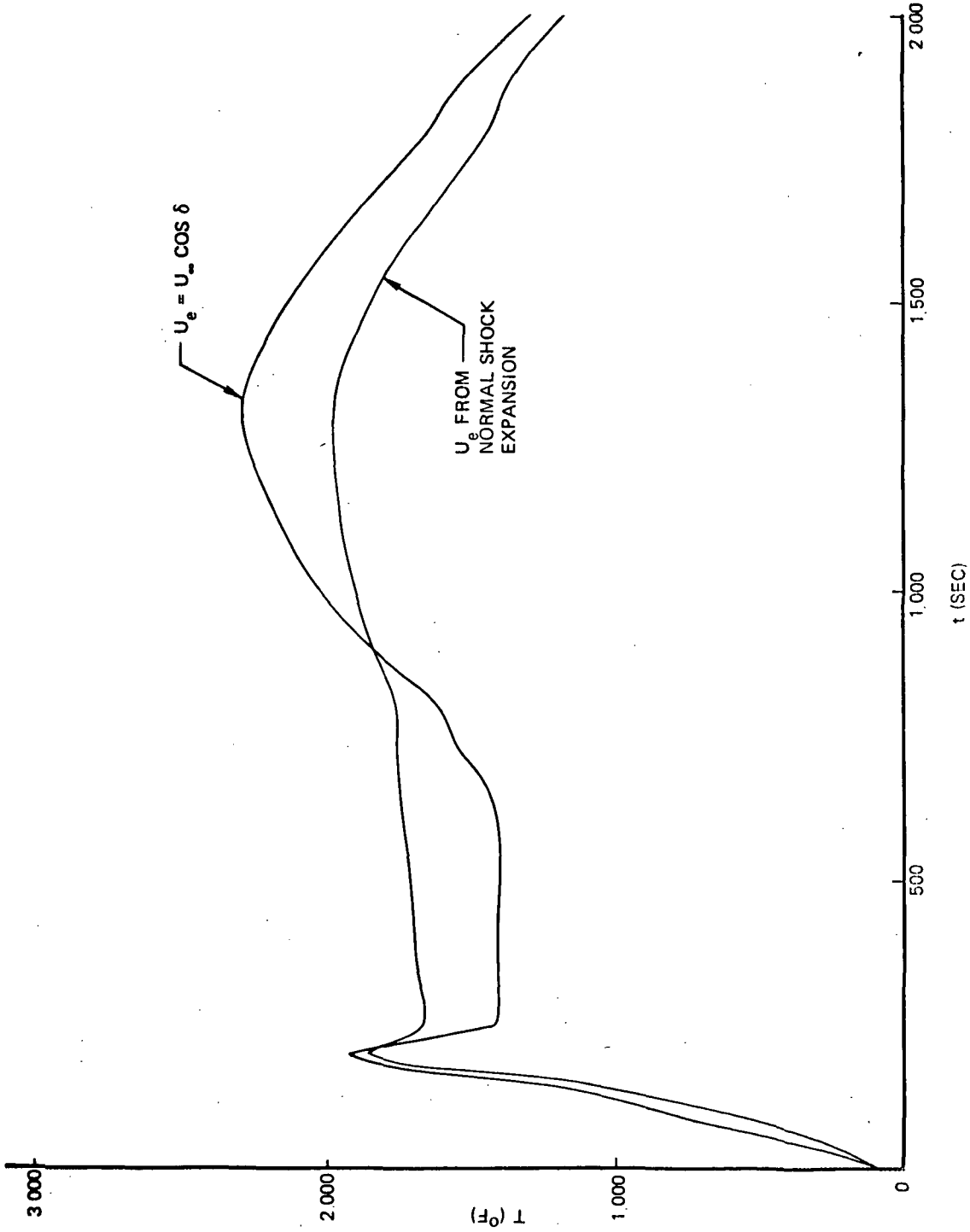


Figure 80. POINT NO. 3 SURFACE TEMPERATURES
 LOCAL VELOCITY PREDICTION METHOD PERTURBATIONS

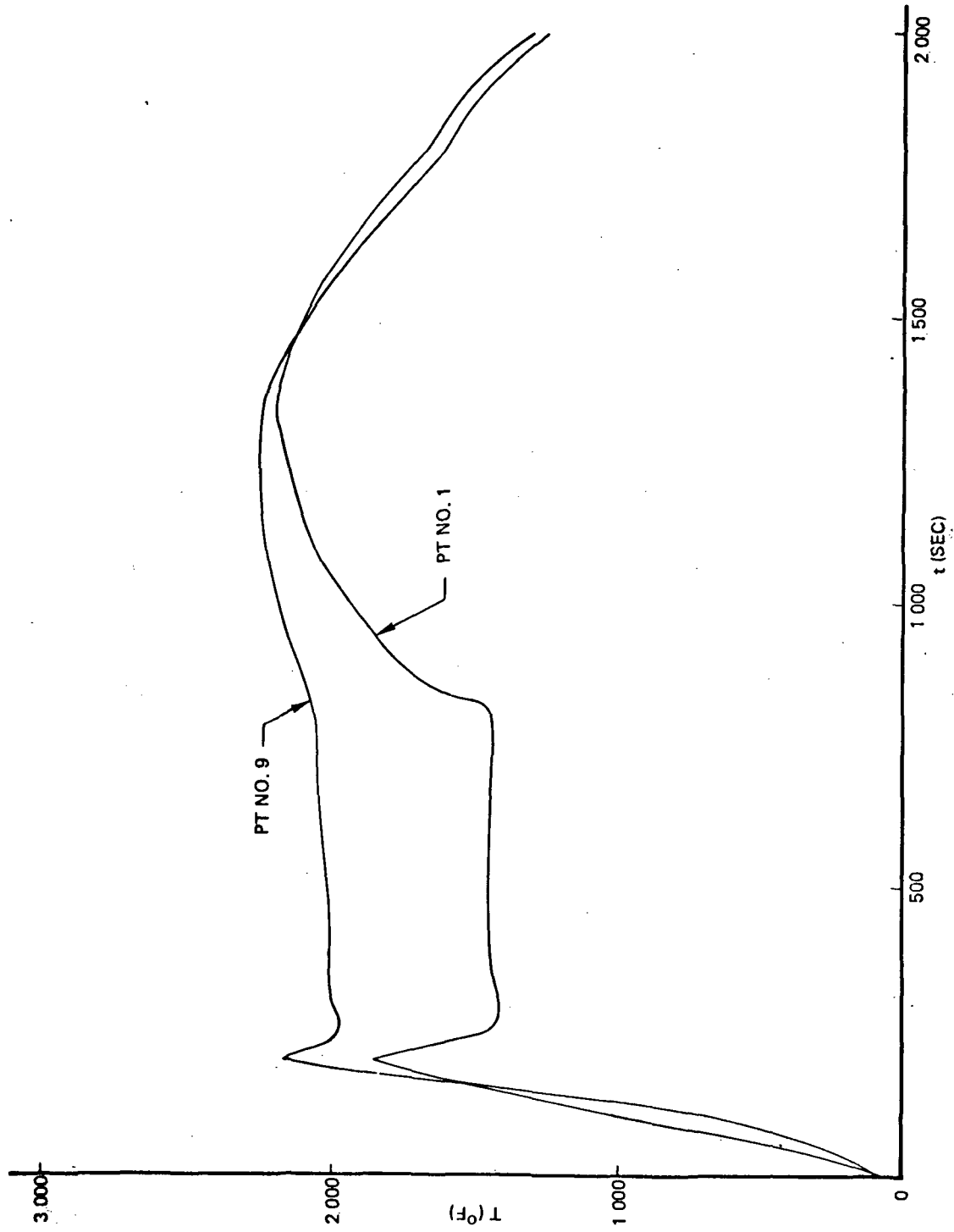


Figure 81. POINTS NO. 1 AND 9 SURFACE TEMPERATURES-BASELINE

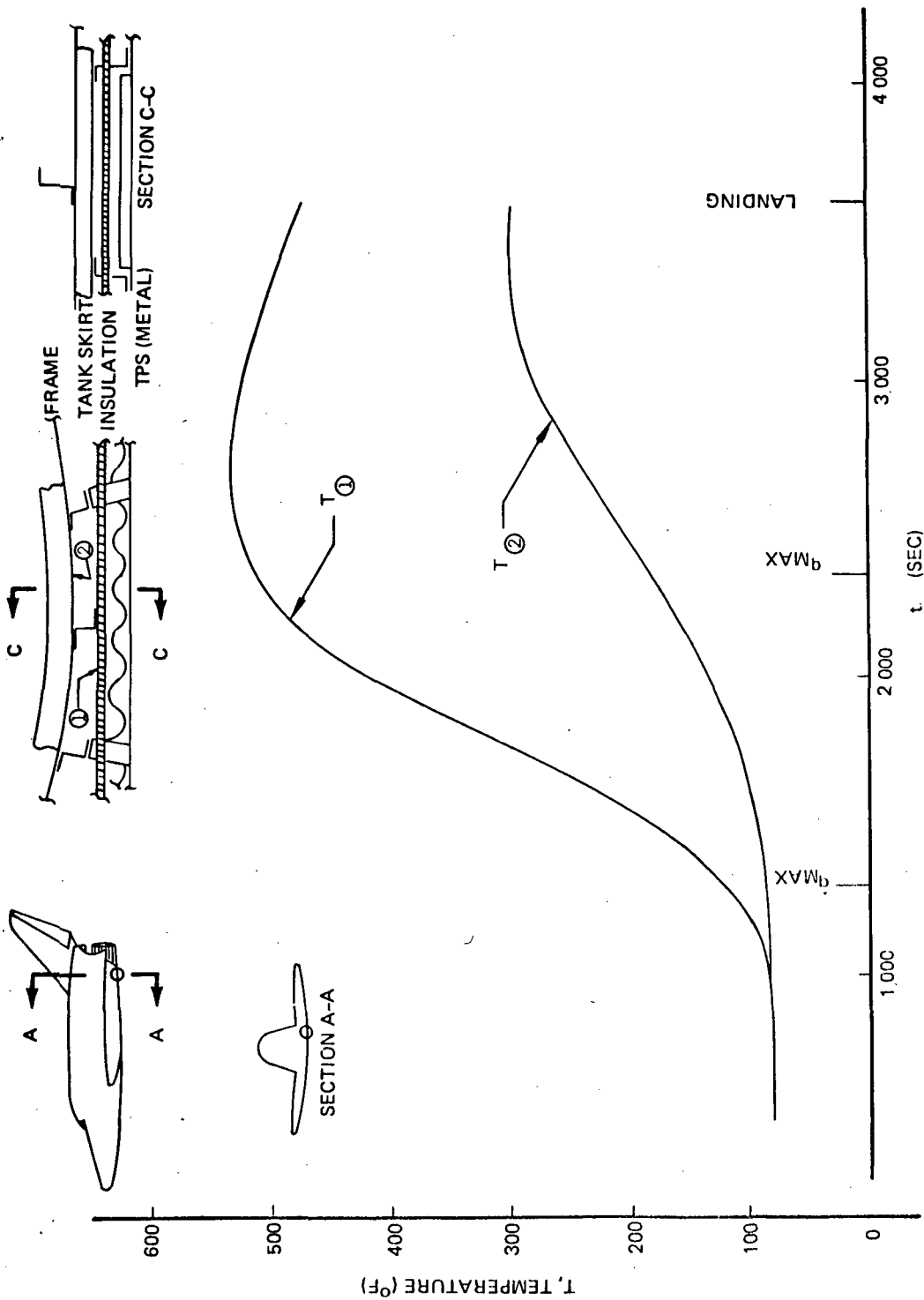


Figure 82: POINT NO. 9 INTERNAL TEMPERATURES-BASELINE

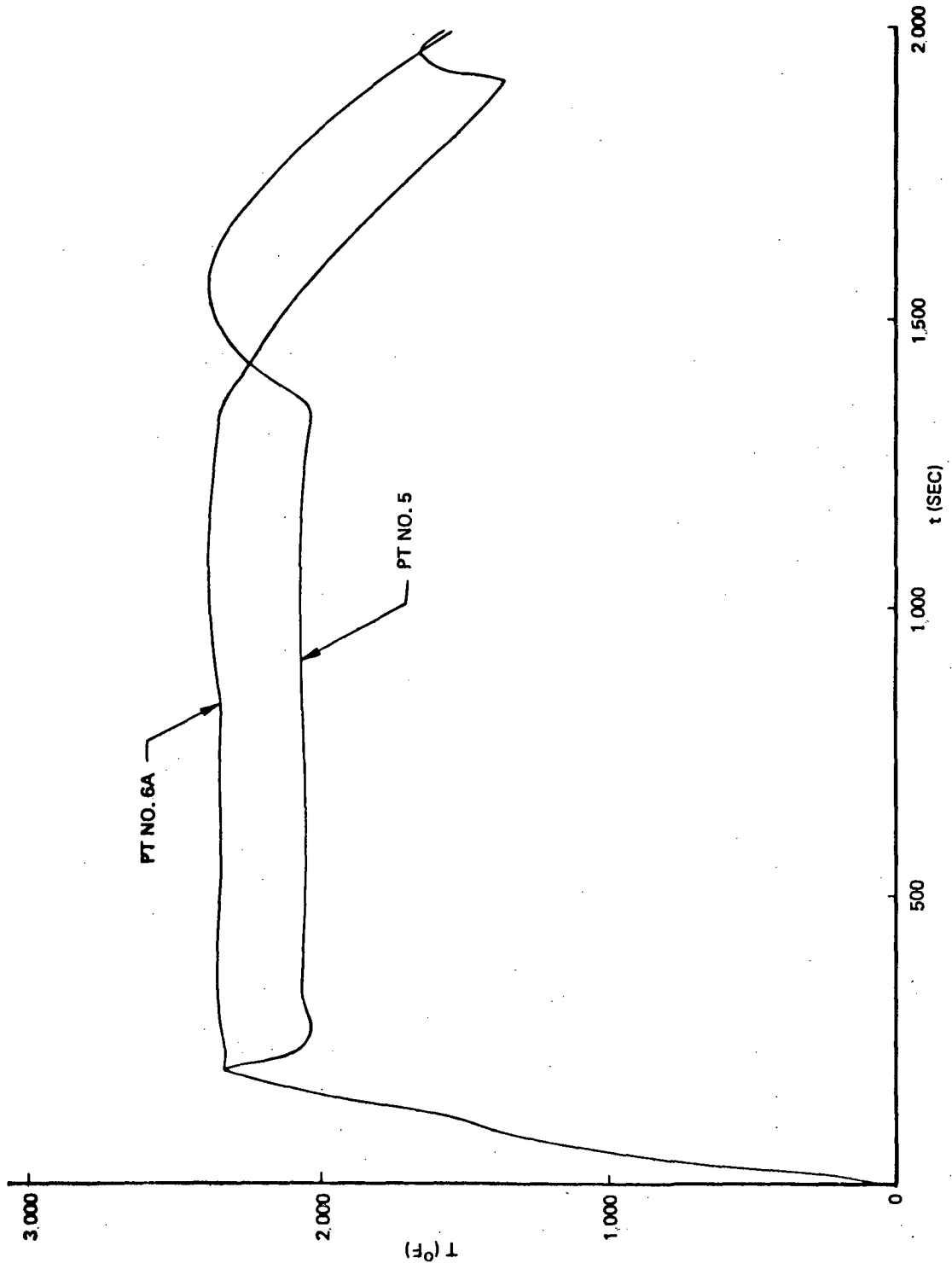


Figure 83: POINTS NO. 5 AND 6A SURFACE TEMPERATURES - BASELINE

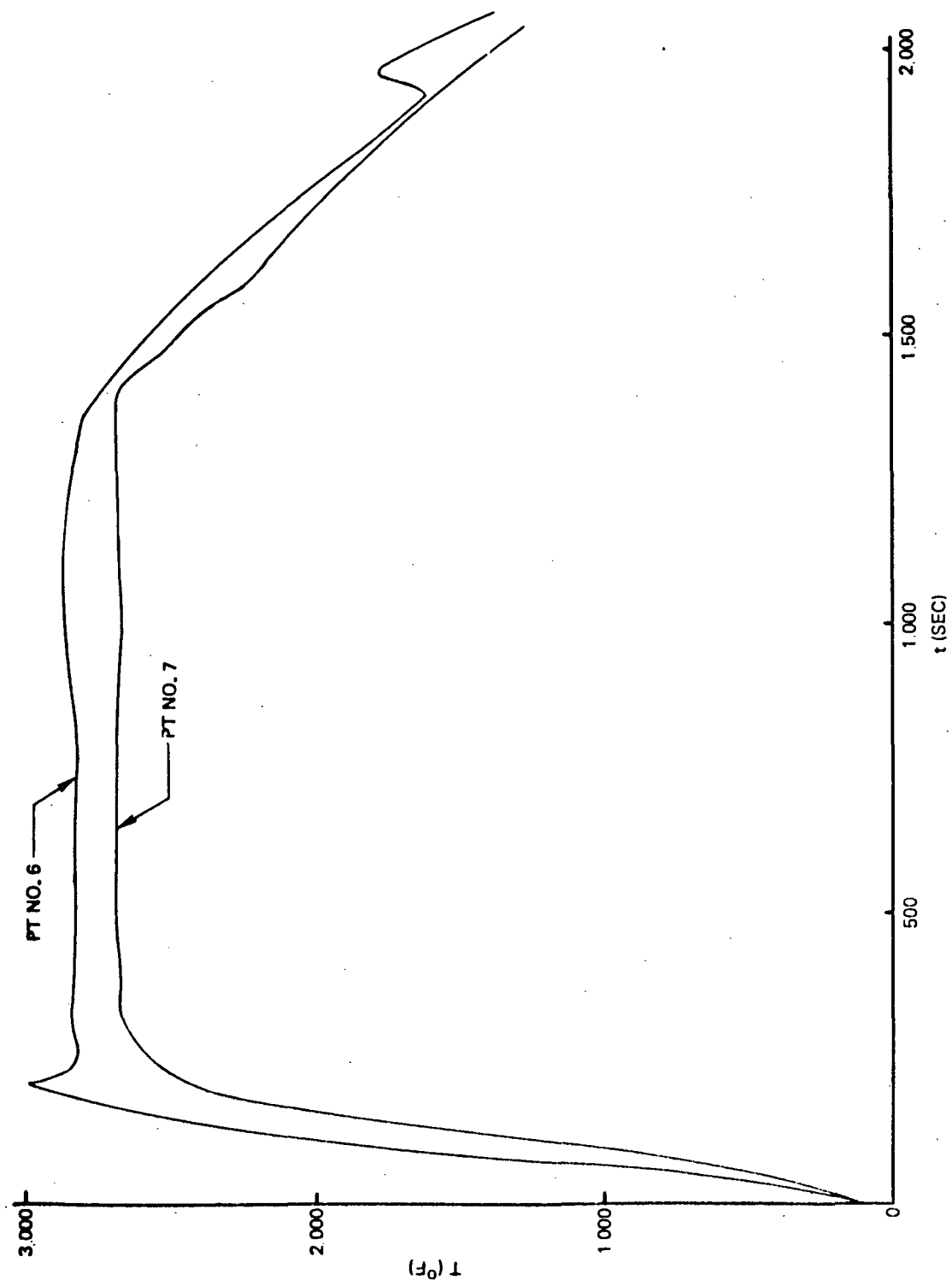


Figure 84: POINTS NO. 6 AND 7 SURFACE TEMPERATURES-BASELINE

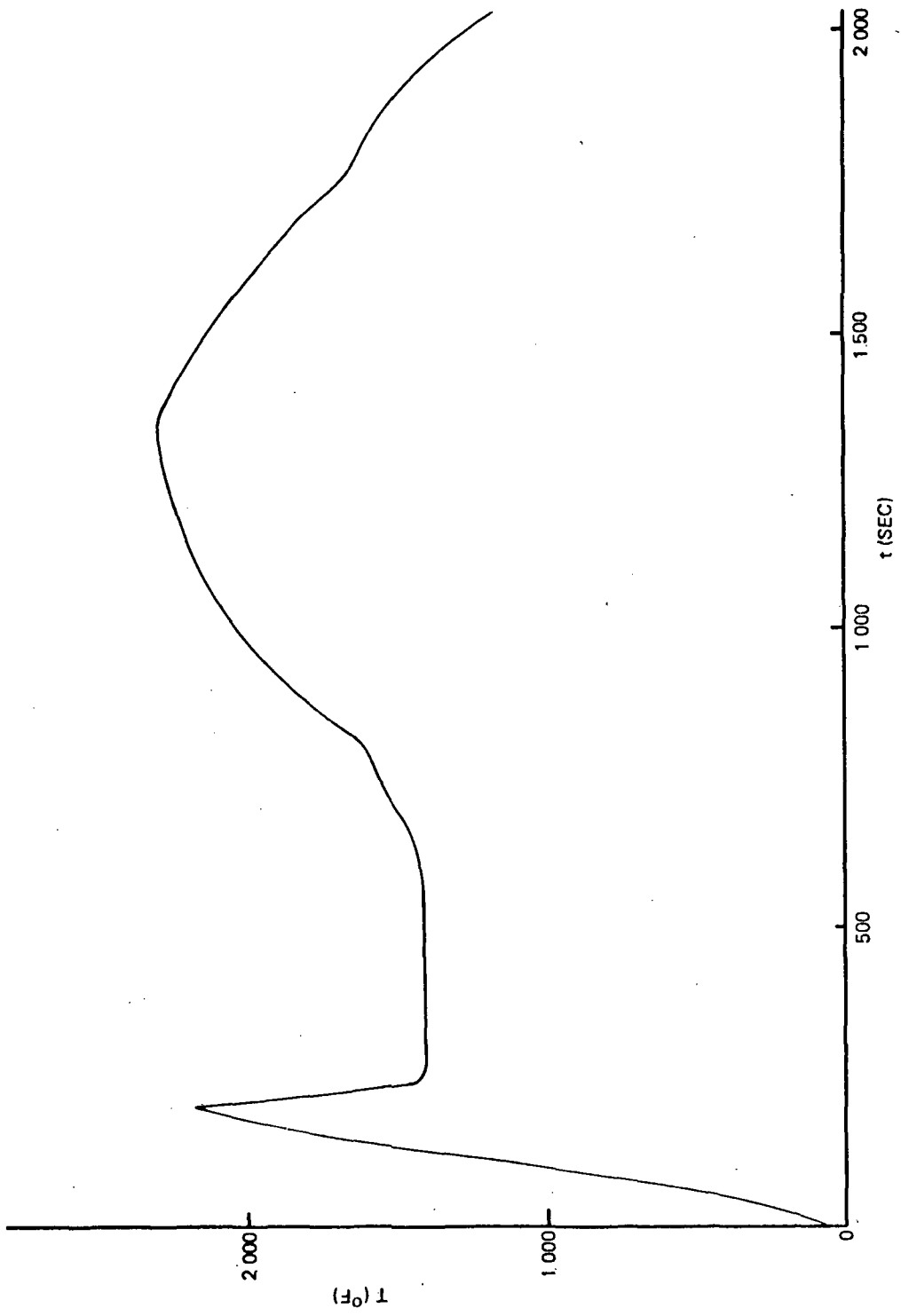


Figure 85 : POINT NO. 3A SURFACE TEMPERATURES-BASELINE

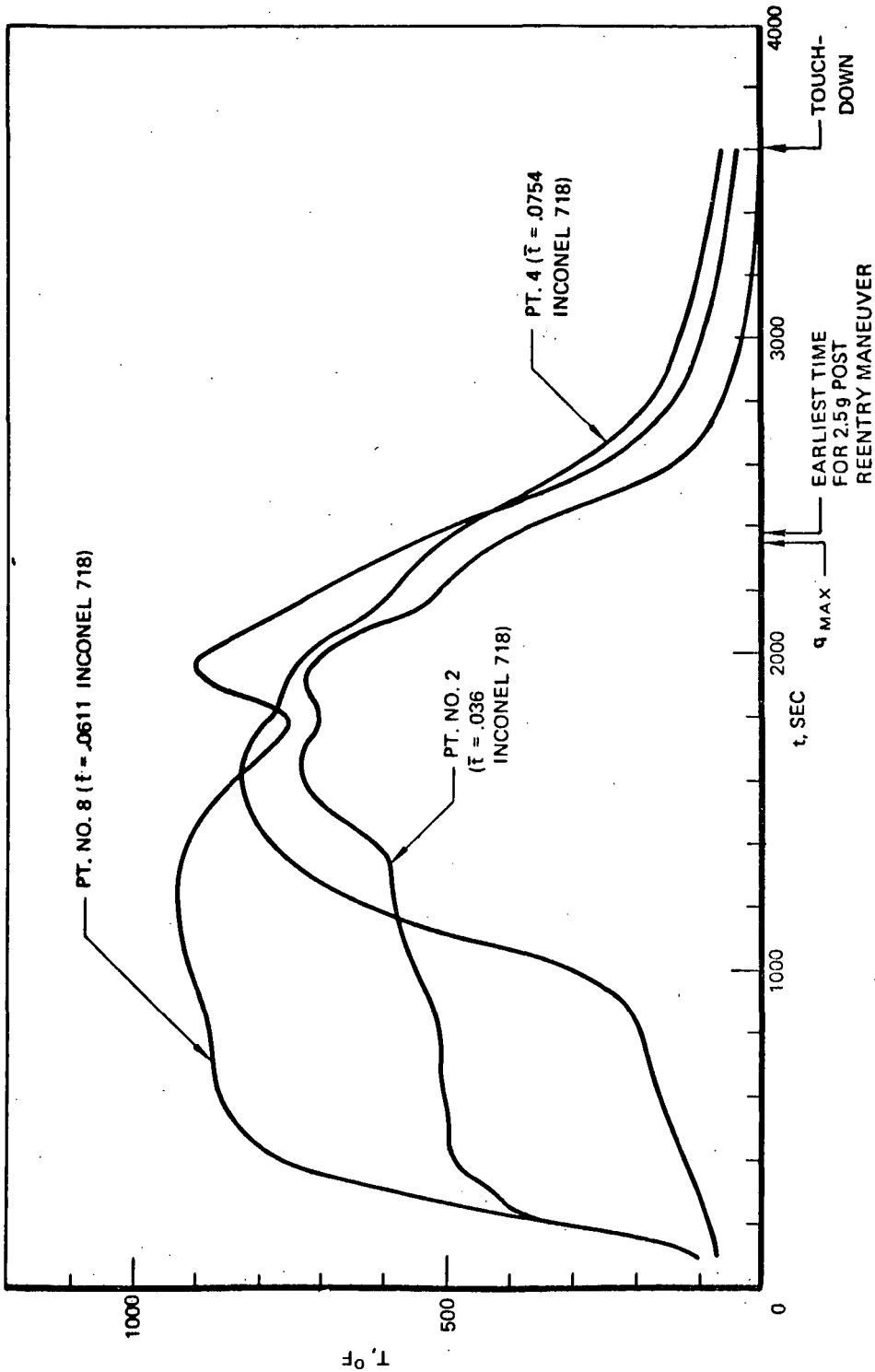


Figure 86. BASELINE HOT STRUCTURE TEMPERATURES, POINT NO. 2, 4, AND 8

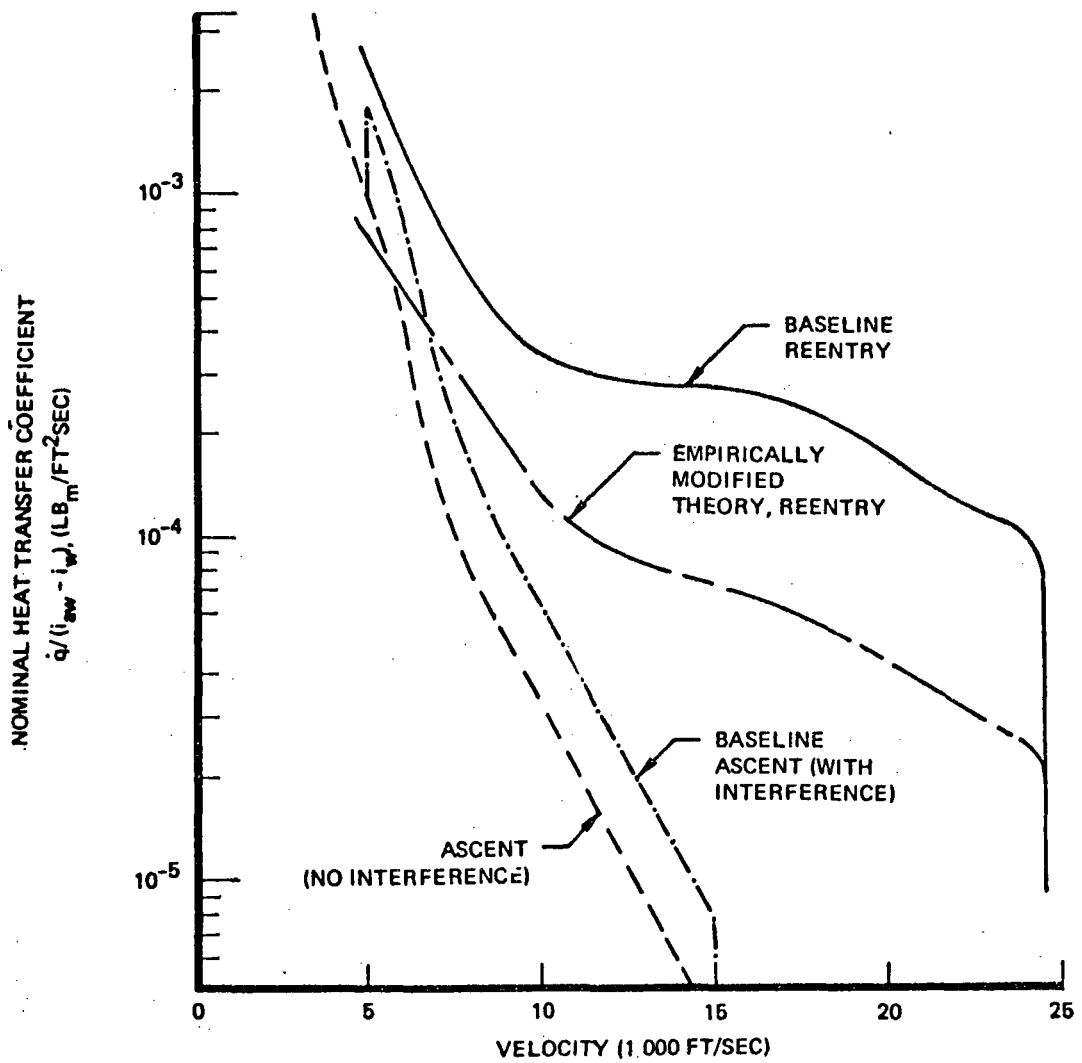


Figure 87: POINT NO. 8, ASCENT - REENTRY HEATING COMPARISONS

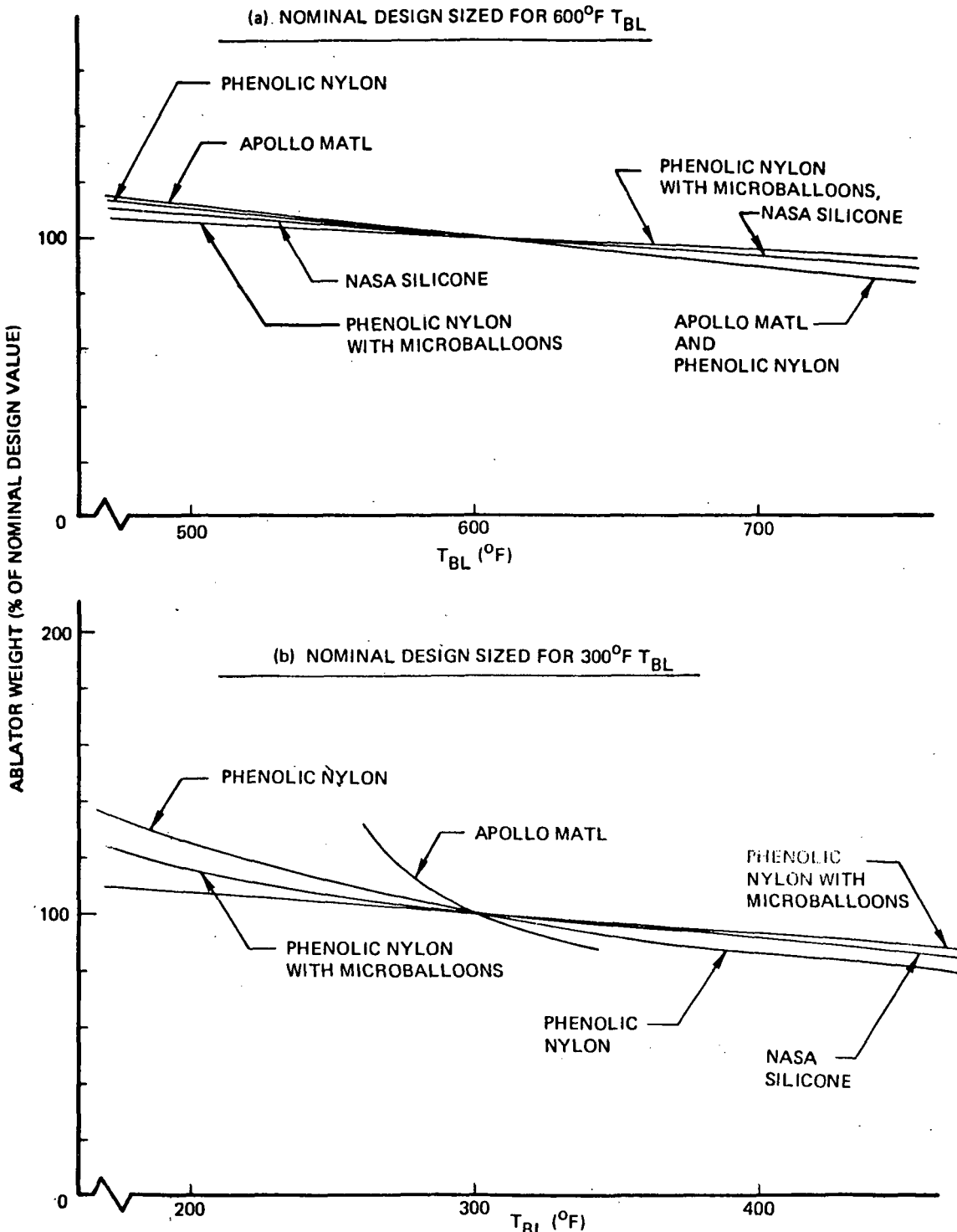


Figure 88. ABLATOR WEIGHTS VS BOND LINE TEMPERATURES

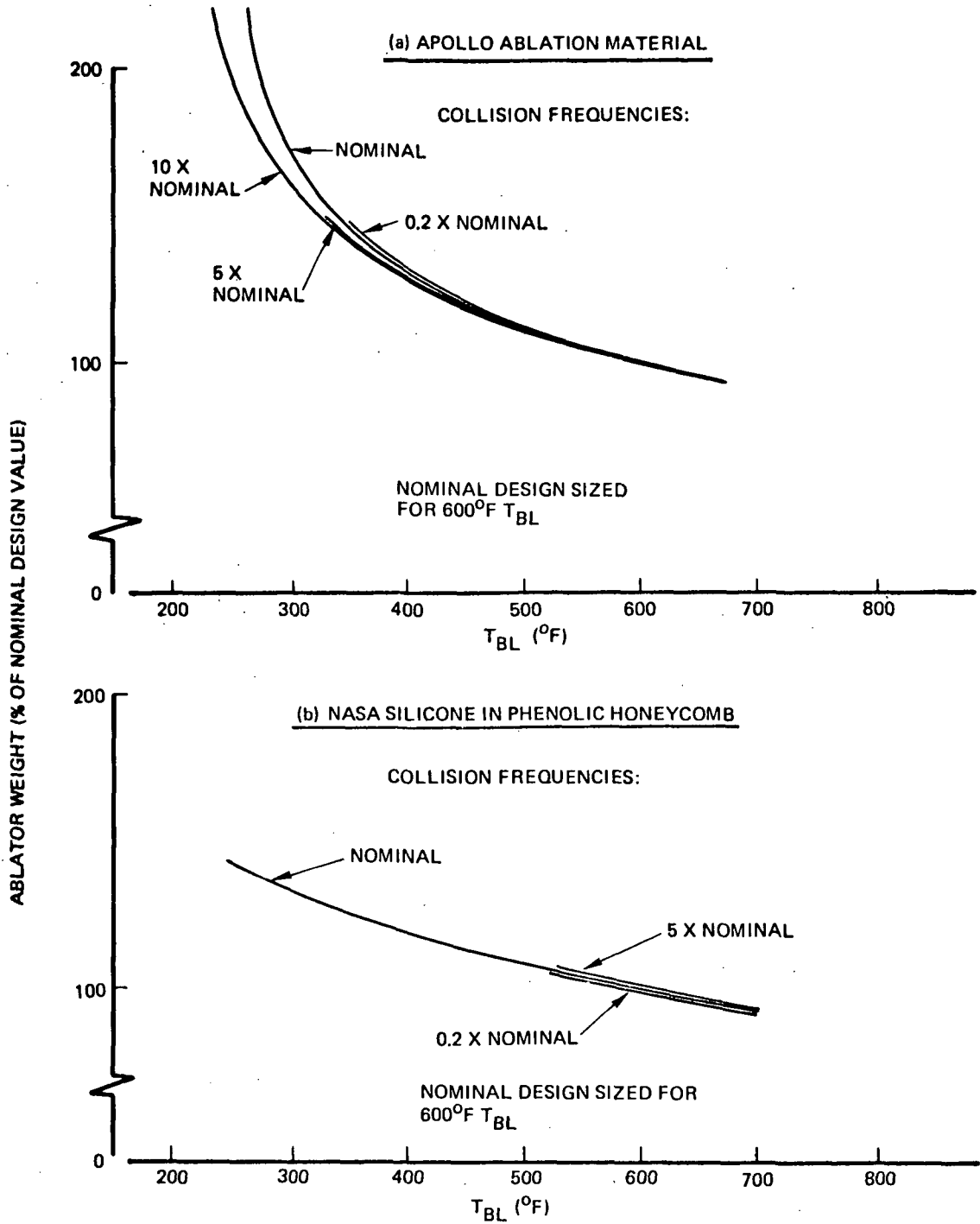


Figure 89. ABLATOR DECOMPOSITION RATE PERTURBATIONS

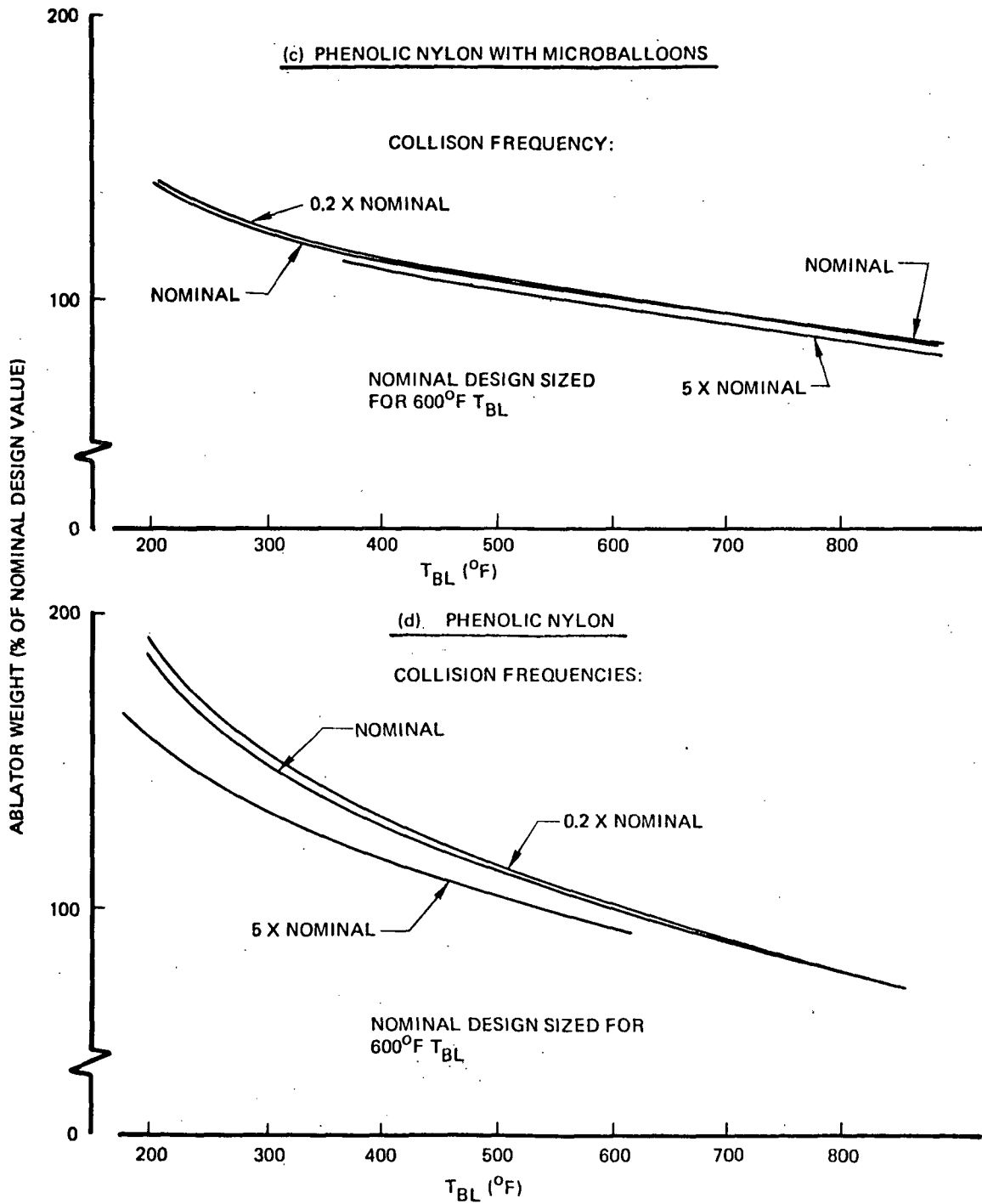


Figure 89. ABLATOR DECOMPOSITION RATE PERTURBATIONS (Cont)

INITIAL THICKNESSES - 2.0 IN.
 t = 2,200 SEC
 ALL TEMPERATURES IN °F

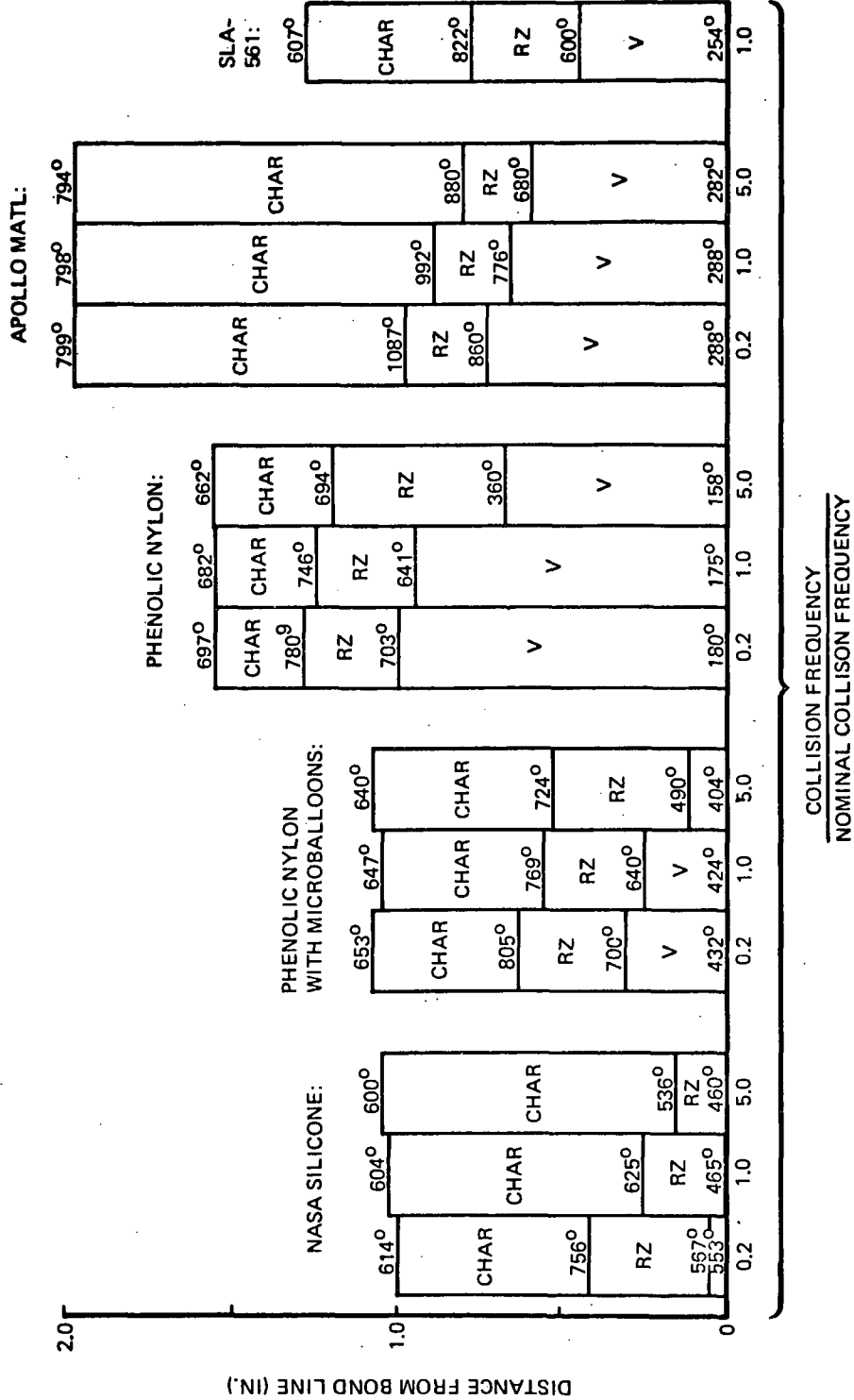


Figure 90: ABLATOR CHARACTERISTICS

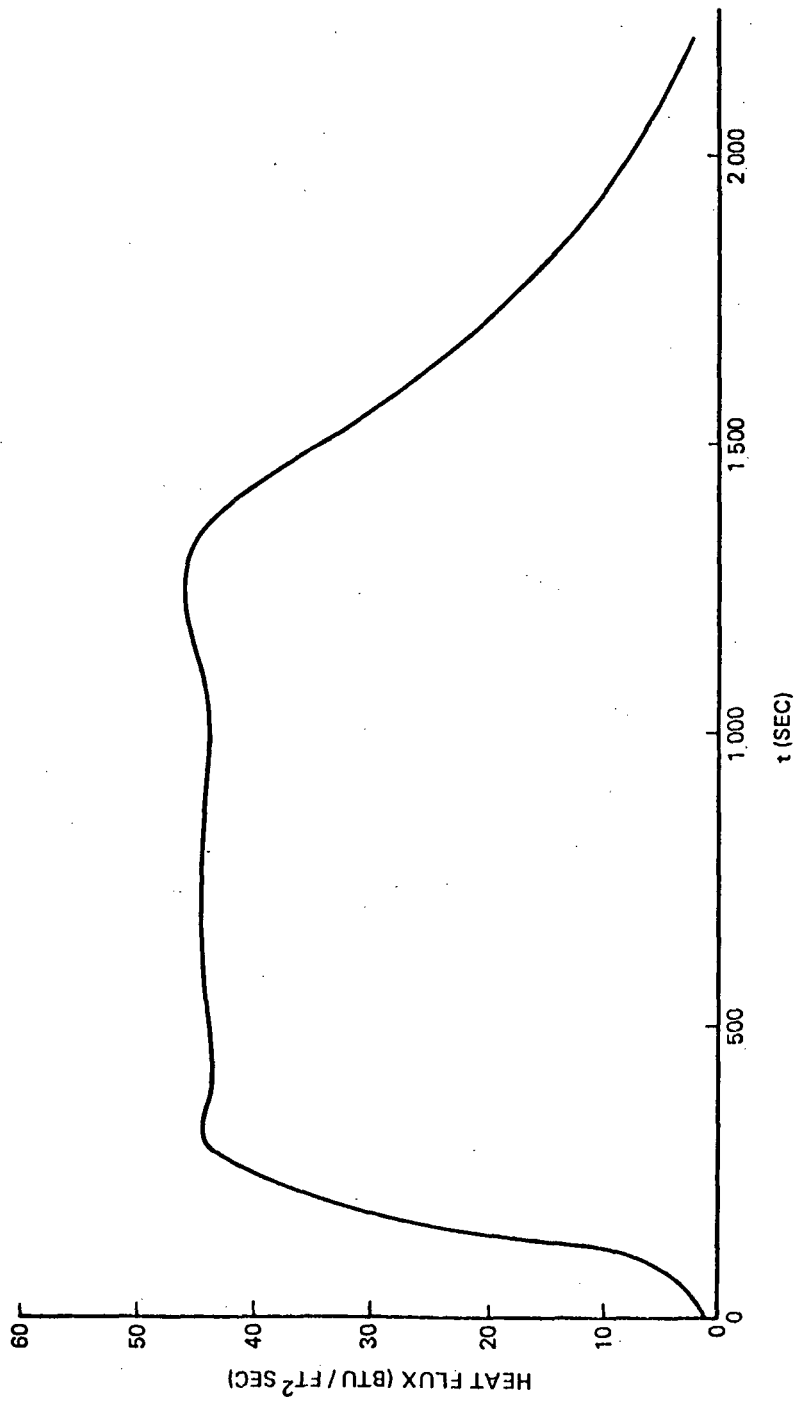


Figure 91: POINT NO. 7 - COLD WALL HEAT FLUX

APOLLO AS-501 REENTRY TRAJECTORY
 BODY POINT 707 (REF. 51)
 DEPTH VALUES ARE FROM ORIGINAL SURFACE

— FAIRED THERMOCOUPLE FLIGHT DATA } REF. 46
 - - - CHAD PROGRAM PREDICTION
 - - - CHAP PROGRAM PREDICTION

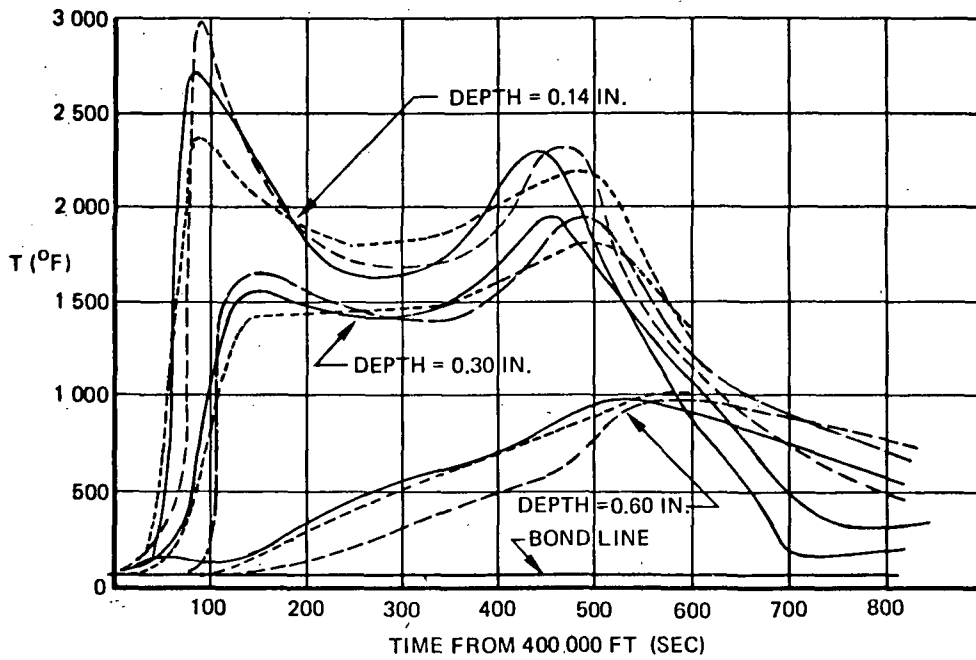


Figure 92. APOLLO ABLATION MATERIAL TEMPERATURES

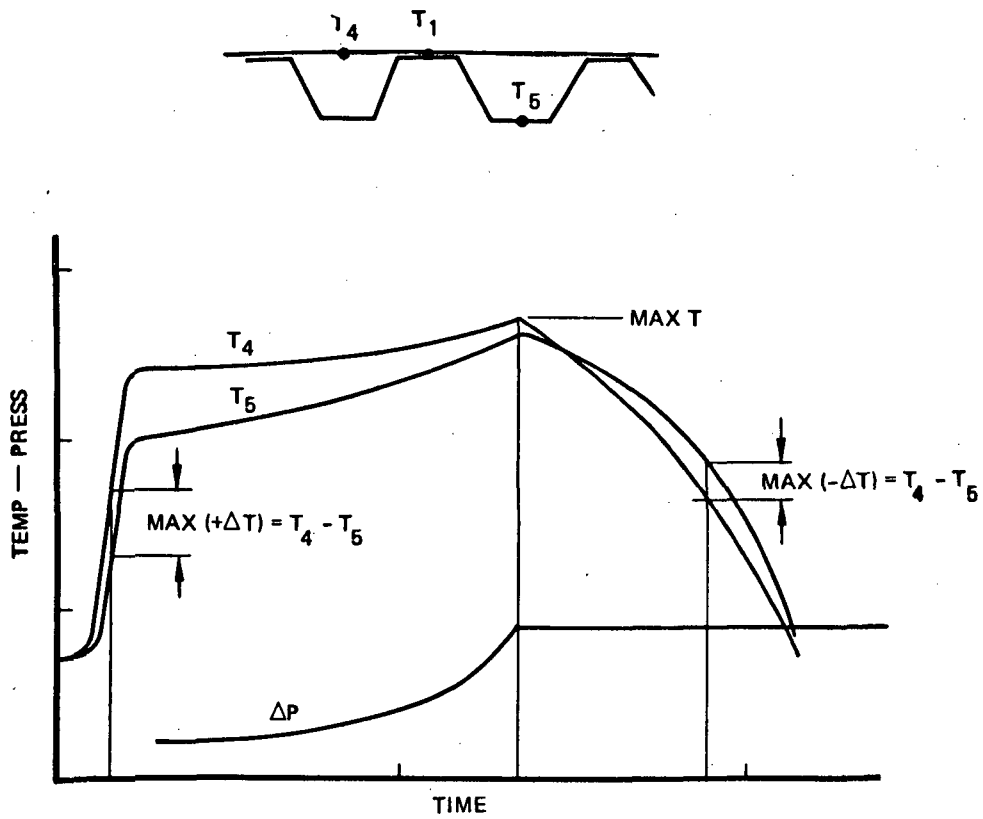


Figure 93: TYPICAL METALLIC TPS PANEL REENTRY ENVIRONMENT

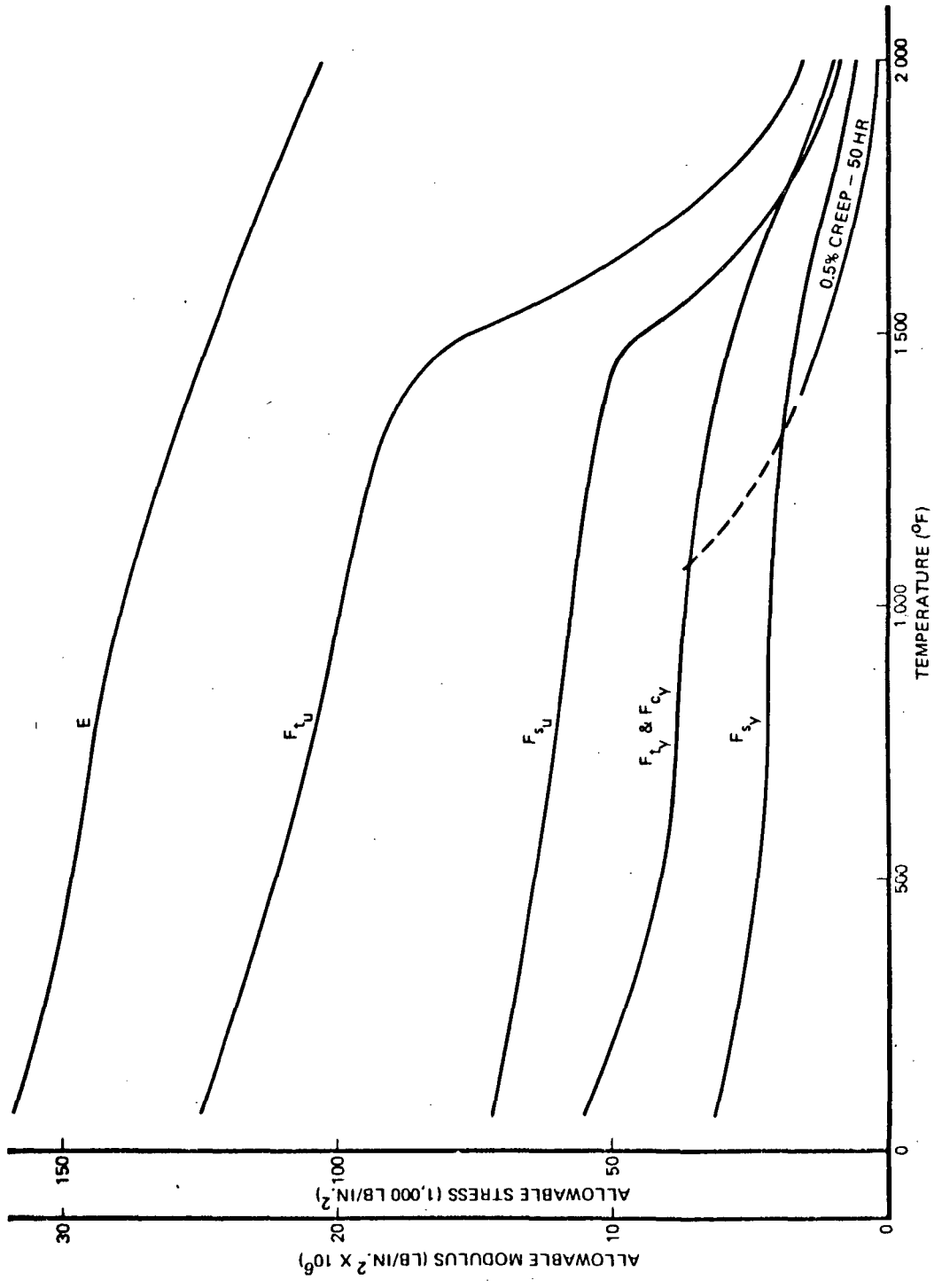


Figure 94. HAYNES 188 (ANNEALED) MECHANICAL PROPERTIES

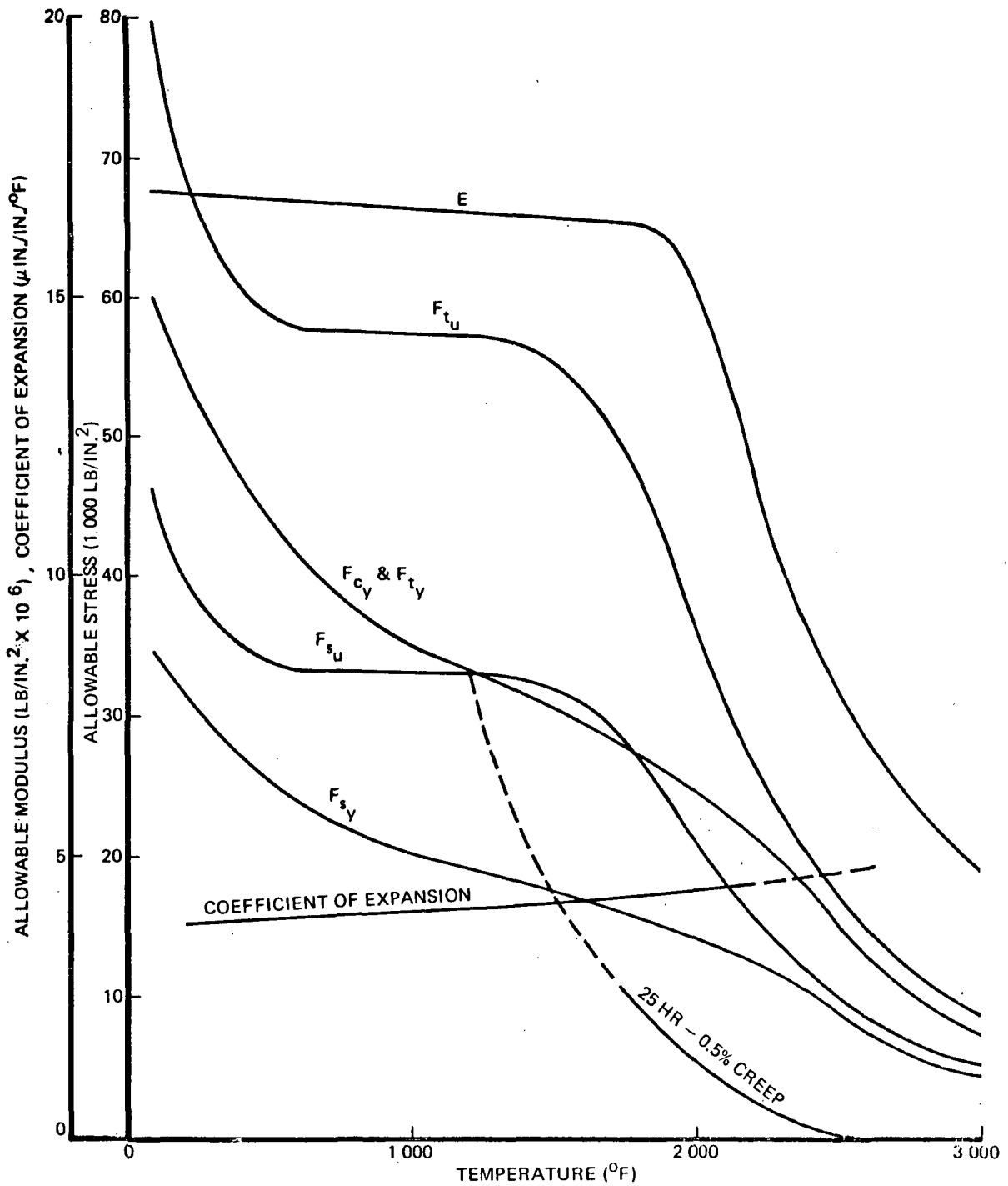


Figure 95. COLUMBIUM C-129Y MECHANICAL PROPERTIES

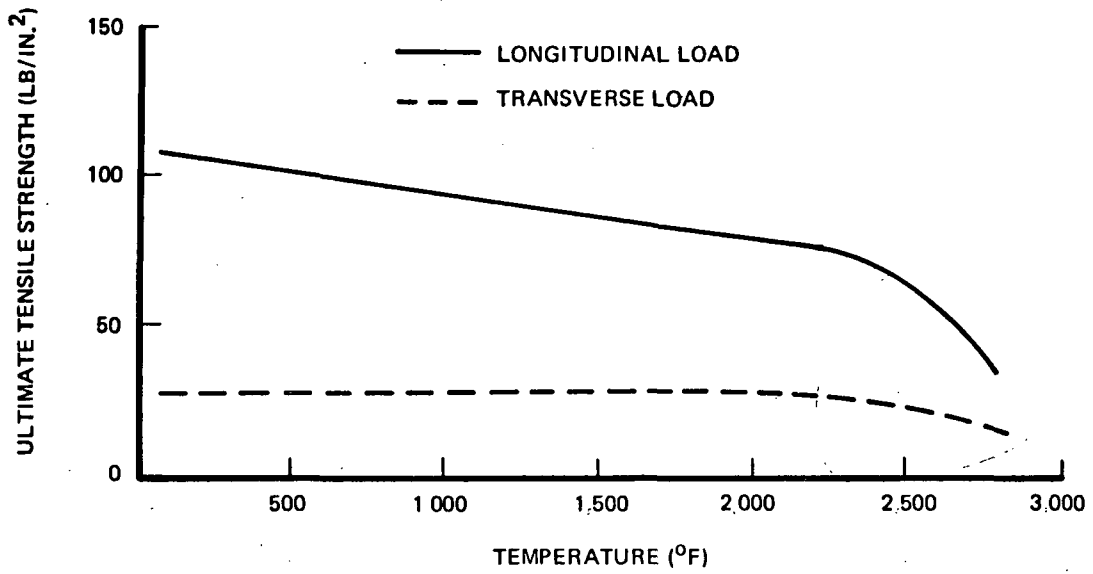


Figure 96. AVERAGE TENSILE STRENGTH, 15 LB/CU FT HCF MULLITE

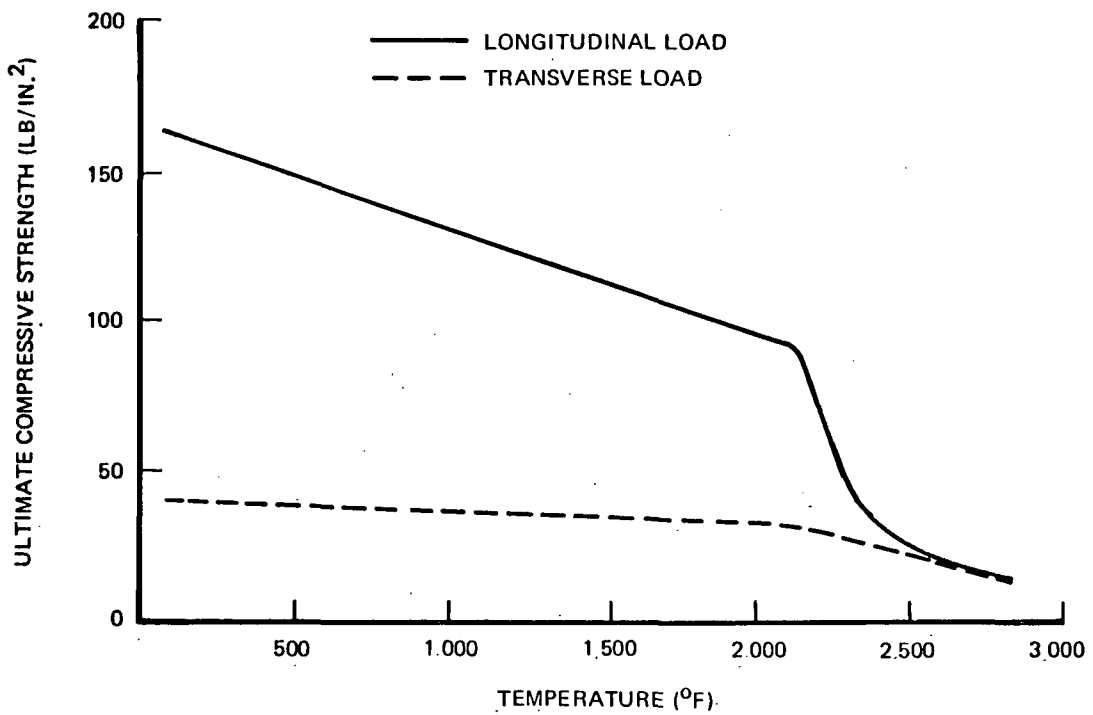


Figure 97. AVERAGE COMPRESSIVE STRENGTH, 15 LB/CU FT HCF MULLITE

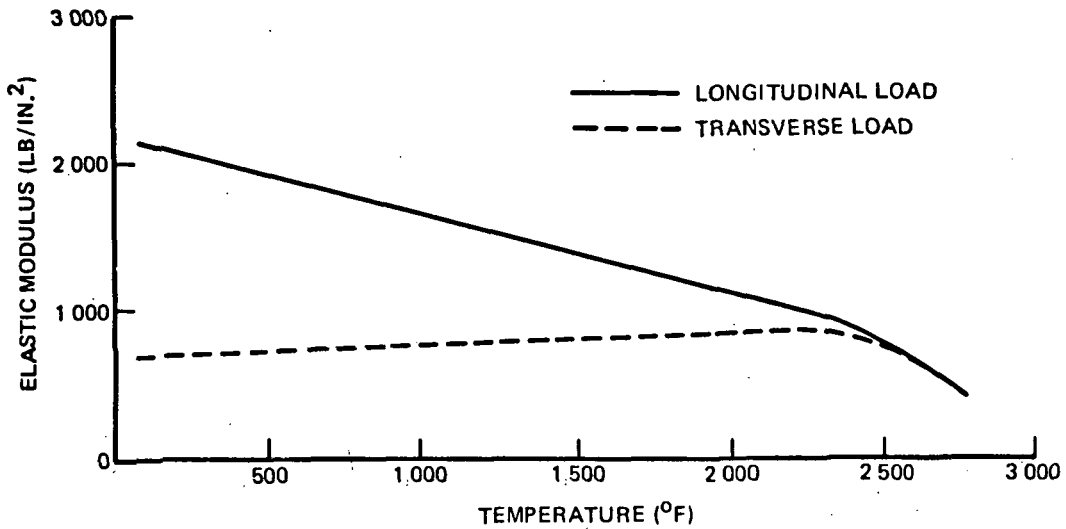


Figure 98: AVERAGE TENSILE MODULUS OF ELASTICITY,
15 LB / CU FT HCF MULLITE

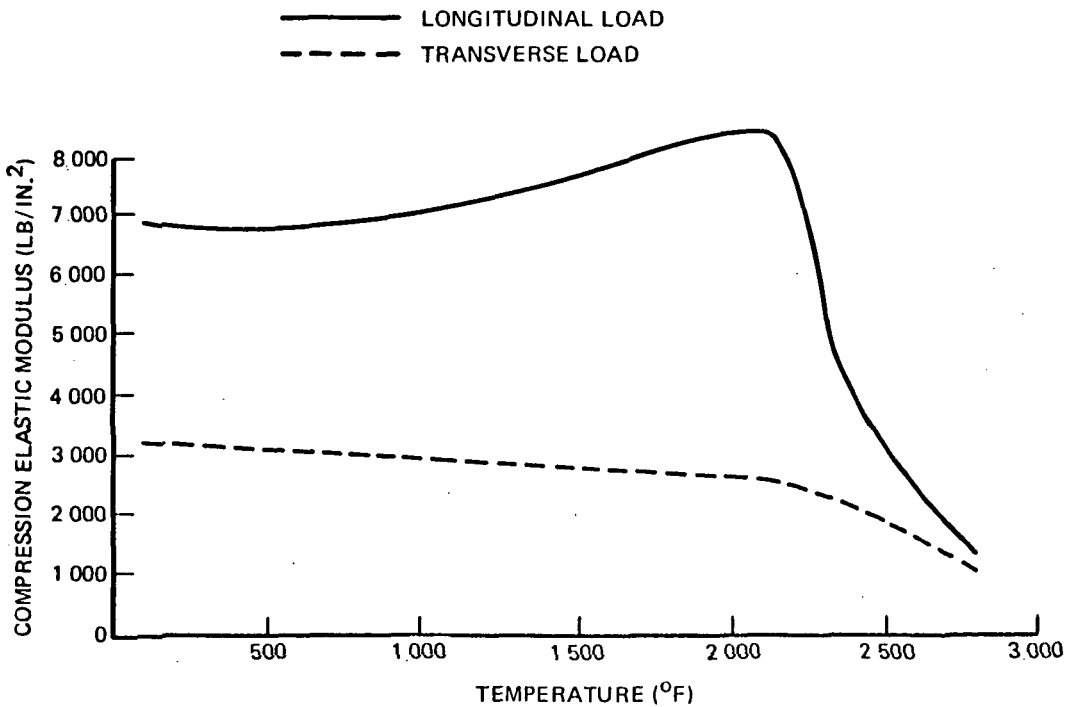


Figure 99. AVERAGE COMPRESSIVE MODULUS OF ELASTICITY,
15 LB / CU FT HCF MULLITE

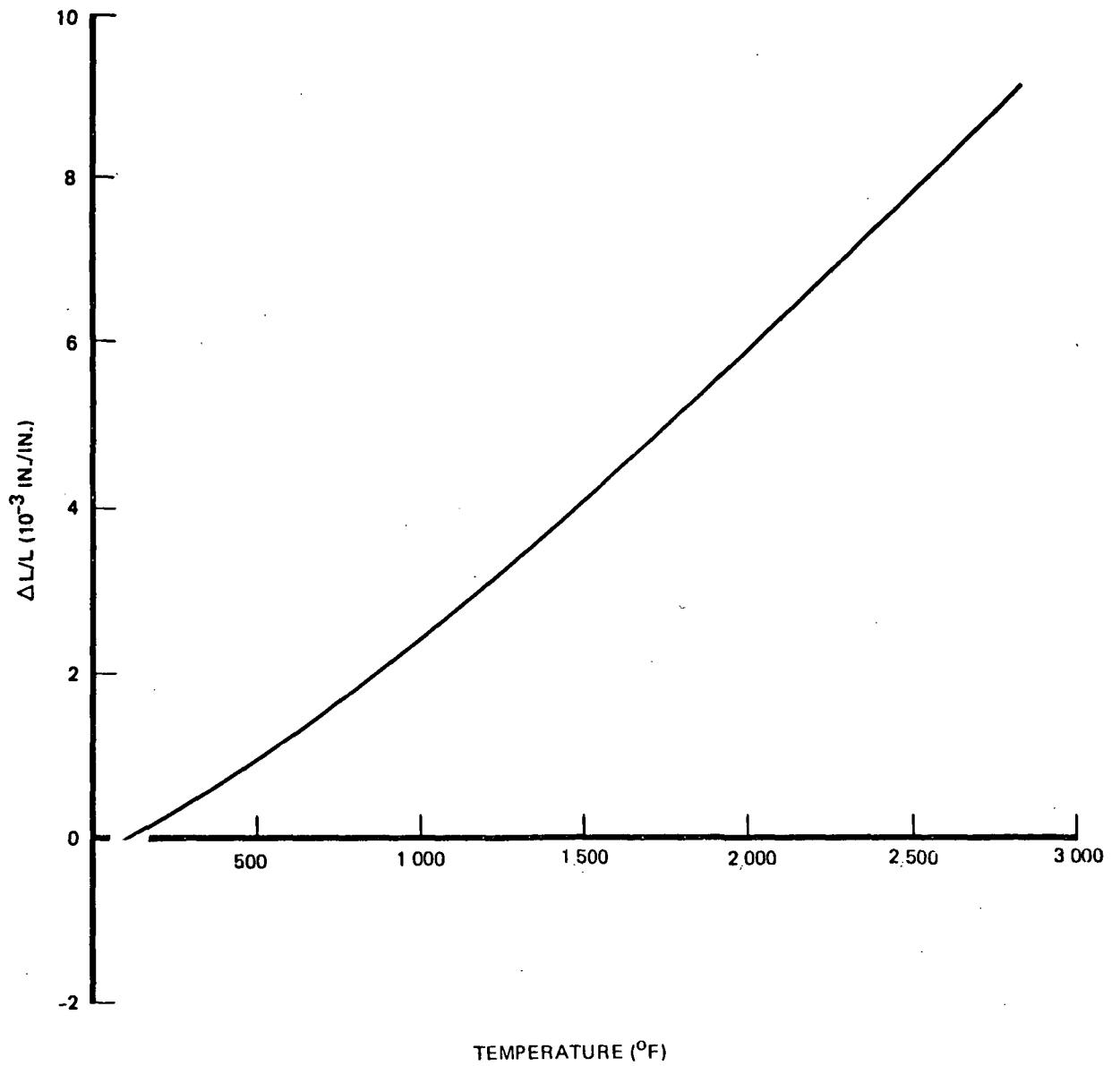


Figure 100. THERMAL EXPANSION OF RIGIDIZED HCF MULLITE

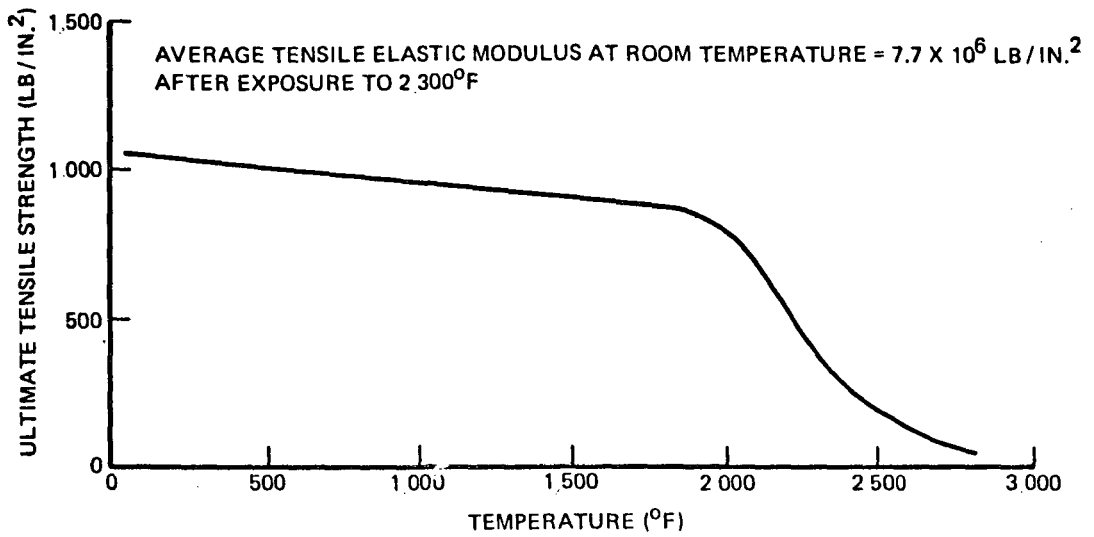


Figure 101: AVERAGE ULTIMATE TENSILE STRENGTH OF M25A7 COATING FOR HCF MULLITE

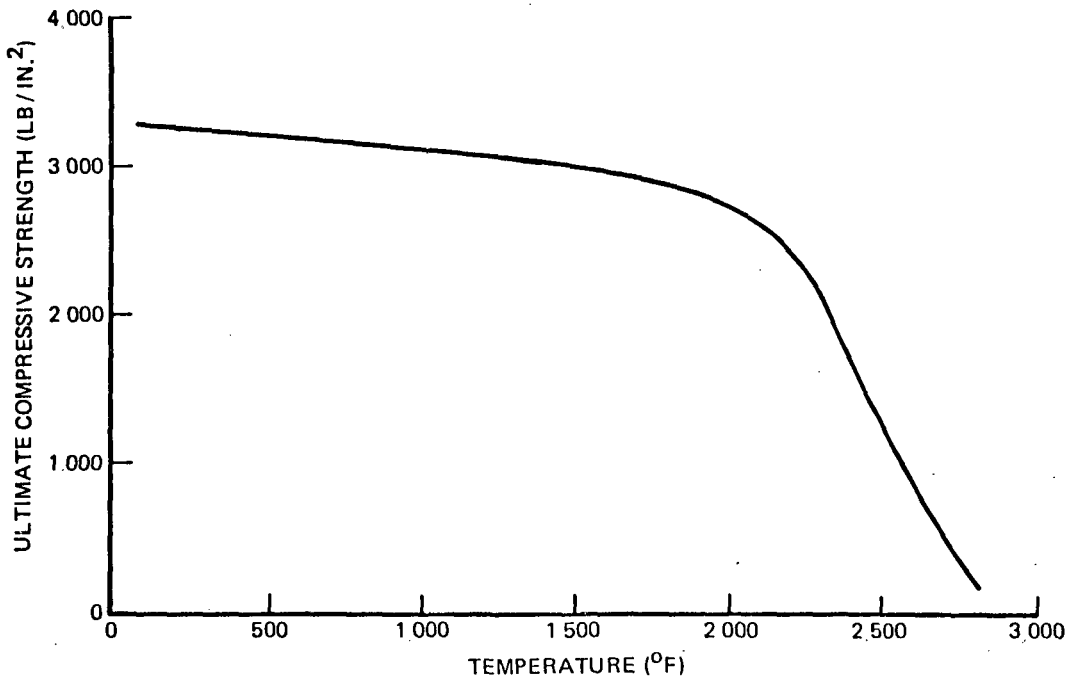


Figure 102: AVERAGE ULTIMATE COMPRESSIVE STRENGTH OF M25A7 COATING FOR HCF MULLITE

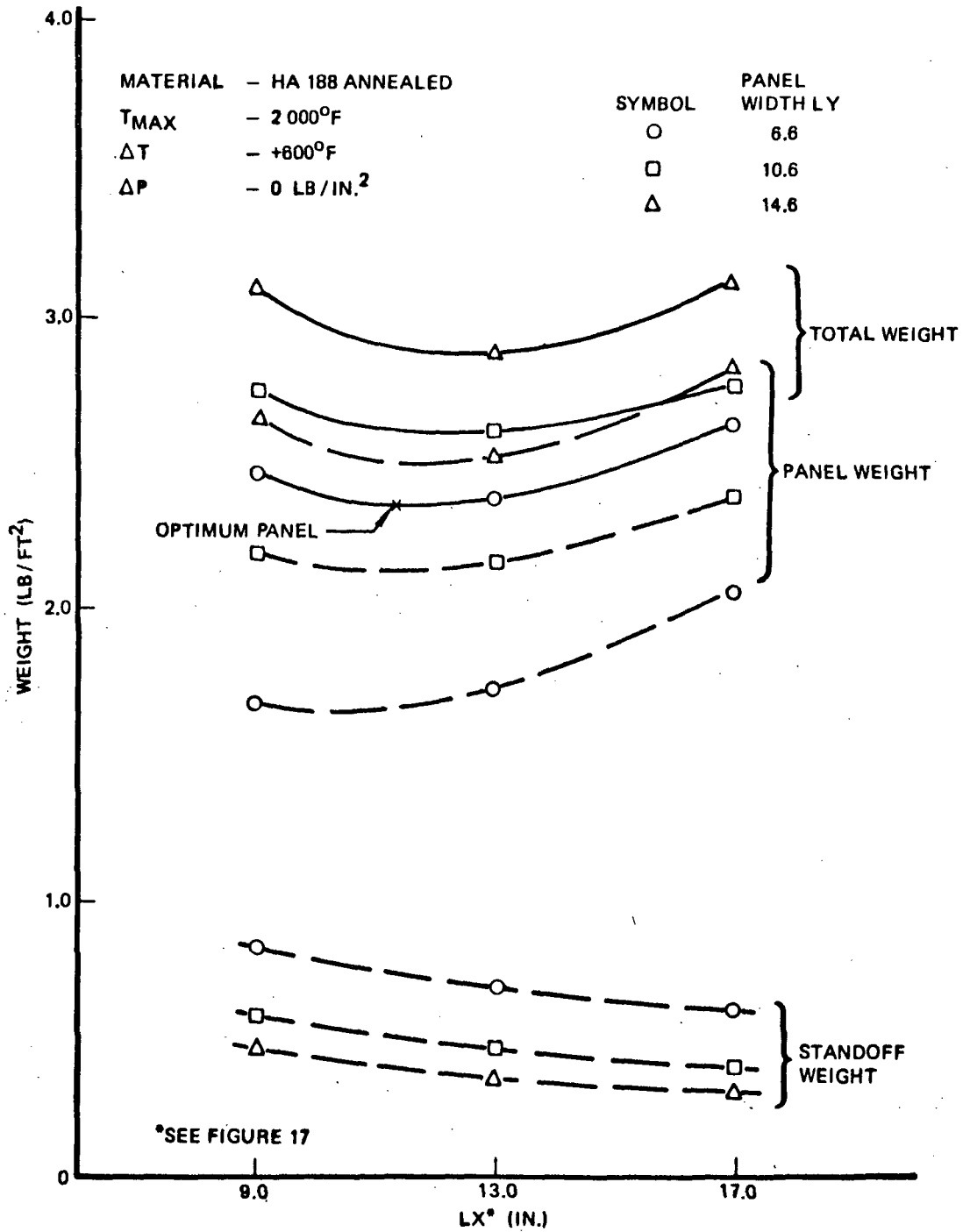


Figure 103. METALLIC TPS PANEL OPTIMIZATION

SYMBOL	POINT NO.
-----	6
—————	7

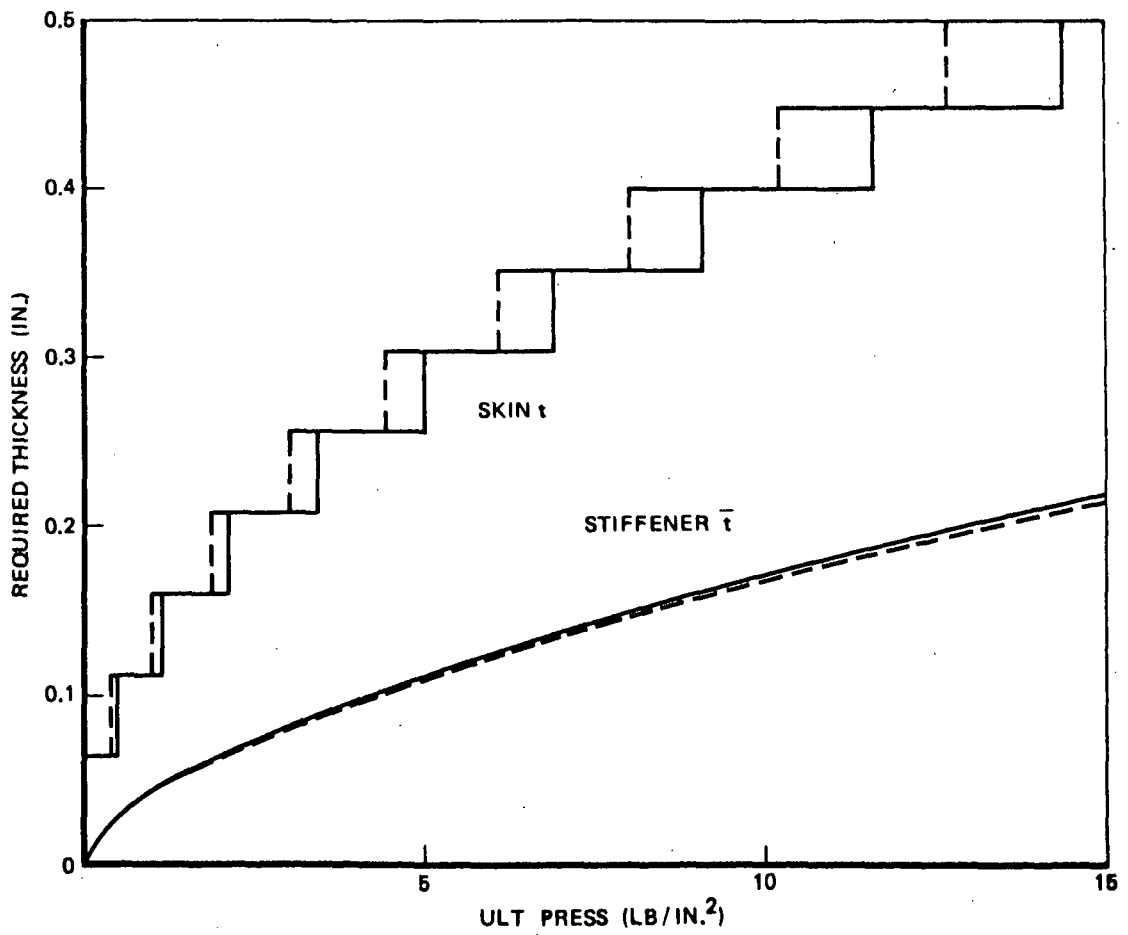
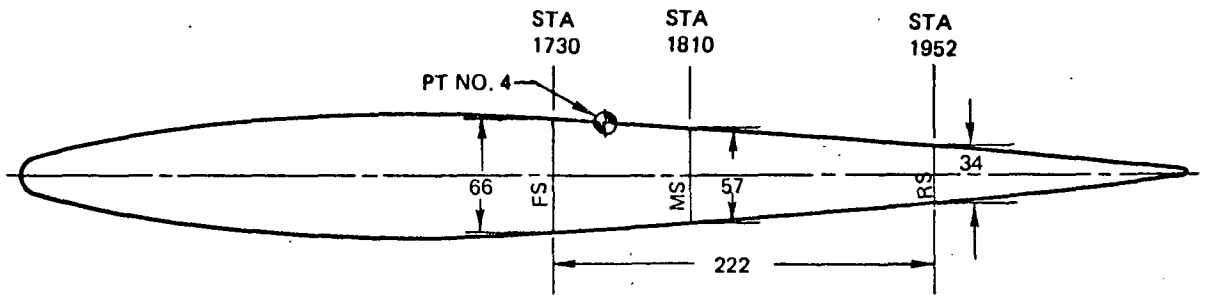


Figure 104. REINFORCED CARBON TPS PANEL REQUIREMENTS



SECTION A-A

ALL DIMENSIONS IN INCHES

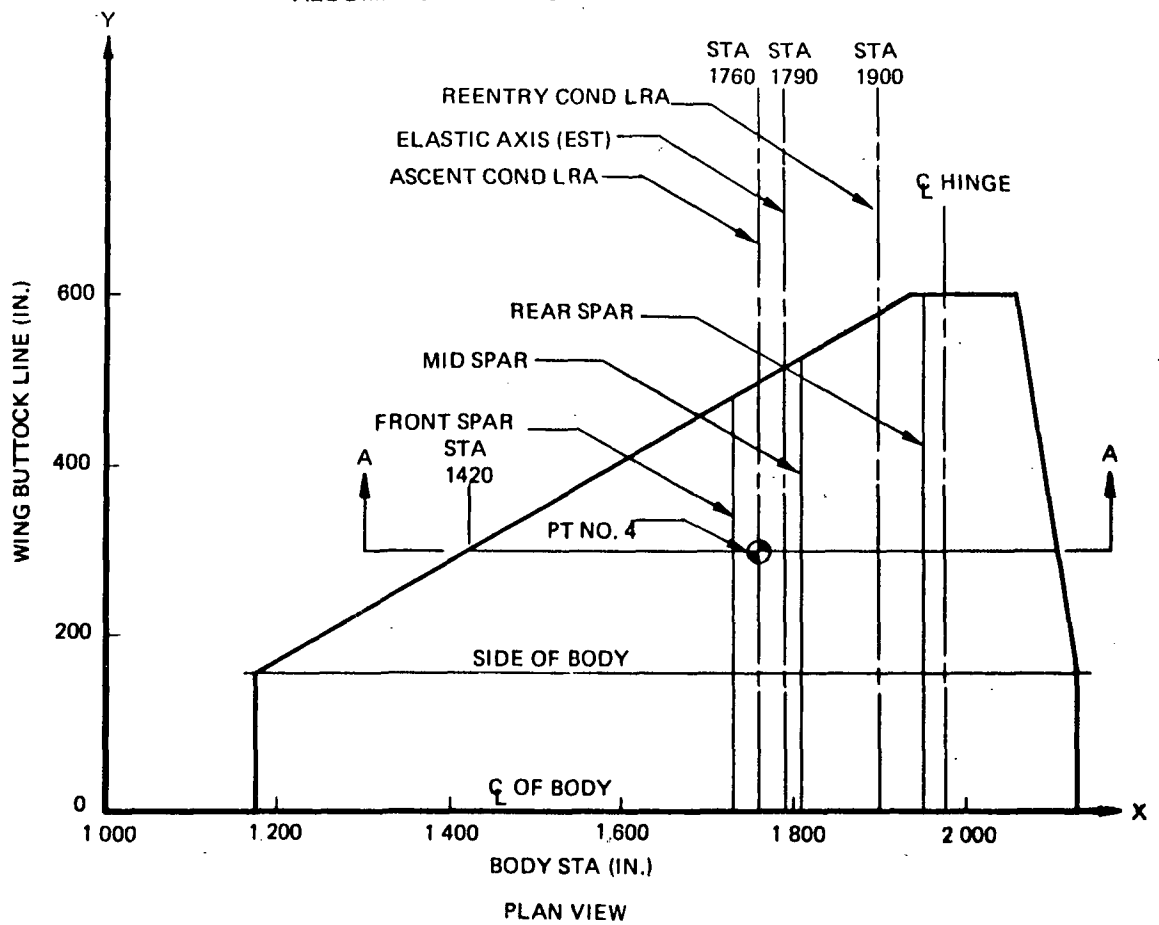


Figure 105: WING GEOMETRY

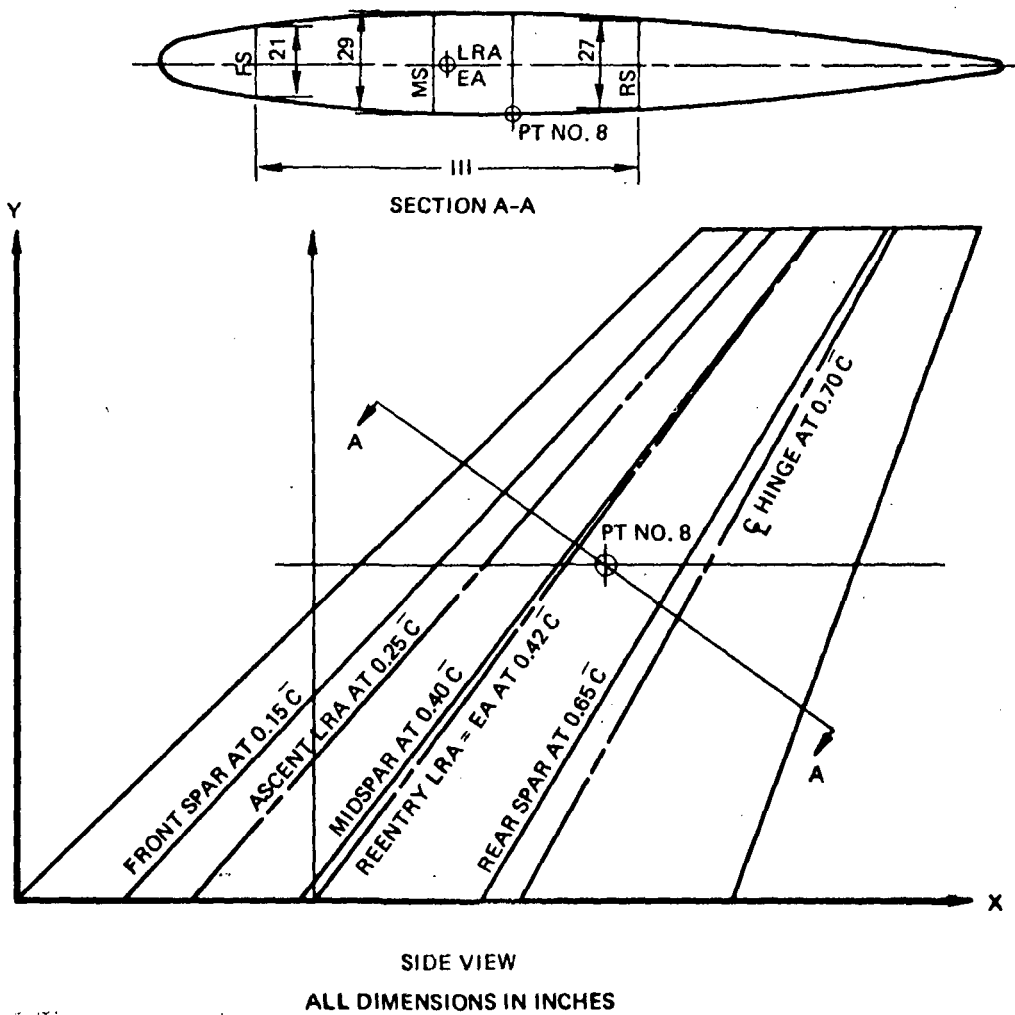


Figure 106: FIN GEOMETRY

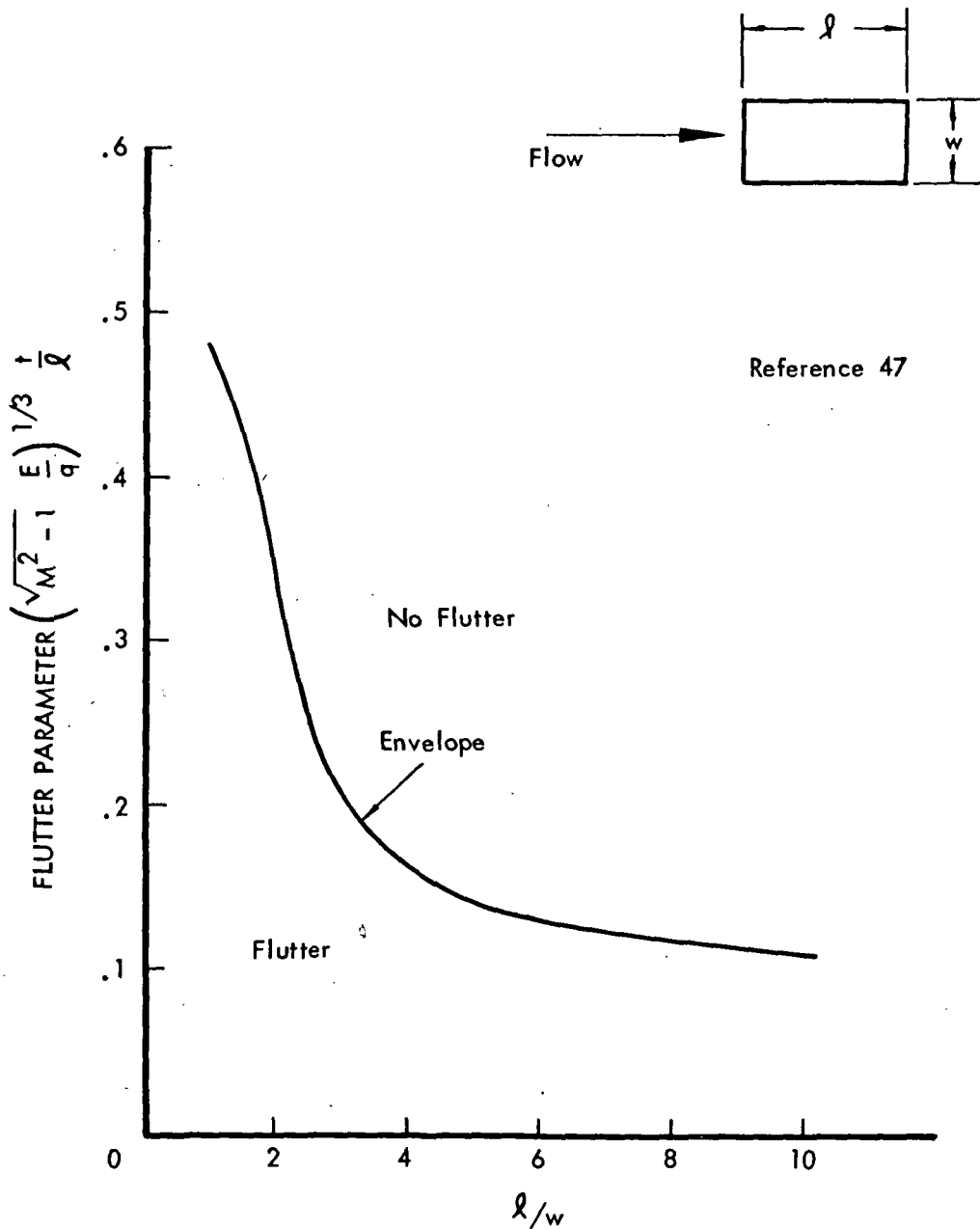


Figure 107. UNSTIFFENED FLAT PANEL DESIGN PARAMETERS

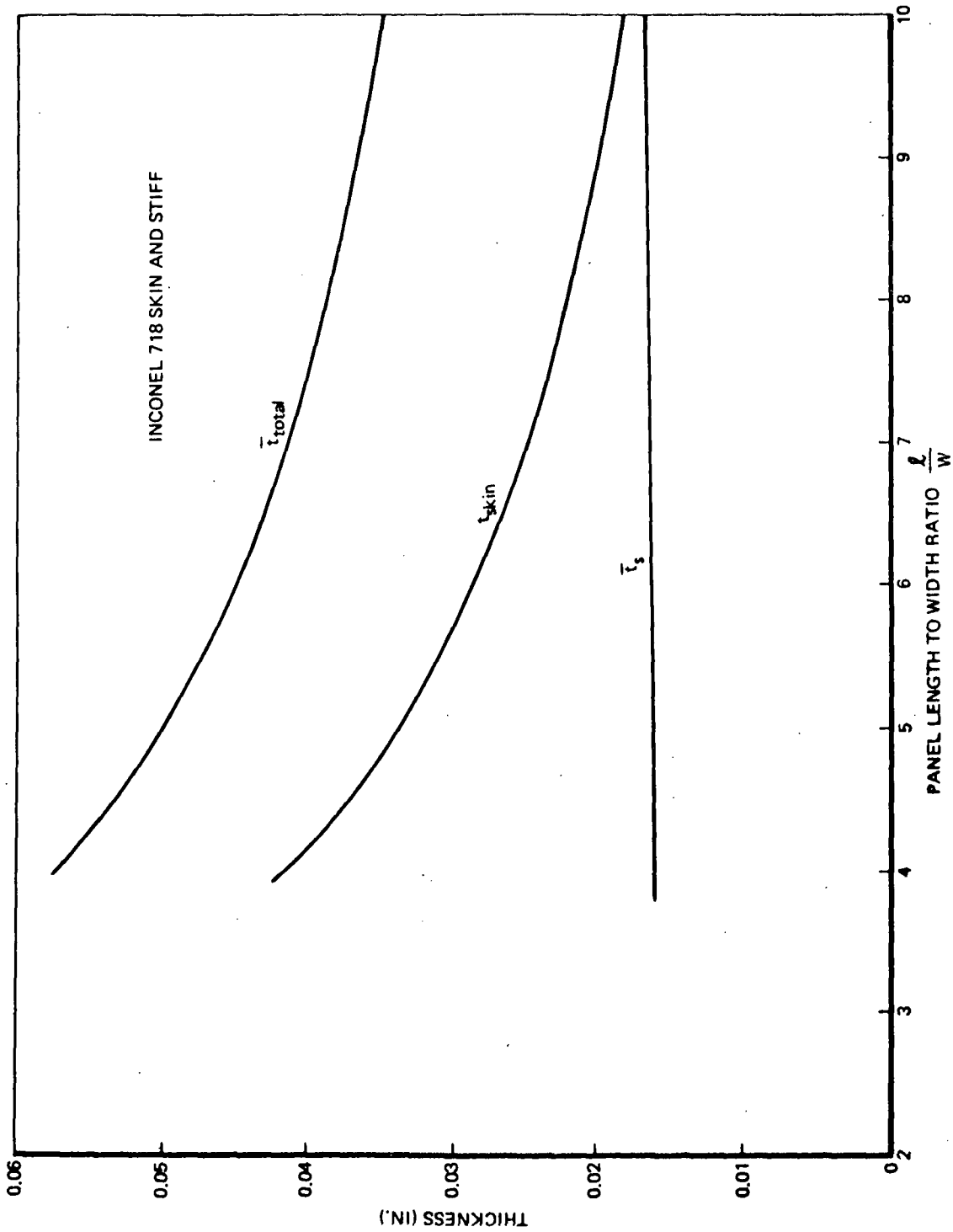


Figure 108. HOT STRUCTURE POINT NO. 2 - STRUCTURAL REQUIREMENT

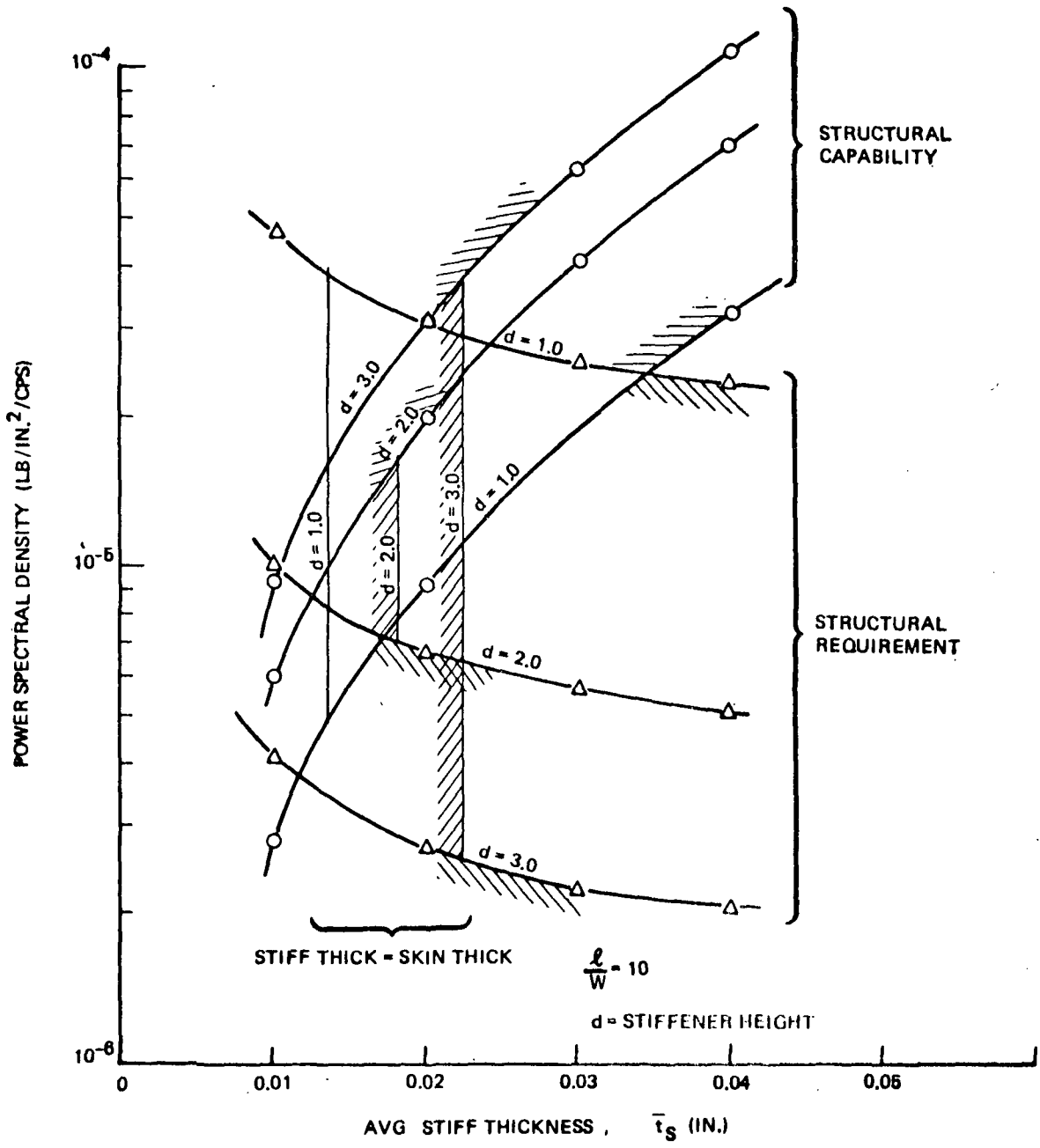


Figure 109: HOT STRUCTURE POINT NO. 2 – STIFFENER OPTIMIZATION

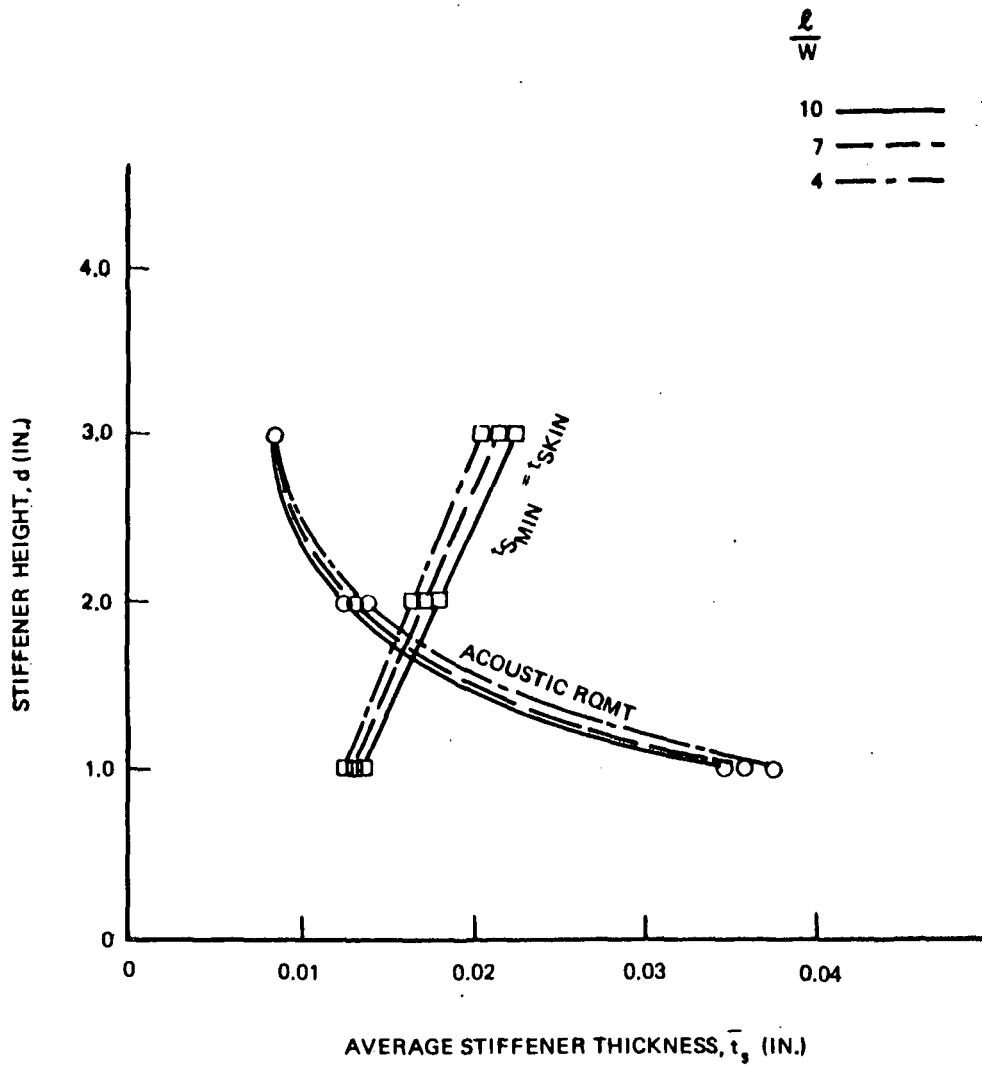
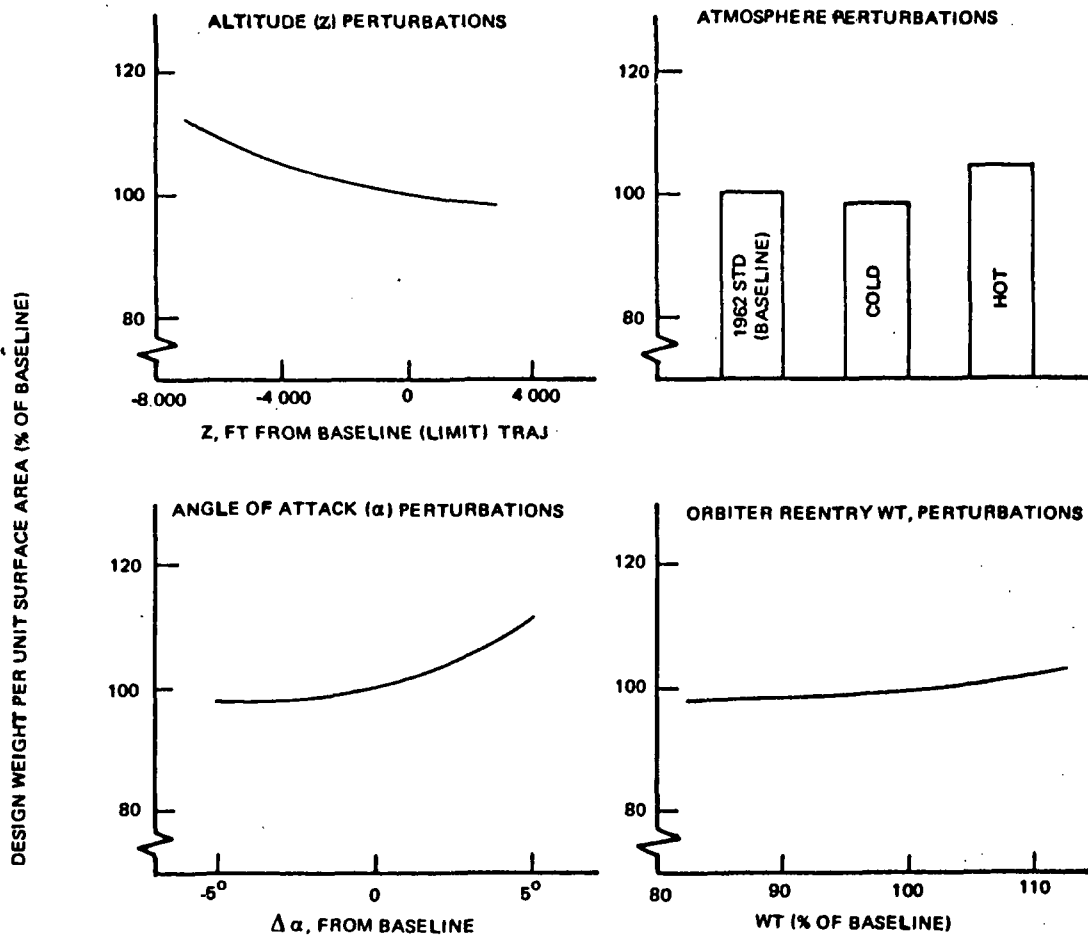
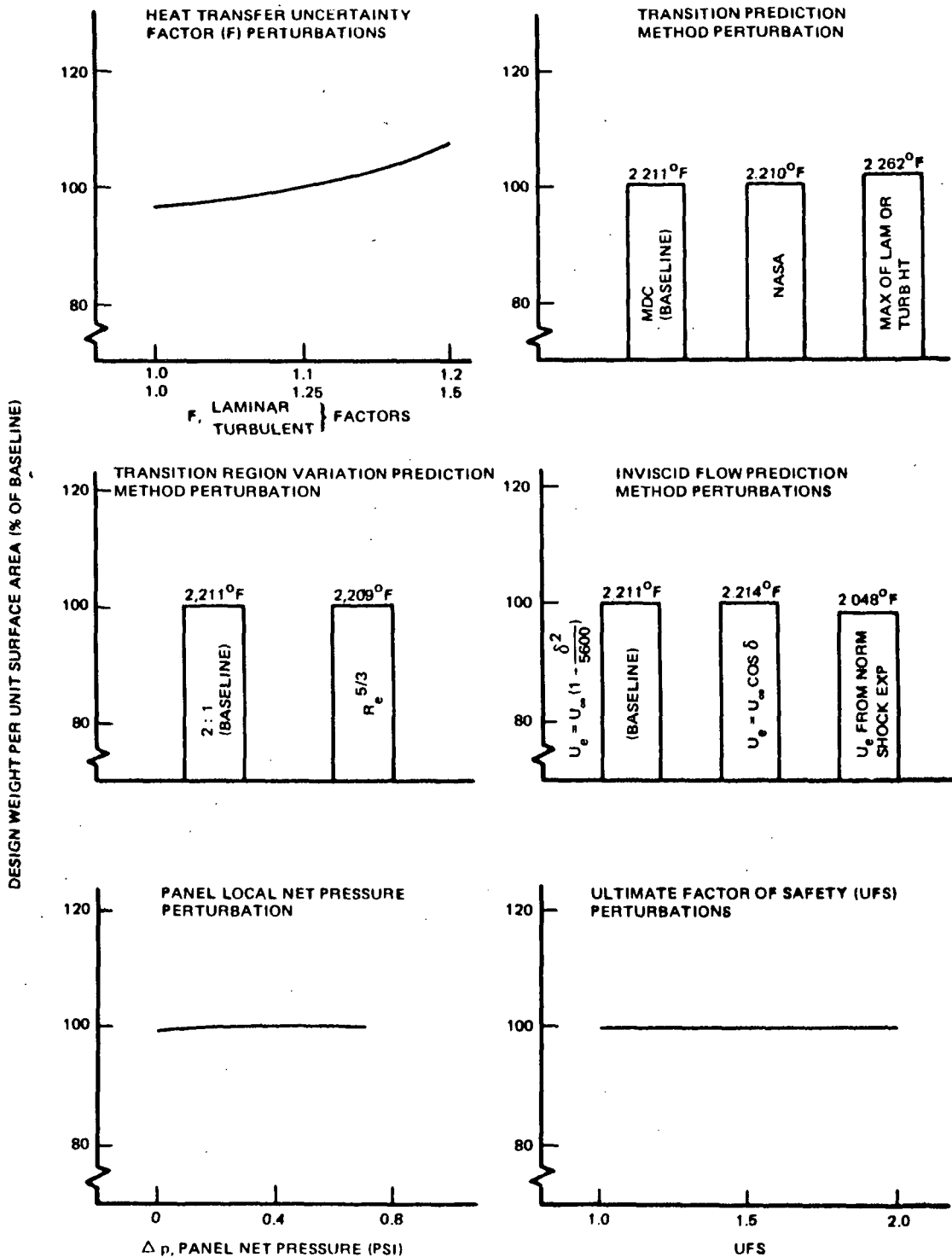


Figure 110: HOT STRUCTURE POINT NO. 2 – STIFFENER REQUIREMENT



**Figure 111. WEIGHT SENSITIVITIES
POINT NO. 1 - LOWER MID-BODY-METAL HEAT SHIELD TPS**



**Figure 111. WEIGHT SENSITIVITIES
POINT NO. 1 - LOWER MIDBODY - METAL HEAT SHIELD TPS (Cont)**

NOTE: POINT NO. 2 REMAINS ASCENT - CRITICAL FOR ALL PERTURBATIONS

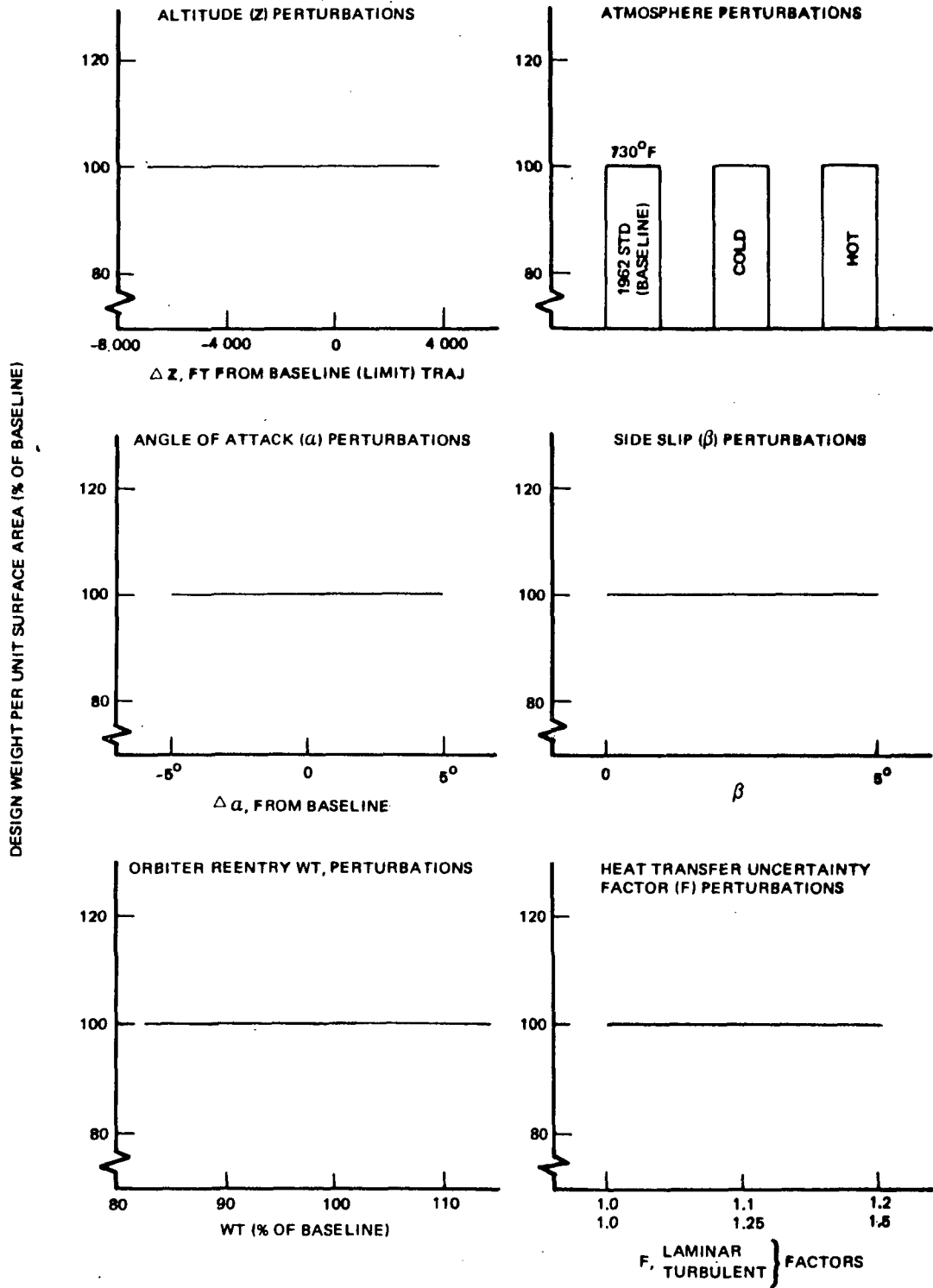


Figure 112. WEIGHT SENSITIVITIES POINT NO. 2 - BODY SIDE - HOT STRUCTURE

NOTE : POINT NO. 2 REMAINS ASCENT - CRITICAL FOR ALL PERTURBATIONS

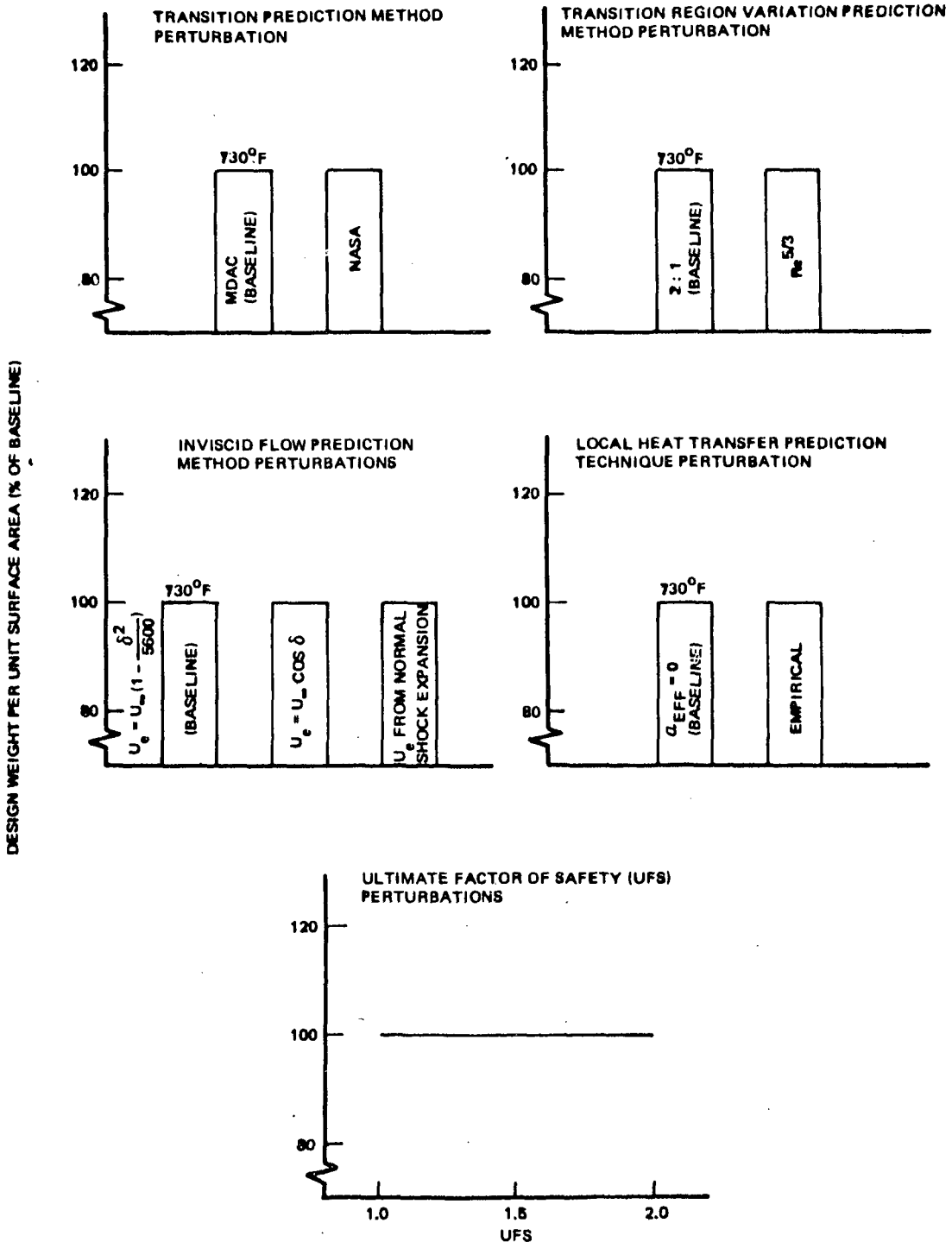


Figure 112. WEIGHT SENSITIVITIES POINT NO. 2 - BODY SIDE - HOT STRUCTURE (Cont)

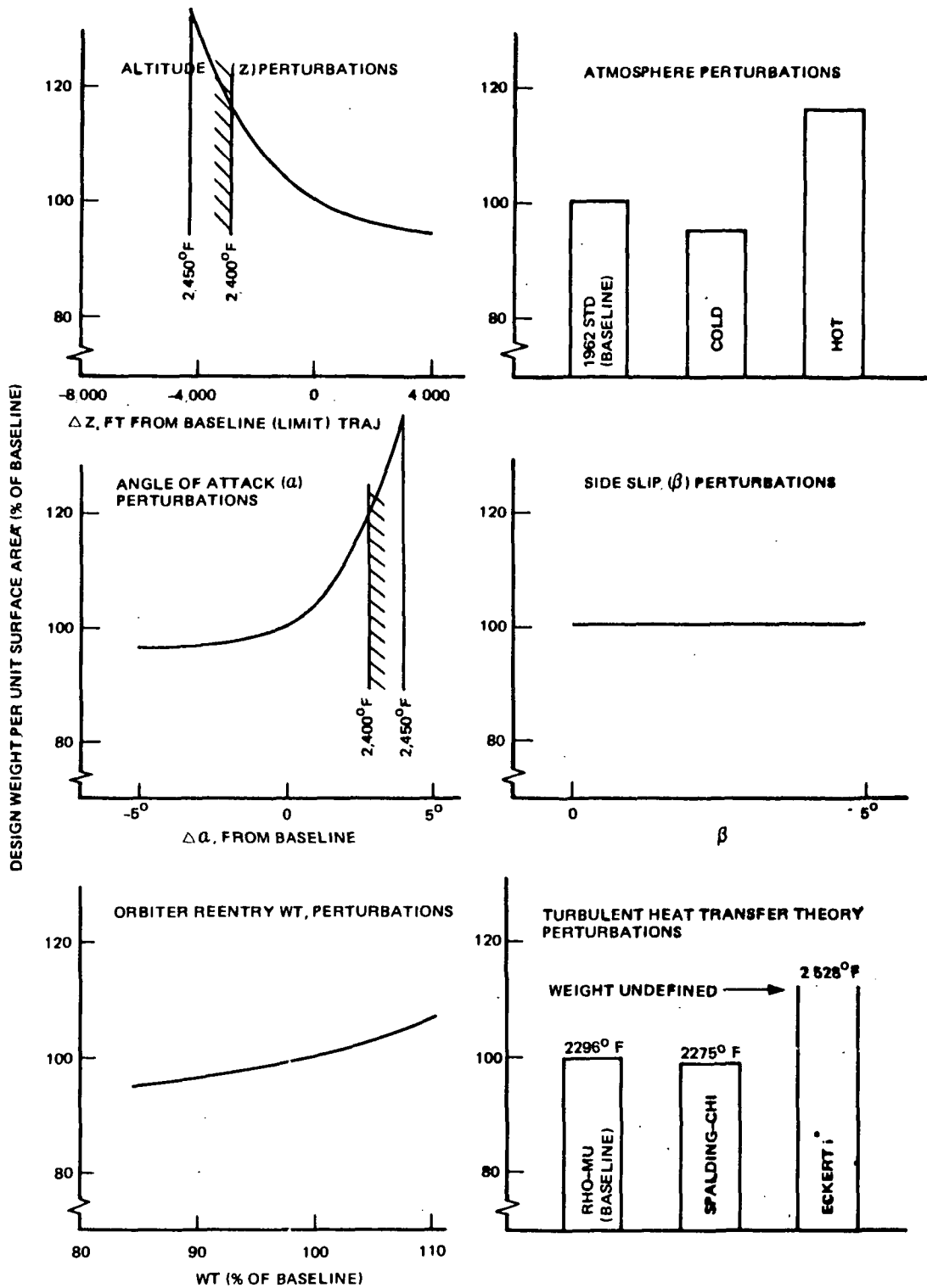
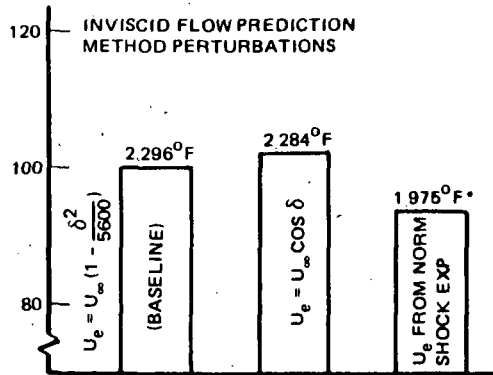
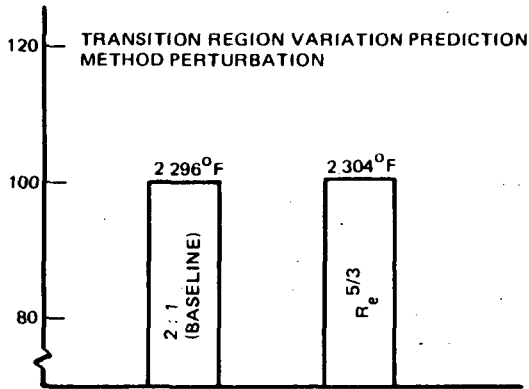
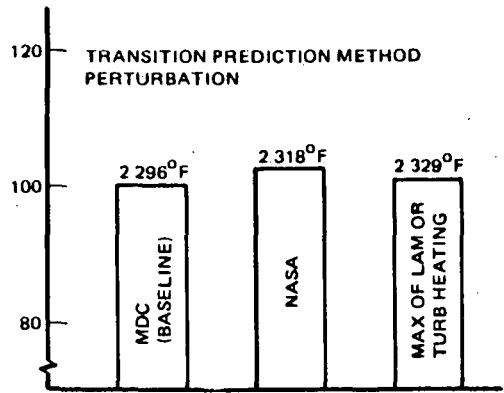
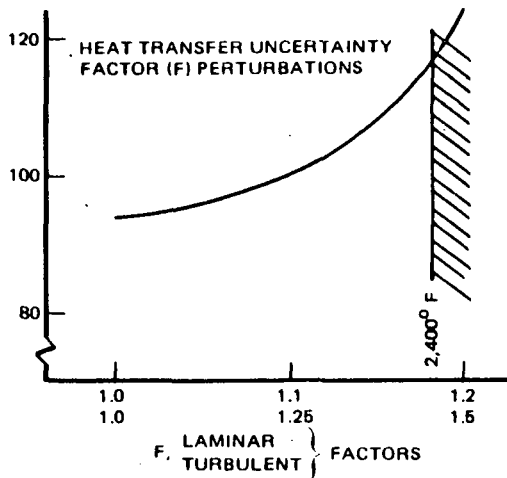


Figure 113. WEIGHT SENSITIVITIES
POINT NO. 3 – LOWER WING, MID-SEMISPAN, MIDCHORD – METAL TPS

DESIGN WEIGHT PER UNIT SURFACE AREA (% OF BASELINE)



* -- HAYNES 188 TPS

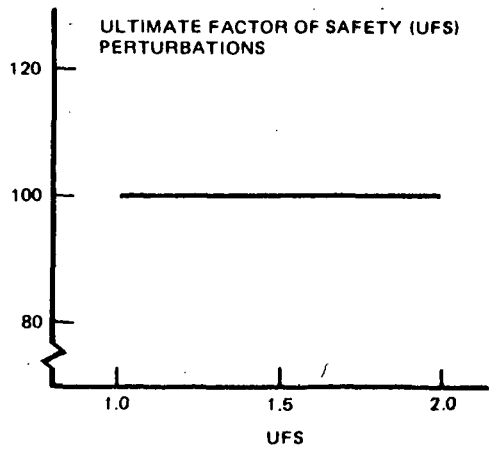
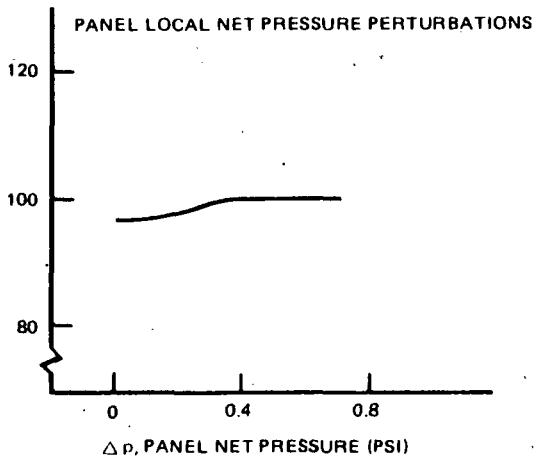


Figure 113. WEIGHT SENSITIVITIES
POINT NO. 3 - LOWER WING, MID-SEMISPAN, MIDCHORD - METAL TPS (Cont)

DESIGN WEIGHT PER UNIT SURFACE AREA (% OF BASELINE)

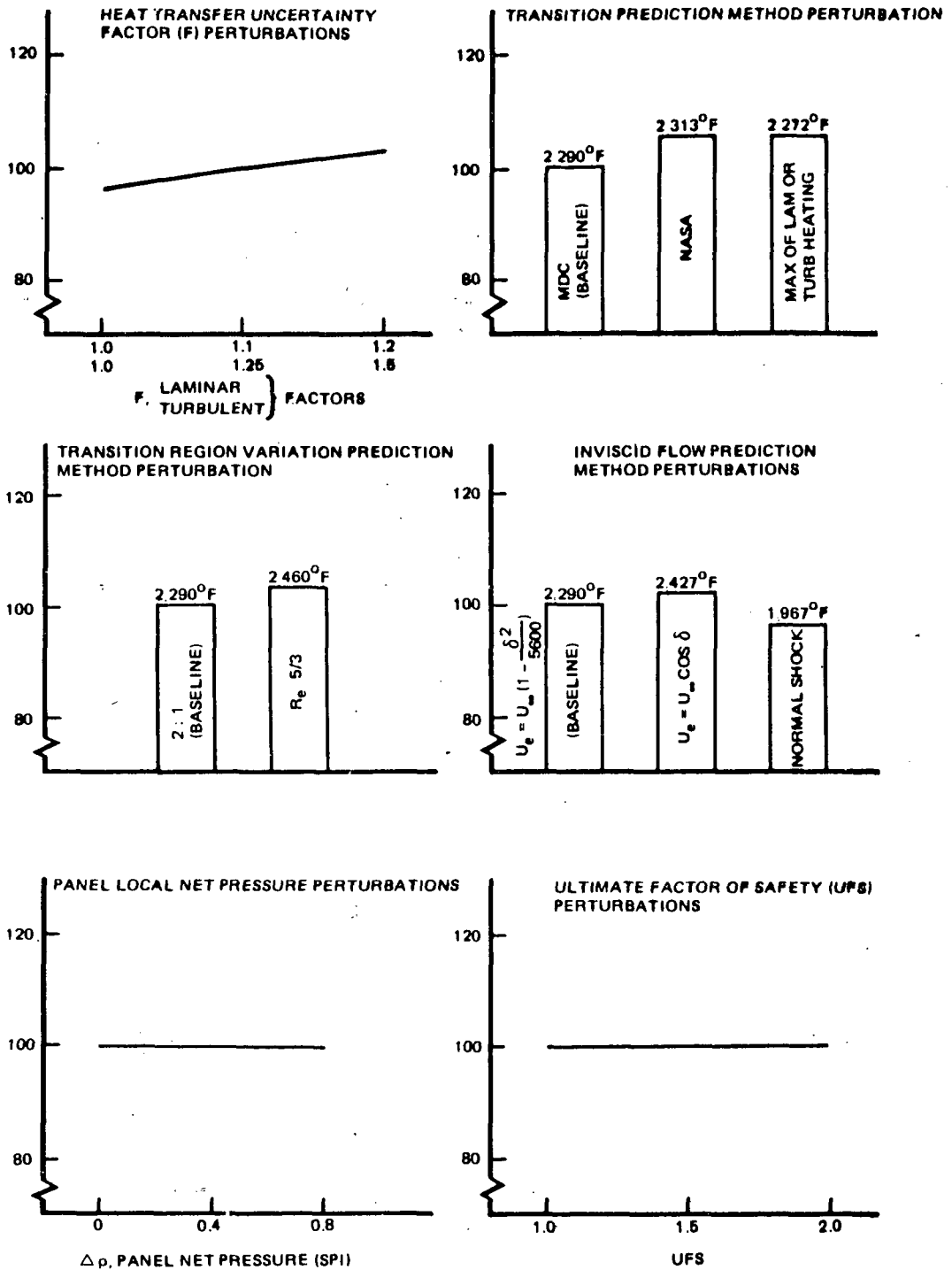
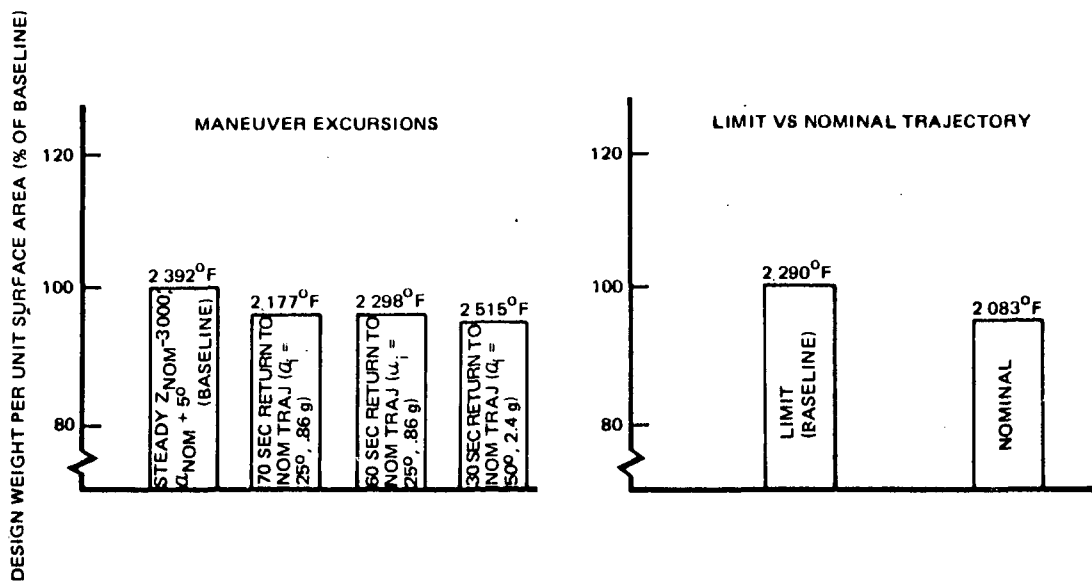
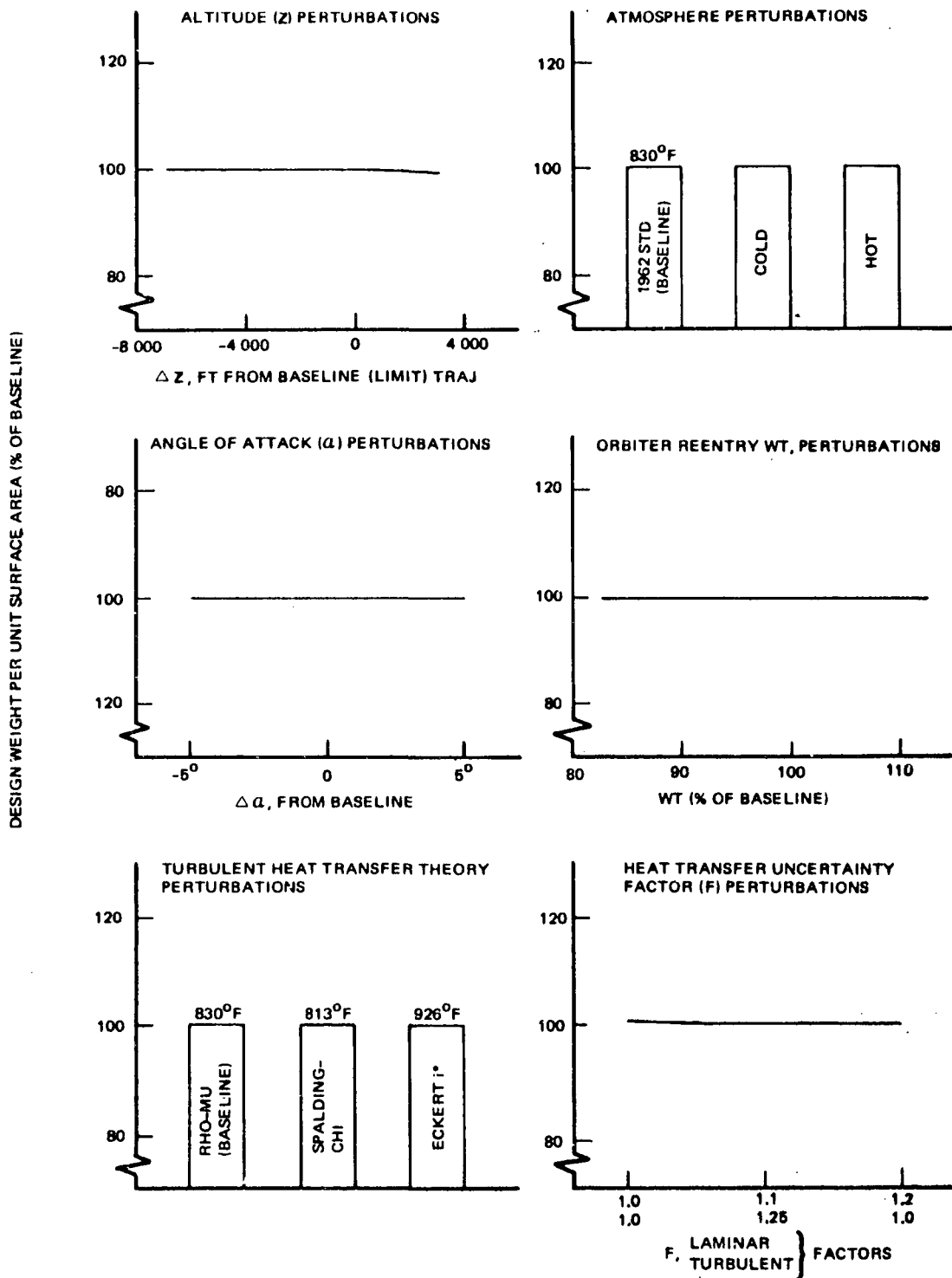


Figure 114. WEIGHT SENSITIVITIES
POINT NO. 3A – LOWER WING, MID-SEMISPAN, MIDCHORD – REI (Cont)



**Figure 114: WEIGHT SENSITIVITIES
POINT NO. 3A – LOWER WING, MID-SEMISPAN, MIDCHORD – REI (Cont)**



**Figure 115. WEIGHT SENSITIVITIES
POINT NO. 4 – WING UPPER SURFACE, MID-SEMISPAN, MIDCHORD – HOT STRUCTURE**

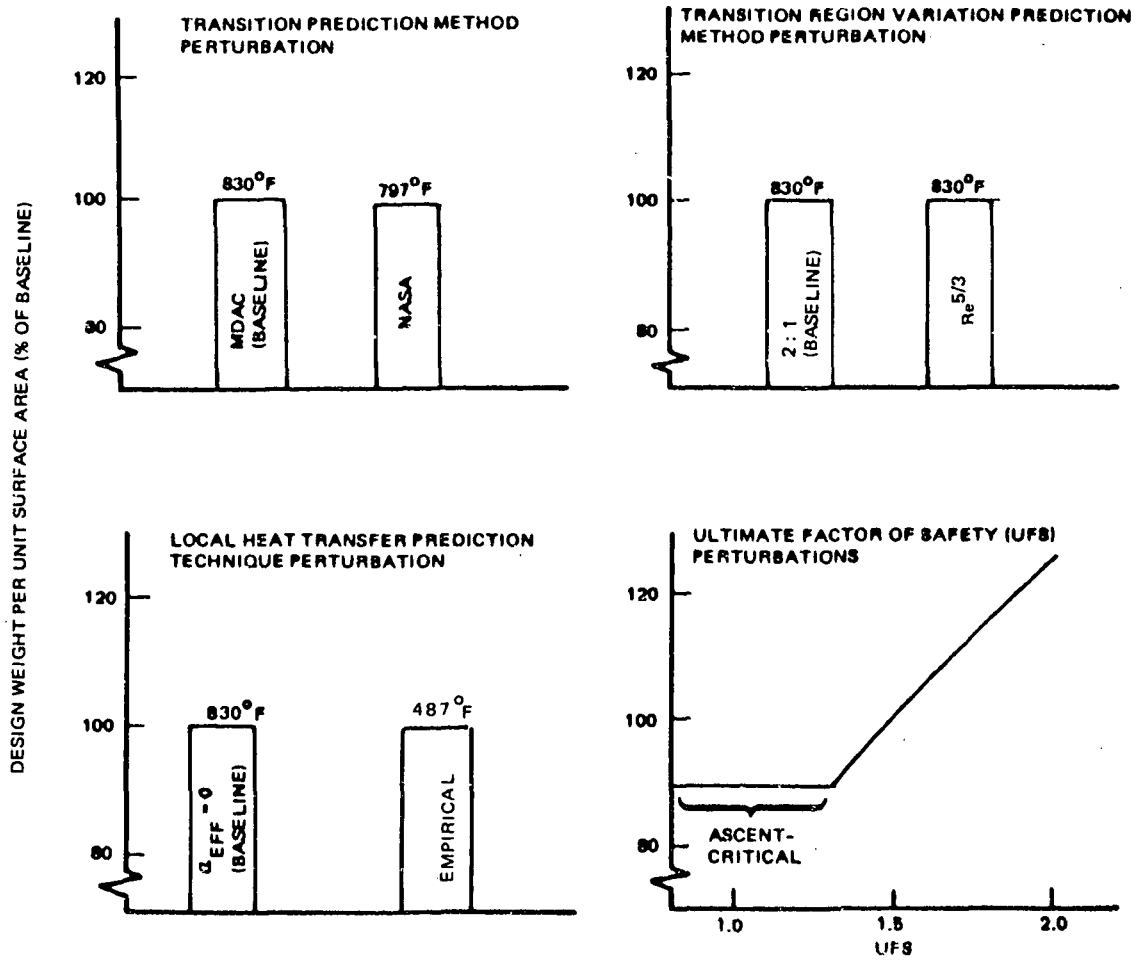


Figure 115. WEIGHT SENSITIVITIES
 POINT NO. 4 – WING UPPER SURFACE, MID-SEMISPAN, MIDCHORD – HOT
 STRUCTURE (Cont)

DESIGN WEIGHT PER UNIT SURFACE AREA (% OF BASELINE)

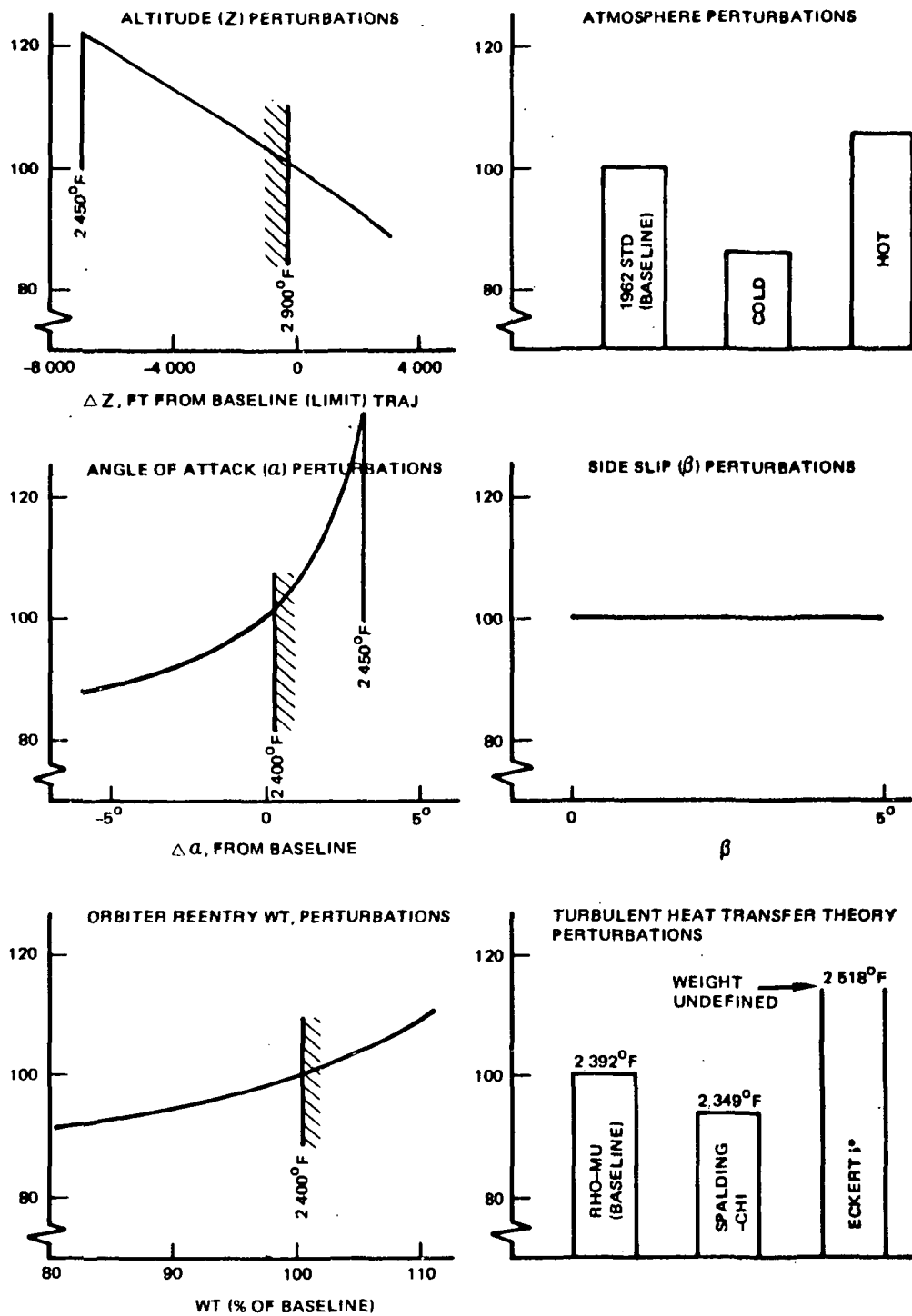


Figure 116: WEIGHT SENSITIVITIES
 POINT NO. 5 - LOWER WING, MID-SEMISPAN, LE BEAM-METAL TPS

DESIGN WEIGHT PER UNIT SURFACE AREA (% OF BASELINE)

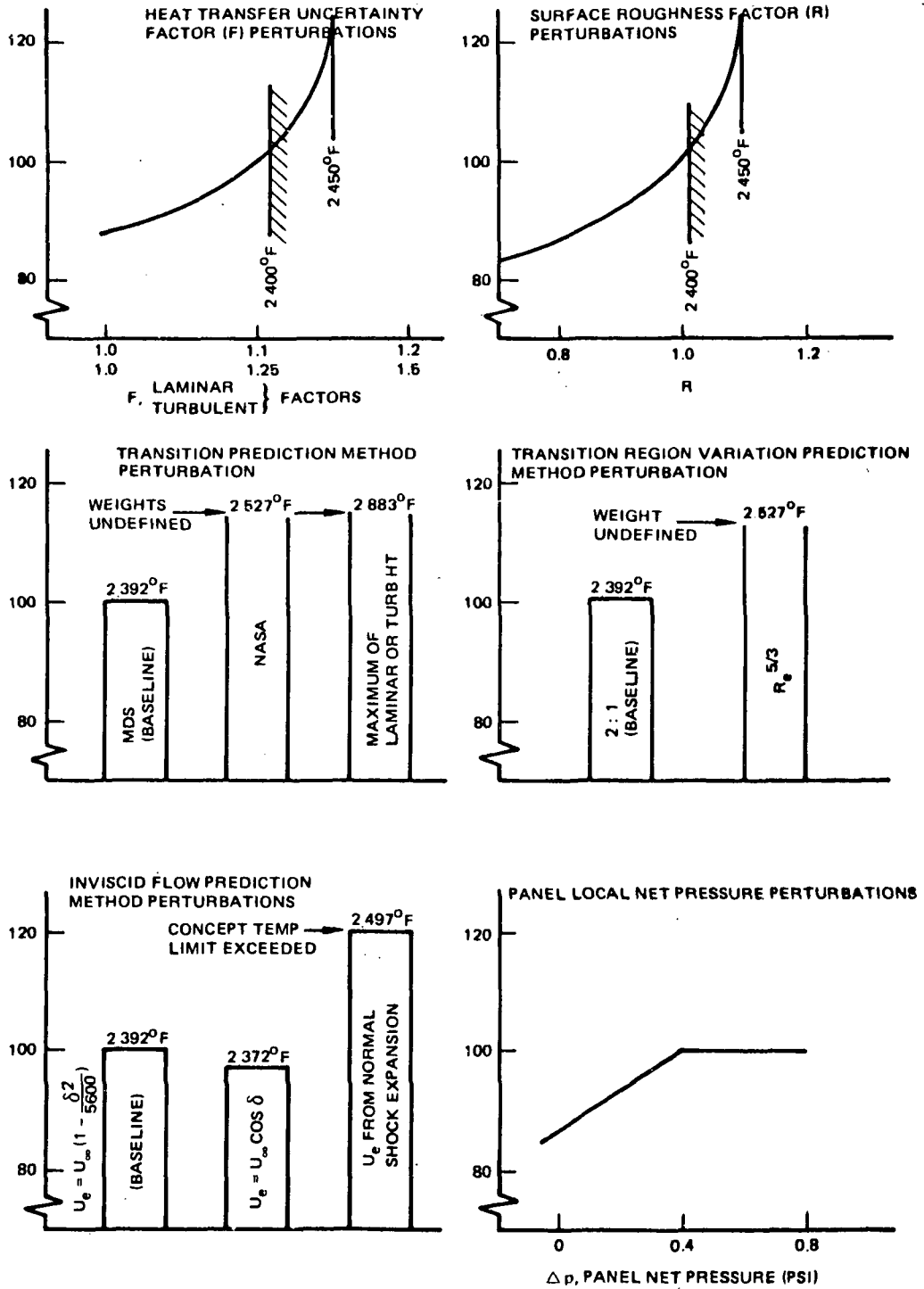
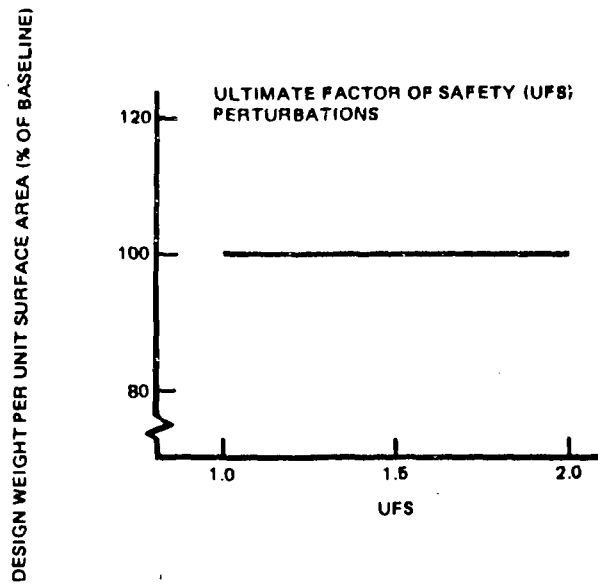


Figure 116. WEIGHT SENSITIVITIES
POINT NO. 5 – LOWER WING, MID-SEMISPAN, LE BEAM – METAL TPS (Cont)



**Figure 118. WEIGHT SENSITIVITIES
POINT NO. 5 – LOWER WING, MID-SEMISPAN, LE BEAM – METAL TPS (Cont)**

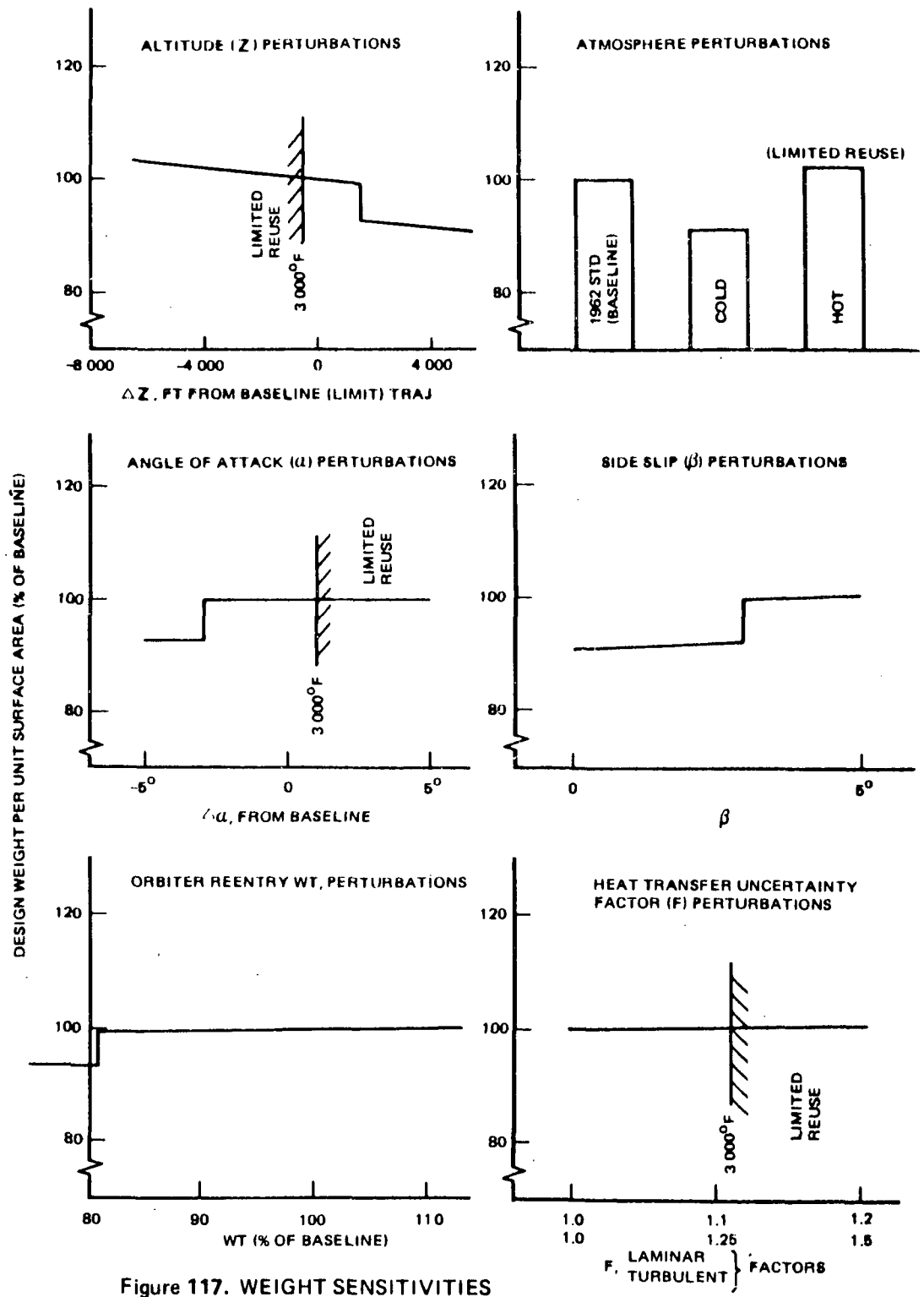


Figure 117. WEIGHT SENSITIVITIES
 POINT NO. 6 -- LE STAGNATION LINE -- CARBON / CARBON COMPOSITE

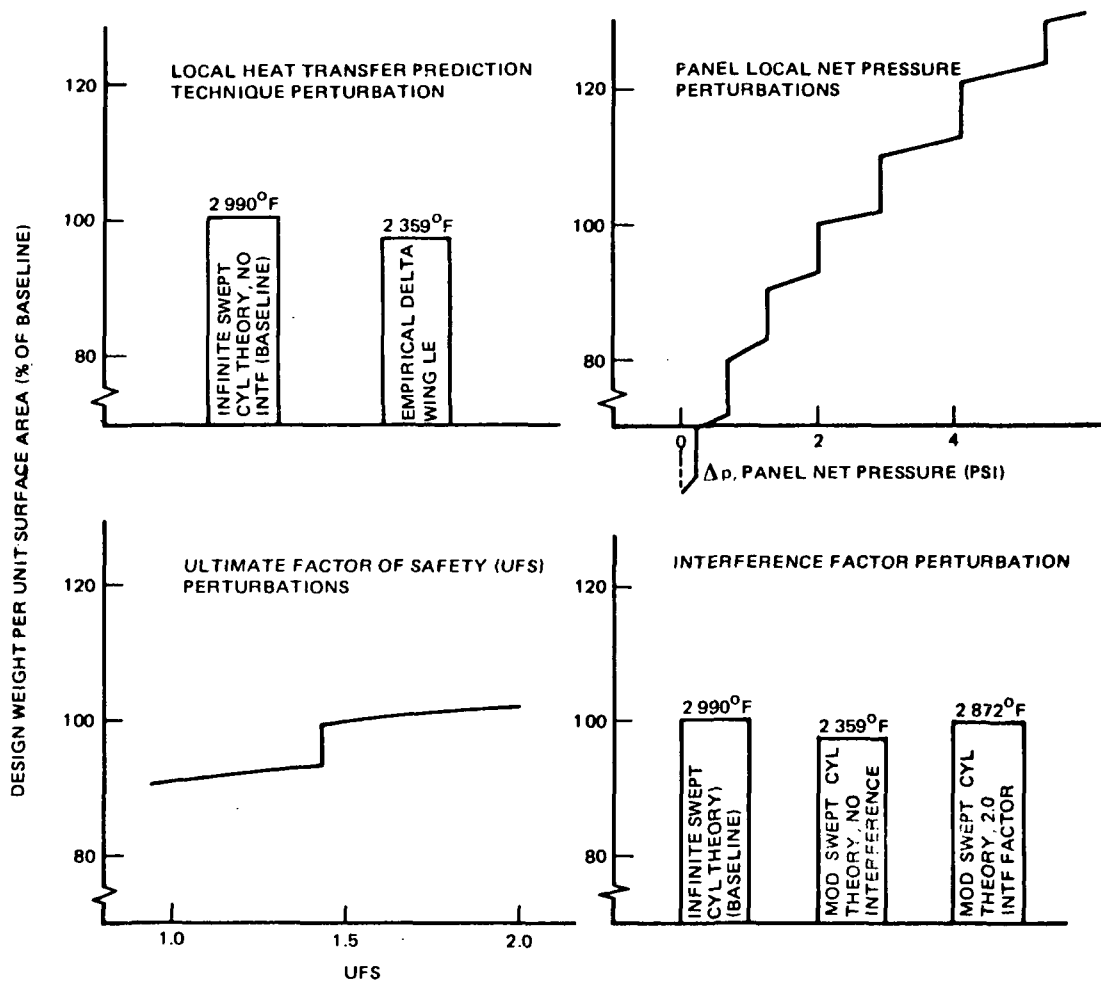


Figure 117. WEIGHT SENSITIVITIES
 POINT NO. 6 -- LE STAGNATION LINE -- CARBON / CARBON COMPOSITE (Cont)

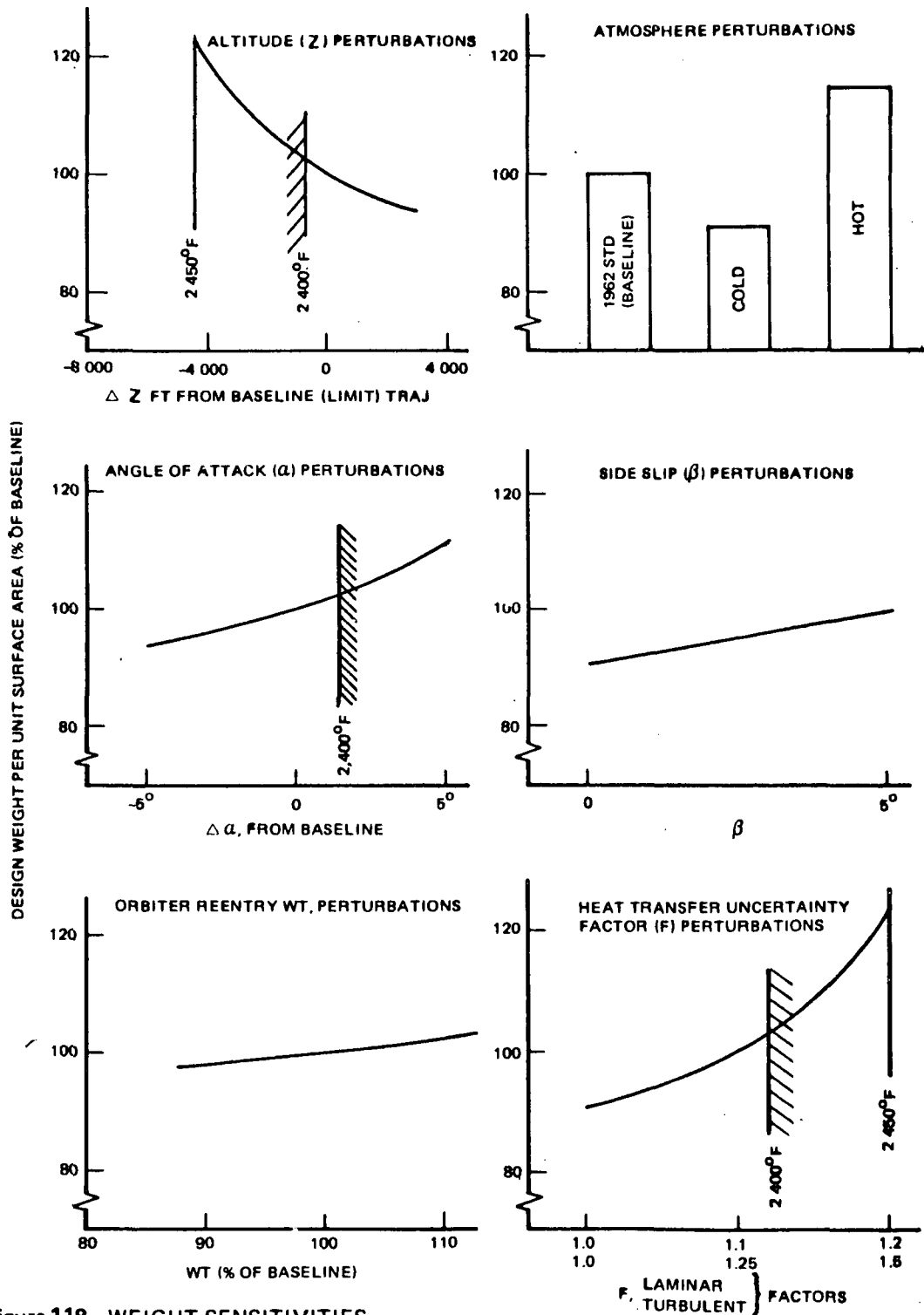


Figure 118. WEIGHT SENSITIVITIES
 POINT NO. 6A - WING LEADING EDGE STAGNATION LINE - METAL HEAT SHIELD TPS

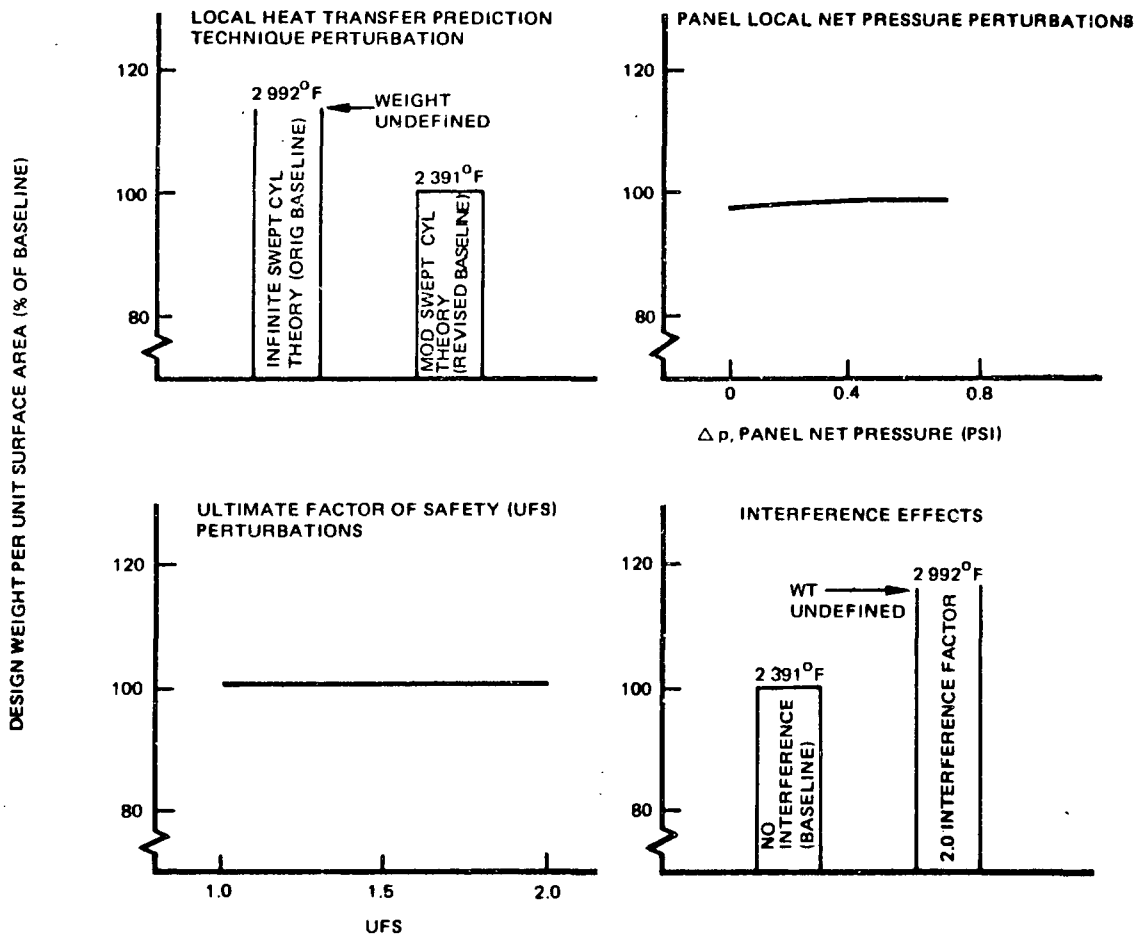


Figure 118. WEIGHT SENSITIVITIES
 POINT NO. 6A – WING LEADING EDGE STAGNATION
 LINE – METAL HEAT SHIELD TPS (Cont)

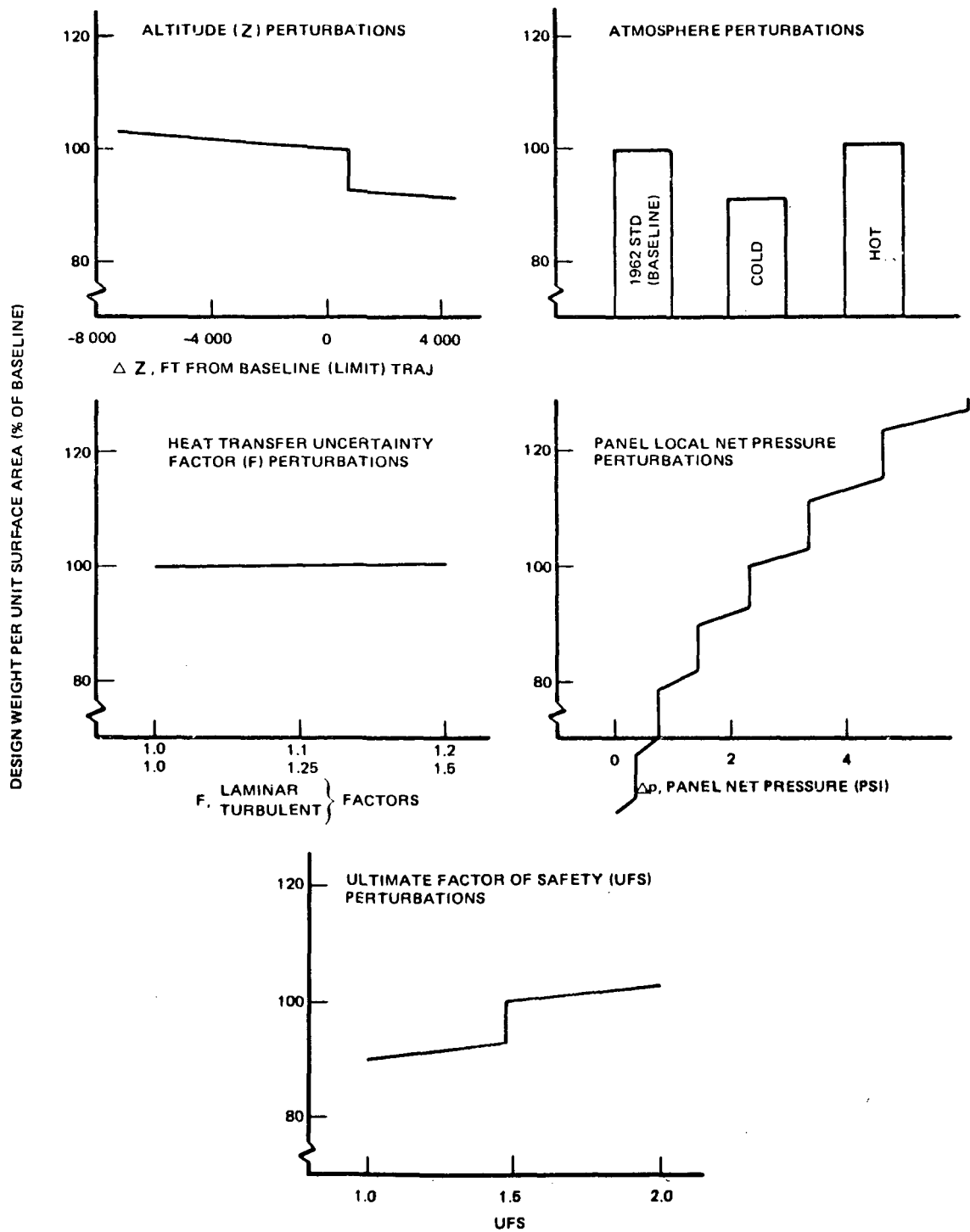


Figure 119. WEIGHT SENSITIVITIES
 POINT NO. 7 – NOSE STAGNATION POINT – CARBON / CARBON COMPOSITE

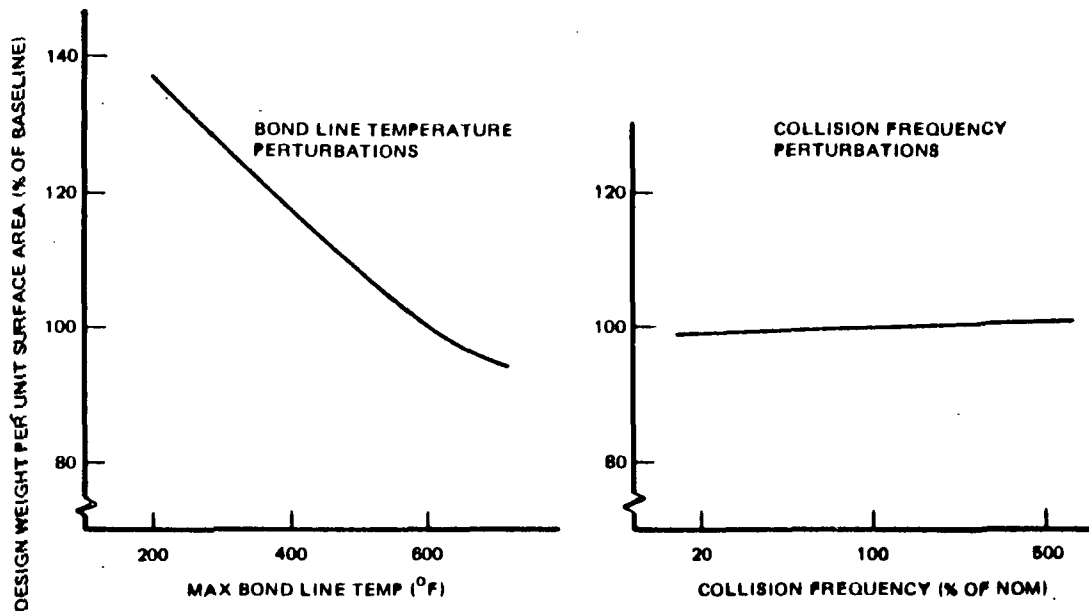


Figure 120: WEIGHT SENSITIVITIES
 POINT NO. 7A – NOSE STAGNATION POINT – NASA SILICONE ABLATOR

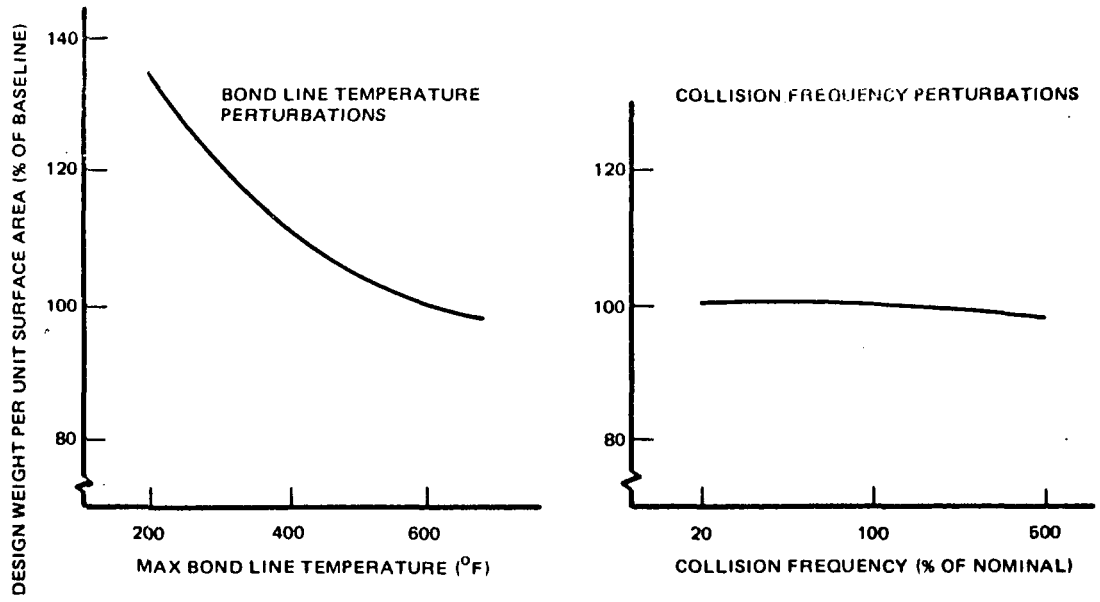


Figure 121: WEIGHT SENSITIVITIES
 POINT NO. 7B – NOSE STAG POINT – PHENOLIC NYLON WITH MICROBALLOONS

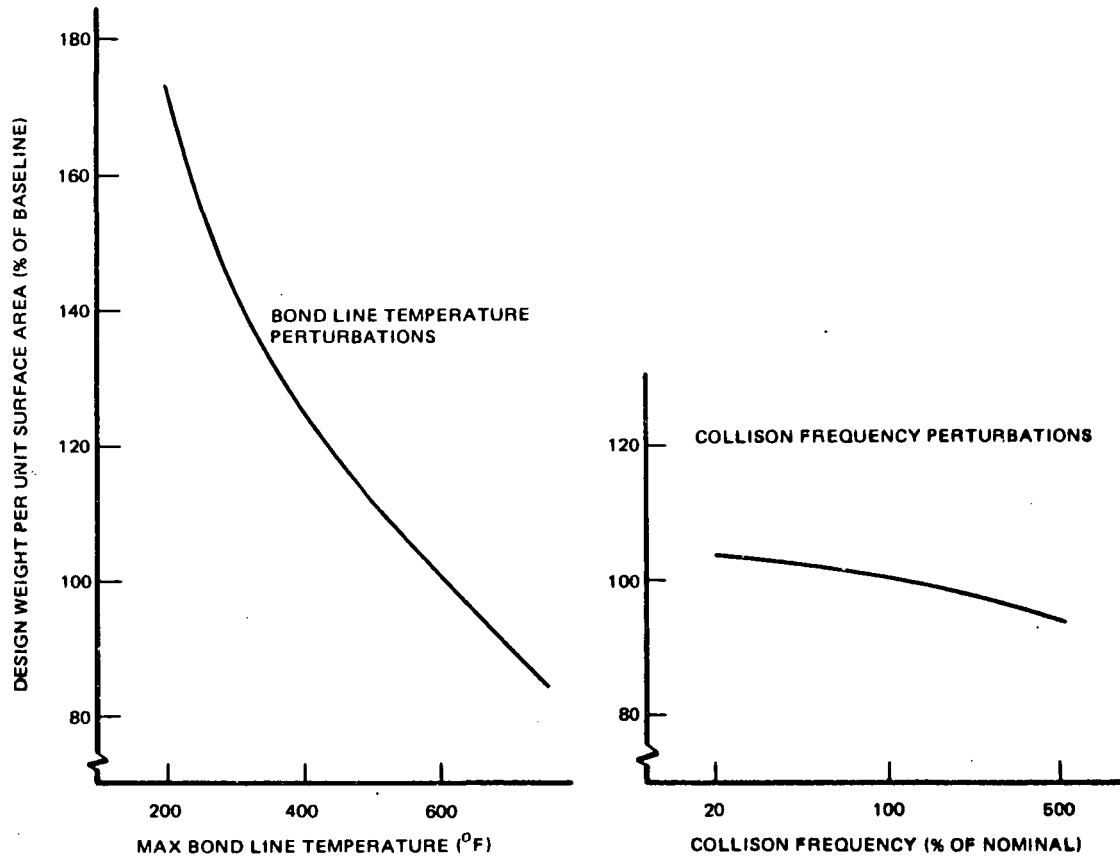


Figure 122. WEIGHT SENSITIVITIES
 POINT NO. 7B1 – NOSE STAGNATION POINT – PHENOLIC NYLON ABLATOR

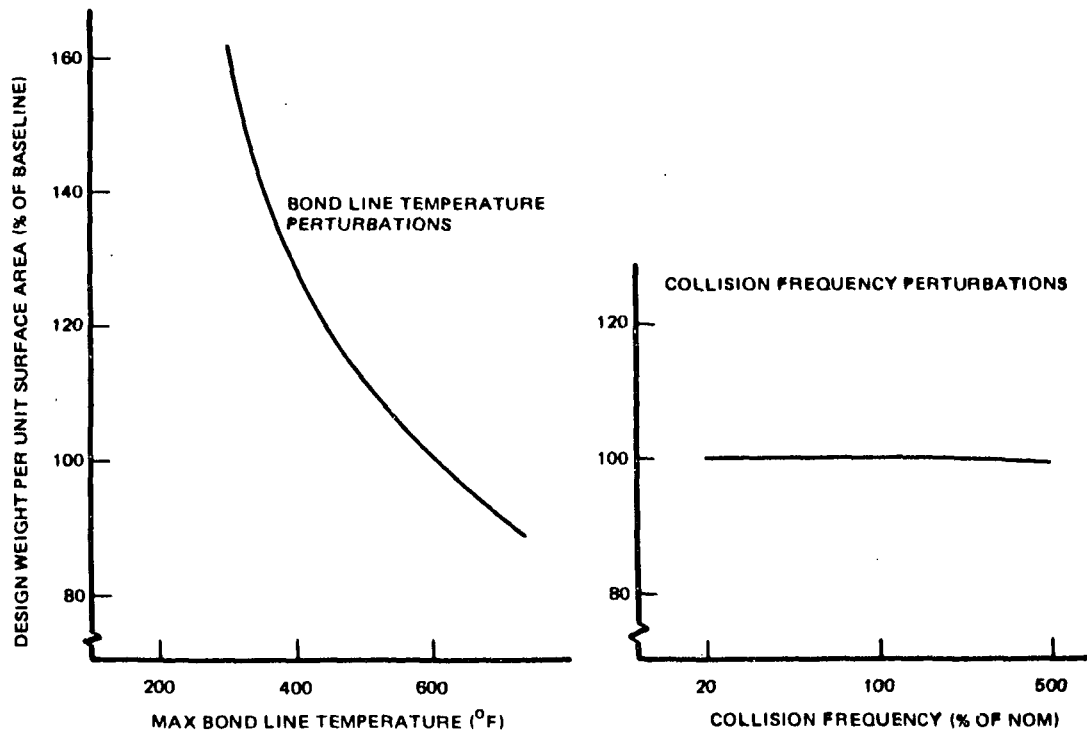


Figure 123. WEIGHT SENSITIVITIES
 POINT NO. 7C - NOSE STAGNATION POINT - APOLLO MATERIAL ABLATOR

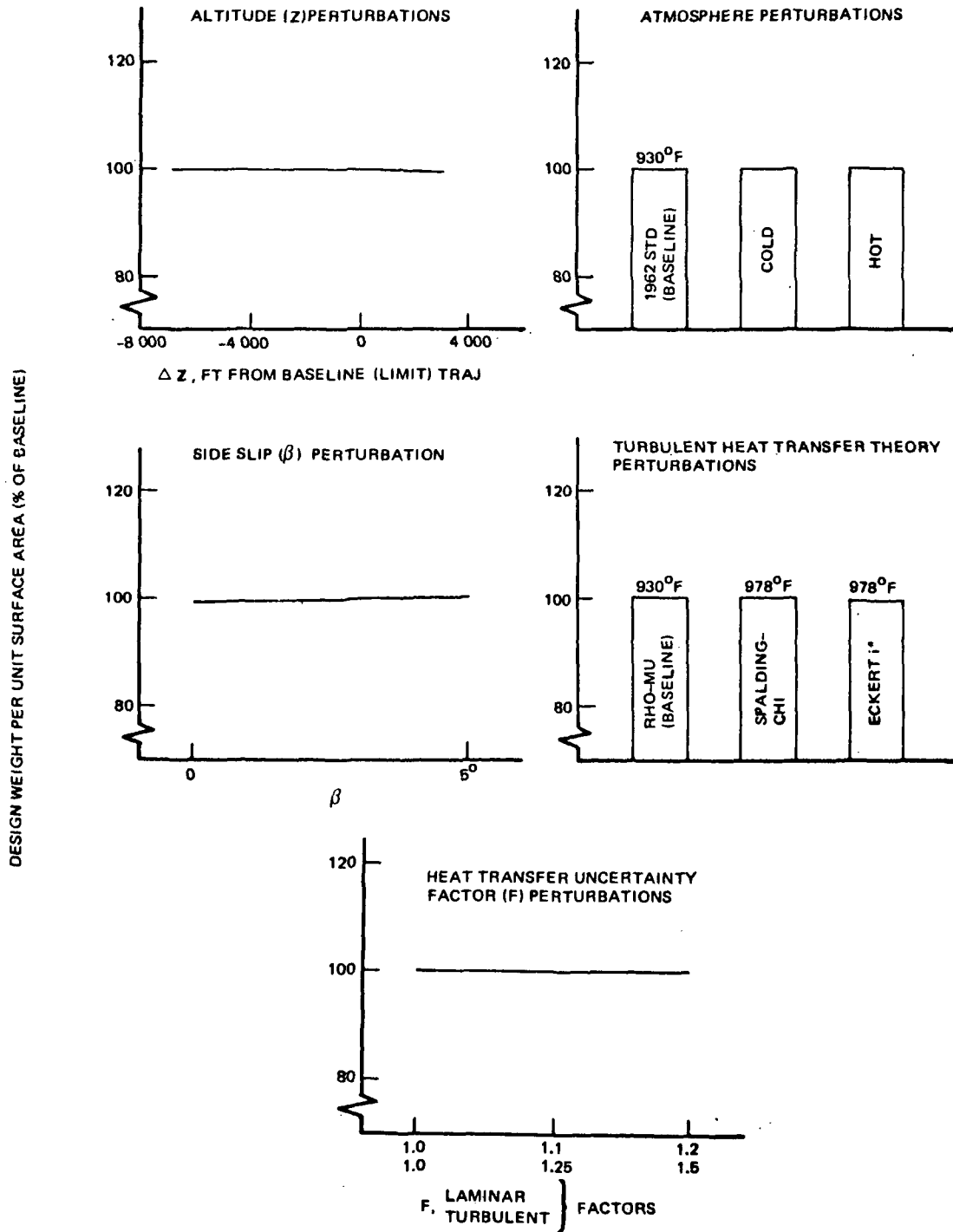


Figure 124. WEIGHT SENSITIVITIES
 POINT NO. 8 - FIN SIDE, MIDSPAN, MIDCHORD - HOT STRUCTURE

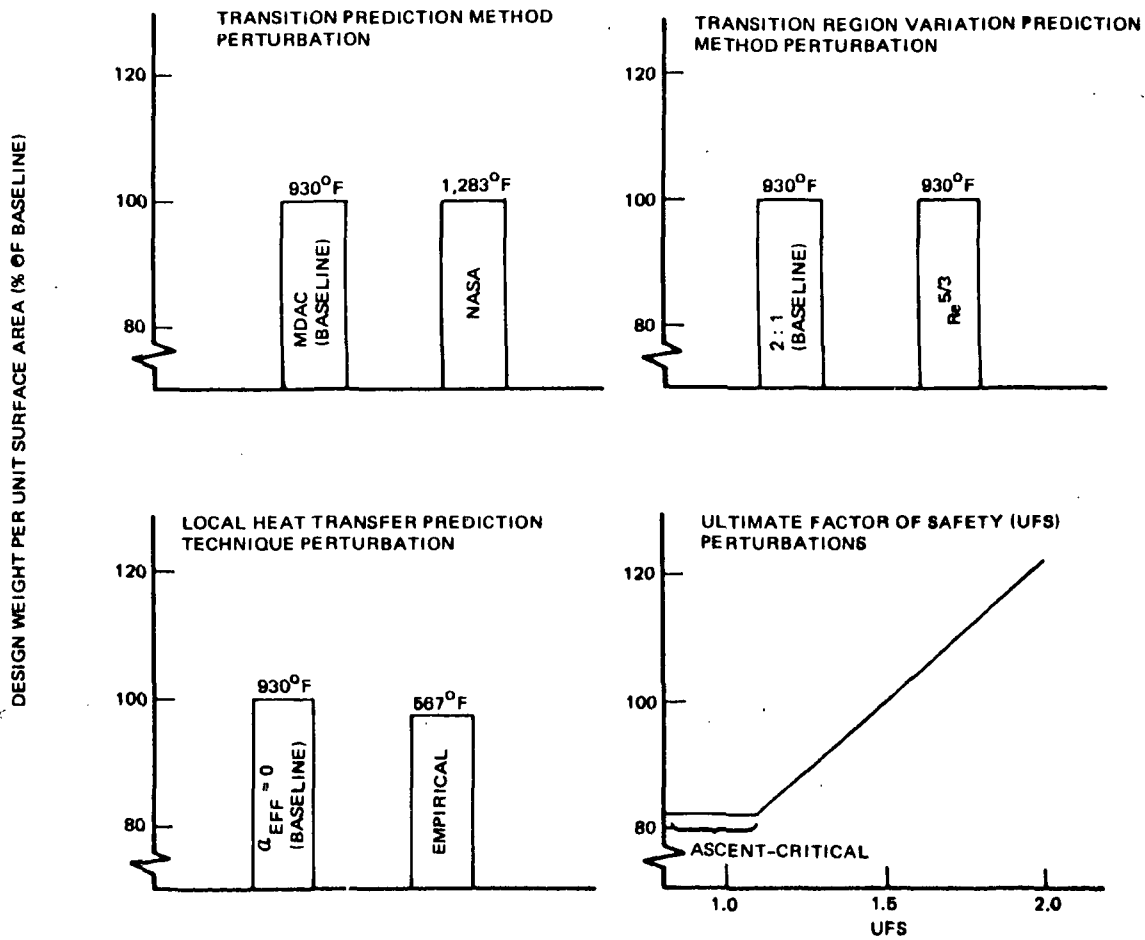


Figure 124 . WEIGHT SENSITIVITIES
 POINT NO. 8 - FIN SIDE, MIDSPAN, MIDCHORD - HOT STRUCTURE (Cont)

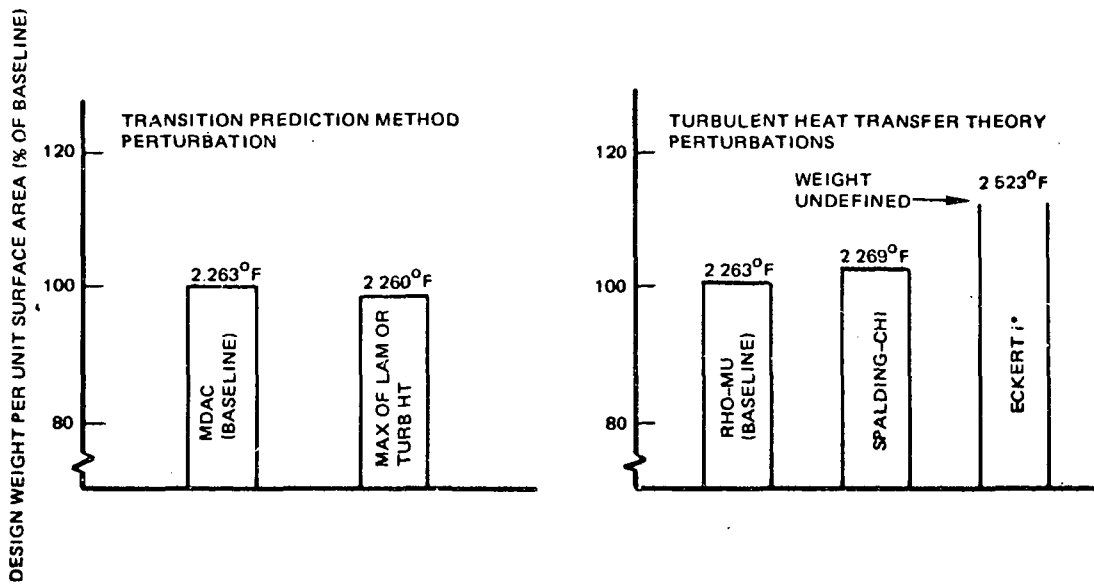


Figure 125. WEIGHT SENSITIVITIES
 POINT NO. 9 - LOWER AFT BODY - METAL HEAT SHIELD TPS

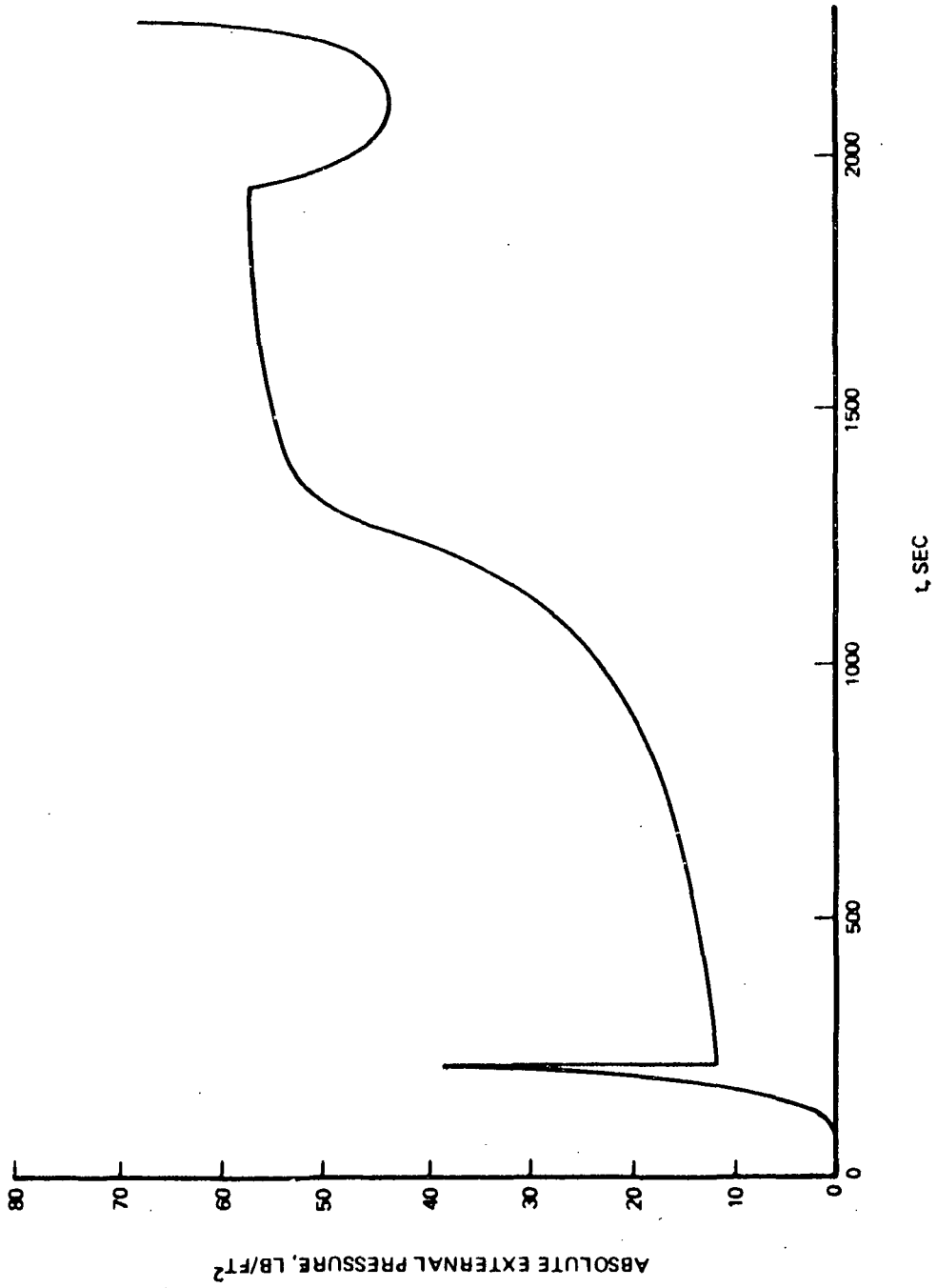


Figure 126. POINT NO. 3 EXTERNAL SURFACE PRESSURE

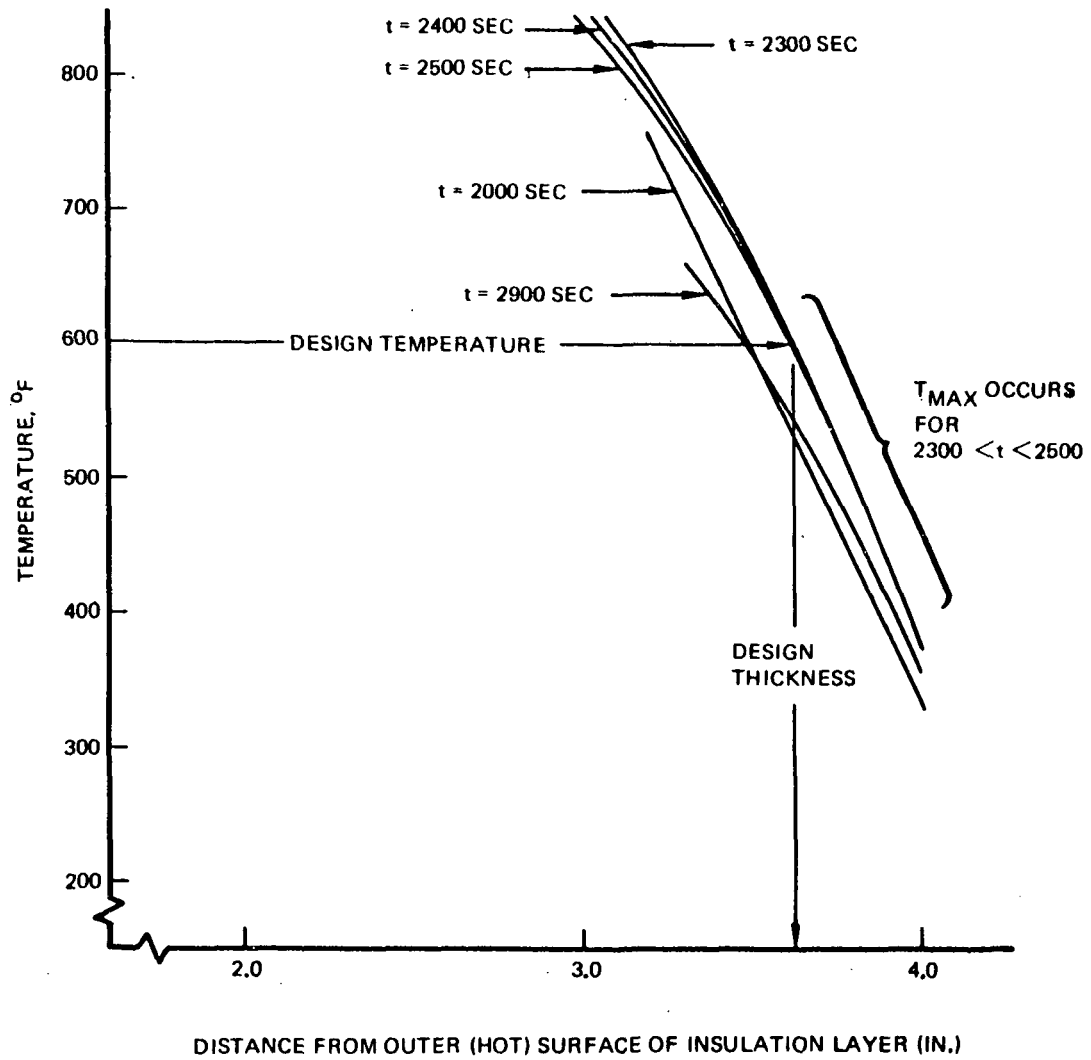


Figure 127: POINT NO. 3 BASELINE INSULATION TEMPERATURES

REFERENCES

1. Technical Summary Draft, Space Shuttle Program Phase B Systems Study Final Report. McDonnell Douglas Corporation, Report MDC #0308; March 1971.
2. Daniels, G. E.: Terrestrial Environment (Climatic) Criteria Guidelines for Use in Space Vehicle Development, 1969 Revision. Second printing, NASA TM-X-53872, March 1970.
3. Space Shuttle Phase B Final Report. Space Division, North American Rockwell, Report SD71-114-2, March 1971.
4. Space Shuttle Baseline Descriptions. Space Division, North American Rockwell, Report SV 71-8, January 1971.
5. Nathan, A. (Grumman Aerospace Corporation): Personal Communication to E.W. Brogren (The Boeing Company), May 1971.
6. Boll, R. T.: Unpublished Boeing Company Data, January 1964.
7. Anon.: Unpublished Boeing Company Data, January 1964.
8. Alternate Space Shuttle Concepts Study Final Report. Grumman-Boeing, Report MSC-03810, July 1971.
9. Smith, W. (NASA MSFC): Personal Communication to W. Trotter (The Boeing Company), June 1971.
10. Structural Design Criteria Applicable to a Space Shuttle. NASA SP-8057, January 1971.
11. Hammersley, J. M., and Handscomb, D. C.: Monte Carlo Methods. John Wiley and Sons, New York, 1964.
12. Merchant, D. H.: Lunar Landing Statistical Loads Analysis Final Report. The Boeing Company, Document D2-84124-7, June 1967.
13. Becker, J. V.: "The X-15 Program in Retrospect."
III. Eugen-Sanger-Gedachtnisvorlesung, Raumfahrtforschung, Heft 2/69.
14. Analysis and Design of Supersonic Wing-Body Combinations Including Flow Properties in the Near Field. NASA CR-73106.
15. Wells, P. B.: A Method for Predicting the Thermal Response of Charring Ablation Materials. The Boeing Company, Document D2-23256, June 1964, AD-443144.
16. Ames Research Staff: Equations, Tables, and Charts for Compressible Flow, NACA Report 1135, 1953.
17. Nagel, A. L.; Fitzsimmons, H. D.; and Doyle, L. B.: Analysis of Hypersonic Pressure and Heat Transfer Tests on Delta Wings with Laminar and Turbulent Boundary Layers, NASA CR-535, August 1966.
18. Savage, R. T.; and Jaeck, C. L.: Investigation of Turbulent Heat Transfer at Hypersonic Speeds; AFFDL-TR-67-144, December 1967 (Volumes 1 and 3).

19. Hanks, R. A., and Savage, R. T.: Thermal Design Methods for Recoverable Launch Vehicles with Consideration of Arbitrary Wall Temperature and Surface Conditions, The Boeing Company, Document D2-90770-1, August 1965.
20. Wilson, R. E.: "Viscosity and Heat Transfer Effects," Sections 13 and 14, Handbook of Supersonic Aerodynamics, NAVORD Report 1488, Vol. 5, August 1966.
21. Wilson, R. E.: "Laminar Boundary Layer Growth on Slightly Blunted Cones at Hypersonic Speeds," J. Spacecraft, Vol. 2, No. 4, pp. 490-496, 1965.
22. Jaeck, C. L.: Analysis of Pressure and Heat Transfer Tests on Surface Roughness Elements with Laminar and Turbulant Boundary Layers: NASA CR-537, 1966.
23. Johnson, C. B.: "Boundary Layer Transition and Heating Criteria Applicable to Space Shuttle Configurations from Flight and Ground Tests," NASA Space Shuttle Technology Conference, Vol. 1, NASA TM-X-2272, April 1971.
24. Dunnivant, J. C. (NASA-LRC): Personal Communication to A. C. Thomas (The Boeing Company), May 1971.
25. Wilson, J. L.; Pennelegion; Cash, R. F.; and Shilling, M. J.: Heat Transfer and Transition Measurements at $M = 8.5$ on a Delta Model and a Flat Plate of Incidence. Ministry of Technology Aeronautical Research Council Reports and Memoranda No. 3574, March 1968.
26. Spalding, D. B., and Chi, S. W.: "The Drag of a Compressible Turbulent Boundary Layer on a Smooth Flat Plate with and without Heat Transfer," J. Fluid Mech. 18 (1), pp. 117-143, 1964.
27. Eckert, E. R. G.: Survey on Heat Transfer of High Speeds, WADC Technical Report 54-70, 1954.
28. Jew, M.: (Grumman Aerospace Corporation), Personal Communication, June 1971.
29. Reshotko, E.: "Heat Transfer to a General Three Dimensional Stagnation Point," Jet Propulsion, pp. 58-60, January 1958.
30. Jaeck, C.: Evaluation of Flow Field Parameters and Data/Theory Comparisons of Heat Transfer for Vehicles at High Angles of Attack, The Boeing Company, Document D180-10112-1, July 1970.
31. Ellison, J. C.: Experimental Stagnation Point Velocity Gradients and Heat Transfer Coefficients for a Family of Blunt Bodies of Mach 8 and Angles of Attack. NASA TN-D-5121, April 1969.
32. Marvin, J. G.; and Sinclair, A. R.: "Convective Heating in Regions of Large Favorable Pressure Gradients," AIAA Journal, November 1967, pp. 1940.
33. Forney, A. (NASA-MSFC): Personal Communication to A. C. Thomas (The Boeing Company), August 1971.
34. Whitehead, A. H.; and Dunavant, J. C.: A Study of Pressure and Heat Transfer Over an 80° Sweep Slab Delta Wing in Hypersonic Flow. NASA TN-D-2708, March 1965.
35. Everhart, P. E.; and Dunavant, J. C.: Heat Transfer Distributions on 70° Swept Slab Delta Wings at a Mach Number of 9.86 and Angles of Attack up to 90° . NASA TN-D-2302, October 1964.

36. Marvin, J. G.; Lockman, W. K.; Mateer, G. G.; Seegmiller, H. L.; Pappas, C. C.; DeRose, C.; and Kaatari, G. E.: "Flow Fields and Aerodynamic Heating of Space Shuttle Orbiters," NASA Space Shuttle Technology Conference, NASA, TM-X-2272, April 1971.
37. Stallings, R. L.; Burbank, P. B.; and Howell, D. T.: Heat Transfer and Pressure Measurements on Delta Wings at Mach Numbers of 3.51 and 4.65 and Angles of Attack from -45° to 45° , NASA TN-D-2387, August 1964.
38. Bertram, M. H.; and Everhart, P. E.: An Experimental Study of the Pressure and Heat Transfer Distributions on a 70° Sweep Slab Delta Wing in Hypersonic Flow, NASA TR-153, 1963.
39. Guard, F. L.; and Schultz, H. D.: Space Shuttle Aerodynamic Heating Considerations, Paper No. 70-HT/SPT-16, Presented at the Space Technology and Heat Transfer Conference in Los Angeles, California, June 21-24, 1970.
40. Turbulent Reference, Roughness, Leakage and Deflected Surface Heat Transfer and Pressure Tests for The Boeing Company conducted in the CAL 48 Hypersonic Shock Tunnel, The Boeing Company, Document D2-80910, January 1963.
41. Fay, J. A.; and Riddell, F. R.: "Theory of Stagnation Point Heat Transfer in Dissociated Air," Journal of the Aerospace Sciences, Vol. 25, No. 2, pp. 73, 1958.
42. Milhous, M. (Grumman Aerospace Corporation): Personal Communication, February 1971.
43. Thermal Protection Branch, Structures Division, NASA Langley Research Center, Private Communication to L. H. Hillberg (The Boeing Company).
44. Gaudette, R. S.; del Casal, E. P.; and Crowder, P. A.: Charring Ablation Performance in Turbulent Flow. The Boeing Company, Document D2-114031-1, September 1967.
45. Strauss, E. L.: "Superlight Ablative Systems for Mars Lander Thermal Protection," J. Spacecraft, Vol. 4, No. 10, pp. 1304-1309, 1967.
46. Gaudette, R. S.; del Casal, E. P.; Halstead, D. W.; and Deriugin, V.: Analysis of the Apollo Heat Shield Performance. The Boeing Company, Document D2-114433-1, March 1969, Contract NAS9-7964.
47. Kordes, E. E.; Tuovila, W. J.; and Guy, L. D.: Flutter Research on Skin Panels, NASA TN-D-451, September 1960.
48. Anon.: Unpublished Boeing Company data, 1970.
49. Wah Chang Albany Data Book, Columbium, Tantalum, and Tungsten Alloys, Vol. III, The Wah Chang Corporation, January 1968.
50. Rigidized Surface Insulative TPS Development. McDonnell-Douglas Corporation Report MDC EO312, February 1971.
51. "Mullite RSI Material Description and TPS Design," McDonnell Douglas Astronautics Company-East, paper presented at the NASA Langley Research Center sponsored REI Mini-Symposium at the University of Washington, Seattle, Washington, September 1971.

52. Greenshields, D. H. (NASA-MSD): Personal Communication to W. C. Thornton (NASA-LRC), June 1971.
53. Crawford, R. F.; and Burns, A. B.: Strength, Efficiency, and Design Data for Beryllium Structures. Lockheed Missiles & Space Company, ASD Technical Report 61-692, February 1962.



POSTMASTER: If Undeliverable (Section 158
Postal Manual) Do Not Return

"The aeronautical and space activities of the United States shall be conducted so as to contribute . . . to the expansion of human knowledge of phenomena in the atmosphere and space. The Administration shall provide for the widest practicable and appropriate dissemination of information concerning its activities and the results thereof."

—NATIONAL AERONAUTICS AND SPACE ACT OF 1958

NASA SCIENTIFIC AND TECHNICAL PUBLICATIONS

TECHNICAL REPORTS: Scientific and technical information considered important, complete, and a lasting contribution to existing knowledge.

TECHNICAL NOTES: Information less broad in scope but nevertheless of importance as a contribution to existing knowledge.

TECHNICAL MEMORANDUMS: Information receiving limited distribution because of preliminary data, security classification, or other reasons. Also includes conference proceedings with either limited or unlimited distribution.

CONTRACTOR REPORTS: Scientific and technical information generated under a NASA contract or grant and considered an important contribution to existing knowledge.

TECHNICAL TRANSLATIONS: Information published in a foreign language considered to merit NASA distribution in English.

SPECIAL PUBLICATIONS: Information derived from or of value to NASA activities. Publications include final reports of major projects, monographs, data compilations, handbooks, sourcebooks, and special bibliographies.

TECHNOLOGY UTILIZATION PUBLICATIONS: Information on technology used by NASA that may be of particular interest in commercial and other non-aerospace applications. Publications include Tech Briefs, Technology Utilization Reports and Technology Surveys.

Details on the availability of these publications may be obtained from:

**SCIENTIFIC AND TECHNICAL INFORMATION OFFICE
NATIONAL AERONAUTICS AND SPACE ADMINISTRATION
Washington, D.C. 20546**